AD________________

Award Number: W81XWH-07-1-0099

TITLE: Development of Highly Sensitive Bulk Acoustic Wave Device Biosensor Arrays for Screening and Early Detection of Prostate Cancer

PRINCIPAL INVESTIGATOR: Anthony J. Dickherber, Ph.D.

CONTRACTING ORGANIZATION: Georgia Tech Research Corporation
Atlanta, GA 30332

REPORT DATE: January 2009

TYPE OF REPORT: Annual Summary

PREPARED FOR: U.S. Army Medical Research and Materiel Command
Fort Detrick, Maryland 21702-5012

DISTRIBUTION STATEMENT: Approved for Public Release;
Distribution Unlimited

REPORT DOCUMENTATION PAGE	*Form Approved* *OMB No. 0704-0188*

1. REPORT DATE 1 Jan 2009	**2. REPORT TYPE** Annual Summary	**3. DATES COVERED** 1 Jan 2007 – 31 Dec 2008

4. TITLE AND SUBTITLE Development of Highly Sensitive Bulk Acoustic Wave Device Biosensor Arrays for Screening and Early Detection of Prostate Cancer	**5a. CONTRACT NUMBER**
	5b. GRANT NUMBER W81XWH-07-1-0099
	5c. PROGRAM ELEMENT NUMBER
6. AUTHOR(S) Anthony J. Dickherber, Ph.D., Christopher D Corso, William D Hunt E-Mail: dickherber@gmail.com	**5d. PROJECT NUMBER**
	5e. TASK NUMBER
	5f. WORK UNIT NUMBER
7. PERFORMING ORGANIZATION NAME(S) AND ADDRESS(ES) Georgia Tech Research Corporation Atlanta, GA 30332	**8. PERFORMING ORGANIZATION REPORT NUMBER**
9. SPONSORING / MONITORING AGENCY NAME(S) AND ADDRESS(ES) U.S. Army Medical Research and Materiel Command Fort Detrick, Maryland 21702-5012	**10. SPONSOR/MONITOR'S ACRONYM(S)**
	11. SPONSOR/MONITOR'S REPORT NUMBER(S)

12. DISTRIBUTION / AVAILABILITY STATEMENT
Approved for Public Release; Distribution Unlimited

13. SUPPLEMENTARY NOTES

14. ABSTRACT

In this research, I present several novel contributions to the field of microelectronic acoustic biosensors that approach the goal of developing a cost-effective, highly sensitive and highly selective sensor array for the detection of early cancer proliferation. First I report on the development of a novel solidly mounted shear-mode resonator employing piezoelectric ZnO as an appropriate base device for liquid-phase sensing applications. Second I report on the development of a novel and appropriate chemical surface preparation protocol for the covalent immobilization of monoclonal IgG antibodies to the surface of this device, thereby functionalizing it as a biosensor. Proof of functionality is demonstrated employing these sensors for the detection of various known cancer biomarkers in complex media as well as progress towards developing a packaged disposable sensor array system is also reported.

15. SUBJECT TERMS
Prostate cancer, early detection, biosensor, microelectronic acoustics

16. SECURITY CLASSIFICATION OF:			**17. LIMITATION OF ABSTRACT**	**18. NUMBER OF PAGES**	**19a. NAME OF RESPONSIBLE PERSON** USAMRMC
a. REPORT U	**b. ABSTRACT** U	**c. THIS PAGE** U	UU	270	**19b. TELEPHONE NUMBER** *(include area code)*

Table of Contents

Introduction

Microelectronic acoustic devices have long been recognized as offering great potential as biomedical sensors; specifically microelectronic piezoelectric resonators. Excitation of a thickness shear mode (TSM) in a piezoelectric crystal bulk is ideal for liquid-phase applications (*e.g.* blood or serum) as aqueous solutions cannot support propagation of a shear wave. Therefore, minimal acoustic energy is lost into the liquid media. The resonance condition (or resonance frequency) of the device then becomes a highly sensitive real-time indicator of any changes in surface conditions. The resonator is functionalized as a biosensor by immobilization of a bio- or chemi-specific layer at the surface of the device. Specific binding events at the biolayer interface therefore cause changes in the surface conditions resulting in a change of the resonance frequency, which is an easily monitored parameter. Employing common fabrication methods from the microelectronic device industry, this very cost-effective biosensor could be used for multiple applications. As a screening tool, this sensor device offers the possibility of detecting extremely low concentrations of multiple targets in a physiologically noisy environment at a very low cost. For researchers, it is a powerful tool for conducting basic proteomics research in the laboratory.

The implementation of this biosensor technology towards early cancer detection is reliant upon the discovery of appropriate biomarkers. Prostate cancer is an especially attractive initial focus for this research as much work has already gone into identifying various potential diagnostically relevant biomarkers. Of course early indicators involve the various forms of prostate specific antigen (PSA), but more recently a great deal of excitement has surrounded the relevance of early prostate cancer antigen (EPCA-2) [1].

The purpose of this research is to design and develop a new biosensor array technology that offers near real-time reporting and high specificity simultaneously for multiple targets, with a high degree of specificity, producible at low cost. This proposal builds upon a significant amount of past research that demonstrates the feasibility of this goal, yet has thus far fallen short. A new piezoelectric material to supplant crystal quartz is required to achieve greater sensitivity over the widely used quartz crystal microbalance (QCM) biosensor [2, 3] and allow for miniaturization. A novel surface chemistry is required to immobilize specific capture molecules on the surface of that crystal which likely will not have been developed before. Finally, the biosensor array system will need to be packaged in such a way that liquid samples can be introduced to the sensor surface in a controlled fashion.

Body

Three primary research goals were submitted in the *statement of work* for this training project. In general, they were as follows:

1. *The design and development of acoustic resonator arrays that could be employed as liquid-phase biosensors;*
2. *The development of a repeatable surface chemistry protocol appropriate for our resonator material for immobilization of specific capture molecules;*
3. *Testing the sensor array system for known cancer biomarkers in an effort to establish a protocol for early cancer detection.*

I present evidence showing completion of the first two goals with significant achievements to report on the third. Practical developments with regards to packaging and testing the devices prevented completion of the third goal in the two-year time frame allowed for this research. A great deal has been learned with regards to accomplishing this final goal and are presented at the end of this report. A more thorough treatment of the entire body of research is available in the attached Doctoral Thesis document included in the Appendix.

Goal 1: Device design and development

Microelectronic biosensors are comprised of a transducer element coupled with a molecularly-specific surface treatment. As indicated in the submitted statement of work, the transducer element selected for this biosensor application is an acoustic resonator. It was decided early that a bulk acoustic wave (BAW) device should be employed rather than a surface acoustic wave (SAW) device for this liquid-phase biosensor application. Past success with BAW devices is demonstrated by the QCM towards liquid-phase biosensor applications swayed this decision, as these devices have already been shown to exhibit strong qualities as liquid biosensors [2, 3]. Furthermore, it is easier to achieve higher resonant frequencies with BAW devices than with SAW devices, which is a requirement for developing acoustic sensors with higher sensitivity.

ZnO solidly mounted resonator

A BAW resonator functions by maintaining the acoustic energy within the piezoelectric crystal film. This occurs by maintaining an apparent acoustic impedance of zero on opposing sides of the crystal film, which is the acoustic impedance of air. Thin film bulk acoustic resonators (FBAR) are generally implemented in the membrane form by etching the supporting material beneath the piezoelectric film yielding a device similar to the one seen in Figure 1 (left). This implementation is a mechanically fragile design and requires difficult and often very expensive fabrication steps. The solidly mounted resonator (SMR) implementation is a solution to this problem originally described by Newell [4] and is achieved through the use of an acoustic mirror; analogous to an optical Bragg reflector. Considering that the device package must be easily fabricated with existing

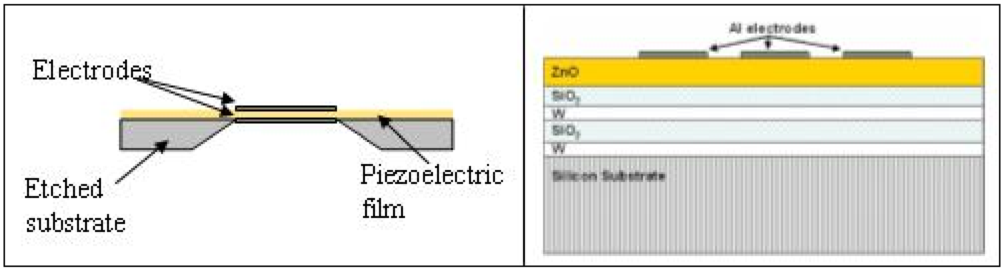

Figure 1. Comparison of traditional thin-film bulk acoustic resonator (FBAR) design (left figure) with solidly mounted resonator design (right figure) offers simple and robust fabrication alternative to traditional FBAR approach.

microelectronic fabrication equipment, a SMR package was selected as the base resonator design, as seen in Figure 1 (right).

Two piezoelectric crystal species were considered in developing the bulk acoustic resonator device that could be employed for our liquid-phase biosensor. Zinc oxide (ZnO) yielded results far superior to the tantalum pentoxide (Ta_2O_5) alternative that was attempted. Preliminary results for the quality of the ZnO resonators achieved were summarized and published in the *Journal of Applied Physics* [5]. Incidentally, the significance of this work was quickly recognized by and jointly published in the *Virtual Journal of Biological Physics Research*. The 2 GHz TSM resonator was achieved by lateral field excitation (LFE) of thin-film (< 1 μm) *c*-axis oriented ZnO, deposited by RF sputtering. Theoretical treatment of LFE of ZnO to achieve a TSM acoustic resonator has been available since the late 1980s [6] and some attempts published in the research literature prior to this work [7, 8], but these implementations had either very difficult fabrication requirements or yielded dubious results. Furthermore, LFE of ZnO had never been realized in an SMR implementation before this work. While these results are promising, it is felt that the device quality must be higher still than what has been achieved thus far in order to obtain the biosensor sensitivity promised by a device that exhibits such a high operating frequency. A more thorough treatment of issues relating to improving device quality is offered later in this section.

Device testing

Further testing was performed on the ZnO devices to evaluate their susceptibility to changing temperature and solution conductivity. Thermal testing is a standard resonator evaluation criterion, in which the reported parameter is the standard *temperature coefficient of resonant frequency* (TCF). Conductivity susceptibility tests had to be conducted due to the LFE method employed in this design. Since oppositely polarized electrode materials are deposited plane-parallel on the surface of the piezoelectric thin film and both exposed to the liquid sample under test, it is possible that the conductivity of the fluid might divert significant electrical energy away from the piezoelectric crystal and thereby substantially affect device performance. The results of both of the temperature susceptibility and sample conductivity tests were submitted to the IEEE Sensors 2007 Annual Conference by June of 2007 and presented in October of 2007 [9]. Thermal evaluation of the resonator yielded a low TCF of ~25 ppm/°C, which is desirable for biosensor application. Conductivity tests indicate that solution conductivity did have some effect on device performance as the device quality diminished with increasing solution conductivity. That is to say, that the resonance condition became more difficult to track with increasing solution conductivity, which is not a surprising result for the reason indicated above. Significantly, however, the solution conductivity did not have a significant effect on the resonance frequency itself, as can be seen from Figure 2 below. Further, it is expected that the degradation in monitoring precision will be substantially improved by further improving device quality factor, *Q*.

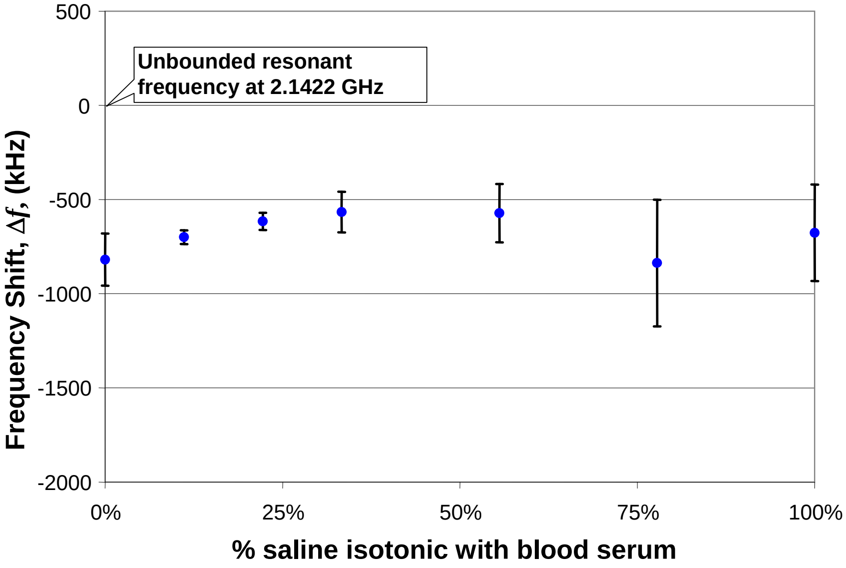

Figure 2. Change in resonant frequency as a function of increasing fluid sample conductivity

Tests were performed to evaluate device performance as a function of electrode geometry. Due to the difficulty of fabrication and various issues regarding spurious resonance activity, it was decided that a new electrode configuration was required that balanced the electromagnetic field incident on the piezoelectric film. There was also reason to believe that a superior resonator could be achieved by fabricating a device in which the gap size between electrodes was significantly larger than the piezoelectric film thickness, as described by Rosenbaum as preferable for LFE [6]. The new design was accomplished by implementing a more symmetric electrode design that surrounded the signal electrode with ground electrodes, rather than establishing the ground on a single side as seen in Figure 3. The two electrode geometries were then implemented with various electrode widths and gap sizes for each configuration. These results were summarized and submitted for publication in the *Sensors & Actuators A: Physics* journal [10].

In general, it was found that there was a marginal trade-off in performance parameters (*Q* and coupling coefficient, K^2) between the two electrode geometries implemented. Surprisingly, electrode width and inter-electrode gap width had very little effect on

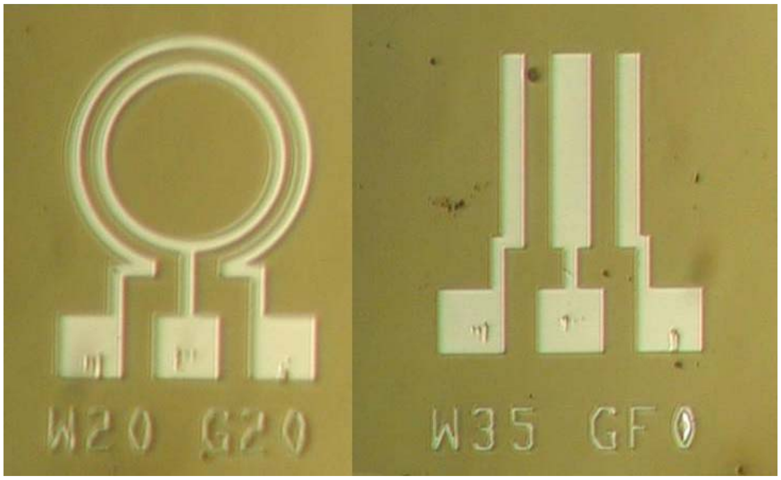

Figure 3. Various electrode shapes fabricated in an effort to determine the optimal LFE resonator configuration. [Note the left figure has electrode widths of 20 μm and a gap size of 20 μm, and the right figure has electrode widths of 35 μm and a gap size of 40 μm]

device performance. The results of these experiments are summarized in Table 1 below and graphically displayed in Figure 4.

Recall that resonators may function as sensors by monitoring the resonance frequency condition as a reflection of changing environmental conditions. For this reason, it was clear that device quality, *Q*, was the most important parameter to optimize, as it is the best predictor of how clearly the resonance condition can be monitored. The straight finger electrode design was therefore selected for implementation in an eight-device array structure, as seen in Figure 5. It was then necessary to quantify any loss in performance due to the array configuration. It was found that device *Q* deteriorated by approximately 30% as a result of the electrode configuration in the array structure. This is not surprising as the additional metallization required to implement the array structure would likely disturb the electric field distribution and thereby reduce the amount of electrical energy focused on stimulating the piezoelectric crystal. These results are also discussed further in the publication in *Sensors & Actuators A* [10].

Device	Shape	Electrode Width (μm)	Electrode Gap (μm)	# Tested	Average Q	Average K^2
A	Circular	20	10	92	198	0.86%
B	Circular	20	20	72	195	0.87%
C	Circular	20	40	70	192	0.86%
D	Straight	20	10	69	198	0.84%
E	Straight	35	20	74	217	0.78%
F	Straight	35	40	98	206	0.77%
G	Straight	20	50	25	220	0.74%
H	Straight	35	50	44	221	0.73%

Table 1. Assessment of device performance of tested resonators from analysis of collected S11 parameters.

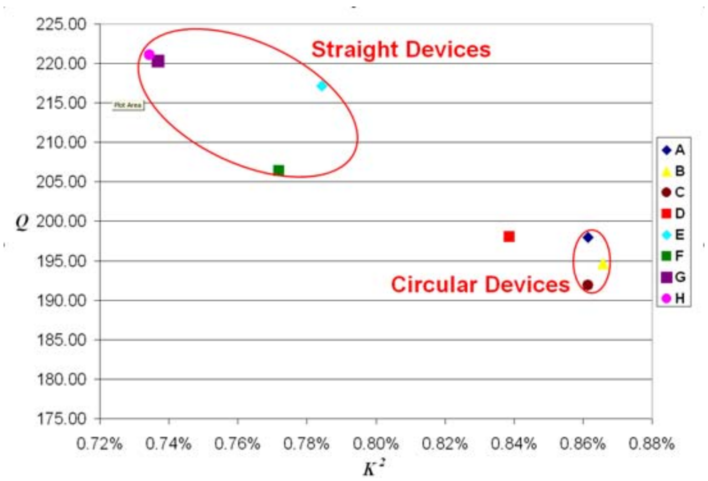

Figure 4. Comparison of various electrode configurations using Q and K^2.

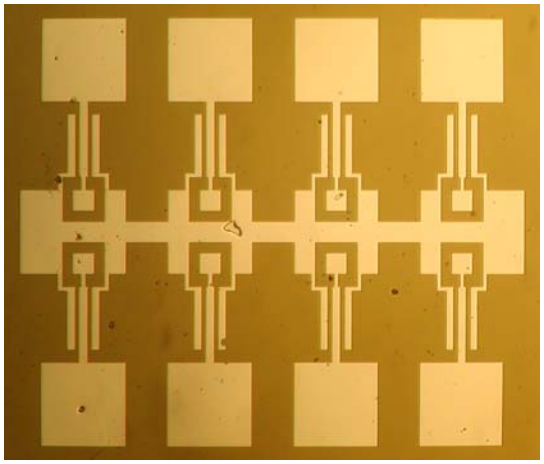

Figure 5. Digital image of fabricated 8-device array. Device is designed for probing with Cascade Microtech ACP40 GSG150 probes and with pads large enough for subsequent wire bonding. These devices have electrode widths of 50 μm and a gap size of 20 μm.

As mentioned earlier, the acoustic mirror functions similarly to an optical Bragg reflector. Alternating quarter-wavelength thin films of materials with high acoustic impedance mismatches are deposited as a substrate for the piezoelectric crystal layer in order to mimic an air boundary. That is to say, the acoustic mirror is meant to "appear" as having an acoustic impedance of zero in order to force acoustic energy to remain within the piezoelectric crystal, thereby achieving the resonance function. Investigations thus far have indicated that the mirror does not perform nearly as well as theoretical calculations predict, which is not a surprising result as theoretical calculations are based on perfect crystal uniformity and surface uniformity. Extensive investigation of the acoustic mirror performance was not able to yield a configuration for improved device *Q*. Significant efforts over the past year have gone towards improving device quality with limited success. It is strongly felt that the key to optimizing resonator device quality resides in optimization of the acoustic mirror for the given mode of operation. The time required for such an exhaustive investigation of the acoustic mirror for this application was impracticable given the two year time restriction for this research. I am quite confident, however, that optimization of device *Q*, and therefore optimization of the resonator for sensor applications, is a key component for sufficient development of this technology for commercial applications.

Goal 2: Surface preparation

It is a requirement of any analytical instrument that the output signal, or response, be repeatable given multiple identical samples under test. One of the most critical aspects in the development of high precision biosensors is the controlled immobilization of appropriate capture molecules to form a molecularly-specific surface on the device. Excessive variation in this process would obviate the achievement of a highly sensitive sensor, as deviations due to inconsistent immobilization would make impossible the ability to compare results from one sensor to any other; a control sensor, for example.

Covalent antibody immobilization

Attachment of antibodies to the surface of ZnO can be achieved through simple adsorption. The resulting surface coverage, uniformity and repeatability from this method are not sufficient for biosensor applications. Formation of a covalent bond between the antibody and ZnO surface via a chemical crosslinker is the preferred method over adsorption for several reasons. First, the stable bonds that are formed yield a more robust sensor. Further, it is often the case that biosensor experiments require that the sensor be subjected to fluidic flow. Therefore covalent immobilization of antibodies is important to withstand fluidic washing steps for preventing detachment of the antibodies from the surface. Detachment of capture molecules from the surface would erroneously affect the sensor's output signal.

To date, the literature pertaining to functionalizing crystal oxides through covalent methods has largely been focused on SiO_2. Hydroxyl groups at the surface of an oxide provide sites for reaction with cross-linking molecules to form covalent bonds [11]. One of the more common methods for functionalizing SiO_2 surfaces involves the use of organosilane molecules as primary crosslinkers. Organosilane molecules react at room temperature with surface hydroxides to link the silane molecules to the oxide surface. Success with immobilizing antibodies on silica surfaces has been shown using amine- and thiol-terminal silanes such as 3-Mercaptopropyltrimethoxysilane (MTS). Subsequent binding of a secondary crosslinker, such as N-γ-maleimidobutyryloxy succinimide ester (GMBS) [11, 12] serves the purpose of transforming the end group of the silane into a group that will bind covalently with functional groups on an antibody. It was initially intended to adopt methods described by Bhatia *et al* to compare the use of MTS and aminopropyl triethoxysilane (ATS) as the primary crosslinker to the crystalline ZnO surface [11, 12]. Results of these preliminary experiments demonstrated their inadequacy for use with ZnO.

Other work in modifying SiO_2 surfaces has focused on forming self-assembled monolayers using expoxysilanes [13, 14]. One advantage of using an expoysilane such as (3-glycidoxypropyl)trimethoxysilane (GPS) for forming self-assembled monolayers (SAMs) on oxide surfaces is that it eliminates the need for a heterobifunctional crosslinker between the silane molecule and target antibodies since the exposed epoxy groups react readily with amine groups on lysine residues of the antibody. The usefulness of this antibody immobilization technique has been illustrated on indium-tin oxide (ITO) substrates for the development of *Escherichia coli* O157:H7 sensors [15, 16]. One of the problems with modifying surface oxides using organosilanes is that the quality of surface modification is sensitive to the amount of water in the solvent or adsorbed to the surface of the oxide [17]. In anhydrous conditions, a partial monolayer of organosilane molecules forms. In excess H_2O, self-condensation can occur between the silane molecules and a multilayer will form. An alternative to organosilanes for surface modification of oxides is the use of phosphonic acids. Phosphonic acids do not suffer from the same susceptibility to hydration levels that organosilanes do. They have been used for the functionalization of ITO electrodes for development of electrochemical sensors [18] and for modifying TiO_2 particles [19]. In another study, phosphonic acids were used to pattern ITO and Indium Zinc Oxide (IZnO) through microcontact printing and subsequent wet etching [20].

A comparison between antibody immobilization protocols on device-quality sputtered ZnO surfaces was conducted with two different primary crosslinking molecules. Early results reported in the January 2008 annual technical summary indicated results that were submitted to the journal *Langmuir*. This submission was insufficient for acceptance in this journal and required a more exhaustive investigation of the crosslinking protocol. The results of this more extensive investigation of just two of the molecules were published in *Biosensors & Bioelectronics* in 2008 [21], and provided a foundation for further research in developing highly uniform antibody immobilization protocols for planar ZnO surfaces.

MTS and GPS were deposited onto the ZnO surface using both a conventional wet method and an evaporation method. Subsequent secondary crosslinking with GMBS was performed for ZnO surfaces coated with MTS. To provide visual confirmation of the density and uniformity of antibody immobilization, fluorescently labeled antibodies were incubated with the surface. The results were investigated using water contact angle measurements, atomic force microscopy, and confocal microscopy. As demonstrated in Figure 6 below, the results indicate that MPA immobilized via the liquid protocol provides the highest surface coverage and most repeatable antibody immobilization procedure. It is concluded that thiol-terminated phosphonic acids are therefore a viable option for immobilization of antibodies onto planar crystalline ZnO surfaces.

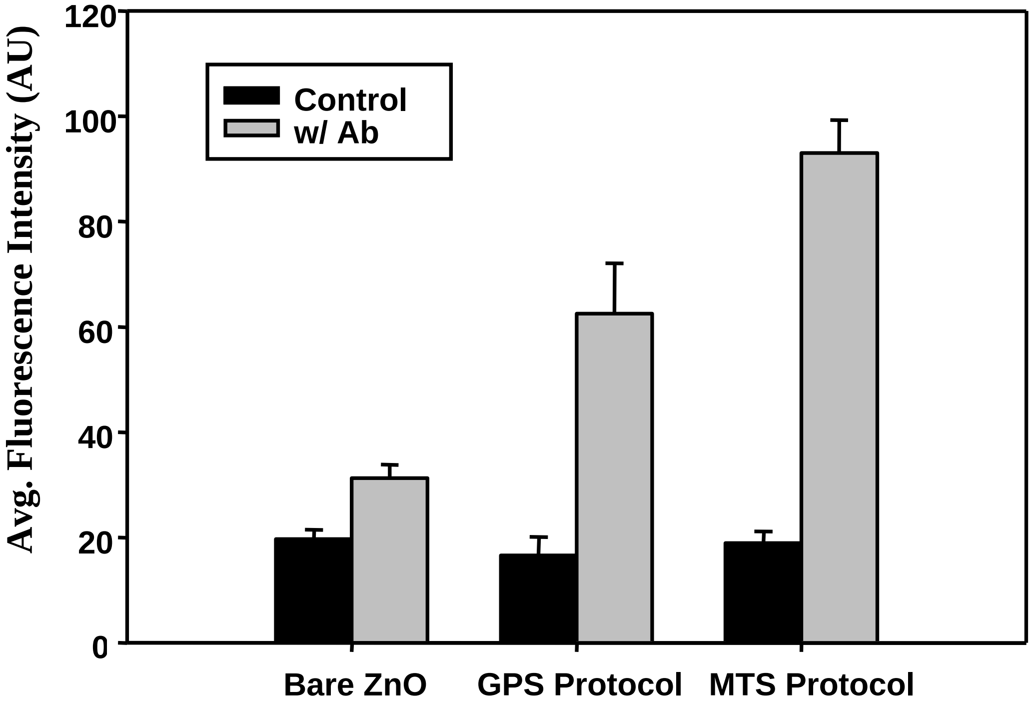

Figure 6. Plot of the average overall fluorescent antibody coverage for each of the antibody immobilization procedures. The values were calculated based on image analysis performed on confocal fluorescence images of the surfaces resulting from treatment with fluorescent antibodies. (Error Bars = Standard Error)

Goal 3: Sensor array system

The foundational components of my novel acoustic wave, label-free, immunosensor microarray have now been developed. It is therefore appropriate to apply these sensors towards cancer-relevant biomarker detection. The testing was broken up into two approaches. First, in assessing the potential sensitivity of the sensors, a dose response curve was generated for increasing concentrations of recombinant mesothelin-Fc protein in buffer. Positive indications from these experiments allowed me to pursue the second step in testing, which is application of these devices towards targets in more physiologically relevant media. The immunosensor microarrays were prepared for detection of PSA in conditioned medium (CM) from a LNCaP prostate cancer cell line. In order to test in an alternate and more complex media, the sensors were prepared to detect phosphor-Akt in cell lysate. Cell lysate is significantly more complex environment than conditioned medium and therefore represents an appropriate environment to assess the capability of these sensors for broader commercial application. Eight-device sensor arrays were fabricated as for previous experiments, designed to operate at ~2 GHz, for these experiments.

Sensitivity Assessment

Sensitivity testing was executed by preparing sensors to target mesothelin and applying them to varying concentrations of recombinant mesothelin-Fc protein in PBS. Purified recombinant mesothelin-Fc protein in buffer was obtained from Dr. Ira Pastan at the NCI. Serial dilutions were prepared using PBS (pH 7.38) to create concentrations of 1 ng/mL, 10 ng/mL, 100 ng/mL, 10 μg/mL, and 50 μg/mL. The functionalization protocol was performed with anti-mesothelin "MB" polyclonal IgG antibodies also supplied by Dr. Pastan on five separate 8-device arrays. 30 μL of each concentration of the purified protein solution was then deposited on the surface of each sensor array and allowed to incubate at room temperature for 20 minutes. After the incubation period, devices were rinsed with PBS buffer then deionized water then dried with a N_2 stream prior to measurement. S_{11} scattering responses for each device of each array were collected both prior to exposure to mesothelin solutions and again after the 20 minute incubation time.

Individual devices are measured both before and after exposure to the liquid sample under test. An example of the frequency shift observed after exposure to the sample is depicted in Figure 7. Figure 8 shows the device detection with increasing frequency shifts

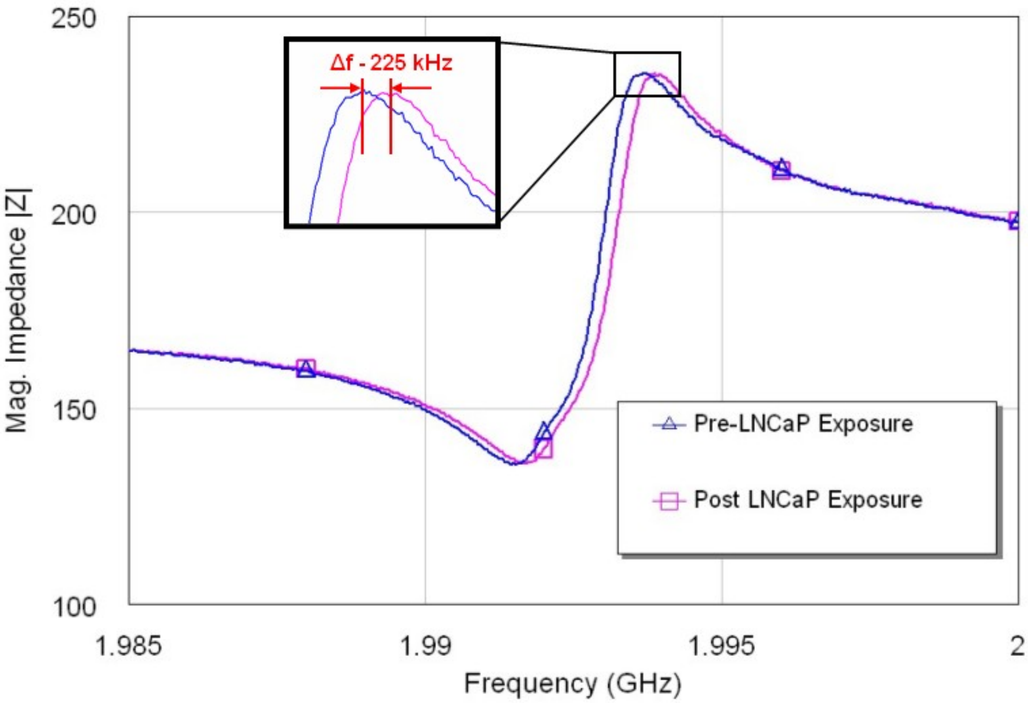

Figure 7. Typical impedance response of single sensor device showing response before (Δ) and after (□) exposure to the liquid sample under test. The peak of each curve represents the condition of parallel resonance.

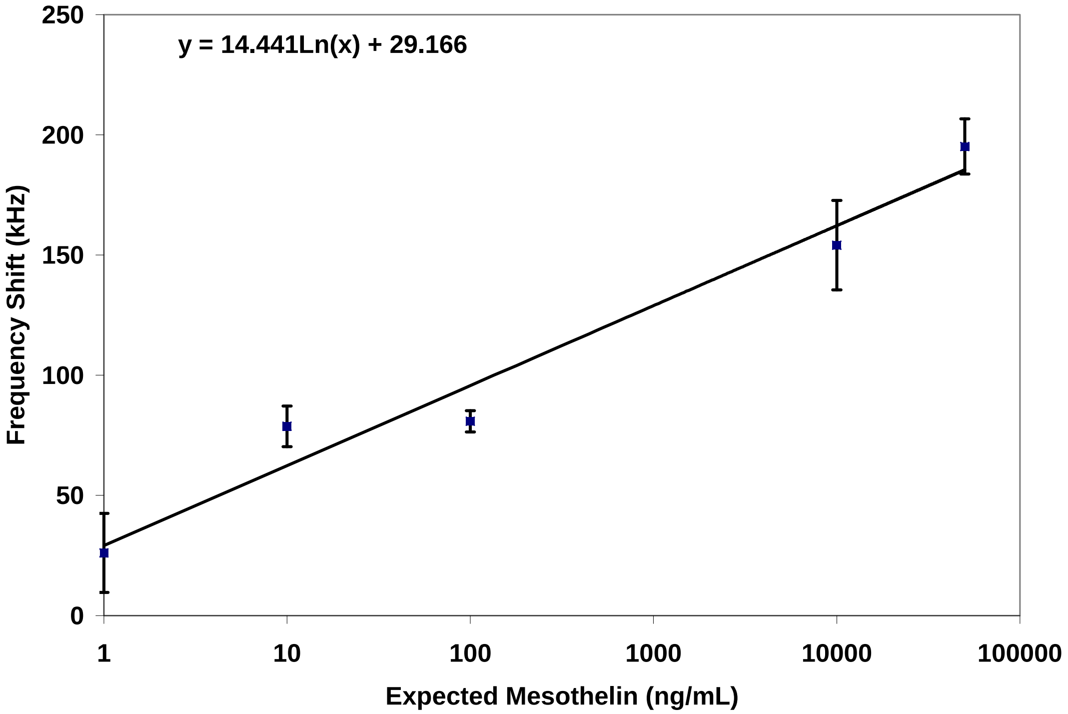

Figure 8. Dose response curve due to varying concentrations of purified recombinant mesothelin-Fc in PBS buffer (pH = 7.38). n = 8 for each case above. [Error bars represent standard error (σ/√n)]

in response to increasing sample concentrations, returning a 195 kHz shift for the 50 mg/mL concentration and 29 kHz shift for the 1 ng/mL concentration. It is important to put the magnitude of these shifts in context. Prior investigations using QCMs (see Figure 9) as the sensor for detection of a known target (sonic hedgehog, SHH) in the same LNCaP CM yielded only an 80 Hz frequency shift due to ~3 ng/mL concentration [22].

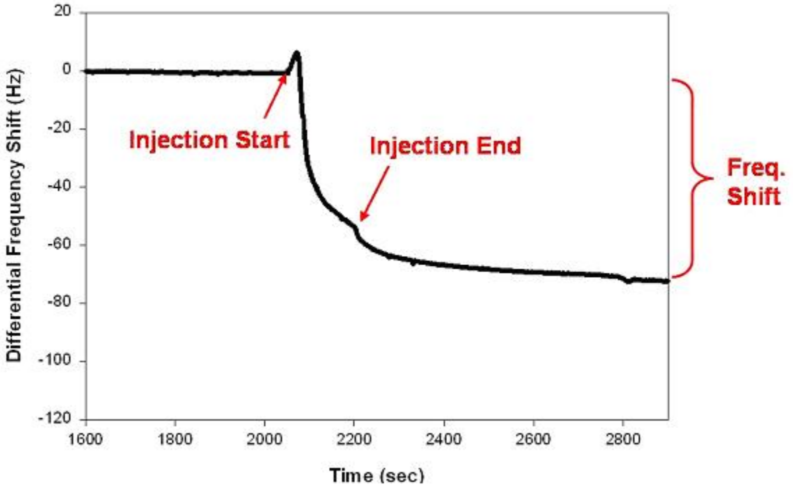

Figure 9. QCM sensor detection yields 80 Hz shift due to 3 ng/mL concentration of mesothelin in sample. While non-specific binding could compound the results, a control FITC antibody was used to subtract background binding [22].

The actual concentration of SHH was determined by ELISA to be 0.2 ng for 70 µL of sample, or ~3 ng/mL [22]. At the lower concentrations, I observed frequency shifts almost 400 times greater in magnitude. This demonstrates an exceptional capability regarding *potential* limit of detection but cannot be directly compared due to the difference in targets and antibody affinities, *et cetera*. Further device optimization will no doubt improve the sensitivity. Currently, however, the devices were clearly capable of broadly distinguishing increasing concentrations. Obviously the device response slows below 100 ng/mL, which indicates that more work must be done to reconcile overall mass resolution.

A control experiment was performed using buffer solution of 10 µg/mL of recombinant mesothelin-Fc with a sensor array coated with anti-mesothelin and a separate sensor array coated with anti-FITC. The results are summarized in Figure 5.6. While the anti-mesothelin coated devices clearly indicate positive detection of the target protein over the anti-FITC coated devices, using analysis of variance I found that there was statistically little difference between the frequency shift associated with exposure of the anti-mesothelin devices to the 1.0 ng/mL solution and the anti-FITC control sensor ($p = 0.409$). As a result, no further testing was performed below 1 ng/mL because I determined this to be below the limit of detection for statistically significant differentiation from the reference.

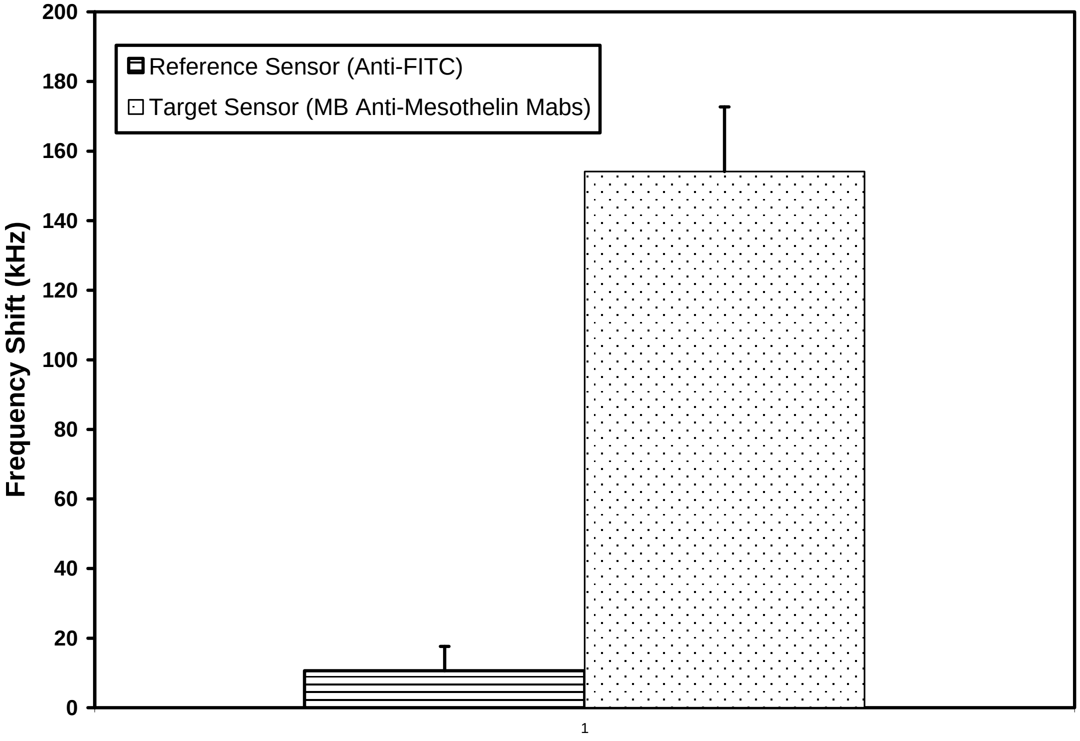

Figure 10. Control experiment depicting average frequency shift observed by a reference sensor (coated with anti-FITC, n = 4) and a target sensor (coated with anti-mesothelin, n = 6) after exposure to a purified solution of 10 µg/mL of recombinant mesothelin-Fc in PBS buffer. [Error bars represent standard error ($\sigma/\sqrt{n}$)]

It must be noted that sensor sensitivity is often defined as the slope of the sensor response curve to varying loads [23]. A traditional approach to determining this with gravimetric sensors is to deposit a known amount of mass on the sensor surface and measure the frequency shift. This is not plausible with biological samples, however, so a more useful method is to describe the overall sensitivity trends displayed under the given test conditions. As can be seen from Figure 5, the active region makes up only a very small portion of the total area of the array, all of which is exposed to the LSUT. Note that the vast majority of the device footprint is inactive, which includes the electrodes themselves. Deposition of the 30 μL sample more than covers the entire array. Future investigations should involve the development of an appropriate micro-fluidic flow cell which can limit the exposure to only the active resonance area of the sensor array to the LSUT, thereby making a sensitivity determination more reasonable. For this reason, I made an attempt to describe only the overall sensitivity trends displayed under the given test conditions.

Specificity Assessment

LNCaP CM was obtained from Dr. Milton Datta at the Winship Cancer Institute at Emory University. The CM is considered a sufficiently “noisy” environment for preliminary testing of device selectivity because it contains many proteins and other molecules from the cells. The functionalization protocol was performed with anti-FITC and anti-tPSA each on a separate 8-device array. Anti-FITC is employed as a negative control, targeting a molecule not to be found in CM. As a secondary control (marked ‘Control’ during the experiment), the functionalization protocol was performed on a set of devices but the final step of incubation with some antibody solution was replaced with incubation with plain PBS. 30 μL of LNCaP CM was then deposited on the surface of each functionalized sensor array and allowed to incubate at room temperature for 20 minutes. After the incubation period, devices were rinsed with aliquots of PBS buffer then a light stream of DI H_2O then dried with a N_2 stream for measurement. S_{11} scattering responses of each device of each array were collected both prior to exposure to LNCaP CM and again after the 20 minute incubation period.

The results of testing multiple sensor arrays for our two targets are summarized in Figure 5.7. It is clear that the devices could distinguish the presence of PSA, though not as clearly as would be desired ($p = 0.139$). It is expected that due to the extensive molecular diversity of the LSUT, a significant degree of non-specific binding is likely occurring. This is demonstrated by the 70 kHz (on average) shift from the Control sensors, having the crosslinking molecules but no antibodies attached to the surface, as compared with the 49 kHz shift (on average) from the FITC-targeted negative control sensors exposed to CM.

A commercially-obtained enzyme-linked immunoassay (EIA) kit for PSA (Biocheck, Inc: BS-1019) was used to independently determine the concentration of PSA in the LNCaP CM. The protocol was followed as described by the manufacturer using n=3 for control standards and blank wells and n=6 for the LNCaP CM wells. LNCaP CM was diluted to 1:7 and 1:15 in PBS buffer. The results of the EIA are demonstrated in Figure 12 below. A commercially available EIA kit for PSA (total) was used to determine the actual

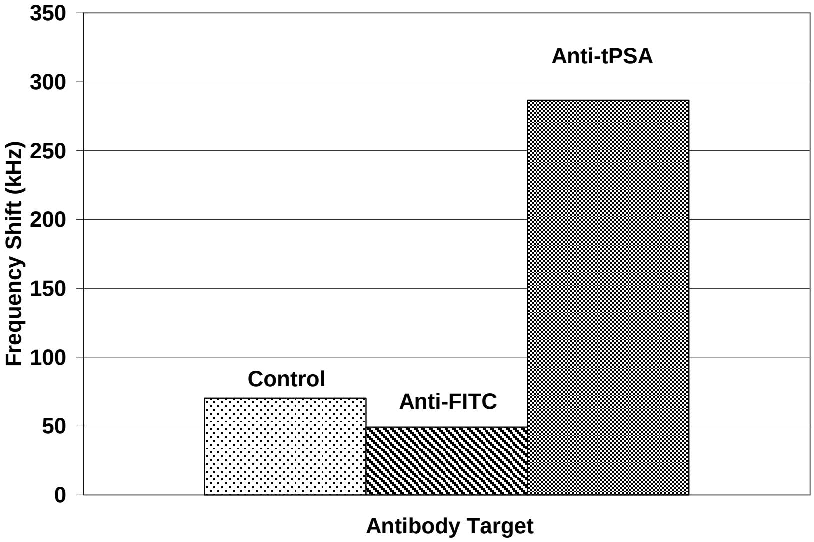

Figure 11. Comparison of the average frequency shift observed by sensors coated without antibodies (Control) [n=48], with anti-FITC (negative control) [n=44], and anti-tPSA [n=45] after 20 minute incubation with LNCaP CM.

concentration of PSA in the LNCaP conditioned medium. The results indicated the concentration of PSA to be roughly 950 ng/mL. Given this very high concentration of our target, it is obvious that the sensor behaves differently given the "noise" of this testing environment.

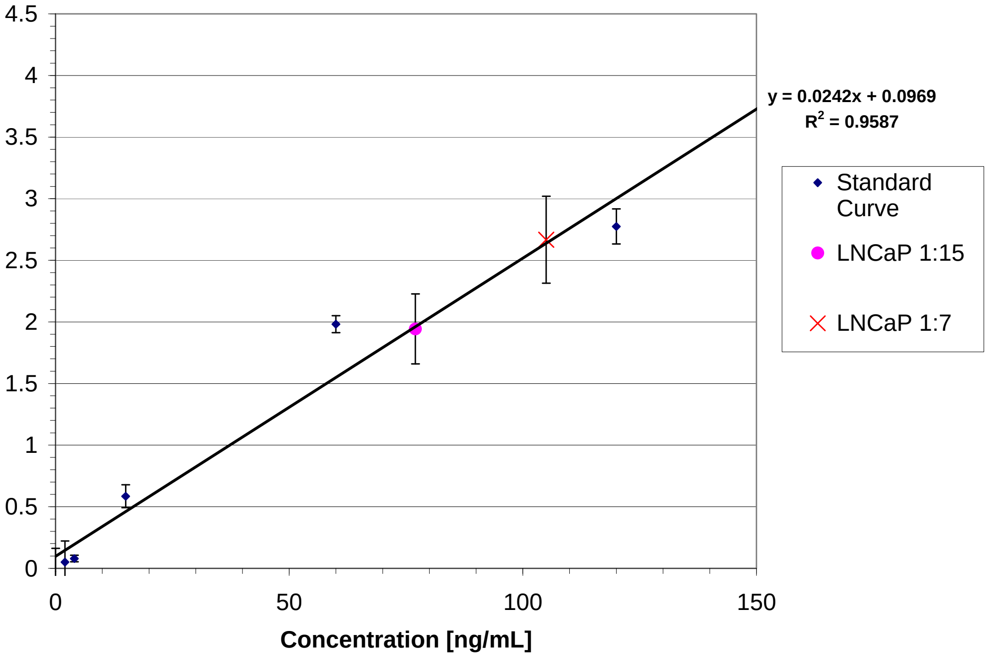

Figure 12. ELISA results for total PSA found in LNCaP conditioned medium using Biocheck, Inc BS-1019. (n = 3 for all standards, n = 6 for test samples).

Another test for specificity involved looking for phospho-Akt in cell lysate of the 686LN cell line, which is a more complex medium than conditioned medium. FITC and bare ZnO were again used as reference sensors, in a manner similar to the PSA experiment just described. The presence of pAkt in the cell lysate was again confirmed with a commercially available ELISA. As can be seen from Figure 13 below, the presence of pAkt is again easily detected in the cell lysate. There is a significant difference in the baseline shift, as demonstrated by the behavior of both control sensors, when compared with those from the PSA experiment. This is somewhat expected due to the significantly greater population of diverse proteins and lipids populating the cell lysate, as compared with conditioned medium. Without proper controls about the testing sample environment, which could be accomplished with an appropriately designed flow cell, it would be difficult to draw anything more than this very generalized conclusion regarding the discrepancy.

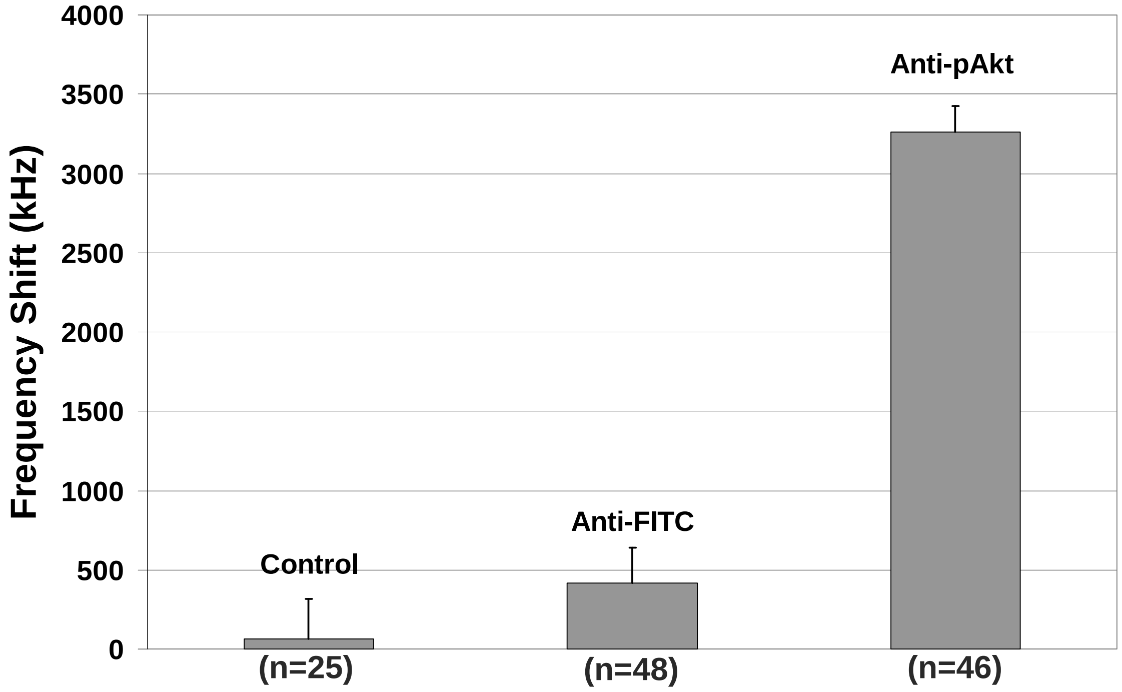

Figure 13. Presence of pAkt is clearly distinguished in the 686LN cell lysate using fabricated sensor arrays.

As stated at the beginning of this chapter, it was my goal to obtain preliminary results regarding the application of this sensor in a physiologically relevant medium. While the sensors are capable of distinguishing activity due to the appropriate target from control cases, they provide very little information regarding relative concentration. The testing protocol as it exists allows for many variables that must be controlled for, much of which can be solved with the development of an appropriate flow cell. Some of the variables I am referring to include varying distributed stress due to the application of the testing probes, drying of the surface environment, and uncontrolled exposure volumes are the most obvious.

Peripheral developments

AcμRay^{TM} Assembly

As described in the annual technical summary submitted in January of 2008, I described steps taken towards developing a packaging system we are calling the AcμRay^{TM} (Acoustic Micro-Array, pronounced – ak′ ū rā) that introduces controls for the variables I have listed in the previous section. The AcuRay^{TM} system involves the development of two printed circuit boards (PCB), fabricated by Express PCB, which includes fixed electrical connections to each device, a fixed volume flow cell, and connectivity to an appropriate network analyzer for monitoring. The package is shown in Figure 14 and is made up of a disposable array sensor board and a RF switch board. In order to achieve the fixed electrical connections, the electrode array needed to be redesigned in order to make connections with the disposable array sensor PCB board. Connections for each device were established by fusing electrodes from the fabricated sensor chip to the electrodes of the test board using conductive epoxy. A jig was developed (see Figure 15) to properly align the chip with the disposable PCB board and press the two pieces together while the conductive epoxy was allowed to set. Note that the test board also housed the liquid sample space that would expose the sensor surface to the liquid sample (Figure 14). It was envisioned that a flow cell could be attached to the sensor board here. Once set, the sensor board was connected via a PC card connector to the RF switch board. The RF switch board includesa SP8T RF rapid switching integrated circuit (IC) from Hittite Microwave Corporation (HMC253QS24). The switching IC was set up to be controlled by a computer via a National Instruments test controller (NI USB-6008). Once

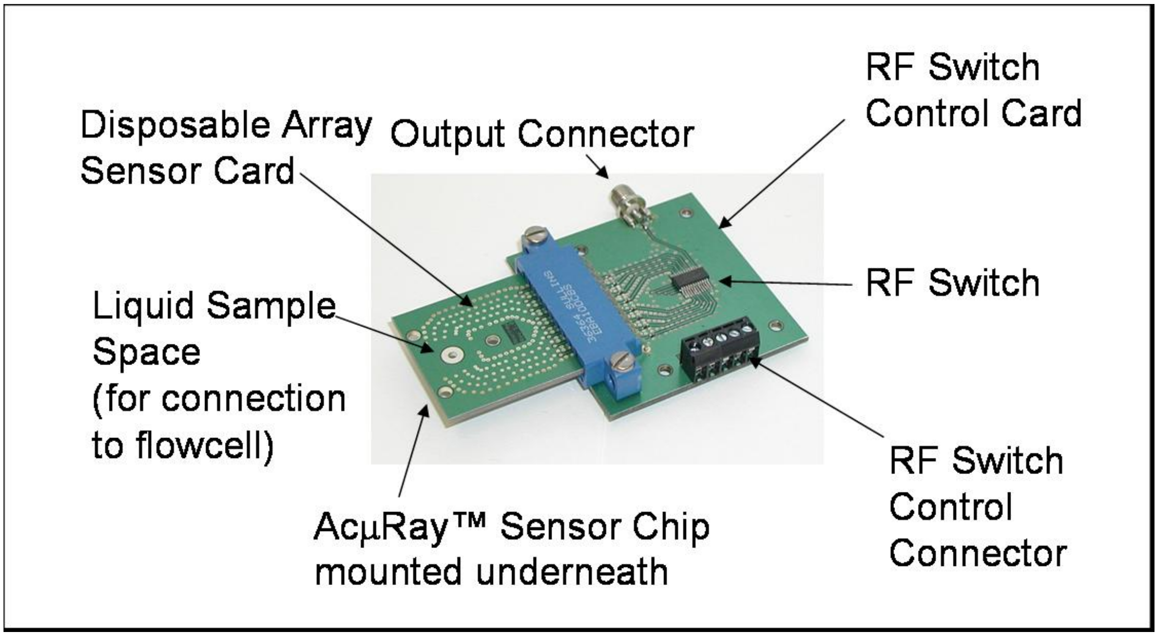

Figure 14. AcμRay^{TM} System consisting of disposable array sensor card and RF switch card with appropriate connections.

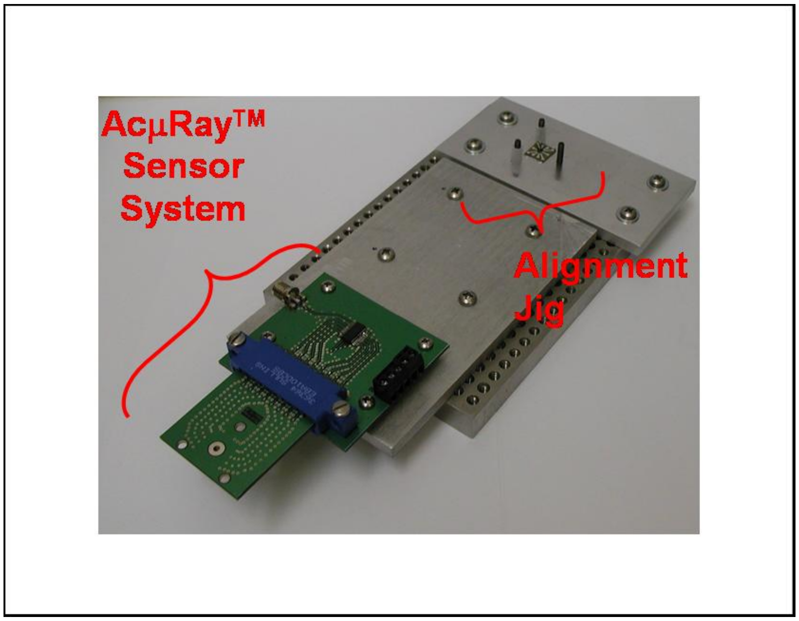

Figure 15. AcμRay^{TM} sensor system, including alignment jig for loading sensor chips onto disposable sensor array board.

the network analyzer was connected the to the output of the sensor array via the SMA connector shown in Figure 14, the responses of each device could be obtained periodically as controlled by the RF switch.

The initial array design, shown in Figure 16, resulted in loss of resonance function. Significant pursuit of the reason for the resonator loss of function with this particular electrode configuration met with limited success. There is significant evidence suggesting that energy is being scattered into the underlying crystal by the *approach* traces resulting in insufficient energy to induce the resonance response at the active region. Further investigations into developing an adequate array for the AcμRay^{TM} system were not pursued due to insufficient time remaining for the research. Follow up research is planned for colleagues remaining in the group.

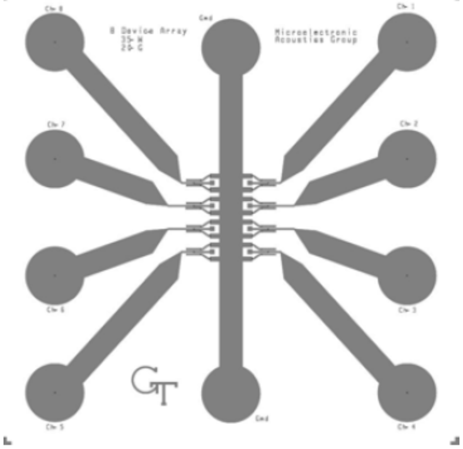

Figure 16. Array design for use in AcμRay^{TM} system consisting of 8 individual resonators with straight-finger electrodes. Overall area of array is roughly 10 mm x 10 mm.

Oscillator-free, remote array operation

One problem with the traditional approach to acoustic resonator sensor system design is that an oscillator circuit is required to drive the acoustic device at its resonant frequency. Because of the fixed operating bandwidth of an oscillator circuit, devices operating at radically different non-harmonic frequencies cannot be driven by the same oscillator circuit, increasingly exacerbated by higher frequencies of operation. This is a significant restriction during the design and testing stage of acoustic sensor development. Further, one of the forefronts of acoustic sensors research is exploration into the use of multi-device arrays [24, 25]. This research proposes an array of multiple sensors, each designed to potentially sense a different biological marker. The motivation being through the use of a multi-element array, the expression level of multiple biomarkers could be measured resulting in a much more robust and reliable screening test.

Oscillator-based sensor detection systems implementing acoustic wave devices as part of the feedback element present four significant concerns in their operating characteristics, especially if more than one acoustic wave device is used. The first concern involves the stability of the oscillator due to the thermal drift and load pulling of the amplifier portion of the circuit. The other concern is the instability due to possible coupling of modes between adjacent acoustic wave devices that would introduce injection-locking phenomena from stray coupling within the oscillators. An oscillator "averages" any frequency or time related anomaly associated with a sensed substance. Finally, the transient and settling times associated with oscillators makes high speed switching between devices difficult and a separate oscillator for each device in an array is not cost-effective nor does it lend itself to system miniaturization.

We have developed an innovative theoretical sensor system which utilizes acoustic wave device elements in a ladder or lattice filter network configuration. The sensor does not require the use of an oscillator for driving the acoustic resonance. The resulting frequency response can be analyzed to assess the activity of each sensor of the array. The results of simulations based on a Butterworth-Van Dyke circuit model show that perturbations of the shunt and series resonator elements can individually affect the overall frequency response, thereby making the filter network useful as a multi-element sensor. Full treatment of this approach was presented at the 2008 IEEE Sensors Conference in Lecce, Italy [26].

Key Research Accomplishments:

1. Fabrication of ZnO LFE SMRs
    a. Found to work better than Ta_2O_5
    - ➢ Published: *Journal of Applied Physics*
        - ➢ Jointly published: *Virtual Journal of Biological Physics Research*
2. Device optimization
    a. By electrode dimensions
    b. By geometry (straight vs. circular)
    c. Arrays
    - ➢ Published: *Sensors & Actuators A: Physics*
3. Device susceptibility testing
    a. Temperature: TCF of 25 ppm/°C
    b. Conductivity: ↑ conductivity yields ↓ device quality
    - ➢ Presented: *IEEE Sensors 2007 Conference*, Atlanta, GA USA
4. Surface chemistry
    a. Surface chemistries attempted: (various protocols for each)
        i. Aminopropyl triethoxy-silane (APS)
        ii. Mercaptopropyl trimethoxy-silane (MPS)
        iii. Mercatodecyl-phosphonic acid (MPA)
        iv. Glycidoxy propyl-trimethoxy-silane (GPS)
        v. Mercapto undecanoic acid (MUDA)
        vi. Mercapto-benzoic acid (MBA)
        vii. Passive adsorption (Control)
    b. MPA has statistically greater success with ZnO
    - ➢ Published: *Biosensors & Bioelectronics*
5. Biosensor testing
    a. Poor statistical performance with initial test
        i. Improved surface chemistry procedure should fix this
    - ➢ Presented: *AACR 2008 Annual Meeting,* San Diego CA
6. Remote power-free array implementation
    - ➢ Presented: *IEEE Sensors 2008 Conference*, Lecce, Italy

Reportable Outcomes

1. Christopher D. Corso, Anthony Dickherber, and William D. Hunt, "Lateral field excitation of thickness shear mode waves in a thin film ZnO solidly mounted resonator," *Journal of Applied Physics*, vol. 101, pp. 054514, 2007.
    a. Jointly published in the May edition of the *Virtual Journal of Biological Physics Research*
2. Anthony Dickherber, Christopher D. Corso, William D. Hunt, Ira K. Pastan, Mitchell Ho, Raffit Hassan, "Mesothelin-fc fusion protein detection using a novel microelectronic acoustic sensor platform," presented at *2007 AACR Molecular Diagnostics in Cancer Therapeutic Development Conference*, Atlanta, GA, Sept 17-20, 2007
    a. Selected for press release by the AACR and featured by WebMD, RxPG News, Dentalplans.com, PhysOrg.com, ScienceDaily, CBC News, Health Central.com, WFIE 14 Indiana (NBC affiliate), LEX 18 Kentucky (NBC affiliate), Forbes, US News & World Report, Health Scout, HealthCentral.com, KOLD News Arizona (CBS Affiliate), and finally the CNN News Room September 19, 2007 Wednesday special report by Dr. Sanjay Gupta
3. Anthony Dickherber, Christopher D. Corso, William D. Hunt, "Stability of a RF sputtered ZnO solidly mounted resonator sensor in varying temperature and conductivity environments," presented at *IEEE Sensors 2007 Conference*, Atlanta, GA USA, Oct 2007
4. Anthony Dickherber, Christopher D. Corso, William D. Hunt, "Optimization of the thickness shear mode in ZnO solidly mounted resonators," *Sensors & Actuators A: Physics*, 144(1) pg 7-12, May 28, 2008
5. Christopher D. Corso, Anthony Dickherber, William D. Hunt, "A comparison of antibody immobilization methods employing organosilanes and phosphonic acids on planar crystalline ZnO surfaces," *Biosensors & Bioelectronics,* 24(4) pg. 811-817, Dec 1, 2008
6. Anthony Dickherber, Christopher D. Corso, John Petros, Milton W. Datta, William D. Hunt, "A microelectronic bulk acoustic wave biosensor array for the detection of PSA in complex solutions," *2008 AACR Annual Conference*, San Diego, USA, April 10-16, 2008
7. Christopher D. Corso, Peter Edmonson, Anthony Dickherber, William D. Hunt, "Ladder multi-element filter implementation," *IEEE Sensors 2008 Conference*, Lecce, Italy, Oct. 2008

Conclusion

In summary, significant progress has been made towards completing the goals outlined in the submitted *statement of work*. I was able to attend several conferences including the AACR Annual and Molecular Diagnostics Conferences, having presented this research at both. I have continued to attend weekly urology grand rounds at the Winship Cancer Institute, which have helped significantly with my own understanding of the clinical environment surrounding prostate cancer and how the technology being developed through this research could be best adopted. The weekly meetings have further helped in keeping me aware of the latest clinical developments in the field regarding everything from the identification of novel indicators for diagnosis to novel therapies and on-going clinical trials. Furthermore, a joint 6-month collaborative effort has been initiated by two of my mentors, Prof. William Hunt and Dr. John Petros, in large part due to their involvement in this research. Such collaborations as this one and others I have witnessed over the course of this training period have inspired me to pursue a career that seeks to develop better communication among researchers from different fields and with the broader public. Further, my experience with the VA hospitals has inspired me delve further into the work of public policy, especially as it relates to issues surrounding our national health care.

So what?

What has been accomplished to date is the design and development of a novel acoustic resonator array that can be employed for liquid phase biosensing. Some final optimization experiments are currently underway, but this alone is a significant accomplishment that garnered the unsolicited recognition of the editors of the *Virtual Journal of Biological Physics Research* which selected it for publication. A novel and sufficient protocol for covalent immobilization of monoclonal IgG antibodies on the planar surface of the ZnO crystal has been developed and published in *Biosensors & Bioelectronics* for those pursuing the many immunoassay sensor technologies that incorporate this crystal. The early use of these biosensor arrays to detect the widely studied cancer biomarker mesothelin-fc was presented at the *AACR Molecular Diagnostics in Cancer Therapeutic Development Conference* where it garnered significant unsolicited media attention, demonstrating widespread interest in this research. Proof of functionality using the sensors to detect various known cancer markers in various complex media was accomplished and presented at the *2008 Annual Meeting of the AACR*. The issue of parallel high-frequency oscillators necessary to drive the resonance activity of the sensors was foreseen and addressed in a presentation at the *2008 IEEE Sensors Conference*. The preliminary development of interface circuitry and packaging that incorporates the flow cell as well as the switching element makes significant steps towards making the overall system compact and portable.

Future work

As indicated above, a great deal of work is still required to develop these sensor arrays to the point that they could be used for commercial applications. The high degree of sensitivity of these devices requires extraordinarily strict regulation of sample environments and other experimental protocol. Much of this can be accomplished with an appropriately designed flow cell with special care directed towards managing the monitoring circuitry and the connections involved. Due to the ultra high frequencies involved, the significantly minute device dimensions, the tenuousness of the resonance activity and the need to properly preserve the integrity and viability of the biological test sample, this step is by no means trivial. Once this step is accomplished, the establishment of an appropriate protocol for incorporating the IgG immobilization protocol must be determined. Finally, the establishment of a robust testing protocol, including determination of sample volumes, flow rates, incubation times, environmental conditions, and near real-time reporting hardware and software will be required to fully demonstrate the potential of this technology. These are all very solvable problems that are currently being pursued by remaining and future members of the Hunt lab at Georgia Tech. I look forward to reading and hearing about their progress through the next few years.

References:

[1] *E. S. Leman, G. W. Cannon, B. J. Trock, L. J. Sokoll, D. W. Chan, L. Mangold, A. W. Partin, and R. H. Getzenberg, "EPCA-2: a highly specific serum marker for prostate cancer," Urology, vol. 69, pp. 714-20, Apr 2007.*

[2] *V. T. S. Matthew A. Cooper, "A survey of the 2001 to 2005 quartz crystal microbalance biosensor literature: applications of acoustic physics to the analysis of biomolecular interactions," Journal of Molecular Recognition, vol. 20, pp. 154-184, 2007.*

[3] *H. Nakamura and I. Karube, "Current research activity in biosensors," Anal Bioanal Chem, vol. 377, pp. 446-68, Oct 2003.*

[4] *W. E. Newell, "Face-mounted piezoelectric resonators," Proceedings of the IEEE, vol. 53, pp. 575-581, 1965.*

[5] *C. D. Corso, A. Dickherber, and W. D. Hunt, "Lateral field excitation of thickness shear mode waves in a thin film ZnO solidly mounted resonator," Journal of Applied Physics, vol. 101, p. 054514, 2007.*

[6] *J. F. Rosenbaum, Bulk acoustic wave theory and devices. Boston: Artech House, 1988.*

[7] *M. Link, M. Schreiter, J. Weber, R. Gabl, D. Pitzer, R. Primig, W. Wersing, M. B. Assouar, and O. Elmazria, "c-axis inclined ZnO films for shear-wave transducers deposited by reactive sputtering using an additional blind," Journal of Vacuum Science & Technology A: Vacuum, Surfaces, and Films, vol. 24, pp. 218-222, 2006.*

[8] *W. Pang, H. Yu, J. W. Kwon, H. Zhang, and E. S. Kim, "Self-aligned lateral field excitation film acoustic resonator with very large electromechanical coupling [FBAR]," in Frequency Control Symposium and Exposition, 2004. Proceedings of the 2004 IEEE International, 2004, pp. 558-561.*

[9] *A. Dickherber, C. D. Corso, and W. D. Hunt, "Stability of a RF sputtered ZnO solidly mounted resonator sensor in varying temperature and conductivity environments," in IEEE Sensors 2007 Conference, Atlanta, GA USA, 2007, pp. 735-6.*

[10] *A. Dickherber, C. D. Corso, and W. D. Hunt, "Optimization of the thickness shear mode in ZnO solidly mounted resonators," Sensors & Actuators A, vol. Publication pending, 2007.*

[11] *S. K. Bhatia, L. C. Shriver-Lake, K. J. Prior, J. H. Georger, J. M. Calvert, R. Bredehorst, and F. S. Ligler, "Use of thiol-terminal silanes and heterobifunctional crosslinkers for immobilization of antibodies on silica surfaces," Anal Biochem, vol. 178, pp. 408-13, May 1 1989.*

[12] *L. C. Shriver-Lake, B. Donner, R. Edelstein, K. Breslin, S. K. Bhatia, and F. S. Ligler, "Antibody immobilization using heterobifunctional crosslinkers," Biosensors & Bioelectronics, vol. 12, pp. 1101-1106, 1997.*

[13] *I. Luzinov, D. Julthongpiput, A. Liebmann-Vinson, T. Cregger, M. D. Foster, and V. V. Tsukruk, "Epoxy-terminated self-assembled monolayers: Molecular glues for polymer layers," Langmuir, vol. 16, pp. 504-516, Jan 2000.*

[14] V. V. Tsukruk, I. Luzinov, and D. Julthongpiput, "Sticky Molecular Surfaces: Epoxysilane Self-Assembled Monolayers," Langmuir, vol. 15, pp. 3029-3032, 1999.

[15] C. M. Ruan, L. J. Yang, and Y. B. Li, "Immunobiosensor chips for detection of Escherichia coli O157 : H7 using electrochemical impedance spectroscopy," Analytical Chemistry, vol. 74, pp. 4814-4820, Sep 2002.

[16] L. Yang and Y. Li, "AFM and impedance spectroscopy characterization of the immobilization of antibodies on indium-tin oxide electrode through self-assembled monolayer of epoxysilane and their capture of Escherichia coli O157:H7," Biosens Bioelectron, vol. 20, pp. 1407-16, Jan 15 2005.

[17] P. H. Mutin, G. Guerrero, and A. Vioux, "Organic-inorganic hybrid materials based on organophosphorus coupling molecules: from metal phosphonates to surface modification of oxides," Comptes Rendus Chimie, vol. 6, pp. 1153-1164, Aug-Oct 2003.

[18] M. A. Aziz and H. Yang, "Electrochemical immunosensor using the modification of an amine-functionalized indium tin oxide electrode with carboxylated single-walled carbon nanotubes," Bulletin of the Korean Chemical Society, vol. 28, pp. 1171-1174, Jul 2007.

[19] G. Guerrero, P. H. Mutin, and A. Vioux, "Anchoring of phosphonate and phosphinate coupling molecules on titania particles," Chemistry of Materials, vol. 13, pp. 4367-4373, Nov 2001.

[20] T. L. Breen, P. M. Fryer, R. W. Nunes, and M. E. Rothwell, "Patterning Indium Tin Oxide and Indium Zinc Oxide Using Microcontact Printing and Wet Etching," Langmuir, vol. 18, pp. 194-197, 2002.

[21] C. D. Corso, A. Dickherber, and W. D. Hunt, "An investigation of antibody immobilization methods employing organosilanes on planar ZnO surfaces for biosensor applications," Biosens Bioelectron, vol. 24, pp. 811-7, Dec 1 2008.

[22] C. D. Corso, A. Dickherber, P. Shah, A. Migdal, M. W. Datta, S. Datta, and W. D. Hunt, "Development of a simple inexpensive bulk acoustic wave nanosensor for cancer biomarkers: Detection of secreted sonic hedgehog from prostate cancer cells," in 2006 Annual Meeting of the AACR, Washington D.C., 2006.

[23] J. r. Janata, Principles of chemical sensors. New York: Plenum Press, 1989.

[24] L. C. Shriver-Lake and F. S. Ligler, "The array biosensor for counterterrorism," Sensors Journal, IEEE, vol. 5, pp. 751-756, 2005.

[25] Y. Zuo, S. Chakrabartty, Z. Muhammad-Tahir, S. Pal, and E. C. Alocilja, "Spatio-Temporal Processing for Multichannel Biosensors Using Support Vector Machines," Sensors Journal, IEEE, vol. 6, pp. 1644-1651, 2006.

[26] C. D. Corso, P. Edmonson, A. Dickherber, and W. D. Hunt, "Ladder multi-element filter implementation," in IEEE Sensors Conference, Lecce, Italy, 2008.

Appendices:

Included in this section are copies of all manuscripts outlined in the "Reportable Outcomes" section of this document, as well as the doctoral thesis manuscript of the author which provides greater technical detail for all aspects of this research. The final appendix item is the author's *curriculum vitae*.

JOURNAL OF APPLIED PHYSICS **101**, 054514 (2007)

Lateral field excitation of thickness shear mode waves in a thin film ZnO solidly mounted resonator

Christopher D. Corso
School of Biomedical Engineering, Georgia Institute of Technology, Atlanta, Georgia 30332

Anthony Dickherber and William D. Hunt[a]
School of Electrical and Computer Engineering, Georgia Institute of Technology, Atlanta, Georgia 30332

(Received 7 November 2006; accepted 2 January 2007; published online 14 March 2007)

In recent years, interest in the development of highly sensitive acoustic wave devices as biosensor platforms has grown. A considerable amount of research has been conducted on AT-cut quartz resonators both in thickness excitation and in lateral excitation configurations. In this report, we demonstrate the fabrication of a ZnO solidly mounted resonator operated in thickness shear mode (TSM) using lateral field excitation of the piezoelectric film. Theoretical Christoffel equation calculations are provided to explore the conditions for excitation of a TSM wave in *c*-axis-oriented ZnO through lateral excitation. The existence of a TSM wave is verified through the comparison of theoretical and experimentally obtained acoustic velocity values from frequency versus thickness measurements and water loading of the resonators. A major strength of this design is that it incorporates a simple eight-layer, single-mask fabrication process compatible with existing integrated circuit fabrication processes and can be easily incorporated into multidevice arrays. With minimal electrode optimization, we have been able to fabricate resonators with nearly 100% yield that demonstrate Q values of up to 550 and K^2 values of 0.88% from testing of more than 30 devices. © *2007 American Institute of Physics*. [DOI: 10.1063/1.2562040]

I. INTRODUCTION AND BACKGROUND

The interest in developing highly sensitive acoustic wave devices for chemical and biological sensing purposes has dramatically increased in the past decade. Acoustic devices offer an attractive alternative to other sensor schemes such as surface plasmon resonance[1] (SPR) and electrochemical sensors[2] because they are small, relatively inexpensive to produce, and offer a potentially superior sensitivity to surface perturbations. The acoustic wave resonating in the piezoelectric cavity acts as a probe querying the surface for any changes in boundary conditions such as mass loading. This is the fundamental concept behind the operation of acoustic biosensors.

In the past, piezoelectric ZnO thin films have been used in the fabrication of thin film bulk acoustic resonators (FBARs) for high frequency filters.[3] Typically, these devices are operated in the thickness-excited longitudinal mode in which the frequency can be tuned simply by varying the thickness of the ZnO thin film. The particle displacement of the propagating acoustic wave in a longitudinal bulk mode is normal to the surface of the film and generates compressional waves in the medium adjacent to the device surface. When operated in an adjacent liquid medium, the longitudinal mode energy is dissipated into the liquid for devices utilizing waves that propagate at a velocity higher than the sound velocity in the liquid. This results in a highly reduced quality factor, Q, and poor mass resolution in a sensor application. The thickness shear mode (TSM) is better suited for liquid sensing applications due to the shear particle displacement of the acoustic wave in the piezoelectric film. Since the adjacent liquid medium cannot effectively support a shear wave, very little energy is transferred into the liquid, and this results in minimal damping of the thickness shear mode.

The most common type of TSM resonator is the quartz crystal microbalance (QCM). QCMs are made from thin plates of AT-cut quartz. These devices have been shown to be highly sensitive as gravimetric sensors in both vapor phase and in liquid phase sensing.[4–7] The frequency dependence of the resonator-based biosensor has been characterized by many, including Sauerbrey,[8] Kanazawa and Gordon,[9] and most recently Hunt *et al.*,[10] but all agree that the frequency sensitivity of these devices is proportional to a power of the fundamental resonant frequency f_0. QCMs typically operate in the frequency range of 5–35 MHz. In AT-cut quartz plates, it is difficult to further increase the fundamental operating frequency because of its dependence on the thickness of the quartz plate. At very low thicknesses, the quartz plate becomes extremely fragile and is difficult to handle. It is possible to achieve higher frequencies with the QCM by monitoring harmonic modes beyond the fundamental, but these become progressively diminished with increasing harmonic number. Solidly mounted FBARs, on the other hand, do not suffer from this problem because the piezoelectric film is grown directly onto a solid foundation. Solidly mounted resonators (SMRs) are made possible by the fabrication of an acoustic mirror directly below the piezoelectric thin film. This so-called Bragg reflector in effect presents the lower side of the piezoelectric material with an acoustic impedance close to that of air over a fairly broad range of frequencies,[11] resulting in the reflection of the acoustic en-

---

[a] Author to whom correspondence should be addressed; electronic mail: bill.hunt@ece.gatech.edu

ergy back into the piezoelectric film. This allows for the utilization of extremely thin piezoelectric sensing layers and, ultimately, very high frequency devices (i.e., gigahertz range) can be produced.

The sensitivity of acoustic waves in AT-cut quartz plates has been widely exploited in QCMs which use thickness excitation (TE) to excite the wave. It has been shown, however, that lateral field excitation (LFE) can be used to excite the TSM wave[12–15] and that the resulting device may be more sensitive to surface perturbations than the standard TE QCM for liquid phase sensing applications.[16–19] The advantages of LFE over TE are mainly attributed to the fact that in LFE, the electrodes that generate the electric field are not directly in the path of the acoustic wave, as in TE. Since the metal material that forms the electrode is a source of acoustic wave scattering and damping, its removal from the acoustic path results in higher Q values. Other advantages include increased stability at a given harmonic and reduced aging of the crystal since the electrode is absent from the area of greatest vibrational motion.[20] For biosensor applications, removing the electrode from the acoustic path means that biological molecules can be immobilized directly onto the region of highest particle displacement which should result in greater sensitivity of the sensor.

There has been varied interest, thus far, in generating a thickness shear mode in ZnO for acoustic devices. One of the more highly investigated methods involves the growth of inclined *c*-axis oriented films[21] coupled with an electrode pattern in which the electrodes are situated on opposite sides of the thin film to produce an electric field through the thickness. Wang and Lakin had excellent success in fabricating oriented films with the *c*-axis-oriented 40° to the substrate normal.[22] While their resonator Q and electromechanical coupling were high, the operating frequency was low (~293 MHz) and the fabrication procedure required bulk etching of the Si wafer to produce the air-backed ZnO membrane resonators. More recently, Link *et al.*[23,24] have revived the inclined ZnO growth research with the intent of developing ZnO TSM resonators for liquid phase sensing. A shortcoming of the inclined ZnO growth method is that the thickness excitation requires that the electrodes be in the path of the acoustic wave. While it offers the benefit of a higher operating frequency than the QCM for sensing, it still suffers from the same pitfalls as the QCM because the electrodes are located in the area of highest sensitivity.

In a study by Wei *et al.* focusing on noninclined *c*-axis-oriented ZnO, the thickness shear mode was excited through lateral field excitation.[25] The devices were solidly mounted resonators fabricated through the use of a self-aligning process that involved ZnO lift-off and a spiral electrode structure spanning 2 mm in diameter. Operating close to 4.1 GHz, the devices illustrated the ability for ZnO FBARs to be operated at high frequencies with relative ease. However, an acoustic mirror was not implemented in the design, and the quality factor Q of the resonators was very low (roughly 35). Acoustic velocity calculations we made from the numbers given in the study come out to ~3280 m/s as compared to a theoretical value of ~2841 m/s calculated using bulk stiffness properties of ZnO available in Rosenbaum.[26] This value is reasonable considering variations in ZnO thin film material parameters.

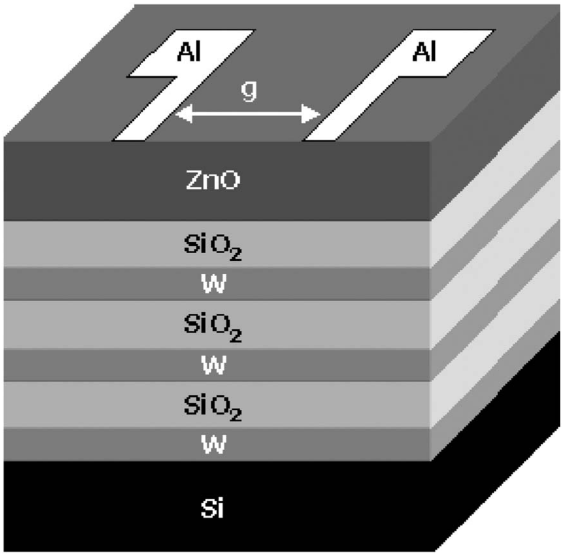

FIG. 1. Electrode and stack configuration.

In this paper, we present a laterally excited ZnO thickness shear mode resonator that is both extremely simple to fabricate and highly sensitive to surface perturbations. The resonator configuration consists of a laterally excited, solidly mounted ZnO thin film resonator that incorporates the use of an acoustic mirror. Future investigations will yield optimized electrode designs and even higher performance devices. It should be noted that this device approach is amenable to array format such that multiple target molecules can be simultaneously detected while also providing reference sensors to add statistical significance to the test results. An additional benefit of these devices is the ease of fabrication of repeatable highly *c*-axis-oriented ZnO thin films by rf sputtering. We will present data on devices which have been fabricated with a single mask step.

II. DEVICE FABRICATION AND EXPERIMENTAL PROTOCOL

The overall device design can be seen in Fig. 1. The thin film six-layer stack of alternating W and SiO_2 was deposited by rf magnetron sputtering using the Unifilm PVD-300 sputtering system to create an acoustic reflector analogous to that of a reflector grating in a surface acoustic wave device.[27,28] Scanning electron microscopy (SEM) analysis of the deposition layers demonstrated that we could achieve greater than 90% uniformity of deposition thickness across a 3 in. wafer. The acoustic mirror is designed according to the model described by Lakin.[28] For the desired resonance frequency of approximately 2 GHz, W and SiO_2 thicknesses of 600 and 1200 nm, respectively, were calculated to achieve the desired mirror response. The results of a model simulation based on actual thickness measurements of the fabricated device are shown in Fig. 2. The plot illustrates that over the frequency range of 1.8–2.3 GHz, the reflection coefficient approaches unity. The layers comprising the reflector stack were alternat-

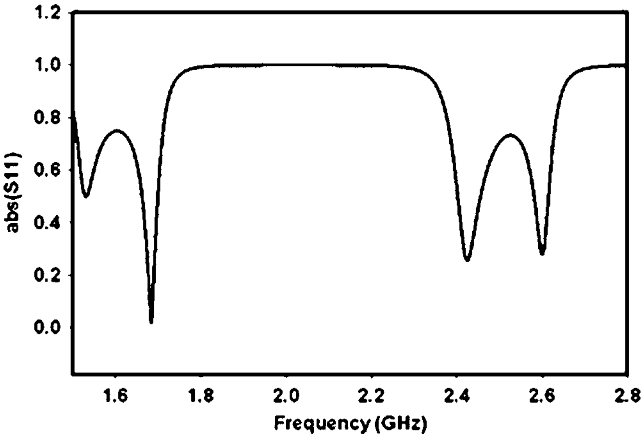

FIG. 2. Simulated reflection coefficient of the acoustic mirror.

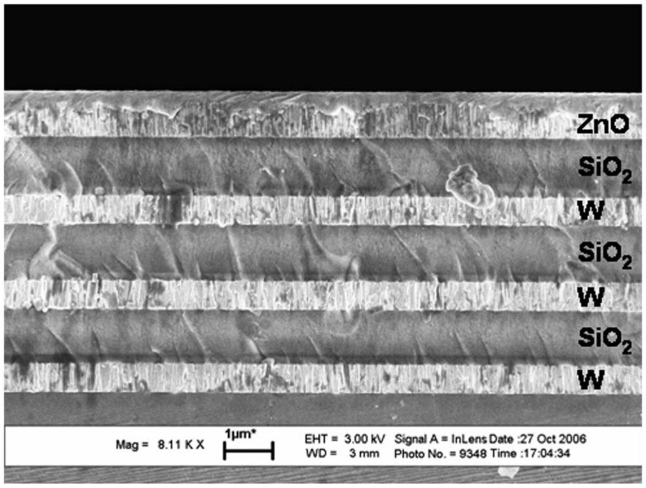

FIG. 3. SEM image of the acoustic mirror and ZnO thin films on a Si substrate.

ing fused SiO_2 and W, in which W was the first layer deposited onto a Si (1 0 0) wafer. All sputtering parameters used for the fabrication of these devices are provided in Table I. Following deposition of the stack, a ZnO thin film was sputtered using the Unifilm PVD-300 sputtering system. The final thicknesses of the thin film layers were verified by imaging a cross section of the fabricated wafer using a LEO 1530 thermally assisted field emission (TFE) scanning electron microscope (SEM), and can be seen in Fig. 3. To finish the fabrication procedure, approximately 120 nm of Al was deposited on top of a 30 nm seeding layer of Cr to create the electrodes using a CVC e-beam evaporator and a standard photolithography lift-off process. The electrodes were designed such that the electric field created upon excitation would be perpendicular to the wafer surface normal. This laterally oriented electric field is important for excitation of a bulk acoustic shear wave in the ZnO. To verify the orientation of the electric field resulting from the electrode geometry, electric field simulations were carried out using the COMSOL MULTIPHYSICS™ finite element modeling software package. The resonator scattering parameters of the finished devices were obtained using a Cascade Microtech 9000 probe station with Cascade Microtech ACP40-GS/SG probes and analyzed using a HP 8753C network analyzer equipped with a 85047A S parameter test set.

The x-ray diffraction (XRD) data were taken on a Philips X'Pert Materials Research Diffractometer™ using a hybrid mirror/monochromator incident optics and a 1/4-degree receiving slit in the diffracted optics beam path. A 2θ-Ω rocking-curve scan of the film indicated a strong peak at approximately 34.26°, indicating a (0 0 2) ZnO hexagonal crystal orientation shown in Fig. 4. The peak has a full width at half maximum (FWHM) of 0.35°, indicating a highly oriented c-axis crystal film. Figure 4 also shows a tight peak at 40.1°, which corresponds to the (1 1 0) orientation of the tungsten layers in the acoustic stack. As expected, no peaks were observed for the SiO_2 layers in the stack because they are amorphous.

III. THEORETICAL BACKGROUND AND FINITE ELEMENT MODELING

With the verification of the ZnO crystal orientation in hand, it is possible to solve the Christoffel equation to find the modes of propagation in the bulk given a defined electrical excitation direction. We begin by considering the nonpiezoelectric Christoffel equation

$$(k^2 l_{iK} c_{KL} l_{Lj}) v_j = \rho \omega^2 v_i, \qquad (1)$$

where $k = \tilde{\omega}/v_a$, ρ is the density of the material, v_i and v_j are the particle polarization direction vectors, and the l_{iK} matrix is in the form of

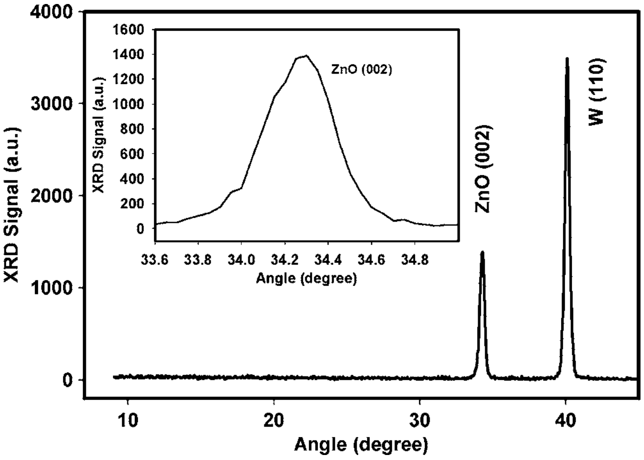

FIG. 4. 2θ-ω rocking-curve scan of the ZnO film sputtered on the six-layer W/SiO_2 acoustic mirror. The inset is a zoomed image of the ZnO peak.

TABLE I. Sputtering parameters for respective layers using a Unifilm PVD-300 sputterer.

	W	SiO_2	ZnO
Power (W)	0.86 dc	281 rf	142 rf
O_2	NA	2.5%	3%
Ar	100%	97.5%	97%
Temperature (°C)	Not heated	Not heated	325
Deposition time (min)	84	139	115
Pressure (torr)	5.00×10^{-3}	5.02×10^{-3}	5.10×10^{-3}

$$l_{iK}=\begin{bmatrix} l_x & 0 & 0 & 0 & l_z & l_y \\ 0 & l_y & 0 & l_z & 0 & l_x \\ 0 & 0 & l_z & l_y & l_x & 0 \end{bmatrix}, \tag{2}$$

where the nonzero terms come from the propagation vector $\hat{\mathbf{l}}=l_x\hat{\mathbf{i}}+l_y\hat{\mathbf{j}}+l_z\hat{\mathbf{k}}$. The l_{Lj} matrix is simply the transpose of l_{iK}, and c_{KL} is the material stiffness tensor rotated according to the desired Euler angles. It follows from the XRD data that the ZnO thin films belong to a hexagonal system with a crystal class of 6 mm.

Since the c axis is oriented normal to the surface, we will arbitrarily choose to align the z coordinate axis along this crystal axis for our calculations. For thickness shear mode propagation, wave propagation is defined to be in the z direction, so l_x and l_y go to zero and l_z goes to 1.

Equation (1) is used to solve for directions and velocities of bulk waves propagating in the substrate, but it does not account for the piezoelectric properties of a material nor the possibility of the generation of these waves by an electric field. For this reason, we turn to the piezoelectric Christoffel equation

$$k^2\left\{l_{iK}\left[c^E_{KL}+\frac{(e_{Kj}m_j)(m_ie_{iL})}{m_i\varepsilon^S_{ij}m_j}\right]l_{Lj}\right\}v_j=\rho\omega^2 v_i, \tag{3}$$

where e_{Kj} is the piezoelectric coupling tensor, ε^S_{ij} is the 3×3 permittivity tensor at constant strain, m is the vector corresponding to the direction of the electric excitation field, and now c^E_{KL} corresponds to the 6×6 stiffness tensor at a constant electric field. As can be seen, Eq. (3) is similar to Eq. (1) but for the inclusion of the piezoelectric and permittivity tensors, which apply piezoelectric "stiffening" to the stiffness tensor.

For the lateral field excitation of the c-axis-oriented ZnO, we desire the electric excitation field to be orthogonal to the wave propagation. Therefore, if the wave propagation is in the direction of the z axis, the electric field is in the x-y plane. Here, we will describe the coupling and acoustic wave propagation for the general case of an electric field along any direction within the x-y plane. The electric field vector m_j is of the form

$$m_j=\begin{bmatrix} m_x \\ m_y \\ m_z \end{bmatrix}. \tag{4}$$

Solving the piezoelectrically stiffened Christoffel equation for laterally excited ZnO, we set $m_z=0$ and $m_x^2+m_y^2=1$. The 6 mm hexagonal system stiffness tensor is of the form

$$c=\begin{bmatrix} c_{11} & c_{12} & c_{13} & 0 & 0 & 0 \\ c_{12} & c_{11} & c_{13} & 0 & 0 & 0 \\ c_{13} & c_{13} & c_{33} & 0 & 0 & 0 \\ 0 & 0 & 0 & c_{44} & 0 & 0 \\ 0 & 0 & 0 & 0 & c_{44} & 0 \\ 0 & 0 & 0 & 0 & 0 & c_{66} \end{bmatrix}, \tag{5}$$

and the form of the piezoelectric matrix is

$$e=\begin{bmatrix} 0 & 0 & 0 & 0 & e_{15} & 0 \\ 0 & 0 & 0 & e_{15} & 0 & 0 \\ e_{31} & e_{31} & e_{33} & 0 & 0 & 0 \end{bmatrix}. \tag{6}$$

The resulting Christoffel matrix is of the form

$$\Gamma=\begin{bmatrix} c44+e_{15}m_x^2/\varepsilon_{11} & e_{15}^2 m_x m_y/\varepsilon_{11} & 0 \\ e_{15}^2 m_x m_y/\varepsilon_{11} & c44+e_{15}m_y^2/\varepsilon_{11} & 0 \\ 0 & 0 & c_{33} \end{bmatrix}. \tag{7}$$

The eigenvalues of this matrix correspond to terms that can be used to solve for v_a, the acoustic velocity in each of the three wave propagation modes, while the corresponding eigenvectors relate to the direction of particle displacement. Solving for the eigenvectors and eigenvalues of Γ gives

$$\begin{gathered} x_1=\begin{bmatrix} -m_y \\ m_x \\ 0 \end{bmatrix}, \quad \lambda_1=c_{44}; \quad x_2=\begin{bmatrix} m_x \\ m_y \\ 0 \end{bmatrix}, \\ \lambda_2=c_{44}+\frac{e_{15}^2}{\varepsilon_{11}}; \quad x_3=\begin{bmatrix} 0 \\ 0 \\ 0 \end{bmatrix}, \quad \lambda_3=c_{33}. \end{gathered} \tag{8}$$

From these results, we find that only one mode is piezoelectrically excited (defined by x_2 and λ_2) and that the particle displacement will be directly aligned with the electric field, regardless of the orientation of the field with respect to the x-y plane. This mode is a pure shear thickness mode and is the mode we seek. Another pure shear mode exists (defined by x_1 and λ_1) with particle displacement also in the x-y plane at an angle perpendicular to that of the piezoelectrically excited mode; however, it is piezoelectrically inactive. The longitudinal mode (defined by x_3 and λ_3), importantly, is also piezoelectrically inactive. These results indicate that an electric field in the x-y plane will excite a pure shear thickness mode with particle displacement aligned with the electric field. The acoustic velocity for this mode can be calculated from

$$v_a=\sqrt{\frac{c_{44}+e_{15}^2/\varepsilon_{11}}{\rho}}. \tag{9}$$

Using bulk values for ZnO from Rosenbaum,[26] $e_{15}=-0.48$, $c_{44}=43\times 10^9\ \mathrm{N/m^2}$, $\varepsilon_{11}=8.6$ (rel.), and $\rho=5700\ \mathrm{kg/m^3}$, the theoretical acoustic velocity for the piezoelectrically stiffened thickness shear mode is approximately 2841 m/s. Since most ZnO thin films include various dopants and are not of pure crystal uniformity, they will have stiffness, density, and piezoelectric constants that are different from these bulk values. This calculated acoustic velocity is therefore an approximate figure and not an absolute value from which to evaluate an experimentally obtained mode. The theoretical piezoelectric coupling constant for the ZnO LFE resonator is given by

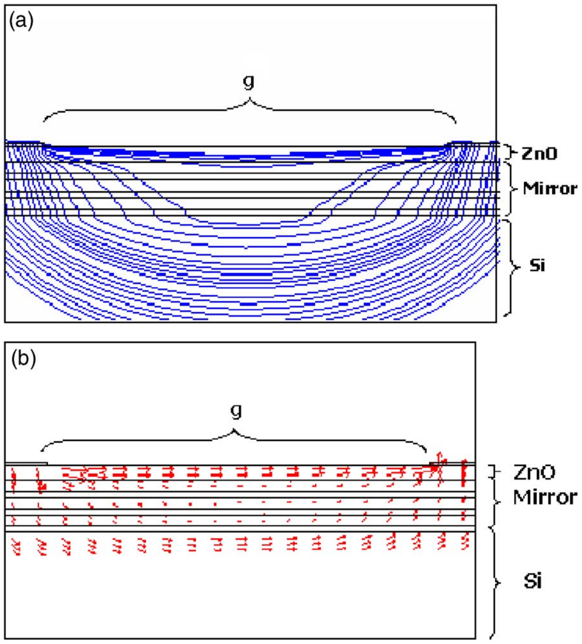

FIG. 5. (Color online) Finite element simulation plots illustrating the electric field characteristics resulting from the electrode configuration in Fig. 1. (a) shows the electric field streamline plot and (b) shows an arrow plot where the electric field direction is indicated by the direction of the arrow, and the relative strength of the electric field (C/m) is indicated by the size of the arrow.

$$K^2 = \frac{e_{15}^2}{c_{44}\varepsilon_{11}}, \tag{10}$$

which is calculated to be approximately 0.07 or 7% for the case of the thickness shear mode.

All of the above calculations rely on the assumption that the lateral excitation field is aligned in the x-y plane. Therefore, it is important to verify that a given electrode structure generates an electric field consisting of a primarily lateral component. To accomplish this, the electromagnetics module of the COMSOL MULTIPHYSICS® finite element modeling software package was used to evaluate the electrode configuration. While multiple electrode geometries have been investigated, only the most basic structure, as shown in Fig. 1, will be discussed here for the sake of simplicity.

Figure 5(a) shows a streamline plot of the electric field lines produced from the simple electrode geometry with a gap of 20 μm. The streamlines visualize the direction of the electric field lines with no information about the strength of the vector field. Figure 5(b) is an image of the electric field produced by the gap depicted through arrows which illustrate the direction (orientation of arrow) and relative intensity of the electric field (size of arrow) in the ZnO. The plots specify that the electric field is aligned parallel to the surface in the area between the gaps, while it is aligned primarily normal to the surface in the area directly below the electrodes. The relative sizes of the arrows in Fig. 5(b) show that the relative strength of the electric field within the electrode gap is approximately twice that of the electric field directly beneath the electrodes (data not shown). These plots indicate that the electric field generated by the proposed electrode configuration will generate a laterally oriented field in the active area of the device with a minimal surface-normal component which is a requisite for lateral field excitation. Further, it is indicated that a weak response due to thickness excitation of the longitudinal mode is expected.

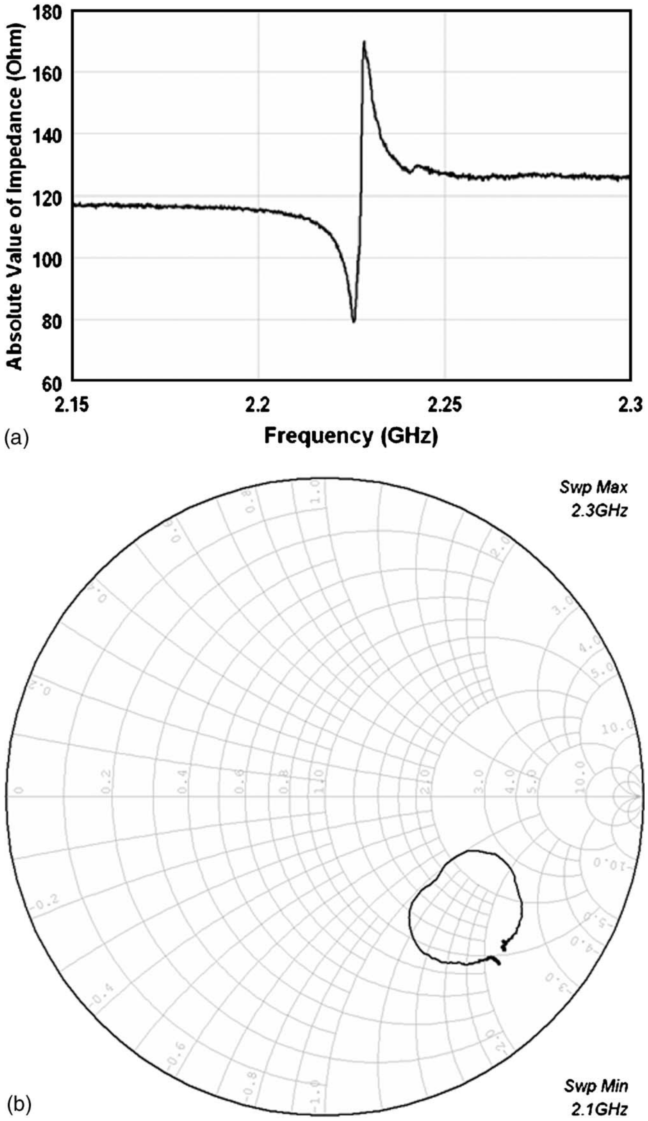

FIG. 6. Network analyzer probe measurements showing (a) the magnitude of the impedance response as a function of frequency and (b) the S_{11} Smith chart plot.

IV. RESULTS AND DISCUSSION

RF probing of individual devices yielded thickness shear mode activity in the ZnO devices over a range of ZnO thin film thicknesses. Testing the acoustic response by fabricating wafers with multiple thicknesses of ZnO is important for verifying that the S_{11} response is due to an acoustic phenomenon rather than some electromagnetic resonance. This can be done by verifying that as the film thickness changes, the resonant frequency changes accordingly. Probing of more than 30 devices yielded impedance and S_{11} responses similar to those shown in Fig. 6. As can be seen from the Smith chart [Fig. 6(b)], a clear loop pattern, indicative of resonant activity, is present. An average unloaded Q of these resonators is

TABLE II. Result of changing ZnO thickness on resonator response.

Measured ZnO thickness (nm)	f_0 (GHz)	Extracted acoustic velocity (m/s)
790	2.0	3160
710	2.2	3130
660	2.35	3100

approximately 340 and the K^2 is approximately 0.4%, with peak values of 550 and 0.88%, respectively. The calculations used to assess Q and K^2 are[26,28]

$$Q = \left(\frac{f}{2}\right)\frac{d\angle Z}{df}, \tag{11}$$

$$K^2 = \left(\frac{\pi}{2}\right)^2 \frac{f_p - f_s}{f_p}. \tag{12}$$

The acoustic velocity was empirically determined to be on the average of 3130 m/s. This is somewhat close to the theoretical value of 2841 m/s, but much closer to the experimental value of 3280 m/s, as calculated from the results of Woo Wai *et al.*[29] The theoretical longitudinal velocity for ZnO is approximately 6300 m/s. This value is much higher than the experimentally obtained acoustic velocity, and is therefore a good indicator that it is the shear mode that is being excited and not the longitudinal. Interestingly, no longitudinal peak was found to exist throughout the frequency spectrum of the resonators and may be attributed to poor reflection characteristics of the mirror at the longitudinal frequency. This can also be explained by the weak electric field component normal to the surface generated by the electrode configuration. To further confirm acoustic wave resonance, we altered the thickness of the ZnO to demonstrate that increasing the film thickness resulted in a corresponding decrease in resonant frequency. The results of these tests are summarized in Table II. We feel that the resonance could be significantly improved through optimization of the electrode configuration to enhance piezoelectric coupling of the electric field energy to the crystal and to provide energy trapping for the acoustic wave.

Aside from comparing the experimentally obtained acoustic velocity to the TSM and longitudinal velocities, another way to further establish the existence of a thickness shear mode is to expose the resonators to water at the surface. If the acoustic activity were longitudinal, application of de-ionized water at the surface would decimate the acoustic resonance observed in the device since water can support a longitudinal wave, but not a shear wave. Figure 7 shows the response before (triangles) and after (squares) application of de-ionized water to the surface. As can be seen, the water had only small effects on the suppression seen in the S_{11} magnitude response, and a negative frequency shift occurred after water was applied to the device of approximately 1.1 MHz. According to Sauerbrey,[8] this response is to be expected from a TSM device, roughly described in his equation

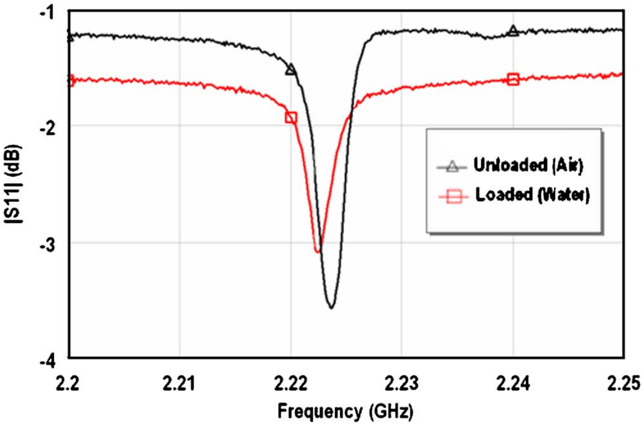

FIG. 7. (Color online) Frequency shift observed in S_{11} measurement in response to loading the surface of the resonator with de-ionized H_2O. Some deterioration of the resonance was observed resulting in the decrease of the Q factor.

$$\Delta f = \left(\frac{-2f_0^2}{A\sqrt{\rho_q \mu_q}}\right)\Delta m_q, \tag{13}$$

where f_0 is the resonant frequency of the device, A is the relevant area, ρ_q is the material density, μ_q is the material stiffness, and Δm_q is the change in mass at the surface. It is reasonable to assume that the observed frequency shift indicates a mass loading on the surface of the device by the de-ionized water. This would also confirm the prediction made by analysis of the Christoffel matrix that the wave is a TSM wave. The response to the water test was shown to be repeatable across different devices in various locations about the wafer.

V. CONCLUSIONS

Theoretical analysis of the Christoffel equation has shown that a TSM wave can be excited in c-axis-oriented ZnO with an in-plane excitation field oriented in any direction on the wafer. Further, it has been shown that the shear particle displacement will be parallel to the excitation field, assuming an entirely lateral field.

To implement the theoretical findings, a solidly mounted resonator consisting of alternating layers of W and SiO_2 were grown on a p-doped $\langle 1\ 0\ 0\rangle$ Si substrate with ZnO as the active piezoelectric layer at the surface. The acoustic mirror was designed to have a reflection coefficient closest to unity near the frequency of operation. The acoustic mirror frequency response was simulated to provide assurance of the frequency range coverage given a fixed number of alternating pairs of W and SiO_2. Finite element modeling was also performed to predict the electric field of an electrode configuration consisting of two long electrodes positioned on the top of the ZnO with a gap between them. Simulations showed that the electric field within the gap between the electrodes was primarily laterally oriented, while the electric field directly beneath the electrodes was shown to be reduced in magnitude with an orientation normal to the surface of ZnO.

To verify the thickness shear mode operation of the devices, we investigated the experimentally extracted acoustic velocity and the effects of water loading on the resonance. Without these tests it is difficult to adequately determine that a resonance is necessarily TSM. We have presented evidence of a TSM wave through exposure of the device to de-ionized water, comparison of extracted acoustic velocity with theoretical acoustic velocity, and varying the piezoelectric film thickness to yield respective changes in the frequency response.

On the basis of these results, it is expected that with an appropriate chemical surface preparation, these devices could be used as a platform for biosensor applications. The simple fabrication and small device size make this an appropriate candidate for fabrication of sensor arrays. The results of our investigation indicate that the lateral excitation of a thickness shear mode in solidly mounted ZnO FBARs is realizable both theoretically and experimentally. In the future, we will experiment with multiple electrode geometries in order to improve device response and performance.

ACKNOWLEDGMENTS

This work was supported by the Georgia Tech/Emory Fund for Innovative Cancer Technologies which derives its funds from The V Foundation and the Georgia Cancer Coalition. In addition, Chris Corso was supported by a NSF Graduate Research Fellowship. Further, we must acknowledge the support of Dr. Colin Wood of the Office of Naval Research under the MURI program “Epitaxial Multifunctional Materials and Applications.” We would also like to thank John Perng and Brent Buchine for their time and help with obtaining the SEM images. The support of all of these organizations is very much appreciated.

[1] J. W. Chung, J. M. Park, R. Bernhardt, and J. C. Pyun, J. Biotechnol. (2006).
[2] M. S. Wilson and W. Nie, Anal. Chem. **78**, 6476 (2006).
[3] S. L. Pinkett, W. D. Hunt, B. P. Barber, and P. L. Gammel, IEEE Trans. Ultrason. Ferroelectr. Freq. Control **49**, 1491 (2002).
[4] A. Shons, F. Dorman, and J. Najarian, J. Biomed. Mater. Res. **6**, 565 (1972).
[5] X. L. Su and Y. Li, Biosens. Bioelectron. **19**, 563 (2004).
[6] Z. Y. Wu, G. L. Shen, S. P. Wang, and R. Q. Yu, Anal. Sci. **19**, 437 (2003).
[7] C. D. Corso, D. D. Stubbs, S. H. Lee, M. Goggins, R. H. Hruban, and W. D. Hunt, Cancer Detect. Prev. **30**, 180 (2006).
[8] G. Sauerbrey, Z. Phys. **155**, 206 (1959).
[9] K. K. Kanazawa and J. G. Gordon, Anal. Chem. **57**, 1770 (1985).
[10] W. D. Hunt, D. D. Stubbs, and L. Sang-Hun, Proc. IEEE **91**, 890 (2003).
[11] S. L. Pinkett, Ph.D. thesis, Georgia Institute of Technology, 2003.
[12] J. V. Atanasoff and P. J. Hart, Phys. Rev. **59**, 85 (1941).
[13] R. Bechmann, 14th Annual Symposium on Frequency Control (US Army Electronics Research and Development Laboratory, Atlantic City, NJ, 1960), pp. 68–88.
[14] E. R. Hatch and A. Ballato, Ultrason. Symp. Proc. (IEEE Group on Sonics & Ultrasonics, Atlanta, GA, 1983), p. 512
[15] A. W. Warner, 17th Annual Symposium on Frequency Control (US Army Electronics Research and Development Laboratory, Atlantic City, NJ, 1963), pp. 248–266.
[16] H. Yihe, L. A. French, Jr., K. Radecsky, M. Pereira da Cunha, P. Millard, and J. F. Vetelino, IEEE Trans. Ultrason. Ferroelectr. Freq. Control **51**, 1373 (2004).
[17] H. Yihe, L. A. French, Jr., K. Radecsky, M. Pereira da Cunha, P. Millard, and J. F. Vetelino IEEE Trans. Ultrason. Ferroelectr. Freq. Control **51**, 1373 (2004).
[18] W. Pinkham, M. Wark, S. Winters, L. French, D. J. Frankel, and J. F. Vetelino, Proc.-IEEE Ultrason. Symp. **4**, 2279 (2005).
[19] C. York, L. A. French, P. Millard, and J. F. Vetelino, Proc.-IEEE Ultrason. Symp. **1**, 44 (2005).
[20] A. Ballato, E. R. Hatch, M. Mizan, and T. J. Lukaszek, IEEE Trans. Ultrason. Ferroelectr. Freq. Control **33**, 385 (1986).
[21] S. V. Krishnaswamy, B. R. McAvoy, W. J. Takei, and R. A. Moore, Ultrason. Symp. Proc. (IEEE Group on Sonics & Ultrasonics, San Diego, CA, 1982), p. 476.
[22] J. S. Wang and K. M. Lakin, Ultrason. Symp. Proc. (IEEE Group on Sonics & Ultrasonics, San Diego, CA, 1982), p. 480.
[23] M. Link *et al.*, J. Vac. Sci. Technol. A **24**, 218 (2006).
[24] M. Link, M. Schreiter, J. Weber, R. Primig, D. Pitzer, and R. Gabl, IEEE Trans. Ultrason. Ferroelectr. Freq. Control **53**, 492 (2006).
[25] P. Wei, Y. Hongyu, K. Jae Wan, Z. Hao, and K. Eun Sok, Proceedings of the 2004 IEEE International Frequency Control Symposium and Exposition, (IEEE UFFC Society, Montreal, Canada, 2004) pp. 558–561.
[26] J. F. Rosenbaum, *Bulk Acoustic Wave Theory and Devices* (Artech House, Boston, 1988).
[27] W. E. Newell, Proc. IEEE **53**, 575 (1965).
[28] K. M. Lakin, G. R. Kline, and K. T. McCarron, IEEE Trans. Microwave Theory Tech. **43**, 2933 (1995).
[29] L. Woo Wai, S. Yonghua, and K. Eun Sok, Proceedings of the 1996 IEEE International Frequency Control Symposium (IEEE UFFC Society, New Brunswick, NJ, 1996), pp. 558–562.

Second AACR International Conference on Molecular Diagnostics in Cancer Therapeutic Development--
Sep 17-20, 2007; Atlanta, GA

Mesothelin-fc fusion protein detection using a novel microelectronic acoustic sensor platform

Anthony Dickherber, Christopher Corso, William Hunt, Ira Pastan, Mitchell Ho and Raffit Hassan

Georgia Institute of Technology, Atlanta, GA, Center for Cancer Research, National Cancer Institute, NIH, Bethesda, MD

Abstract A26

Advances in the proteomics of cancer proliferation are yielding many new potential targets, or biomarkers, for identifying a malignancy at the earliest stages of development. These markers have been difficult to find as they exist in extremely low concentrations in circulating blood. In order to make use of these discoveries at a clinical level, ultra-sensitive biosensors exhibiting high degrees of specificity will be required to identify these proteins in clinical samples, such as patient blood plasma or serum. Further, a sensing technology that identifies a multi-protein signature is most likely to minimize false positives and false negatives. A sensor array incorporating these aspects could have an impact at multiple levels including early detection screening, post-therapy monitoring, as well as on the proteomic discovery process.

The research presented here involves the development of such a tool and its application towards detecting mesothelin, a cell-surface protein that is highly expressed in mesothelioma, ovarian cancer, pancreatic cancer, and some other malignancies. The acoustic resonator array design consists of electrodes fabricated on the surface of a piezoelectric ZnO thin-film. To functionalize the resonators for mesothelin detection, MB Mabs were immobilized on the surface, which have an affinity for mesothelin at 0.6 nmol/L. The Mabs were bound to the surface using a thiol-terminated silane surface chemistry. Reference device arrays coated with anti-FITC antibodies, specific to a molecule not present in the analyte, were also prepared. The goal of the investigation was therefore to gauge the sensitivity of the sensors to the molecular binding of mesothelin. A total of n=16 mesothelin-targeted devices and n=16 reference devices were tested by exposing them to a 10 µg/ml solution of purified mesothelin-rfc protein in PBS buffer for 25 minutes. The devices were washed and the final operating frequencies were measured. The frequency shifts were then compared with the initial "unloaded" operating frequencies. The reference sensors showed a mean shift of 540 kHz while the mesothelin-coated sensors showed a mean shift of 1.25 MHz. ANOVA was performed on the results which indicate a statistically significant difference ($p < 0.001$) in the overall frequency shifts associated with the mesothelin-target sensors and the reference sensors.

The magnitude of these preliminary results promises a detection limit at much lower target concentrations than those tested; potentially well below the ng/ml threshold upheld in the literature as the necessary sensitivity level. An important feature of these devices is that the sensitivity of the sensor platform is scaleable by a simple adjustment of the fabrication parameters. The device design also incorporates standard fabrication practices from the microelectronic device industry, allowing for mass production of extremely low-cost sensors. Work is on-going to demonstrate the efficacy of these devices under realistic physiological conditions and for lower concentrations of target.

EMBARGOED FOR RELEASE:
2:15 p.m. EDT
Tuesday, September 18, 2007

CONTACT:
Greg Lester
267-646-0554
lester@aacr.org
In Atlanta (September 17-20):
404-221-6855

A New Technology for Cancer Screening Listens for the Signs of Cancer

ATLANTA – Cancer-sensing devices built as cheaply and efficiently as wristwatches – using many of the same operating principles – could change the way clinicians detect, treat and monitor cancer in patients. Researchers from the Georgia Institute of Technology have created an acoustic sensor that can report the presence of small amounts of mesothelin, a molecule associated with a number of cancers including mesothelioma, as they attach to the sensor's surface.

According to the researchers, the study is a proof of principle, demonstrating a technique that might work for the detection of nearly any biomarker – a collective term for a molecular signal that denotes the presence of disease. They present their findings today in Atlanta, Georgia at the American Association for Cancer Research's second International Conference on Molecular Diagnostics in Cancer Therapeutic Development.

"It is one thing to be able to identify biomarkers for a disease, but it is another to be able to find them in blood quickly and easily at very low concentrations," said Anthony Dickherber, a graduate student in the School of Electrical and Computer Engineering at Georgia Tech. "We envision that, one day, doctors can use an array of our sensors as a sort of laboratory in their office, where they could use a quick blood sample to detect or monitor the signs of cancer."

According to Christopher Corso, the other graduate student engaged in the project and an M.D., Ph.D. student, such a device would be a boon to healthcare practice, allowing physicians to screen patients for signs of disease before opting for more expensive or invasive diagnostic techniques. Responding to the growing need for such sensors in both research and clinical practice, Dickherber, Corso and research adviser William D. Hunt, Ph.D., conceived of and developed the ACuRay™ (pronounced ak´-u-rā) chip, standing for ACoustic micro-arRay – a device that shares more in common with an inexpensive wristwatch than the sort of cutting edge molecule-sorting apparatuses currently used by researchers and clinical laboratory technicians.

The array consists of a series of electrodes deposited on the surface of a thin film of zinc oxide, which allows the device to resonate, or vibrate, at a specific frequency when a current is applied, much like the quartz timing devices used in many clocks and watches.

-- more --

"The sensor itself is built on a base of silicon, like a computer chip, and could be mass-produced using very well known and inexpensive microelectronic fabrication techniques," Dickherber said.

To turn this array into a sensor, the Georgia Tech researchers coated the zinc oxide surface with mesothelin-specific antibodies generated in the lab of Ira Pastan, M.D., at the National Cancer Institute. These molecules are engineered versions of the antibodies the immune system creates to identify foreign intruders, such as microbial parasites. In this study, the researchers coated the sensor with antibodies for mesothelin, a cell-surface protein that is highly expressed in mesothelioma, ovarian cancer, pancreatic cancer and other malignancies.

When the mesothelin binds to an antibody, the added mass changes the frequency at which the acoustic wave passes between the electrodes on the surface of the device. The device is able to "hear" the pitch change due to nanomolar concentrations of mesothelin (just a few molecules amid billions) binding to antibodies on the chip. The technology has the potential of detecting biomarkers in even lower concentrations than those tested, Dickherber said.

"It is really an elegant engineering solution to a very complicated problem," said Hunt, a professor of electrical and computer at Georgia Tech and lead researcher on the project. "We could, for example, detect a number of different markers for a single disease on a single chip no bigger than the tip of a fountain pen. With refinement, this technology could readily lead to an inexpensive, ubiquitous technology for researchers, physicians and the clinical laboratory."

This research is supported by grants from the U.S. Army Medical Research & Materiel Command Prostate Cancer Research Program, the National Science Foundation, The V Foundation, the National Cancer Institute and the Georgia Cancer Coalition.

# # #

AACR 2007 Conference on Molecular Diagnostics in Cancer Therapeutic Development
September 17-20th, Atlanta, Ga.

Coverage for Tony Dickherber, “A New Technology for Cancer Screening Listens for the Signs of Cancer”*

From our press release:
RxPG News
http://www.rxpgnews.com/research/A-new-technology-for-cancer-screening-listens-for-the-signs-of-cancer_64056.shtml

Dentalplans.com
http://www.dentalplans.com/articles/25102/

PhysOrg.com
http://www.physorg.com/news109349930.html

ScienceDaily
http://www.sciencedaily.com/releases/2007/09/070918144313.htm

Original Stories:

WebMD (Dan DeNoon)
“Sensor Hears Cancer's Call; Tiny Biosensors Detect ‘Song’ of Cancer Markers, Say Researchers”
http://www.webmd.com/cancer/news/20070918/sensor-hears-cancers-call

From the WebMD story above:
Medicine.net
http://www.medicinenet.com/script/main/art.asp?articlekey=83974

From the Amanda Gardner HealthDay story “Tiny Sensor Could Spot Cancer Early”:

CBC News
http://www.cbc.ca/cp/HealthScout/070918/6091806AU.html

Health Central.com
http://www.healthcentral.com/newsdetail/408/608331.html

WFIE 14 Indiana (NBC affiliate)
http://www.14wfie.com/Global/story.asp?S=7094493&nav=3w6r

LEX 18 Kentucky (NBC affiliate)
http://www.lex18.com/Global/story.asp?S=7094493&nav=EQls

Forbes
http://www.forbes.com/forbeslife/health/feeds/hscout/2007/09/18/hscout608331.html

US News & World Report
http://health.usnews.com/usnews/health/healthday/070918/tiny-sensor-could-spot-cancer-early.htm

Dentalplans.com
http://www.dentalplans.com/articles/25095/

Health Scout
http://www.healthscout.com/news/1/608331/main.html

HealthCentral.com
http://www.healthcentral.com/newsdetail/408/608331.html

KOLD News Arizona (CBS Affiliate)
http://www.kold.com/global/story.asp?s=7094493

CNN News Room
(Please see page 3 for transcript)

* We will continue to monitor coverage

CNN
September 19, 2007 Wednesday
SHOW: CNN NEWSROOM 3:00 PM EST
Bail Set For O.J. Simpson; Ahmadinejad to Visit Ground Zero?; Al Sharpton's Planned Protest in Jena, Lousiana
BYLINE: Joe Johns, Paul Vercammen, Deborah Feyerick, Susan Roesgen, Ed Lavandera, Don Lemon, Fredricka Whitfield, Jeffrey Toobin, Sanjay Gupta, Susan Lisovicz, Wolf Blitzer
SECTION: NEWS; International

WHITFIELD: Straight ahead, a high tech computer chip smaller than a penny that can detect cancer. Details on that straight ahead in "THE NEWSROOM".

WHITFIELD: A computer chip could one day make diagnosing cancer as easy as telling time.

Here's CNN's chief medical correspondent, Dr. Sanjay Gupta.

DR. SANJAY GUPTA, CNN CORRESPONDENT: This is something that really fascinates me quite a bit. This is a little chip that I'm holding up here. I'm actually holding it in a pair of tweezers this thing is so small. It's called the ACuRay and it's not something that's going to be widely available quite yet. But researchers have been focusing on this particular chip as a way to detect cancer very, very early.

Again, it's called the ACuRay. You can take at it there. What it is specifically is 140 different electrodes actually bound together by zinc oxide. The theory a simple one -- basically, if you have cancer molecules in your blood and you wash your blood over the sensor, the way that those cancer molecules bind to this

ACuRay gives off a certain resonance, a certain frequency that can be measured. If you have cancer molecules, it's going to sound different than if you don't have cancer molecules in your blood. The whole idea is that you want to detect cancer as early as possible.

Now what does this all mean?

There could be a day when doctors have several different little devices like this in their office and you walk in, you give a drop of blood and they immediately screen to tell if you have any cancer molecules in your bloodstream. It could be used, perhaps, in the future for infectious diseases, as well.

Again, as I mentioned, it's not something we may see in our lifetimes as a general way of practicing, but this whole idea you might be able to find cancer early, earlier than ever before, before it shows up on a C.T. scan or an MRI, when it's just a few still a few molecules in your blood is sort of the holy grail of cancer detection and screening.

Could this be the answer?

Possibly one day. It's something that we're certainly going to keep an eye on -- back to you.

LEMON: All right, Sanjay.

It's time now to check in with CNN's Wolf Blitzer.

WHITFIELD: Yes, in "THE SITUATION ROOM" -- what do you have on tap?

WOLF BLITZER, HOST, "THE SITUATION ROOM": All right, guys, thanks very much.

The Republican presidential candidate, Rudy Giuliani, has a message for MoveOn.org -- bring it on. He talks about his high profile spat with the liberal anti-war group in an exclusive one-on-one interview with our chief national correspondent, John King. That's coming up.

Also, Reverend Jesse Jackson says Democratic presidential candidate Barack Obama -- and I'm quoting now -- "is acting like he's white." We'll show you what's behind that controversial comment.

Also, carefree lives in the face of unimaginable suffering. There are some disturbing newly released images of the men and women who ran the Nazi Auschwitz death camp. All that and a lot more coming up right here in "THE SITUATION ROOM" -- back to you.

LEMON: All right, Wolf, we'll be watching.

Thank you. WHITFIELD: All right, the closing bell and a wrap of the action on Wall Street straight ahead.

Stability of a RF sputtered ZnO solidly mounted resonator sensor in varying temperature and conductivity environments

Anthony Dickherber[†], Christopher D. Corso[‡], and William Hunt[†]
[†]Dept of Electrical and Computer Engineering, Georgia Inst. of Technology, Atlanta, GA 30332
[‡]Dept of Biomedical Eng, Georgia Inst. of Technology, Atlanta, GA 30332
Email: bill.hunt@ee.gatech.edu

***Abstract*–It has been demonstrated that thickness shear mode acoustic wave devices have been extremely useful for liquid phase sensing applications, especially as biosensors. The quartz crystal microbalance is likely the strongest demonstration of this application to date. Recently, we reported a ZnO-based TSM device that is easily fabricated and operates at significantly higher frequencies than the QCM. To further validate the usefulness of the ZnO resonator as a strong candidate for biosensor applications, we report the stability of the device over varying temperature and sample conductivity. A modest thermal coefficient of resonant frequency is reported at ~25 ppm/°C. Further, it is demonstrated that the resonator exhibits reasonable stability over a range of sample conductivities (0.0 to 0.9 % wt/vol NaCl in DI H_20).**

I. INTRODUCTION

To date, the quartz crystal microbalance (QCM) resonator has best demonstrated the potential of bulk acoustic wave (BAW) devices as biosensors. QCM resonators excite a thickness shear mode (TSM) bulk wave through the thickness of a quartz crystal wafer, which is necessary for operation of the resonator in a liquid-phase medium. This is what makes the device so attractive for biosensor applications, especially in the field of medical diagnostics where the samples under test are often in aqueous form. The QCM is additionally attractive because it demonstrates excellent temperature stability which is a property of the AT-cut quartz plates used to make the QCM.

Thin film bulk acoustic resonators (FBARs) are employed widely from front-end filtering applications to resonator-based biosensors. Recently, we reported on a ZnO-based TSM FBAR device that is easily fabricated and operates at significantly higher frequencies than the QCM [1]. Additionally, these resonators have been fabricated in a solidly mounted resonator (SMR) configuration, which allows them to be imbedded in existing silicon or gallium arsenide-based fabrication processes with a very small footprint (<1000 μm^2 per device). In progression towards the development of ultra-sensitive biosensor arrays, these devices have been fabricated in a multi-device configuration.

TSM operation of the resonator is achieved by lateral field excitation (LFE) of the piezoelectric layer, requiring that both the signal and ground electrodes are on the surface of the ZnO. The physics of the ZnO SMR achieved by LFE of the TSM is treated by Corso, *et al* [1]. Exposure of LFE devices to biological environments translates to varying conductivity and possibly varying thermal conditions at the surface of the resonator. Similar work has been done to characterize QCMs employing LFE for biosensor applications [2]. This investigation similarly reports on the response of ZnO SMRs to a range of thermal and surface conductivity conditions.

II. DEVICE DESIGN

SMRs were fabricated by first depositing an acoustic mirror, analogous to an optical Bragg reflector, onto a (1 0 0) mechanical grade silicon wafer (University Wafer). The acoustic mirror consisted of alternating layers of SiO_2 (low acoustic impedance) and W (high acoustic impedance). Highly c-axis oriented ZnO was then deposited onto the mirror followed by aluminum electrodes, as seen in Fig. 1. SiO_2 and ZnO were deposited by RF sputtering, while the W and Al electrodes were deposited by DC sputtering. Electrodes were fabricated on the surface of the piezoelectric ZnO film by standard photolithography methods. All sputtering depositions were performed by a Unifilm PVD-300 multi-target sputtering system, using the sputtering parameters summarized in Table 1. (All sputtering targets were obtained from PureTech, Inc.) Fig. 2 shows one of the 8-device arrays occupying roughly 5 mm^2 of surface space.

Resonators were probed using a Cascade Microtech 9000 Analytical Probe Station and scattering (S) parameters were gathered using a HP 8753C Network Analyzer outfitted with a

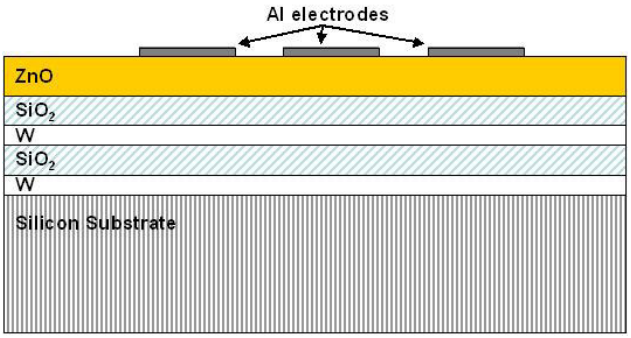

Figure 1. Cross section of the acoustic resonator solidly mounted on a W/SiO_2 acoustic mirror.

TABLE 1. SPUTTERING PARAMETERS

	Pressure (Torr)	Temp.	% Ar	% O_2
SiO_2	5.02×10^{-3}	Ambient	80	20
W	5.00×10^{-3}	Ambient	100	0
ZnO	5.10×10^{-3}	325°C	80	20
Al	5.02×10^{-3}	Ambient	100	0

HP 85047A S-Parameter Test Set. A ThermoChuck (Temptronic Corp.) system was set up on the probe station in order to control the wafer temperature. Finally, saline solutions were prepared using 99.5% NaCl (Sigma) and HPLC-grade deionized H_2O (Burdick & Jackson) and mixed for at least 30 seconds on a mini vortexer (VWR Scientific Products). Saline solutions were deposited on the resonator surface by hand-pipetting ~2 μl directly onto the surface while being probed.

III. RESULTS

It was first empirically verified that the resonator design displayed in Fig. 2 performed as well in the array configuration as individual devices with the same electrode layout. That is to say, it was confirmed that the array structure did not bear any beneficial nor detrimental effects on the resonator's performance. A broad sampling of devices (n>20 each) showed the maximum and average coupling coefficients, K^2, and quality factor, Q, were consistently about equal for both the array layout and the individual resonator layout.

With the goal of employing these resonators in biosensor applications, the arrays were tested over a temperature range of 20°C to 175°C. The equation used to calculate the thermal coefficient of resonant frequency (TCF) was

$$TC(f_x) = \frac{df_x}{dT} \cdot \frac{1}{f_{x,RT}} \tag{1}$$

where T is the temperature, f_x is the relevant resonant frequency and RT represents room temperature (25°C). The results yielded an empirically derived TCF for the series and parallel resonance of 24.6 ppm/°C and 25.6 ppm/°C, respectively. These results are illustrated in Fig. 3.

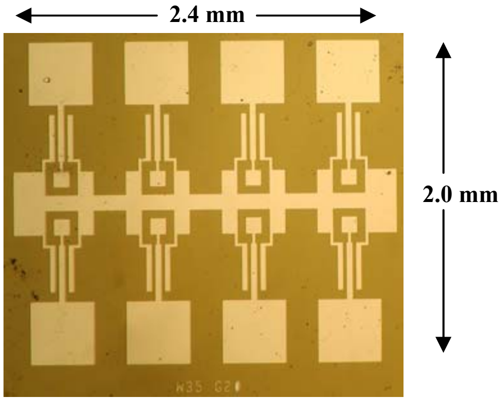

Figure 2. Digital image of fabricated 8-device array. Device is designed for probing with Cascade Microtech ACP40 probes and with pads large enough for subsequent wire bonding.

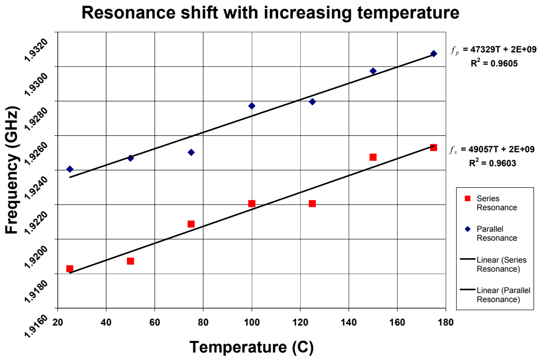

Figure 3. Frequency drift of parallel and series resonance frequency with increasing temperature.

From the collected reflection scattering parameters (S_{11} responses), K^2 and Q were determined as follows:

$$K^2 = \left(\frac{\pi}{2}\right)^2 \frac{f_p - f_s}{f_p} \tag{2}$$

$$Q = \left(\frac{f}{2}\right)\frac{d\angle\Phi_Z}{df} \tag{3}$$

where p denotes parallel and s denotes series of the resonance, f, and Φ_Z is phase of the impedance [3]. It was found that the K^2 remained very stable over the temperature range tested, varying by only 0.1% over the 155°C range. The Q drift of the resonator was slightly more significant, varying by roughly 42% over the 155°C temperature range. Considering application of these sensors towards a common bench-top laboratory system, the Q remained stable enough to consider negligible, exhibiting an average 0.28 point shift per degree Celsius (<0.2% per degree). The results for the temperature stability of K^2 and Q are summarized in Fig. 4.

With the goal of employing these resonators in biosensor applications with biological fluid samples, the resonators were tested over a range of sample conductivities loading the surface with 0.0% to 0.9% wt/vol of NaCl in DI H_2O. A 0.9% NaCl in DI H_2O solution is generally considered to be isotonic with human blood. Results indicated that the magnitude of resonator frequency shift varied little in relation to loading with pure water alone, as indicated in Fig. 5. As can be seen, the percentage of frequency shift with increasing sample conductivity was just slightly more significant than the noise level. Because these devices are not high-Q, the resonance peak is slightly broad and incidental fluctuations in the reflection parameters will cause the monitoring system to register a range in the resonance indicating instability of the resonance condition. Note the error bars in Fig. 5 indicate the measured range of this apparent instability due to these incidental fluctuations. A further indicator of this can be seen in Fig. 6, which represents the results of a typical experiment when sample is deposited on the device surface then subsequently washed with DI H_2O.

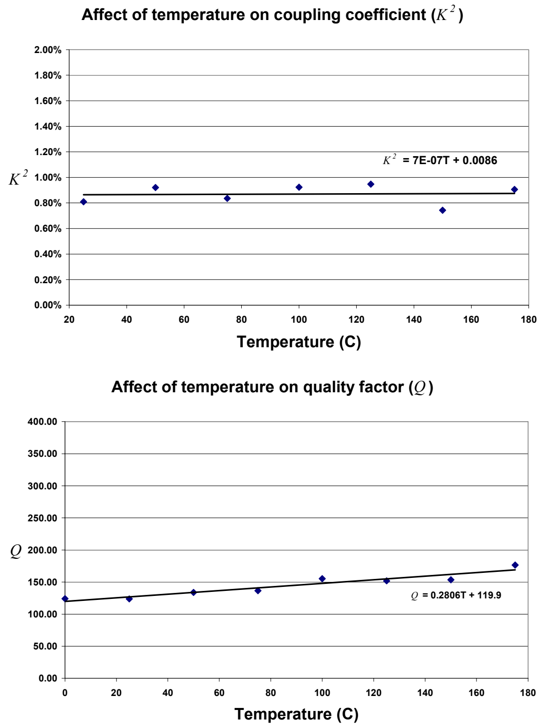

Figure 4. Variation observed over a wide temperature range for the resonator coupling coefficient, K^2, (top) and the resonator quality factor, Q (bottom).

IV. DISCUSSION

A similar investigation of the TCF for ZnO SMRs excited by thickness excitation was performed by Pinkett, *et al.* [4]. These resonators excited a longitudinal acoustic wave, as opposed to the TSM waves seen in this investigation, which yielded a steady decrease in resonance with increasing temperature. It was posited by Pinkett *et al*. that the frequency decrease was due to an expansion of the ZnO thickness, resulting in a longer acoustic path length, and therefore a lower resonant frequency. The frequency of the resonant wave is determined by the following:

$$f = \frac{v_a}{2d} \tag{4}$$

where d is the material film thickness and v_a is the acoustic velocity [3]. This term is defined as

$$v_a = \sqrt{\frac{c}{\rho}} \tag{5}$$

where c is the relevant material stiffness and ρ is the material density. The two investigations were carried out over a similar temperature range on ZnO fabricated in the same sputtering system under the same conditions. One possible explanation for the difference is that expansion of the ZnO film, which would reduce the frequency, was overtaken by an increase in the shear stiffness. This would of course have to be greater than changes in the longitudinal stiffness that would have effected Pinkett *et al*. Another possibility could be the differing expansion properties of W versus Ta_2O_5 which could have altered the resonance frequency over the effects of the piezoelectric film expansion. This latter explanation seems highly unlikely, however, considering the magnitude of the difference between both experiments.

It was found from the conductivity experiments that the noise level of the resonator frequency response rose with increasing salinity of the test solution. The noise in the response is undesirable because it introduces error into the resonance tracking protocol. Ideally, the S_{11} response of the resonator should have as narrow and smooth a peak as possible, so as to result in an easily tracked resonance condition. This parameter is gauged by the Q of the resonator, which can be explained as a ratio of the energy stored versus the energy dissipated per cycle of resonance. If the resonator transduces a wider frequency band, it is likely that the varying wave frequencies will compete for the available energy and also interfere destructively.

The QCM demonstrates extraordinarily high Q, often in the 10's of thousands, and therefore has an easily tracked

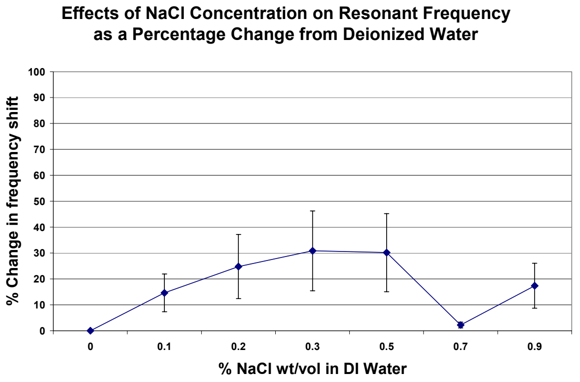

Figure 5. Percent change in resonant frequency as a function of increasing sample conductivity.

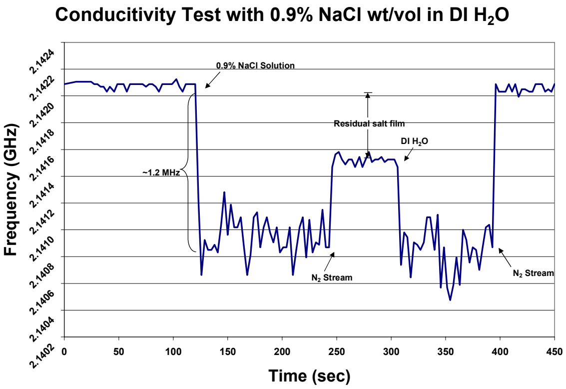

Figure 6. Demonstration of a typical conductivity experiment with 0.9% NaCl in DI H_2O.

resonance. Such a high *Q* is not required for tracking, however, as demonstrated by various other acoustic wave based sensors [5, 6]. Optimization of the ZnO-based resonator presented in this research will be required to stabilize this response and provide a viable ultra-sensitive biosensor. Optimizing the individual device *Q* should result in the resonator only transducing the electrical driving energy about a tight band and therefore yield a reduced noise level.

V. CONCLUSION

In this investigation, it has been shown that ZnO solidly mounted resonators can be fabricated in an array configuration without loss of performance. Further, it has been shown that these resonators can operate stably in biologically equivalent environments. Specifically, these resonators have been shown to exhibit low susceptibility to changes in temperature and conductivity. In order to achieve sensors of greater quality, however, it will be necessary to optimize the device *Q*.

ACKNOWLEDGEMENTS

This work was supported by the Georgia Tech/Emory Fund for Innovative Cancer Technologies which derives its funds from the V Foundation and the Georgia Cancer Coalition (GCC). Anthony Dickherber is supported by the Congressionally Directed Medical Research Program Prostate Cancer Training Program and Christopher Corso is supported by an NSF Graduate Research Fellowship. We would further like to acknowledge the assistance of George Steven Ruff and Alice Wang who developed the tracking software used in conjunction with the HP Network Analyzer.

REFERENCES

[1] C. D. Corso, A. Dickherber, and W. D. Hunt, "Lateral field excitation of thickness shear mode waves in a thin film ZnO solidly mounted resonator," *Journal of Applied Physics & Virtual Journal of Biological Physics Research*, vol. 101, 2007.

[2] Y. Hu, L. A. French, Jr., K. Radecsky, M. P. DaCunha, P. Millard, and J. F. Vetelino, "A lateral field excited liquid acoustic wave sensor," presented at 2003 IEEE Symposium on Ultrasonics, Orono, ME, USA, 2003.

[3] J. F. Rosenbaum, *Bulk acoustic wave theory and devices*. Boston: Artech House, 1988.

[4] S. L. Pinkett and W. D. Hunt, "Temperature Characteristics of ZnO-Based Thin Film Bulk Acoustic Wave Resonators," presented at 2001 IEEE Ultrasonics Symposium, 2001.

[5] F. Josse, F. Bender, and R. W. Cernosek, "Guided Shear Horizontal Surface Acoustic Wave Sensors for Chemical and Biochemical Detection in Liquids," *Anal. Chem.*, vol. 73, pp. 5937-5944, 2001.

[6] S.-H. Lee, D. D. Stubbs, W. D. Hunt, and P. J. Edmonson, "Vapor phase detection of plastic explosives using a SAW resonator immunosensor array," presented at IEEE Sensors, 2005.

Available online at www.sciencedirect.com

ScienceDirect

Sensors and Actuators A 144 (2008) 7–12

SENSORS AND ACTUATORS A PHYSICAL

www.elsevier.com/locate/sna

Optimization and characterization of a ZnO biosensor array

Anthony Dickherber[*], Christopher D. Corso, William D. Hunt

Microelectronics Research Center, Georgia Institute of Technology, 791 Atlantic Drive, Atlanta, GA 30332, USA

Received 2 August 2007; received in revised form 2 January 2008; accepted 2 January 2008
Available online 19 January 2008

Abstract

Practical usage of acoustic biosensors has revealed that high quality factor, Q, is an important attribute of a highly sensitive acoustic sensor. In this research, we present performance optimization of ZnO thin-film bulk acoustic resonators (FBARs) operating in the thickness shear mode through characterization of a variety of electrode geometries. The resulting average Q and K^2 from each of the electrode geometries were calculated and compared. Based on these results, a preferred electrode configuration was selected, and fabricated into an 8-device array. The arrays were tested in physiologically relevant environments to illustrate the effects of temperature and solution conductivity on the stability of the resonators. The devices demonstrated a temperature coefficient of frequency of ∼25 ppm/°C. The resonators also exhibited reasonable stability under varying levels of solution conductivity as tested by exposing the devices to solutions containing a varied amount of NaCl in deionized H_2O.

Keywords: ZnO; Biosensor; Array; TOF; Thickness shear mode; Acoustic wave sensor; Lateral field excitation

1. Introduction

Thin-film bulk acoustic wave resonators (FBARs) are employed widely from front-end filtering applications to resonator-based biosensors. To date, the quartz crystal microbalance (QCM) resonator has best demonstrated the potential of bulk acoustic wave (BAW) biosensors [1]. QCM resonators excite and support a thickness shear mode (TSM) bulk wave through the thickness of the crystal wafer, which is necessary for operation of the resonator in a liquid-phase medium. This is what makes the device so attractive for biosensor applications, especially in the field of medical diagnostics where most clinically relevant samples to be tested are in the liquid phase. The QCM is additionally attractive because it demonstrates excellent frequency stability over a significant frequency range as a result of the AT-cut crystal structure that comprises the QCM [2].

Recently, we reported on a ZnO-based TSM FBAR device that is easily fabricated and operates at significantly higher frequencies than the QCM [3]. Theory predicts that higher operating frequency is desirable as it translates to greater sensitivity to perturbation of the sensor [1]. Additionally, these resonators have been fabricated in a solidly mounted resonator (SMR) configuration, which allows them to be imbedded in existing silicon or gallium arsenide-based fabrication processes with a very small footprint (<0.05 mm^2 per device as compared to a QCM which is roughly 150 mm^2 per device). An SMR configuration involves fabricating the device onto a solid support, which typically includes an acoustic Bragg reflector, comprised of quarter-wavelength alternating high and low impedance materials to reflect the acoustic wave. This acoustic mirror helps to maintain resonance in the piezoelectric film due to an impedance mismatch at the boundary. The very small size and ability to fabricate the devices using standard fabrication processes has made it possible to integrate these resonators into multi-device arrays. The motivation for this stems from the growing consensus in the medical field that the ability to make an accurate diagnosis about a specific disease, such as prostate cancer, depends on the expression levels of multiple biomarkers, rather than a single principal indicator [4]. With the array configuration, it becomes possible to monitor any sample for multiple targets simultaneously in a consistent manner.

Acoustic resonators become liquid sensors by exposing the surface of the device to a fluid sample to be tested. The acoustic wave resonating within the piezoelectric crystal film acts as a probe that effectively queries the crystal surface for changes in the boundary conditions. Certain changes in the boundary conditions register as a shift in the resonant frequency, which is an easily monitored quantity. If a chemical layer that specifically

---

[*] Corresponding author. Tel.: +1 404 894 2945; fax: +1 404 894 5504.
E-mail address: bill.hunt@ece.gatech.edu (W.D. Hunt).

0924-4247/$ – see front matter © 2008 Elsevier B.V. All rights reserved.
doi:10.1016/j.sna.2008.01.007

binds a known target molecule is immobilized at the surface (comprised of antibodies or aptamers for example) the resonator is functionalized as a biosensor. Several models exist to describe the relationship between changes in the resonant condition for a TSM acoustic wave and changes in the boundary conditions. The first significant work attempting to characterize the sensitivity of a TSM acoustic wave sensor was described by Sauerbrey as part of his dissertation research in the late 1950s [5]. This analysis has been shown to be insufficient for operation of the sensor in a liquid phase environment, so a better description comes from Kanazawa and Gordon regarding operation of the QCM in a liquid [6]:

$$\Delta f = -f_{\mathrm{o}}^{3/2}\sqrt{\frac{\eta_{\mathrm{l}}\rho_{\mathrm{l}}}{\pi\mu_{\mathrm{q}}\rho_{\mathrm{q}}}} \tag{1}$$

where μ_q and ρ_q are the stiffness and density of the crystal, ρ_l and η_l are the density and viscosity of the liquid, and f_o is the unloaded resonant frequency of the device. This equation predicts that the resonant frequency of a QCM is affected by the density–viscosity product of the contacting liquid. Further research has been performed to illustrate the QCMs efficacy as a viscosity sensor [7]. Starting from the reciprocity relation (as described by Auld [8]) Hunt et al. derived the following expression to further characterize the factors affecting the TSM resonance using time-dependent perturbation theory [9]:

$$t\frac{\partial\Delta\omega}{\partial t} + \Delta\omega = -\frac{\omega_{\mathrm{u}}^2\cdot h_{\mathrm{f}}}{\pi\sqrt{\rho_{\mathrm{q}}\mu_{\mathrm{q}}}}\left[\Delta\rho_{\mathrm{f}} - \frac{\Delta\mu_{\mathrm{f}}}{V_{\mathrm{S}}^2}\right] + i\cdot\frac{\omega_{\mathrm{u}}\cdot h_{\mathrm{f}}}{\pi\sqrt{\rho_{\mathrm{q}}\mu_{\mathrm{q}}}} \times\left[\frac{\partial\Delta\rho_{\mathrm{f}}}{\partial t} - \frac{1}{V_{\mathrm{S}}^2}\cdot\frac{\partial\Delta\mu_{\mathrm{f}}}{\partial t}\right] \tag{2}$$

where the subscript "u" denotes the unperturbed field condition, the subscript "f" denotes the properties relating to the adjacent molecularly specific film, ω is the radian frequency, V_S is the velocity of the shear acoustic wave, and h_f is the height of the immobilized surface film. If one were to assume that $\Delta\omega$, $\Delta\rho$ and $\Delta\mu$ were independent of time, then we would find that (2) reduces to

$$\Delta f = \frac{-2\cdot f_{\mathrm{u}}^2\cdot h_{\mathrm{f}}}{\sqrt{\rho_{\mathrm{q}}\mu_{\mathrm{q}}}}\left[\Delta\rho_{\mathrm{f}} - \frac{\Delta\mu_{\mathrm{f}}}{V_{\mathrm{S}}^2}\right]. \tag{3}$$

This equation is similar to the Sauerbrey equation with the exception that a term is included taking into account the stiffness of the surface film. This indicates that a change in the resonance condition is subject to both changes in the surface stiffness as well as mass loading at the surface.

TSM operation of the resonator is achieved by lateral field excitation (LFE) of the piezoelectric layer, requiring that both the signal and ground electrodes are plane-parallel on the exposed surface of the ZnO film. The mechanics of the ZnO SMR achieved by LFE of the TSM is thoroughly treated in Ref. [3]. The LFE configuration contrasts with the typical thickness field excitation (TFE) configuration of other BAW devices like the QCM, in which electrodes are on opposite sides of the piezoelectric crystal. The LFE case results in electric field propagation through the adjacent medium, which is in contrast to the TFE configuration. Exposure of these LFE devices to biological environments implies potential field diversions through the adjacent medium as it will exhibit varying degrees of conductivity. This must be considered when assessing the sensor's capabilities in this environment.

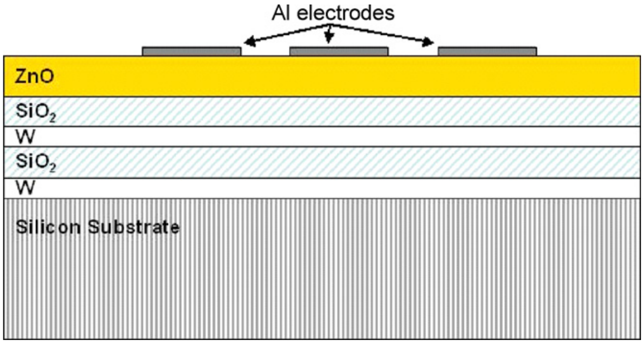

Fig. 1. Profile of device fabrication.

When designing sensors for use with physiological samples, it is important to assess the sensor's performance under varying thermal and sample conductivity conditions. Hu et al. characterized the effects of sample conductivity on QCMs employing LFE rather than the typical TFE for biosensor applications [10]. Presented here is a similar investigation of the characteristics of the TSM in ZnO, analyzing both the impact of the electrode configuration/shape and the stability of the resonator in varying conductivity and temperature conditions.

2. Experimental

2.1. Device fabrication

Solidly mounted resonators were fabricated by first depositing an acoustic mirror, analogous to an optical Bragg reflector, onto a mechanical grade ⟨1 0 0⟩ silicon wafer (University Wafer) as described by Newell [11]. The acoustic mirror consisted of alternating (1/4)-wavelength layers of SiO$_2$ (low acoustic impedance) and W (high acoustic impedance). Highly *c*-axis oriented ZnO was then deposited onto the mirror followed by aluminum electrodes. An illustration showing the overall device design is shown in Fig. 1. SiO$_2$ and ZnO were deposited by RF sputtering using a SiO$_2$ target and a ZnO target, respectively, while the W and Al electrodes were deposited by DC sputtering. Electrodes were fabricated on the surface of the piezoelectric ZnO film by standard photolithography methods. All sputtering depositions were performed by a Unifilm PVD-300 multi-target sputtering system. Resonators were probed using a Cascade Microtech 9000 Analytical Probe Station with ACP40 GSG probes and reflection scattering (S_{11}) parameters were gathered using a HP 8753C Network Analyzer outfitted with a HP 85047A S-Parameter Test Set.

2.2. Susceptibility testing

To test the susceptibility of the devices to varying sample conductivities, saline solutions were prepared using 99.5% NaCl

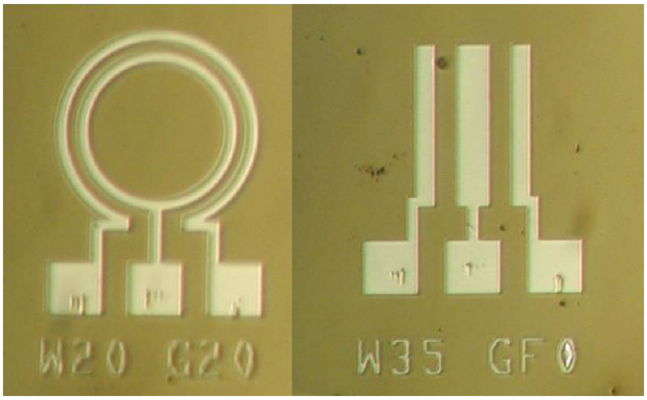

Fig. 2. Various electrode shapes fabricated in an effort to determine the optimal LFE resonator configuration. [Note the left figure has electrode widths of 20 μm and a gap size of 20 μm, and the right figure has electrode widths of 35 μm and a gap size of 40 μm.]

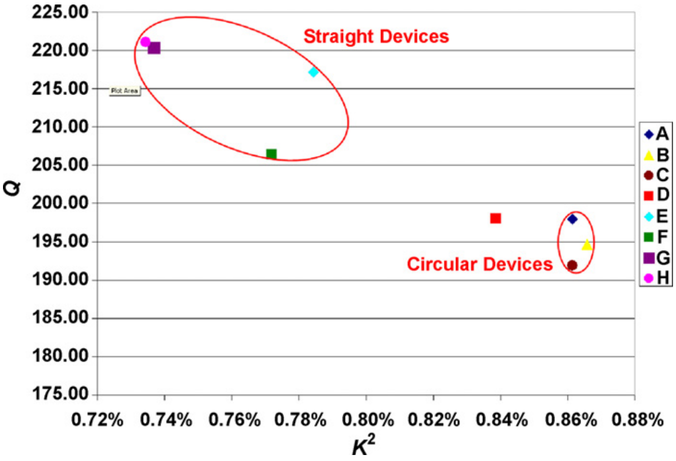

Fig. 3. Comparison of various electrode configurations using Q and K^2.

(Sigma) and HPLC-grade deionized H_2O (Burdick & Jackson) and mixed for at least 30 s on a mini vortexer (VWR Scientific Products) at room temperature. The device arrays were exposed to the saline solutions by hand-pipetting ∼1 μl directly onto the resonator array surface while being probed.

To test the temperature stability of the resonators, a ThermoChuck (Temptronic Corp.) system was set up on the probe station in order to control the wafer temperature. The temperature was varied from 25 °C up to 175 °C in increments of 25 °C and the resonant frequency was measured after the system was allowed to stabilize at each temperature point for at least 10 min.

3. Results and discussion

3.1. Device optimization

A total of eight different electrode configurations were tested using the two electrode shapes depicted in Fig. 2. Among these electrode shapes, the electrode width and the gap between electrodes were varied in an effort to determine the optimal electrode configuration. Devices were evaluated based on quality factor, Q, and coupling coefficient, K^2, as calculated from the S_{11} response of each device. K^2 and Q were determined as described by Rosenbaum [12]:

$$K^2 = \left(\frac{\pi}{2}\right)^2 \frac{f_p - f_s}{f_p} \tag{4}$$

$$Q = \left(\frac{f}{2}\right) \frac{\mathrm{d}\Phi_Z}{\mathrm{d}f} \tag{5}$$

where Φ_Z is phase of the impedance, and ‘p’ and ‘s’ denotes the parallel and series of the resonance frequency, f, respectively. Results obtained from ANOVA analysis of these results demonstrate that a statistically significant gap ($p < 0.01$) emerges between the performance of the circular shaped devices (Fig. 2A) and the straight electrode devices (Fig. 2B) when analyzing their K^2 and Q results. It is evident that the average Q is higher for the straight electrode configuration while the effective K^2 is lower. One possible explanation for this is that the circular electrode configuration has a larger surface area over which excitation of the crystal occurs. Therefore, the coupling of the electric field to the crystal over grain boundaries and crystal non-uniformities is more efficient overall while the added mass of the larger electrodes acts to reduce the Q. These results are demonstrated in Table 1 and summarized in Fig. 3.

As indicated by the strong correlation between devices G and H, it is readily apparent from the data that the electrode widths fabricated had no statistically significant impact on the device performance as assessed by Q and K^2. We had initially hypothesized that greater distribution of the electric field from a constant *power* source to the piezoelectric crystal would result in a more distributed and efficient coupling of electrical energy into acoustic wave energy. Since Q is a ratio of energy conserved to energy dissipated per cycle, it would seem that the

Table 1
Assessment of device performance of tested resonators from analysis of collected S_{11} parameters

Device	Shape	Electrode width (μm)	Electrode gap (μm)	#Tested	Average Q	Average K^2 (%)
A	Circular	20	10	92	198	0.86
B	Circular	20	20	72	195	0.87
C	Circular	20	40	70	192	0.86
D	Straight	20	10	69	198	0.84
E	Straight	35	20	74	217	0.78
F	Straight	35	40	98	206	0.77
G	Straight	20	50	25	220	0.74
H	Straight	35	50	44	221	0.73

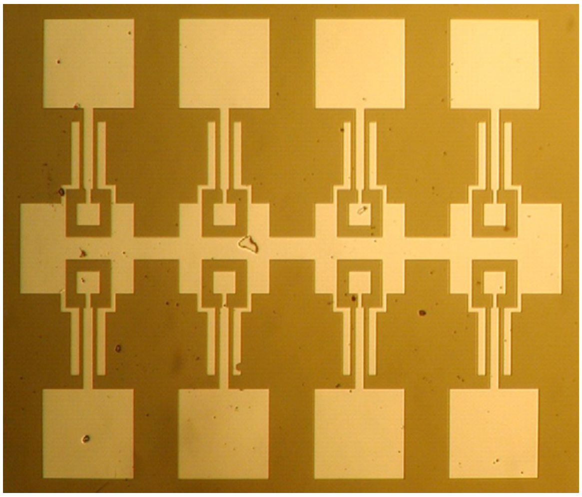

Fig. 4. Digital image of fabricated 8-device array. Device is designed for probing with Cascade Microtech ACP40 GSG150 probes and with pads large enough for subsequent wire bonding. These devices have electrode widths of 50 μm and a gap size of 20 μm.

Q factor should improve as a reflection of this. This result was not substantiated by the data, however, as the size of the gap between electrodes had no clear functional relationship with the device performance. Gap size does have some impact, however, as can be seen from device D in Table 1. Compared with the other straight electrode configurations, the 10 μm gap exhibits a significantly lower Q and higher K^2, on average. It appears that beyond a particular threshold between 10 and 20 μm between straight electrodes, there was a notable improvement in Q. No clear pattern emerges beyond this, however. Rosenbaum asserts that effective implementation of an LFE resonator requires that the gap width between electrodes must be many times greater than the thickness of the film [12]. It could be that this requirement is met somewhere between 12 and 24 times the crystal thickness.

Having determined that the straight electrode configuration yielded higher Q devices, which has been identified as the desired parameter, 8-element arrays of these devices were fabricated in order to verify that the resonator design displayed in Fig. 2 performed as well in the array configuration as individual devices. That is to say, it was our goal to confirm that the array structure did not bear any beneficial nor detrimental effects on the resonator's performance. Sampling 88 arrayed devices similar to those seen in Fig. 4 showed that there in fact was a statistically significant difference in device performance. A 30% decrease in Q and a 15% decrease in K^2 was observed for devices with a 20 μm gap fabricated in the array configuration versus the isolated configuration. For devices fabricated with a 50 μm gap, again a decrease of 30% was observed in Q but only a 5% decrease in K^2. One explanation for the decrease in performance is the addition of a significant amount of conductor material surrounding the active devices for bonding pads and ground–bus connections. The added mass from the electrodes provides a lossy material at the surface boundary which can act to scatter the acoustic energy.

3.2. Device susceptibility

In order to evaluate these devices for potential biosensor applications, the arrays were tested over a temperature range of 25–175 °C to assess their thermal stability. The following equation was used to calculate the thermal coefficient of resonant frequency (TCF):

$$\mathrm{TC}(f_x) = \frac{\mathrm{d}f_x}{\mathrm{d}T} \cdot \frac{1}{f_{x,\mathrm{RT}}} \tag{6}$$

where T is the temperature, f_x is the relevant resonant frequency and RT represents room temperature (25 °C). The results yielded an empirically derived TCF for the series and parallel resonance of 24.6 and 25.6 ppm/°C, respectively. These results are demonstrated in Fig. 5.

Past investigations of ZnO BAW resonators by Pinkett et al., yielded a negative TCF of −30 ppm/°C [13]. The difference between these two findings can be explained by the fact that the two device designs employ very different acoustic modes. The devices reported in this research employ a thickness shear mode while the Pinkett et al. devices employ a longitudinal mode acoustic wave achieved by TFE. Given that the resonant frequency for both devices are described by the following relationship

$$f = \frac{v_\mathrm{a}}{2d} \tag{7}$$

where v_a is the propagating acoustic wave velocity, d is the piezoelectric film thickness and f is the resonant frequency. For the TFE longitudinal case, it is conceivable that increased temperature results in a thickness expansion that outpaces any increase in wave velocity, yielding the negative TCF. The opposite condition could then explain the positive TCF for the LFE case, in which the increased wave velocity outpaces the film expansion. It is important to note that the velocity is a function of the square root of the ratio of the material stiffness to the material density. Given that the lateral (a-axis) thermal expansion of ZnO is significantly greater than the longitudinal (c-axis) thermal expansion, [14] it is conceivable that the shear stiffness coupling is increased with increasing temperature because of the relative expansion coeffi-

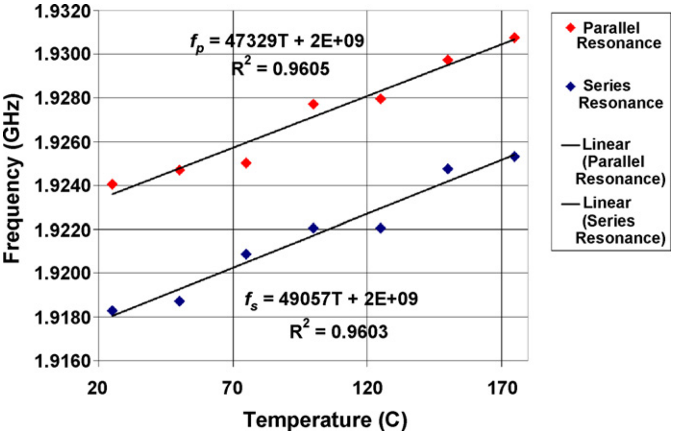

Fig. 5. Frequency drift of parallel and series resonance frequency with increasing temperature.

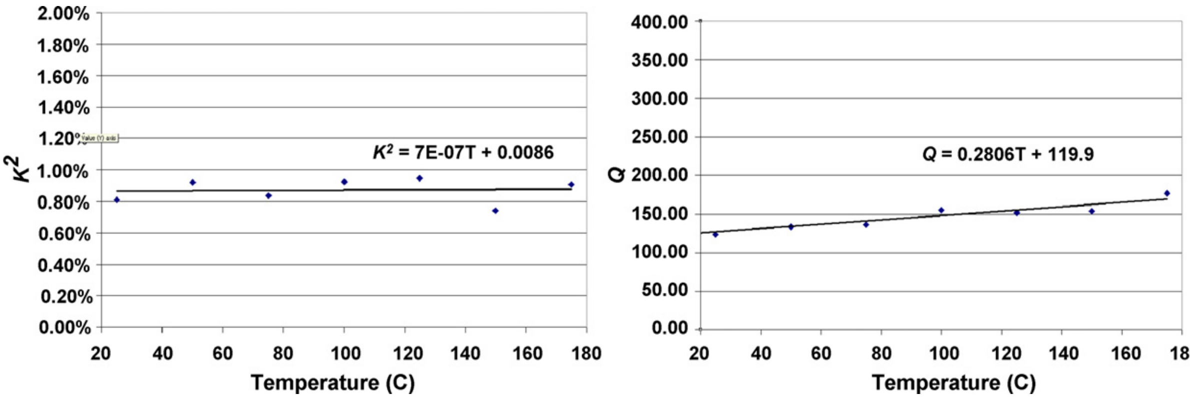

Fig. 6. Variation observed over a wide temperature range for the resonator coupling coefficient, K^2, (left) and the resonator quality factor, Q (right).

cients in either direction. A greater expansion in the lateral axis than in the longitudinal axis will result in an overall “apparent” stiffening in the longitudinal direction. This would result in an increase in the apparent stiffness tensor value pertaining to the shear coupling (c_{44}) with increasing temperature. An alternative possibility is rather that c_{44} decreases because of thermal expansion, but the density is decreased by a greater amount per unit temperature change which results in a higher acoustic velocity overall.

It was found that the K^2 remained very stable over the temperature range tested, varying by only 0.1% over the 155 °C range. The Q drift of the resonator was more significant, varying by roughly 42% over the 155 °C temperature range. For use in bench-top biosensor applications, the Q remained stable enough to consider negligible, exhibiting an average 0.28 point shift per degree Celsius (<0.2% per degree). The results for the temperature stability of K^2 and Q are summarized in Fig. 6.

Considering the goal of employing these resonators in biosensor applications with biological fluid samples, the resonators were tested over a range of sample conductivities loading the surface with 0.0–0.9% (w/v) of NaCl in DI H_2O. It is common in the literature to see 0.9% NaCl in DI H_2O described as an equivalent salinity to blood. Results indicate that the magnitude of resonator frequency shift varied little in relation to loading with pure water alone, as indicated in Fig. 7. A substantial increase in frequency instability was observed, however, with increasing sample conductivity. These devices do not exhibit the high-Q characteristic of the QCM, which translates to a broad resonance peak as observed through the S_{11} response. Incidental fluctuations in the reflection parameters will therefore cause the resonance frequency monitor to register a variance in the resonance. The error bars in Fig. 7 indicate the measured variance due to these incidental fluctuations. A further indicator of this can be seen in Fig. 8, which demonstrates the results of a typical experiment when a 0.9% saline sample (isotonic with human blood) is deposited on the device surface then subsequently washed with DI H_2O.

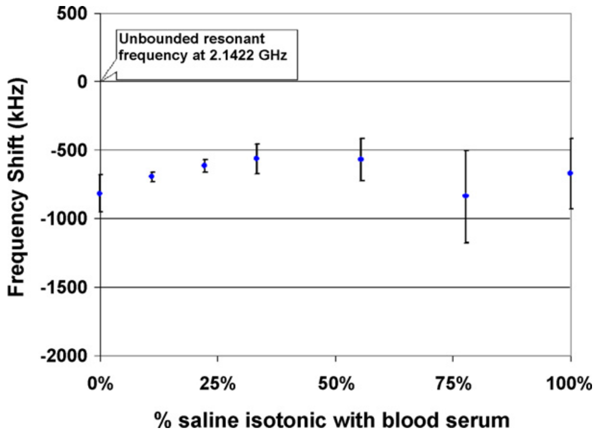

Fig. 7. Change in resonant frequency as a function of increasing fluid sample conductivity.

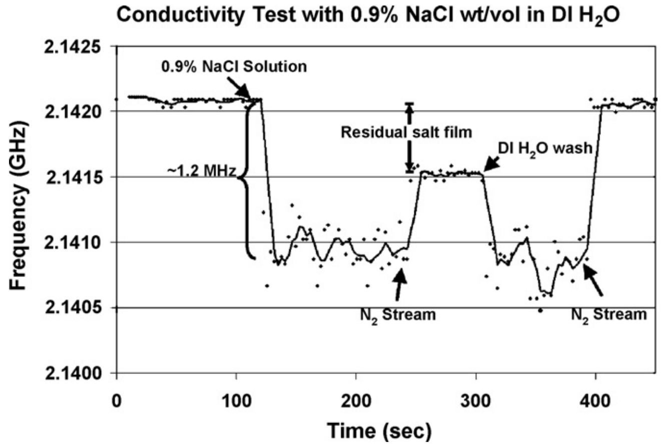

Fig. 8. Demonstration of a typical conductivity experiment with 0.9% NaCl in DI H_2O.

4. Conclusion

In this investigation, it has been shown that thickness shear mode ZnO solidly mounted resonators can be fabricated in an array configuration with only a modest impact on device performance. It is believed that further electrode optimization could mitigate some of this performance loss. Further, it has been shown that these resonators can operate stably in biologically equivalent environments. Specifically, these resonators have been shown to exhibit low susceptibility to changes in temperature and conductivity. In order to achieve sensors of greater quality, however, it will be necessary to improve the overall device *Q* through experimental optimization of the acoustic mirror.

Acknowledgments

This work was supported by the Georgia Tech/Emory Fund for Innovative Cancer Technologies which derives its funds from the V Foundation and the Georgia Cancer Coalition (GCC). Anthony Dickherber is supported by the Congressionally Directed Medical Research Program Prostate Cancer Training Program and Christopher Corso is supported by a National Science Foundation Graduate Research Fellowship. We would further like to acknowledge the assistance of Georgia Tech undergraduates George Steven Ruff and Alice Wang who developed the monitoring software used in conjunction with the HP Network Analyzer.

References

[1] A. Janshoff, H.-J. Galla, C. Steinem, Piezoelectric mass-sensing devices as biosensors—an alternative to optical biosensors? Angewandte Chemie 39 (2000) 4004–4032.

[2] D. Salt, Hy-Q Handbook of Quartz Crystal Devices, Van Nostrand Reinhold (UK) Co. Ltd., Berkshire, England, 1987.

[3] C.D. Corso, A. Dickherber, W.D. Hunt, Lateral field excitation of thickness shear mode waves in a thin film ZnO solidly mounted resonator, J. Appl. Phys. Virtual J. Biol. Phys. Res. 101 (2007).

[4] M.F.-P. Cecilia, Selection of appropriate cellular and molecular biologic diagnostic tests in the evaluation of cancer, Cancer 69 (1992) 1607–1632.

[5] G. Sauerbrey, Use of quartz vibrator for weighting thin films on a microbalance, Z. Phys. 155 (1959) 206–210.

[6] K.K. Kanazawa, J.G. Gordon, Frequency of a quartz microbalance in contact with liquid, Anal. Chem. 57 (1985) 1770–1771.

[7] W.A. Gee, K.M. Ritalahti, W.D. Hunt, F.E. Loeffler, QCM viscometer for bioremediation monitoring, IEEE Sens. J. 3 (2003) 304–309.

[8] B.A. Auld, Acoustic Fields and Waves in Solids, second ed., R.E. Krieger, Malabar, FL, 1990.

[9] W.D. Hunt, D.D. Stubbs, L. Sang-Hun, Time-dependent signatures of acoustic wave biosensors, Proc. IEEE 91 (2003) 890–901.

[10] Y. Hu, L.A. French Jr., K. Radecsky, M.P. DaCunha, P. Millard, J.F. Vetelino, A lateral field excited liquid acoustic wave sensor, Presented at 2003 IEEE Symposium on Ultrasonics, Orono, ME, USA, 2003.

[11] W.E. Newell, Face-mounted piezoelectric resonators, Proc. IEEE 53 (1965) 575–581.

[12] J.F. Rosenbaum, Bulk Acoustic Wave Theory and Devices, Artech House, Boston, 1988.

[13] S.L. Pinkett, W.D. Hunt, Temperature characteristics of ZnO-based thin film bulk acoustic wave resonators, Presented at 2001 IEEE Ultrasonics Symposium, 2001.

[14] J. Albertsson, S.C. Abrahams, A. Kvick, Atomic displacement, an harmonic thermal vibration, expansivity and pyroelectric coefficient thermal dependences in ZnO, Acta Crystallogr. Sect. B 45 (1989) 34–40.

Biographies

Anthony Dickherber earned his bachelor's degree in electrical engineering from Georgia Tech in Atlanta in 1999. He worked for Georgia Tech Research Institute in their Information Technology and Telecommunications Laboratory for the next 4 years, while going to Georgia Tech part time to earn his master's degree in electrical and computer engineering. Tony is currently a PhD candidate in the School of Bioengineering at Georgia Tech and a Sam Nunn Security Program Fellow. His research interests involve developing sensors for early detection of prostate cancer.

Christopher D. Corso graduated from Georgia Tech in 2004 with a bachelor's degree in computer engineering. He is now a graduate student in the joint MD/PhD program between Georgia Tech and Emory. Chris is currently working on his PhD in bioengineering after which he will attend Emory for medical school. His research interests involve the development of acoustic wave devices for medical diagnostics.

William D. Hunt received the BS degree in electrical engineering from the University of Alabama, Tuscaloosa, in 1976, the MS degree in electrical engineering from the Massachusetts Institute of Technology, Cambridge, in 1980, and the PhD degree in electrical engineering from the University of Illinois, Urbana-Champaign, in 1987. From 1976 to 1978, he was an engineer with Harris Corporation. From 1980 to 1984, he was a staff engineer at Bolt Beranek and Newman Corporation, Arlington, VA. In 1987, he joined the Electrical Engineering Faculty at Georgia Institute of Technology, Atlanta. His area of expertise is in the area of microelectronic acoustic devices for wireless applications as well as chemical and biological sensors based on this technology. He has published over 70 papers in refereed journals and conference proceedings. He holds four U.S. patents and five provisional patents.

Biosensors and Bioelectronics 24 (2008) 805–811

Contents lists available at ScienceDirect

Biosensors and Bioelectronics

journal homepage: www.elsevier.com/locate/bios

An investigation of antibody immobilization methods employing organosilanes on planar ZnO surfaces for biosensor applications

Christopher D. Corso[a], Anthony Dickherber[b], William D. Hunt[b,*]

[a] *Department of Biomedical Engineering, Georgia Institute of Technology, Atlanta, GA 30332, United States*
[b] *Department of Electrical Engineering, Georgia Institute of Technology, Atlanta, GA 30332, United States*

ARTICLE INFO

Article history:
Received 23 April 2008
Received in revised form 27 June 2008
Accepted 1 July 2008
Available online 16 July 2008

Keywords:
Organosilane
Antibody immobilization
ZnO
Acoustic sensor
Crosslinker

ABSTRACT

One critical aspect for the development of label-free immunosensors is the employment of highly uniform and repeatable antibody immobilization techniques. In this study, we investigated the use of two different silane molecules (3-glycidyloxypropyl)trimethoxysilane (GPS), and (3-mercaptopropyl)trimethoxysilane (MTS) for the immobilization of fluorescently labeled IgG antibodies on planar ZnO surfaces. The chemical modification of the surfaces was investigated using water contact angle measurements, AFM, and fluorescence microscopy. The results of the water contact angle measurements indicate increased surface hydrophobicity after treatment with GPS and MTS as compared to the control. Surface modification was further verified through AFM measurements which demonstrate an increased surface roughness and particle height after treatment with antibodies. The results of the fluorescence studies indicate that the immobilization protocol employing MTS produced 21% higher fluorescence on average with greater uniformity than the GPS-based protocol, which indicates a higher overall density in antibody coverage on the surface of the ZnO. Acoustic sensor tests were employed to confirm the functionality of sensors treated with the MTS protocol. The results indicate that the immobilization protocol imparts sensitivity and specificity to the ZnO-based devices.

1. Introduction

Acoustic wave biosensors function by detecting changes in the path over which the propagating wave travels. These devices are often referred to as gravimetric sensors since the sensing mechanism is related to the addition or subtraction of mass (Ballantine, 1997). As with most types of biosensors, the ability to obtain repeatable results from an acoustic sensor is related to the repeatability of the biolayer. This molecularly specific biolayer typically consist of antibodies, oligonucleotides, or enzymes depending on the sensor application (Chambers et al., 2008). A requirement for high precision biosensors is that the output signal, or response, be repeatable given multiple identical samples and on different sensor elements prepared in the same manner. Therefore controlled, reproducible immobilization of appropriate capture molecules to functionalize the device is necessary to preclude device-to-device signal variations.

The use of zinc oxide (ZnO) has growing interest because it possesses many qualities that make it a good candidate for sensor applications. Primarily, ZnO thin-films can be deposited with excellent *c*-axis orientation using RF magnetron sputtering techniques (Kang et al., 2005) which allows for integration into standard IC fabrication processes. Furthermore, ZnO possesses a relatively strong piezoelectric coupling coefficient of approximately 7–8% and is therefore capable of supporting both longitudinal and thickness shear mode (TSM) waves (Corso et al., 2007), as well as surface acoustic waves (Yamazaki et al., 1980). Additionally, ZnO has become a material of interest because of the ability to grow single crystal ZnO nanostructures with a variety of useful properties (Wang, 2004).

To date, the literature pertaining to functionalizing oxides through covalent methods has largely been focused on quartz (SiO_2). Hydroxyl groups at the surface of an oxide provide sites for reaction with crosslinking molecules to form covalent bonds (Bhatia et al., 1989). One of the more common methods for functionalizing SiO_2 surfaces involves the use of organosilanes. Success with immobilizing antibodies on SiO_2 surfaces has been shown using amine- and thiol-terminal silanes such as 3-mercaptopropyltrimethoxysilane (MTS) with a variety of heterobifunctional crosslinkers including *N*-γ-maleimidobutyryloxy succinimide ester (GMBS) (Bhatia et al., 1989; Shriver-Lake et al., 1997). Heterobifunctional crosslinkers serve the purpose of transforming the end group of the silane into a group that will bind covalently with functional groups on an antibody. Bhatia et al.

---

[*] Corresponding author. Tel.: +1 404 894 2945; fax: +1 404 894 4700.
E-mail address: bill.hunt@ee.gatech.edu (W.D. Hunt).

0956-5663/$ – see front matter © 2008 Published by Elsevier B.V.
doi:10.1016/j.bios.2008.07.011

reported that antibody immobilization with a number of different organosilanes yielded a comparable amount of antibodies immobilized from one silane to the next and that the resulting covalently bound biofilm maintained similar overall antigen binding capacity. They also found that there was minimal loss of antibody function after immobilizing the antibodies to the silica surface (Bhatia et al., 1989; Shriver-Lake et al., 1997).

Other work in modifying SiO_2 surfaces has focused on forming self-assembled monolayers (SAMs) using expoxysilanes (Luzinov et al., 2000). One advantage of using an expoysilane such as (3-glycidoxypropyl)trimethoxysilane (GPS) for forming SAMs on oxide surfaces is that it eliminates the need for a secondary crosslinker between the silane molecule and target antibodies. The exposed epoxy groups react readily with amine groups on lysine residues of the antibody. The usefulness of this antibody immobilization technique has been illustrated on indium-tin oxide (ITO) substrates for the development of *Escherichia coli* O157:H7 sensors (Ruan et al., 2002; Yang and Li, 2005).

Despite the amount of research that has been performed on various oxides, including SiO_2, there have been relatively few studies involving surface functionalization of ZnO. One such study reports the use of an amine-terminated silane, 3-aminopropyltriethoxysilane (APS), and glutaraldehyde as the secondary crosslinker to bind a protein, interleukin-6, to the ZnO surface (Krishnamoorthy et al., 2006). One drawback to the use of glutaraldehyde, however, is that it is known to form large polymers which may bind many residues and form multiprotein complexes (Bhatia et al., 1989). Apart from surface treatment with silanes, there have been very few other reports of surface modification studies performed on ZnO. In a study by Sadik et al., adsorption of alkane-thiols to Zn and O terminated ZnO surfaces to form SAMs was investigated, but the study did not involve further functionalization with antibodies or any other type of protein (Sadik et al., 2007). Other studies have described methods for functionalizing ZnO nanostructures, however they are of limited use for translation to planar ZnO surface chemistry because of the morphological and crystalline differences between RF sputtered ZnO surfaces and single crystal nanostructures.

The focus of this work is to investigate antibody immobilization protocols on device-quality sputtered ZnO surfaces. MTS and GPS were deposited onto the ZnO surface using a conventional wet method. Subsequent secondary crosslinking with GMBS was performed for ZnO surfaces coated with MTS. To provide visual confirmation of the density and uniformity of antibody immobilization, fluorescently labeled antibodies were incubated with the surface. The results were investigated using water contact angle measurements, atomic force microscopy, and confocal microscopy. Subsequent sensor tests were performed on ZnO-based resonators functionalized using the MTS + GMBS immobilization method to investigate the functionality of the immobilized antibodies. The results provide a foundation for further research in developing highly uniform antibody immobilization protocols for planar ZnO surfaces.

2. Experimental methods

2.1. ZnO preparation

ZnO samples were prepared by depositing 500 nm of ZnO onto 3″ (1 0 0) silicon wafers (University Wafer) by RF magnetron sputtering using the Unifilm PVD-300 sputtering system. We have previously reported X-ray diffraction (XRD) measurements of the sputtered ZnO films which indicate a strong (0 0 2) ZnO hexagonal 6*mm* crystal orientation (Corso et al., 2007). The wafers were diced into 1 cm × 1 cm squares for surface functionalization experiments. Prior to surface functionalization, the ZnO samples were sonicated in acetone for 5 min in an ultrasonic bath before being cleaned using an ion beam mill (Ion Tech, Inc. MPS-3000). The samples were etched in a 20% oxygen/80% argon atmosphere for 5 min with a beam current of 9 mA at 500 V. This was done to remove any adsorbed chemical species from the surface and to provide a reactive surface for the silane to bind.

2.2. Surface modification

The silane solutions for treating the ZnO samples were prepared under a nitrogen atmosphere: a 4% solution by volume of MTS (Fluka) in dry toluene (Sigma); a 4% solution of GPS (Sigma) in dry toluene. Immediately following the ion milling procedure to clean the ZnO surface, samples were placed in vials containing 2 mL of the silane, sealed, and placed in a nitrogen environment for 24 h. The samples were then removed from the vials and rinsed with ethanol followed by sonication for 5 min in ethanol. The samples were then dried with a stream of N_2. Samples treated with the 4% MTS were then placed in vials containing 2 mL of 2 mM GMBS (Fluka) in ethanol (Sigma) and sealed for 24 h. Following sonication in ethanol, GPS-coated samples were immediately treated with the antibody solution as described below. The MTS + GMBS-coated samples were removed from the GMBS solution and sonicated in ethanol for 5 min. The activated ZnO surfaces were then used for covalent attachment of antibodies. All surface modification steps were performed at room temperature.

2.3. Covalent antibody attachment

The activated surfaces were treated with 546 nm Alexa-Fluor labeled Goat anti-rabbit IgG polyclonal antibodies (Invitrogen) at room temperature. 25 μL of a 200 μg/mL solution of the fluorescently labeled antibodies in PBS buffer (pH 7.4) was pipetted onto the surface of the samples. The antibody solution was incubated for 2 h in an opaque container in a nitrogen environment at room temperature, after which the substrate was rinsed with aliquots of PBS buffer followed by ultra-pure water (Burdick & Jackson) to remove any unbound antibodies from the surface. Control samples for testing simple antibody adsorption were prepared by incubating ion etched ZnO samples with the antibody solution for 2 h.

2.4. Water contact angle measurements

Water contact angle measurements were performed using an SEO Phoenix 150 Contact Angle Analyzer. The contact angles for each of the surface treatments were evaluated by averaging the contact angles from at least five separate measurements. The silanized samples were measured and compared to a control sample of untreated, ion etched ZnO. The measurements were used as a semi-quantitative method of determining the film quality and reproducibility as well as to confirm that the surface was being chemically modified. ANOVA was used to analyze the water contact angles for each of the surface treatments.

2.5. AFM measurements

A Digital Instruments (DI) 3000 AFM was used in tapping mode to measure the following: bare ZnO samples; samples after treatment with MTS + GMBS and GPS, respectively; samples after treatment with the croslinkers + antibody solution. AFM probe tips were obtained from Veeco Instruments (FESP). Multiple scans of each sample were taken to across each 1 cm × 1 cm sample and scans were taken on multiple samples. The scans were evaluated for surface roughness and overall average particle height and diameter using the DI Nanoscope software.

2.6. Confocal microscopy

Following the antibody conjugation reaction, the devices were dried with a stream of N_2 and fixed to a glass slide in preparation for confocal microscopy analysis. A Zeiss Laser Scanning Microscope (LSM) 510 equipped with a HeNe laser (543 nm excitation) was used to visualize the distribution and intensity of the fluorescently labeled antibodies. Each sample was viewed at 10× and 40× magnification and images were taken at random locations throughout the area of antibody deposition. Control samples were prepared and analyzed for comparison between fluorescence due to antibody coverage and fluorescence to due background noise. Rather than incubation with the 200 μg/mL antibody in PBS, the control samples were treated with the full crosslinking protocol then incubated with 25 μL of 5 mM azide in PBS to replicate the solution containing the Alexa-Fluor labeled antibodies. Therefore, the only difference between the control and target samples is the presence of antibodies. To quantify the fluorescence for each surface treatment, the detector gain was fixed at a constant value and images were taken for all of the samples. The RGB luminance intensity signal was collected for each pixel in 0.03 mm^2 areas across the samples. The average fluorescence intensity was calculated by taking the mean pixel luminance intensity for all pixels within a 0.03 mm^2 area over at least 25 separate measurements. Statistical analysis was performed using ANOVA to compare the average fluorescence intensity of each surface treatment.

2.7. Sensor testing

In order to assess whether the antibodies remain functional after the immobilization procedure, sensor tests were performed using the MTS silanization protocol to functionalize ZnO thickness shear mode acoustic resonators. These devices are excited with a lateral field excitation electrode configuration, which removes the electrodes from the active area of the device (Corso et al., 2007; Rosenbaum, 1988). The absence of electrodes in the active region of the device necessitates a surface treatment protocol capable of linking the antibodies directly to the ZnO surface. The ZnO TSM resonators employed here are sensitive to perturbations such as mass loading events which produce a shift in the resonant frequency of the device. Here, we test the functionality of the antibody immobilization procedure by exposing the functionalized sensors to solutions containing mesothelin—a protein that is highly expressed in several cancers including mesotheliomas, ovarian and pancreatic cancers, and some squamous cell carcinomas (Argani et al., 2001; Chang and Pastan, 1996; Chang et al., 1992; Ordonez, 2003).

The acoustic sensor devices were fabricated as previously described (Corso et al., 2007). An acoustic mirror of 8 alternating layers of 640 nm of W and 1000 nm of SiO_2 were deposited on a Si wafer. ZnO was RF-sputtered to a thickness of 750 nm to produce devices that have a fundamental operating frequency at approximately 2 GHz. Three 200 nm long electrodes were patterned on the surface of the ZnO with a gap of 30 nm between them for generating and maintaining the acoustic resonance. Functionalization of the resonators was performed using the MTS silanization protocol as described above. Antibody solutions were incubated with the surfaces for 2–3 h and were subsequently washed with buffer followed by purified H_2O. For the mesothelin tests, the target sensors were coated with 20 μg/mL of the MB IgG_{2a} mouse monoclonal antibody solution. The mAb MB antibodies were developed in the laboratory of Ira Pastan at the National Cancer institute. They have been shown to detect mesothelin by immunohistochemistry, fluorescence-activated cell sorting, and ELISA and have high affinity for the mesothelin protein (Onda et al., 2005). The reference sensors were coated with a 20 μg/mL solution of anti-FITC monoclonal IgG antibodies (sc-69871—Santa Cruz) because fluorescein isothiocyanate (FITC) is a synthetic molecule that is not present in the samples of interest.

A series of tests were performed to independently analyze the sensor response to buffer solutions spiked with two different concentrations of purified mesothelin-rFc. Mesothelin-rFc is a recombinant fusion protein which was also developed in the laboratory of Dr. Ira Pastan at the NCI which consists of the 40 kDa COOH-terminal mesothelin protein fused to rabbit Fc (Onda et al., 2005). The mesothelin-rFc fusion protein has been used for developing ELISA calibration standard curves in the past and contains the entire extracellular portion of mesothelin (Hassan et al., 2006).

Following functionalization of the acoustic sensors, the devices were placed in shallow dishes of pH 7.4 PBS buffer to keep the antibody coating hydrated for subsequent antigen binding. The sensors were then tested using an HP8753 network analyzer to record the impedance response of the devices and to establish the initial resonance frequency of each device. The sensors were then incubated with 25 μL of the mesothelin-rFc solution for 25 min. Sensor tests were performed on solutions of mesothelin-rFc in PBS buffer with concentrations of 10 ng/mL, and 10 μg/mL. After the incubation period, the sensors were rinsed with buffer and water to remove any unbound protein, and were then retested using the network analyzer to record the post-exposure impedance response. Sensor responses from before and after exposure to the sample were analyzed. The frequency shifts represent the different between the perturbed and unperturbed resonance frequency. Average frequency shifts across multiple sensors for each solution concentration were calculated and plotted. One-way ANOVA was used to evaluate the statistical significance between the frequency shifts and the concentration of sample solution.

3. Results and discussion

Based on previously described mechanisms (Bhatia et al., 1989; Krishnamoorthy et al., 2006; Yang and Li, 2005), a summary of the reactions for covalently attaching antibodies to the ZnO surface is shown in Scheme 1. Deposition of the silanes is achieved through reaction of the head groups with hydroxyl groups at the ZnO surface. The thiol group on the MTS molecules react with the maleimide region of the secondary crosslinker GMBS in organic solvent. This reaction leaves the succinimide residue of the GMBS available for antibody attachment. The succinimide residue then binds to an available amino group of the antibody to form a covalent bond between the antibody and the ZnO surface. It is important to note, however, that targeting amine-groups on the antibodies does not promote any specific orientation of the antibodies since amine-containing residues such as lysine can be located on many parts of the antibody. Despite this, it has been shown that antibodies immobilized using this approach still maintain a significant amount of activity, albeit less than with oriented immobilization techniques such as those that target the carbohydrate group on the Fc region of the IgG antibody (Shriver-Lake et al., 1997). Additionally, the ease and simplicity of the immobilization protocols studied here make them an attractive option for biosensor applications over oriented immobilization techniques which often require numerous steps, harsh experimental conditions, and high antibody losses prior to immobilization.

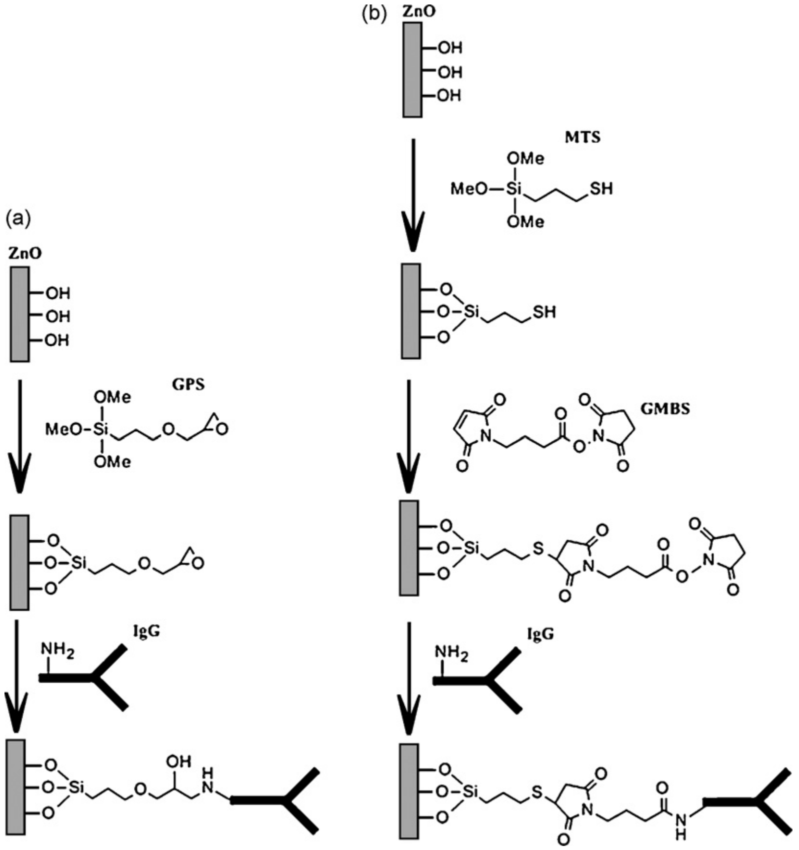

Scheme 1. The immobilization scheme for covalent attachment of IgG antibodies to the ZnO surface using (a) GPS and (b) MTS followed by the secondary crosslinker GMBS.

3.1. Water contact angle measurements

The results from the water contact angle (WCA) measurements after the samples were coated with the silanes indicate that the average WCA for each of the crosslinkers were greater than the WCA of the control, indicating an increase in surface hydrophobicity. Samples coated with MTS had an average water contact angle of 77° ± 1 which were statistically different than the untreated ZnO (control) case which exhibited a water contact angle of 72° ± 1 ($p = 0.002$). The contact angle results for surfaces coated with MTS seem to agree well with previous WCA investigations of thiol-terminated monolayers on gold which were reported to be approximately 83.5° on average (Tlili et al., 2007). The WCA measurements performed with the 4% GPS solutions also suggest that the surface is being chemically modified. The samples coated with GPS yielded an increase in average WCA of 80° ± 5 immediately after the water droplet is placed onto the sample surface. Over the ensuing 20–30 s the water contact angle drops by about 5–10° and then stabilizes. One possible explanation for this phenomenon is that the water droplets react with the exposed epoxy groups, hydrolyzing the ring to form surface hydroxyl groups which would result in a more hydrophilic surface. These WCA results are relatively higher than those reported for MTS and GPS on SiO_2 which were found to be 58° and 52° on average, respectively (Bhatia et al., 1989).

3.2. AFM measurements

AFM was used for monitoring the morphological changes at the surface that result from coating the surface with the crosslinkers and subsequent immobilization of antibodies. Fig. 1 shows stepwise AFM scans for each surface after treatment with the crosslinkers and antibody solution. Fig. 1(a) shows the characteristic cobblestone appearance of the surface of the untreated control ZnO sample, with round grains that have fairly well defined boundaries. For the bare ZnO case, the mean surface roughness is approximately 2.8 (±0.4) nm while the particle height is 3.05 (±0.5) nm. The characteristic AFM scan of the surface after silanization with GPS in Fig. 1(b) shows a surface that is morphologically different from that of the controlled case. The average surface roughness decreases on average by 57% to 1.2 (±0.3) nm. This implies an overall smoothening of the surface which is similarly suggested by the appearance of the scan. One likely explanation is that the GPS molecules have been deposited into the gaps in-between the grains to fill some of the grain boundaries. The results were observed at many locations across any single chip, and from chip to chip. After incubation with the antibody solution, the GPS + Ab treated surface has an increased surface roughness on average to 2.0 (±0.1) nm with an average particle height of 3.3 (±0.8) nm which indicates that the surface is being modified after treatment with the antibody solution. A typical scan is shown in Fig. 1(c).

The AFM scans of the samples treated with MTS + GMBS in Fig. 1(d) show significant differences in the surface morphology as compared to the GPS. Rather than a decrease in surface roughness, we see an increase in surface roughness to 3.7 (±0.7) after treatment with MTS + GMBS. The average particle height for the MTS + GMBS treated samples was increased to 6.8 (±0.4) nm indicating an increase in particle size due to deposition of the MTS + GMBS. Fig. 1(e) clearly shows the subsequent treatment with the antibody solution yields particles on the surface that have a larger average height 13.7 (±0.3) nm which is indicative of the immobilization of the antibodies to the surface. The data from these scans along with the WCA measurements provide confidence that the surface is being chemically modified and that the surfaces are

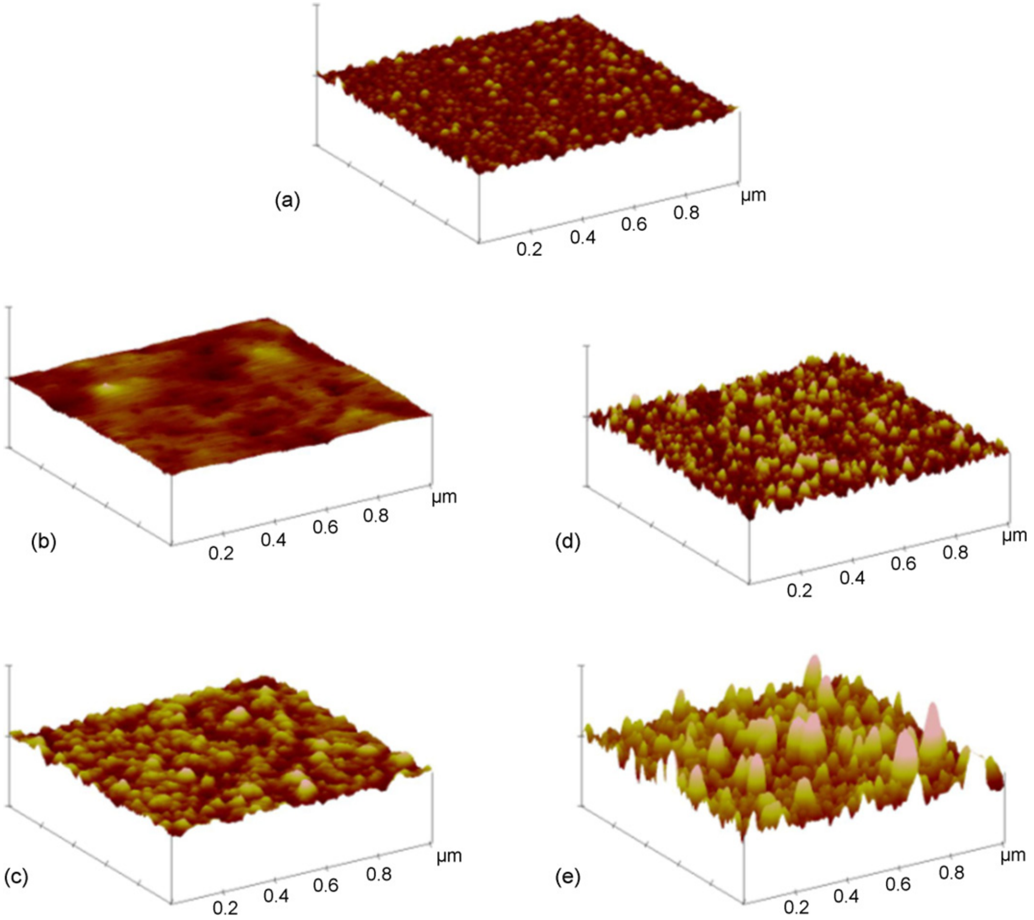

Fig. 1. AFM topographical scans of (a) the untreated ZnO surface and samples treated with (b) GPS, (c) GPS + Ab, (d) MTS + GMBS, and (e) MTS + GMBS + Ab. The scan sizes are 1 µm × 1 µm with a vertical scale of 65.0 nm.

morphologically modified after treatment with the antibody solution.

3.3. Fluorescence microscopy measurements

While the AFM scans tend to indicate that the surfaces are being modified with the surface treatment, fluorescence microscopy was employed to provide more information about antibody surface coverage density and uniformity. Prior studies characterizing antibody immobilization techniques have generated a variety of methods for analyzing the amount of antibodies bound to the surface of a material (Bhatia et al., 1989; Shriver-Lake et al., 1997; Yang and Li, 2005). As acoustic biosensors become increasingly more compact, the antibody immobilization surface coverage becomes increasingly more important. It is necessary to compare the surface treatments quantitatively, which is demonstrated in this study through an analysis of the fluorescence. Fig. 2 shows a comparison of the average fluorescence intensity (luminescence) for the two silane immobilization methods vs. the untreated bare ZnO sample. Included are the average fluorescent intensities for the control samples which serve as an estimation of the combined background fluorescence from the ZnO, the crosslinkers (for the GPS and MTS treated chips), and the PBS buffer. The average intensity was found to be highest for the MTS as compared to the GPS and the ZnO. The fluorescence of the bare ZnO sample treated with antibodies above the control can be attributed to a small amount of antibody adsorption to the surface of the ZnO in the absence of crosslinking molecules. The fluorescence of the samples treated with the MTS were on average about 41% higher than the samples treated with GPS ($p < 0.001$). Since level of the fluorescence within a region of constant size is related to the amount of fluorophor present, these results indicate increased antibody surface coverage with the MTS over the GPS. The MTS fluorescence as compared to the untreated ZnO case indicates roughly a three-fold increase of average fluorescent intensity ($p < 0.001$). The uniformity of the antibody coverage can be correlated to the standard deviation in pixel luminance for each of the

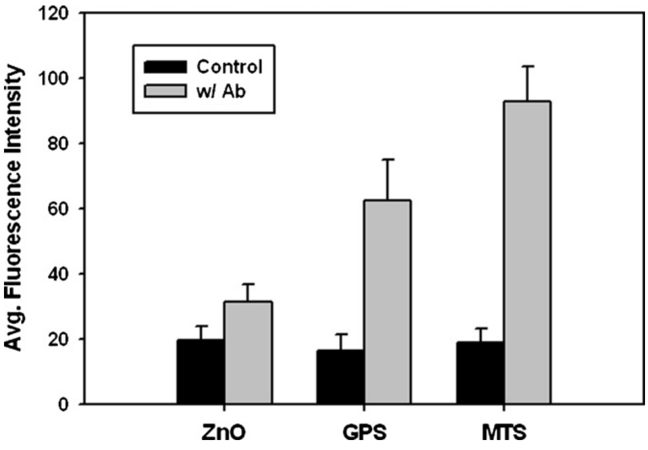

Fig. 2. The average fluorescence intensity for each surface treatment after incubation with antibodies vs. incubation with buffer. A significant difference between MTS and GPS was calculated with ANOVA to be $p < 0.001$. (Error bars = standard deviation).

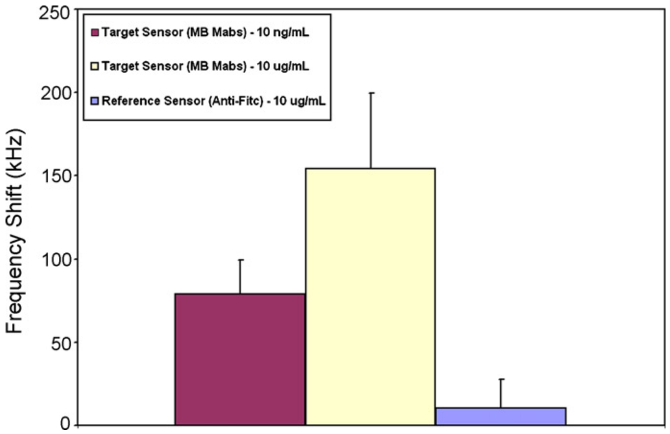

Fig. 3. Average frequency shift measured in the target and reference ZnO-based acoustic sensors after exposure to mesothelin-rFc solutions. $n = 6$ for each test. (Error bars = standard deviation).

samples. We found a lower standard deviation for surfaces treated with MTS (12.2 a.u.; 12.6% of the average) as compared to GPS (18.3 a.u.; 26.4% of the average) which indicates an overall higher uniformity in over 25 separate measurements across multiple samples which include ~9500 pixels each. The increased fluorescence observed in samples treated with MTS over those treated with GPS was repeatable from sample to sample which also indicates robustness in the protocol with each of these surface treatments.

3.4. *Sensor functionality testing*

Based on results from the fluorescence studies, it was concluded that the high uniformity of the MTS immobilization protocol made it more suitable for sensor detection studies than GPS. However, fluorescence studies alone can only indicate where the antibodies are located, but give no information about whether or not the antibodies are functional. To test this, TSM acoustic sensors were employed (Fig. 3).

The sensor tests were performed with two concentrations of purified mesothelin-rFc solutions which resulted in increasing shifts, on average, for the target sensors over the reference sensors. The MB-coated sensors tested with a concentration of 10 ng/mL ($n = 6$) had an average frequency shift of 78 kHz. In contrast, the average frequency shift for MB-coated sensors exposed to a 10 μg/mL solution ($n = 6$) was found to be 154 kHz. This increased frequency shift observed with an increased concentration of the target marker was found to be statistically significant ($p = 0.004$). The reference sensors were tested with a concentration of 10 μg/mL and had an average frequency shift of 10.6 kHz which is significantly lower than the average shifts measured in the two sets of tests performed with sensors coated with MB antibodies ($p < 0.001$). The difference in the response of the target sensors to the two samples of varying concentration is indicative of the activity of the antibody coating after the immobilization protocol. Furthermore, the fact that the target responses are significantly greater in magnitude than those of the reference sensors confirms that the antibody coating imparts molecular specificity to the sensors.

Since the FITC antigen is not present in the samples that were tested, the shift observed in the reference sensors coated with anti-FITC antibodies can be attributed to non-specific protein adsorption to the sensor surface. The issue of non-specific protein adsorption must be considered in any label-free sensor system. With acoustic sensor platforms, the use of reference sensors is a common method for mitigating the effects on non-specific protein adsorption on sensor detection outcomes (Corso et al., 2006; Lee et al., 2003). This is because the reference sensor response can be subtracted from the target sensor response to give a signal due to specific antibody–antigen interactions only. However, for sensor systems where a reference sensor is not feasible or not desired, other methods can be implemented to block non-specific protein adsorption such as treating the surface with bovine serum albumin (BSA) prior to exposure to the target sample (Bhatia et al., 1989).

4. Conclusions

We have provided an investigation of two antibody immobilization techniques on planar ZnO surfaces. The surfaces were analyzed using water contact angle measurements, atomic force microscopy, and fluorescence microscopy to determine the surface characteristics and antibody surface coverage. We found that protocols employing both GPS and MTS are effective in immobilizing antibodies to the ZnO surface, but that MTS offers greater surface coverage, on average. We achieved uniform and repeatable surface coverage using both methods which is a necessary requirement for biosensor functionalization. The antibody functionality was investigated using ZnO-based acoustic resonators. Target sensors treated with the MTS protocol were found to be sensitive to solutions containing mesothelin-rFc and an increased frequency shift was observed corresponding to exposure to solutions with a higher concentration of the protein.

This study is offered as an initial study for immobilization of antibodies on planar ZnO surfaces. Functionalization of crystalline ZnO surfaces is becoming an increasingly important topic as new biosensor platforms are being developed with this material. Further work should build upon the studies detailed here for optimizing immobilization times to maximize the density and uniformity of covalent antibody immobilization procedures. It is concluded that MTS is a viable option for moving forward in functionalizing ZnO-based sensors due to the fact that it is a commercially available chemical and provides high antibody surface coverage with good uniformity.

Acknowledgements

This work was supported by the Georgia Tech/Emory Fund for Innovative Cancer Technologies and the V foundation. Chris Corso is supported by a National Science Foundation Graduate Research Fellowship, and Anthony Dickherber is supported by the Congressionally Directed Medical Research Program Prostate Cancer Training Award. The authors would like to thank Dr. Pastan for his generous donation of the MB antibodies and the mesothelin-rFc protein. We would also like to thank Debin Wang for his help and expertise in making the water contact angle measurements.

References

Argani, P., Iacobuzio-Donahue, C., Ryu, B., Rosty, C., Goggins, M., Wilentz, R.E., Murugesan, S.R., Leach, S.D., Jaffee, E., Yeo, C.J., Cameron, J.L., Kern, S.E., Hruban, R.H., 2001. Clin. Cancer Res. 7 (12), 3862–3868.

Ballantine, D.S., 1997. Acoustic Wave Sensors: Theory, Design, and Physico-Chemical Applications. Academic Press, San Diego.

Bhatia, S.K., Shriver-Lake, L.C., Prior, K.J., Georger, J.H., Calvert, J.M., Bredehorst, R., Ligler, F.S., 1989. Anal. Biochem. 178 (2), 408–413.

Chambers, J.P., Arulanandam, B.P., Matta, L.L., Weis, A., Valdes, J.J., 2008. Curr. Issues Mol. Biol. 10, 1–12.

Chang, K., Pastan, I., 1996. Proc. Natl. Acad. Sci. U.S.A. 93 (1), 136–140.

Chang, K., Pastan, I., Willingham, M.C., 1992. Int. J. Cancer 51 (4), 548–554.

Corso, C.D., Dickherber, A., Hunt, W.D., 2007. J. Appl. Phys. 101 (5), 54511–54514.

Corso, C.D., Stubbs, D.D., Lee, S.H., Goggins, M., Hruban, R.H., Hunt, W.D., 2006. Cancer Detect. Prev. 30 (2), 180–187.

Hassan, R., Remaley, A.T., Sampson, M.L., Zhang, J., Cox, D.D., Pingpank, J., Alexander, R., Willingham, M., Pastan, I., Onda, M., 2006. Clin. Cancer Res. 12 (2), 447–453.

Kang, D.J., Kim, J.S., Jeong, S.W., Roh, Y., Jeong, S.H., Boo, J.H., 2005. Thin Solid Films 475 (1–2), 160–165.

Krishnamoorthy, S., Bei, T., Zoumakis, E., Chrousos, G.P., Iliadis, A.A., 2006. Biosens. Bioelectron. 22 (5), 707–714.
Lee, S.H., Stubbs, D.D., Cairney, J., Hunt, W.D., 2003. Proceedings of IEEE Sensors 2003, Toronto, Ont., Canada, pp. 1194–1198.
Luzinov, I., Julthongpiput, D., Liebmann-Vinson, A., Cregger, T., Foster, M.D., Tsukruk, V.V., 2000. Langmuir 16 (2), 504–516.
Onda, M., Willingham, M., Nagata, S., Bera, T.K., Beers, R., Ho, M., Hassan, R., Kreitman, R.J., Pastan, I., 2005. Clin. Cancer Res. 11 (16), 5840–5846.
Ordonez, N.G., 2003. Am. J. Surg. Pathol. 27 (11), 1418–1428.
Rosenbaum, J.F., 1988. Bulk Acoustic Wave Theory and Devices. Artech House, Boston.
Ruan, C.M., Yang, L.J., Li, Y.B., 2002. Anal. Chem. 74 (18), 4814–4820.
Sadik, P.W., Pearton, S.J., Norton, D.P., Lambers, E., Ren, F., 2007. J. Appl. Phys. 101 (10), 104514–104515.
Shriver-Lake, L.C., Donner, B., Edelstein, R., Breslin, K., Bhatia, S.K., Ligler, F.S., 1997. Biosens. Bioelectron. 12 (11), 1101–1106.
Tlili, A., Abdelghani, A., Aguir, K., Gillet, M., Jaffrezic-Renault, N., 2007. Mater. Sci. Eng. C-Biomimetic Supramol. Systs. 27 (4), 620–624.
Wang, Z.L., 2004. Annu. Rev. Phys. Chem. 55, 159–196.
Yamazaki, O., Mitsuyu, T., Wasa, K., 1980. IEEE Trans. Sonics Ultrasonics SU-27 (6), 369–379.
Yang, L., Li, Y., 2005. Biosens. Bioelectron. 20 (7), 1407–1416.

99th AACR Annual Meeting-- Apr 12-16, 2008; San Diego, CA

Abstract #5130

A microelectronic bulk acoustic wave biosensor array for the detection of PSA in complex solutions

Anthony Dickherber, Christopher Corso, John Petros, Milton Datta and William Hunt

Georgia Institute of Technology, Atlanta, GA, Emory University & Atlanta VA Medical Center, Atlanta, GA, Abbott Northwestern Hospital & University of MN, Minneapolis, MN

INTRODUCTION: Microelectronics offers the opportunity to develop inexpensive biosensors for portable disposable biomarker assays that are easily multiplexed, highly sensitive, and highly specific. Such biosensors could impact clinical diagnosis through point of care testing for biomarkers that predict tumor diagnosis or clinical recurrence. We have previously demonstrated such technology using quartz crystal microbalance (QCM) sensors. Here we extend our findings with a bulk acoustic wave (BAW) sensor that provides magnitudes of greater potential sensitivity with multiplexing capabilities. In this research we present a mass produced inexpensive 8-device array and demonstrate detection of the biomarker PSA from LnCap conditioned medium.

METHODS: The ZnO BAW sensor chip platform involves an 8-device array that can be used as a biosensor in complex solutions such as serum. The sensors utilize molecular perturbation of acoustic waves generated by electrodes as the detection mechanism. An appropriate surface-preparation process was determined for covalently binding monoclonal antibodies to the zinc oxide crystal to functionalize each sensor toward a specific target. The sensor arrays were then used to assay for the presence of PSA (sc-52170) and FITC (negative control, sc-69871) in conditioned medium from LNCaP prostate cancer cells.

RESULTS: Covalent immobilization of monoclonal antibodies to the ZnO crystal surface via a crosslinker and an organosilane monolayer was assessed via atomic force microscopy, confocal laser scanning microscopy and contact angle measurements. Results indicate the significant presence of antibodies bound to the surface. Subsequent exposure of the device arrays to LnCap conditioned medium demonstrated a significant device response of the PSA-targeted sensor over the FITC-targeted sensor. The antibody immobilization process currently requires only about 3 steps and takes roughly 1 day to prepare. Detection of targeted markers in the sample is evident nearly instantaneously once presented to the device surface. Binding of conjugated PSA from the conditioned medium yielded an easily measured 12 kHz shift on average.

CONCLUSIONS: Here we present an inexpensive BAW sensor array that can be rapidly and efficiently conjugated with antibodies and used for the detection of circulating biomarkers in complex solutions such as serum. This extends our prior proof of concept work with quartz crystal microbalances to a smaller inexpensive device while offering potentially greater sensitivity by several orders of magnitude. We have demonstrated an appropriate protocol for the rapid and efficient covalent binding of monoclonal antibodies to the sensor surface and the subsequent detection of PSA in LnCap conditioned medium. This system allows for multi-component biomarker array formation for rapid multiplex testing and extensive statistical data analysis.

Passive sensor networks based on multi-element ladder filter structures

Christopher D. Corso[1], Anthony Dickherber[2], William D. Hunt[2]
[1] Department of Biomedical Engineering
[2] Department of Electrical Engineering
Georgia Institute of Technology
Atlanta, GA

Peter J. Edmonson
P. J. Edmonson Ltd.
Hamilton, ON Canada

Abstract—**This work explores a novel acoustic resonator sensor system in a departure from the standard approach requiring an oscillator circuit to drive the resonance. The work is motivated by the need to monitor multiple sensors simultaneously in a near real-time manner. The system employs an arrangement of discrete resonators in a ladder network filter configuration. This arrangement establishes a passive structure in which the overall frequency response reports perturbations to individual resonators within the network. Here, we focus on the contribution of individual resonators to the overall response and explore methods for designing a passband response which has useful features for sensor experiments. It is concluded that an arrangement in which the resonant frequencies of the series and shunt resonators are offset results in a response that can be tracked during sensor experiments.**

I. INTRODUCTION

One problem with the traditional approach to acoustic resonator sensor system design is that an oscillator circuit is required to drive the acoustic device at its resonant frequency. Such a requirement is problematic because of the fixed operating bandwidth. Devices operating at radically different non-harmonic frequencies cannot be driven by the same oscillator circuit, which presents a significant restriction during the design and testing of acoustic wave sensors.

Communication systems including digital radios have employed ladder and lattice type structures as filters for well over a decade [1, 2]. These filters consist of interconnected series and shunt resonators that form a monolithic structure on a single die. Since the requirements of a sensor system are fundamentally different from that of a communications system, a novel implementation of the ladder filter network comprised of multiple individual sensors can be exploited to obtain a passive, multi-element sensor structure. In such a structure, the overall frequency response changes uniquely as specific sensor elements are perturbed. This research explores how an individual resonator located in the series or shunt positions of the sensor filter network, when perturbed, affects the frequency response of the entire structure.

A common design requirement for filters in the communications industry is a smooth passband, in which all signals within the desired frequency band are passed with approximately the same attenuation. For sensor applications, however, this requirement is irrelevant. A ladder filter network such as the one proposed here would not require a smooth passband. In fact, ripples in the passband that arise by offsetting the fundamental resonant frequencies of the devices that comprise the network can be useful for reporting detection events. An additional benefit of this approach is that fabrication tolerances of such networks for sensor applications can be relaxed and overall production costs could be reduced in mass production.

A circuit model of a simple 4-element ladder filter is shown in Fig. 1. For circuit simulation purposes, the individual resonators can be modeled with a basic BVD model (shown in Fig. 2). The BVD model is one of many electronic circuit representations of a resonator. It has been widely used in a variety of forms throughout the literature as a representation for an acoustic resonator [3, 4].

In the simplest form, the BVD model contains a constant clamped capacitance, C_0, which represents the inherent capacitance of the structure. The clamped capacitance is in parallel with a motional arm consisting of a

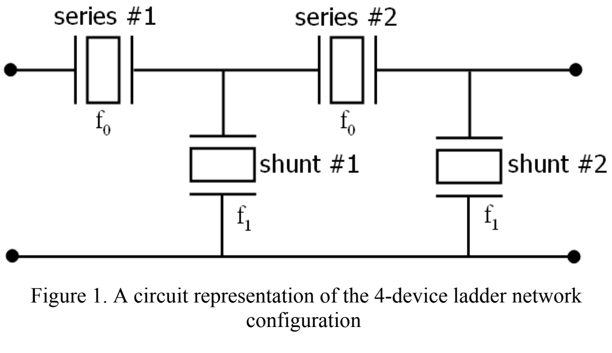

Figure 1. A circuit representation of the 4-device ladder network configuration

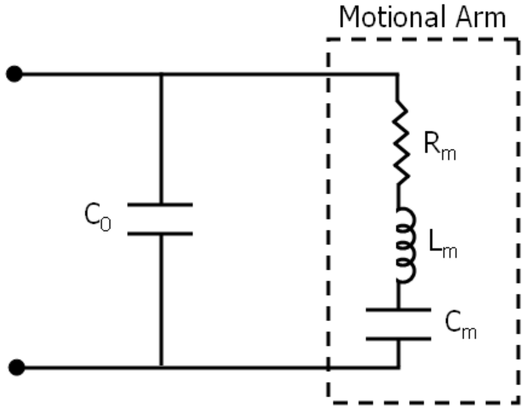

Figure 2. Butterworth Van-Dyke equivalent circuit used for simulating each resonator

motional inductance, L_m and motional capacitance, C_m. The motional components in this model represent the electromechanical response of a piezoelectric material. The BVD model shown in Fig. 2 represents a lossy resonator because it makes use of a motional resistance, R_m, which provides for energy absorption in the device as a result of acoustic attenuation.

In this work, we implement a ladder filter network using a circuit analysis package to explore the capabilities of the network from a sensor system point of view. Specifically, we aim to gain understanding about the contributions of individual resonators/sensors to the frequency response of the multi-element network. The circuit network is analyzed to obtain the throughput scattering response (S_{21}) of the ladder filter before and after the individual resonators are "perturbed" to simulate sensor detection events (i.e. mass loading). Perturbation of the individual resonators is modeled by altering the components of the BVD model to shift the series frequency downwards – an effect that typically occurs in mass loading events for acoustic resonators. The resulting electrical responses are analyzed and compared to the unperturbed response to determine the contributions of each of the individual resonators to the overall network response. A technique is described for configuring the fundamental frequencies of the individual resonators so that perturbation of each resonator can be monitored separately by analyzing changes in the S_{21} response of the filter network. The passive structure does not require individual oscillator circuits for driving the resonance of the individual devices. For practical biosensor applications, the proposed configuration would make it possible to have multiple sensors within the same network sensing multiple targets simultaneously in a package separate from the driving circuitry.

II. METHODS

Initial simulations of the configuration shown in Figure 1 were performed in which the unperturbed series resonators #1 and #2 operate at f_0 (1.71 GHz) and the unperturbed shunt resonators #1 & #2 operate at f_1 (1.8 GHz). The individual resonator structure we chose to simulate using the BVD model is a thin-film FBAR resonator operating in the longitudinal mode with a thickness excitation electrode configuration. The network configuration described in this paper is not limited to BAW devices, however, and can be configured to accommodate a variety of narrow-band acoustic resonators, including SAW devices and other MEMS devices. The devices that are simulated using the BVD model consist of a thin-film modeled as piezoelectric c-axis oriented ZnO with electrodes placed on opposing surfaces of the film. A series of simulations were performed by individually perturbing each resonator and observing the effect on the overall frequency response. The values of the BVD circuit elements were altered such that the resonant frequency was shifted downwards by 10 MHz. The calculations to derive the capacitor, inductor, and resistor values were performed using the equations described in [5]. The S_{21} response for the resulting filter networks were calculated and compared with the original S_{21} response.

In the initial simulations, the series resonators were configured to operate at f_0 while the shunt resonators were configured to operate at f_1. This is typical of a ladder or lattice filter network configuration because it aids in developing a flat passband response. By setting the series and shunt resonators to opposing fundamental frequencies, however, the resulting S_{21} response contains more information about the individual resonators that comprise the network. To test this, a series of simulations were performed. The resonant frequency of series resonator #1 was set to f_1 while series resonator #2 was kept at f_0. Additionally, shunt resonator #2 was set to operate at f_0 while shunt resonator #1 was kept at f_1. The initial S_{21} response was recorded. Subsequent perturbations were individually simulated by shifting the resonator fundamental frequency of each of the four resonators downwards by 10 MHz in a manner similar to the prior tests. The frequency response of the resulting networks were calculated and compared to the unperturbed response.

III. RESULTS

Figures 3a and 3b illustrate the effects of individually perturbing the two series resonators and the two shunt resonators when they are initially set at f_0 and f_1, respectively. We see that the individual contributions of the perturbed resonators to the overall response are not very discernible when the resonators are operated in this configuration. We observed that in the standard configuration, common to most communication filter designs, it is difficult to determine if a sensor detection event occurred in the first or second series/shunt resonator. Rather, it is only evident that a perturbation occurred in the shunt or series elements of the circuit. In this configuration, shunt perturbation manifests itself as a change in the lower cutoff frequency notch of the passband while series perturbation results in a change in the upper cutoff

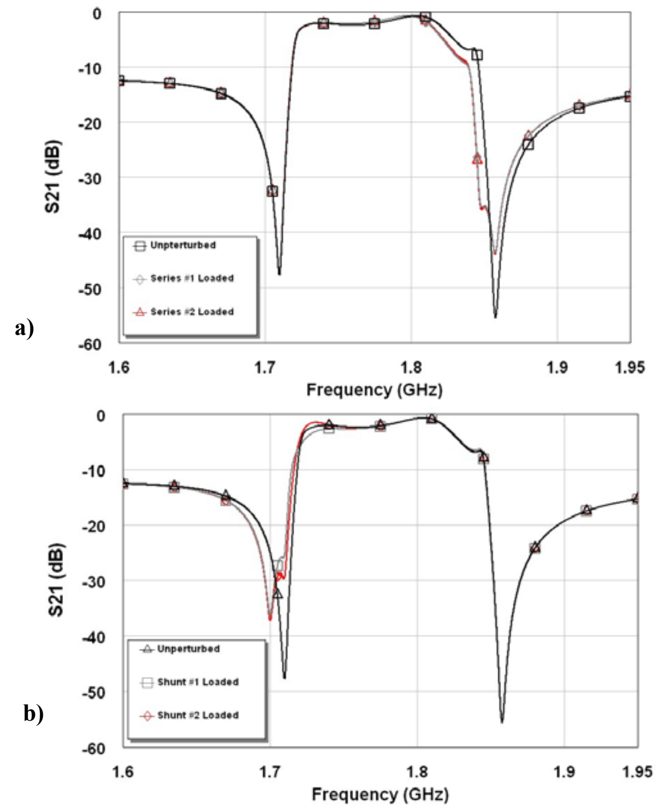

Figure 3. (a) The effects of perturbing series #1 and #2 resonators (both at f_0) independently and, (b) the effects of perturbing the shunt #1 and #2 resonators (both at f_1) independently

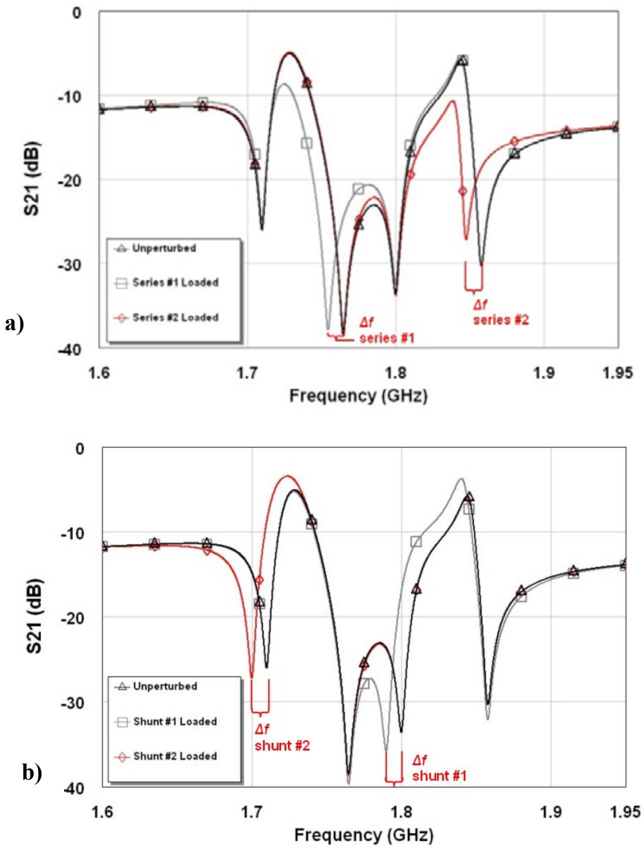

Figure 4. Simulation results of the modified ladder network showing the frequency shift resulting from (a) perturbation of series #1 (f_1) and #2 (f_0) resonators independently and, (b) perturbation of the shunt #1 (f_0) and #2 (f_1) resonators independently.

frequency notch of the passband. The frequency responses of Figures 3a and 3b follows with ladder filter design theory where the low-frequency side notch is determined by the series resonance of the shunt resonator(s) and the high frequency notch is determined by the parallel resonance of the series resonator(s) [6].

Based on these results, it seems that a filter network employed as a multi-element sensor system could potentially be used for the detection of two targets. The series portion of the circuit would be configured to detect one target, while the shunt portion could be configured to detect the other. The drawback with this configuration, however, is that it would be difficult to independently monitor each of the sensors through analysis of the S_{21} response of the network.

Results from the second series of simulations are shown in Figures 4a and 4b. In these simulations, series resonator #1 was configured to operate at f_1 and shunt resonator #2 was configured to operate at f_0. Figures 4a and 4b illustrate the original passband response of this configuration as well as the effects of individually perturbing the two series resonators and two shunt resonators, respectively. Note that the unperturbed frequency response is drastically different from the more traditional passband response shown in Figures 3a and 3b. The departure from a typical passband response is a result of offsetting the resonant frequencies and is not something that would typically be desirable for filter design. We observe, however, that the S_{21} response contains 4 separate "notches" which each correspond to the series or parallel resonant frequency of an individual resonator within the structure. This is because the notches in the S_{21} response occur at the parallel resonance frequency for the series resonators and at the series resonance frequency for the shunt resonators. As a result, the location of the notches in the response is determined by the impedance characteristics of the individual resonators. The results indicate that perturbation of either a series or shunt resonator results in a downward frequency shift (Δf) in the location of the notch in the S_{21} response without shifting the location of the notches which correspond to the other three resonators. This indicates that with this offset frequency configuration, it is possible to extract the location and magnitude of the perturbation within the network structure. Therefore a single S_{21} response holds information about all four resonators within the structure. In order to increase the number of devices within the structure, a third device with parallel and series resonant frequencies separated by the desired bandwidth could be positioned in the series and shunt portions of the ladder structure. This would add two additional notches to the S_{21} response – one at the series resonance and one at the parallel resonance.

IV. CONCLUSIONS

Simulations indicate that we can design a frequency response so that the frequency of 4 separate sensors can be individually monitored simultaneously in a passive network configuration. In a practical biosensor implementation, each resonator could be individually functionalized to detect a different biomarker in a complex sample. With the proper circuitry, the resulting frequency response can be measured in real-time and the response of multiple sensors can be read simultaneously without the need for complicated switching schemes or oscillators. This design includes a multi-element sensor array configuration that circumvents many of the problems associated with conventional acoustic sensor arrays. Further analysis of ladder and lattice structures may lead to improved methods for utilizing such structures in sensor systems. Experimental results to supplement the modeling data are currently being explored.

ACKNOWLEDGMENTS

This work was supported by the Georgia Tech/Emory Fund for Innovative Cancer Technologies which derives its funds from the V Foundation and the Georgia Cancer Coalition. Chris Corso is supported by an NSF Graduate Research Fellowship and Anthony Dickherber is supported by the Congressionally Directed Medical Research Program Prostate Cancer Research Program Training Award.

REFERENCES

[1] K. M. Lakin, G. R. Kline, and K. T. McCarron, "Development of miniature filters for wireless applications," *Microwave Symposium Digest, 1995., IEEE MTT-S International,* pp. 883-886, 1995.

[2] G. G. Fattinger, J. Kaitila, R. Aigner, and W. Nessler, "Thin film bulk acoustic wave devices for applications at 5.2 GHz," *Ultrasonics, 2003 IEEE Symposium,* vol. 1, pp. 174-177, 2003.

[3] A. Arnau, Y. Jimenez, and T. Sogorb, "An extended Butterworth Van Dyke model for quartz crystal microbalance applications in viscoelastic fluid media," *Ultrasonics, Ferroelectrics and Frequency Control, IEEE Transactions on,* vol. 48, pp. 1367-1382, 2001.

[4] K. Yoonkee, J. R. Vig, and A. Ballato, "Doubly rotated resonators for sensing the properties of liquids," *Ultrasonics, 2003 IEEE Symposium,* vol. 1, pp. 52-55, 2003.

[5] J. F. Rosenbaum, *Bulk acoustic wave theory and devices*. Boston: Artech House, 1988.

[6] K. M. Lakin, J. Belsick, J. F. McDonald, and K. T. McCarron, "Improved bulk wave resonator coupling coefficient for wide bandwidth filters," *Ultrasonics Symposium, 2001 IEEE,* vol. 1, pp. 827-831, 2001.

DESIGN AND IMPLEMENTATION OF AN ACOUSTIC RESONATOR-BASED BIOSENSOR FOR THE EARLY DETECTION OF PROSTATE CANCER

A Thesis
Presented to
The Academic Faculty

by

Anthony Dickherber

In Partial Fulfillment
of the Requirements for the Degree
Doctorate of Philosophy in the
School of Electrical and Computer Engineering

Georgia Institute of Technology
December 2008

DESIGN AND IMPLEMENTATION OF AN ACOUSTIC RESONATOR-BASED BIOSENSOR FOR THE EARLY DETECTION OF PROSTATE CANCER

Approved by:

Dr. William Hunt, Advisor
School of Electrical and Computer Engineering
Georgia Institute of Technology

Dr. Robert Butera
School of Biomedical Engineering
Georgia Institute of Technology

Dr. Peter Hesketh
School of Mechanical Engineering
Georgia Institute of Technology

Dr. Alfred Merrill
School of Biology
Georgia Institute of Technology

Dr. John Petros
Winship Cancer Institute
Emory University

Date Approved: October 28, 2008

DESIGN AND IMPLEMENTATION OF AN ACOUSTIC RESONATOR-BASED BIOSENSOR FOR THE EARLY DETECTION OF PROSTATE CANCER

Approved by:

Dr. William Hunt, Advisor
School of Electrical & Computer Engineering
Georgia Institute of Technology

Dr. Robert Butera
School of Biomedical Engineering
Georgia Institute of Technology

Dr. Peter Hesketh
School of Mechanical Engineering
Georgia Institute of Technology

Dr. Alfred Merrill
School of Biology
Georgia Institute of Technology

Dr. John Petros
Winship Cancer Institute
Emory University

Date Approved: October 28, 2008

ACKNOWLEDGEMENTS

TABLE OF CONTENTS

LIST OF TABLES

LIST OF FIGURES

Page

LIST OF ABBREVIATIONS

AA	Amino Acid
AACR	American Association for Cancer Research
Ab	Antibody
AFM	Atomic Force Microscopy
ANOVA	Analysis of Variance
APS	3-Aminopropyl triethoxy Silane
AUC	Area Under the Curve
BAW	Bulk Acoustic Wave
BMI	Body Mass Index
BPH	Benign Prostatic Hyperplasia
BVD	Butterworth-Van Dyke
CDMRP	Congressionally Directed Medical Research Program
CM	Conditioned Medium
CVD	Chemical Vapor Deposition
DI H_2O	Deionized Water
DNA	Deoxy-ribonucleic Acid
ELISA (EIA)	Enzyme Linked Immunosorbent Assay
EPCA	Early Prostate Cancer Antigen
FBAR	Thin Film Bulk Acoustic Resonator
FITC	Fluorscein Isothiocyanate
FWHM	Full Width at Half Maximum
GHz	Gigahertz (10^9)
GMBS	N-γ-maleimido Butyryloxy Succinimide Ester

GPS	3-Glycidoxy-Propyl trimethoxy Silane
HMDS	Hexamethyldisilazane
HPLC	High Performance Liquid Chromatography
IC	Integrated Circuit
IDT	Interdigitated Transducers
IgX	Immunoglobulin X
kHz	Kilohertz (10^3)
LFE	Lateral Field Excitation
mAb	Monoclonal Antibody
MHz	Megahertz (10^6)
MOCVD	Metal-organic CVD
MPF	Megakaryocyte Potentiating Factor
MTS	3-Mercapto-propyl Trimethoxy Silane
NCI	National Cancer Institute
NIH	National Institutes of Health
NOC	Non-Organ Confined
OC	Organ Confined
PAP	Prostatic Acid Phosphatase
PBS	Phosphate Buffer Solution
PCa	Prostate Cancer
PCB	Printed Circuit Board
PCR	Polymerase Chain Reaction
PCRP	Prostate Cancer Research Program
PSA	Prostate Specific Antigen
PVD	Plasma Vapor Deposition

QCM	Quartz Crystal Microbalance
RF	Radio Frequency
RGB	Red Green Blue
RNA	Ribonucleic Acid
ROC	Receiver Operator Characteristic
S_{11}	Reflection Scattering Response
SAM	Self-Assembled Monolayer
SAW	Surface Acoustic Wave
SELEX	Systematic Evolution of Ligands by Expontial enrichment
SEM	Scanning Electron Microscope
SHH	Sonic Hedge Hog
SH-SAW	Shear Horizontal SAW
SMR	Solidly Mounted Resonator
SPR	Surface Plasmon Resonance
TCE	Trichloro Ethylene
TCF	Temperature Coefficient of Resonant Frequency
TE	Thickness Excitation
TFE	Thermally Assisted Field Emission
TSM	Thickness Shear Mode
USAMRMC	United States Army Medical Research and Materiel Command
USFDA	United States Food and Drug Administration
VDC	Voltage DC
WCA	Water Contact Angle
XRD	X-ray Diffraction

SUMMARY

The objective of this thesis research is to develop microelectronic acoustic technology towards biosensor applications. The development of a simple and robust resonator that employs simple microelectronic fabrication techniques for its construction could provide the foundation for a cost-effective sensor platform. Subsequent development of an appropriate surface chemistry treatment would functionalize the resonator as a biosensor. Implementation of this design in an array configuration allows for the development of ligand microarrays, which subsequently allows for multi-ligand recognition signatures as well as testing redundancy. The applications for such a tool extend to a myriad of applications, but the focus of this research is to develop this technology towards an early cancer detection capability.

Specifically, I develop a solidly-mounted resonator with thin-film ZnO as my active piezoelectric layer. These resonators undergo an extensive development process to arrive at a final device design and are fully characterized throughout by X-ray diffraction and scattering analysis. Employing silane chemistry, these resonators are functionalized as immunosensors by covalently binding antibodies to the surface of the device. The quality of the surface chemistry is fully assessed using water contact angle, atomic force microscopy and confocal laser scanning microscopy. Functionalized biosensors are then used to quantify the concentration of known proteins marker in both a purified medium and a physiologically-relevant medium.

CHAPTER 1

INTRODUCTION

The objective of my research was to develop a biosensor technology appropriate for application towards the early detection of cancer. Biosensors can generally be broken down as follows: (shown in Figure 1.1)

1. A specific molecular recognition event (generally achieved by an immobilized capture agent) occurs at a particular location due to exposure of the sensor to a sample medium
2. This event causes a change in the operation of an adjacent or otherwise proximal transducer.
3. The change in operating conditions of that transducer is detected by associated electronic detection equipment.

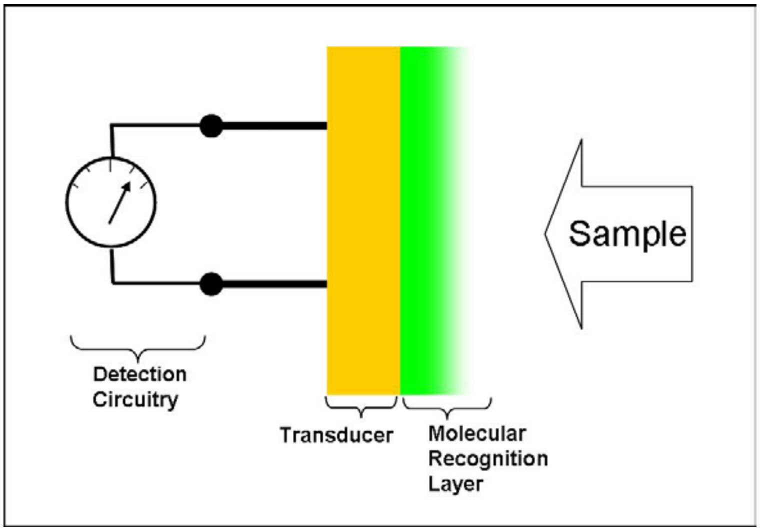

Figure 1.1. Principles of a biosensor.

Given that prostate cancer represents one of the best understood at the earliest stages of development, I will focus on application of this sensor towards detection of prostate cancer relevant biomarkers. The overall goal, therefore, is to develop a microelectronic acoustic sensor design that will lead to point-of-care, label-free detection capability with the following three attributes:

1. a cost-effective design that allows for simple mass production using currently available facilities;
2. a sensor capable of sufficient sensitivity and selectivity to detect targets at pathologically relevant concentrations in physiologically relevant media; and
3. a simple sensing protocol that accommodates little training and near real-time response while minimizing false negatives and false positives.

There exist many problems to be solved in accomplishing such a system. For such an early detection system to be useful for broader clinical diagnostic applications, the sensor design must be highly cost effective. The microelectronics industry has made extraordinary progress in pushing economies of scale to reduce the price of any hardware produced by microelectronic fabrication. A sensor can be developed that takes advantage of the use of these techniques. Medical diagnostics are generally made more expensive by the duration and complexity of the testing protocol. The more complex the system, the greater the qualifications required of the technician performing the test, generally increasing the cost. Development of a near real-time reporting system that requires little training to perform would significantly mitigate these costs.

The applications for such a sensor technology are extensive. In the field of cancer treatment alone, such sensors could be used for early diagnosis, post-treatment monitoring, and by proteomics researchers for new marker exploration and validation. Beyond cancer research, such devices could be employed for everything from battlefield chemical weapons detection, to narcotics and explosives detection, to water quality monitoring [1-3].

I will demonstrate significant progress towards realizing such a tool. Specifically, contributions by the author include:

A. The development of a novel thickness shear mode bulk acoustic resonator array utilizing zinc oxide (ZnO).
B. The novel application of an appropriate surface chemistry protocol for functionalization of planar ZnO with monoclonal antibodies.
C. Combination of these two and demonstration of capability as a sensor.

The first point represents an original contribution by the author that simultaneously addresses points 1-3 enlisted on page 2 of this dissertation. The resonator design can be fabricated with existing microelectronic fabrication equipment with a small footprint, easily implemented in a microarray configuration. The device array can easily yield as many as 1,000 arrays with eight devices each on a single 3-inch wafer. Further, the design is such that it could be fabricated on nearly any polished substrate. The second point is also an original contribution by the author, allowing for the application of the resonators developed as biosensors, as well as the functionalization of any other ZnO-based transducer. As neither of the first two components had ever existed before, the third point is obviously another original contribution by the author. The accomplishments listed above have led to the following peer-reviewed publications:

- Christopher D Corso, Anthony Dickherber, William D. Hunt, 'An investigation of antibody immobilization methods employing organosilanes on planar crystalline ZnO surfaces for biosensor applications,' *Biosensors & Bioelectronics* 2008, Article in Press
- Cleon Davis, Anthony Dickherber, William D. Hunt, Gary S. May, 'In-Situ acoustic temperature measurement during variable frequency microwave curing,' *IEEE Transactions on Electronics Packaging Manufacturing*, 2008, Article in Press
- Anthony Dickherber, Christopher D Corso, William D. Hunt, 'Optimization and characterization of a ZnO biosensor array,' *Sensors & Actuators A: Physics*, 144(1) pg 7-12, May 28, 2008
- Christopher D Corso, Anthony Dickherber (joint first author), William D. Hunt, 'Lateral field excitation of thickness shear mode waves in a thin film ZnO solidly mounted resonator,' *Journal of Applied Physics*, 101, 054514, 2007
    - Article was independently selected for publication in the *Virtual Journal of Biological Physics Research*, May 2007, indicating recognition of the potential impact of this research

the following conference presentations:

- Anthony Dickherber, Christopher D Corso, William D. Hunt, 'Stability of a RF sputtered ZnO solidly mounted resonator sensor in varying temperature and conductivity environments,' *IEEE Sensors Conference*, Atlanta, GA Oct 30 2007
- Anthony Dickherber, Christopher D Corso, William D. Hunt, 'Dual Mode Sensing,' *IEEE Engineering in Medicine and Biology Conference*, NYC NY, Sept 2 2006
- Anthony Dickherber, William D. Hunt, 'Towards integration of ZnO resonator components with GaAs microelectronics,' *Motorola University Partnership in Research Program Conference*, Chicago IL, Oct 2004

and the following professional poster presentations:

- Anthony Dickherber, Christopher D. Corso, John Petros, William D. Hunt, 'A microelectronic bulk acoustic wave biosensor array for the detection of PSA in complex solutions,' *2008 Annual Meeting of American Association for Cancer Research*, San Diego, CA, April 10-16, 2008

- Christopher D. Corso, Anthony Dickherber, and William D. Hunt, 'A thickness shear mode zinc oxide liquid sensor with off-axis excitation,' *IEEE Sensors Conference*, Atlanta GA, Oct 29-31 2007

- Anthony J. Dickherber, Christopher D. Corso, William D. Hunt, Ira Pastan, Mitchell Ho, Raffit Hassan, 'Mesothelin-fc fusion protein detection using a novel microelectronic acoustic sensor platform,' *2007 AACR International Conference on Molecular Diagnostics in Cancer Therapeutic Development*, Atlanta, GA Sept 17-20, 2007

- Anthony Dickherber, William Hunt, 'Breaking Down Cost Barriers to Improve Public Health,' *The Sam Nunn Bank of America Policy Forum*, Atlanta, GA March 27 2006

- Christopher Corso, Anthony Dickherber, Payal Shah, Alexandra Migdal, Milton Datta, Sumana Datta, William Hunt, 'Development of a Simple Inexpensive Bulk Acoustic Wave Nanosensor for Cancer Biomarkers: Detection of Secreted Sonic Hedgehog from Prostate Cancer Cells,' *2006 Annual Meeting of American Association for Cancer Research*, Washington DC, April 4, 2006

- William Hunt, Christopher Corso, Anthony Dickherber, 'Piezoelectric Bulk Acoustic Wave Biosensors for Real-Time Biomarker Detection in Complex Media,' *Moving Biosensors to Point-of-Care Cancer Diagnostics* (National Cancer Institute Conference), Rockville, MD, June 8-9, 2005

In addition, this research was supported by a pre-doctoral training award to the author of $67,824 from the US Army Medical Research and Materiel Command's (USAMRMC) Prostate Cancer Research Program (PCRP). The USAMRMC is a research initiative of the Congressionally Directed Medical Research Program (CDMRP).

I will begin with a discussion of the need for a tool that meets the criteria described at the beginning of this chapter and lay out the specific aims of this thesis research. In Chapter 2, I will explore the advantages of acoustic wave biosensors, as opposed to alternative transducer technologies, and discuss the principles of their operation. Chapter 3 will include a theoretically confirmation of the proposed acoustic wave transducer (or resonator) and the subsequent development of that design. In Chapter 4 I will discuss the challenges of developing an appropriate molecular recognition layer for the resonator followed by a thorough characterization of the chosen protocol. Chapter 5 will demonstrate the performance of the device in various sensor applications and challenges therein. Chapter 6 will provide a concluding discussion of the accomplishments made, a short discussion of some late-breaking developments and finally a presentation of some directions for follow-up work.

Motivation

President Richard Nixon launched the US war against cancer in his 1971 State of the Union Address, in which he pledged an extraordinary boost to the National Cancer Institute's (NCI) budget and granted cancer researchers the US Army's Fort Detrick as a research center [4]. Considered his most significant act was the signing of the National Cancer Act later that year, at which time he famously declared, "I hope in the years ahead we will look back on this action today as the most significant action taken during my Administration." While historians are quite likely to argue that point, the question remains regarding how we've progressed on this "War on Cancer." Since that time, extraordinary progress has been made in understanding the etiology of various cancers and in providing new lines of therapies. The need to maintain efforts regarding this campaign, however, are still very strong.

Today the National Institutes of Health (NIH) estimate that more than 1,500 people die each day from a cancer-related cause in the U.S., accounting for one in four American deaths overall [5]. Perhaps more disturbing, however, is the fact that mortality rates for *most* cancers have not improved significantly over the past three decades [6]. As can be seen in Figure 1.2, cancer mortality has recently surpassed heart disease mortality rates for individuals under the age of 85, making it the largest killer in the US for that age group [5]. One major component of the progress to date involves advances made through genomic and proteomic studies revealing the presence of serum level molecular targets, or biomarkers, indicative of various cancers and their proliferation [6]. Detection of these biomarkers in circulating blood is one of the clearest paths to achieving early detection. While early detection of any cancer has been identified as likely the best determinant for long-term survival, broadly available diagnostic tools and techniques available for general clinical diagnostics have not yet emerged to significantly take advantage of these discoveries [7, 8].

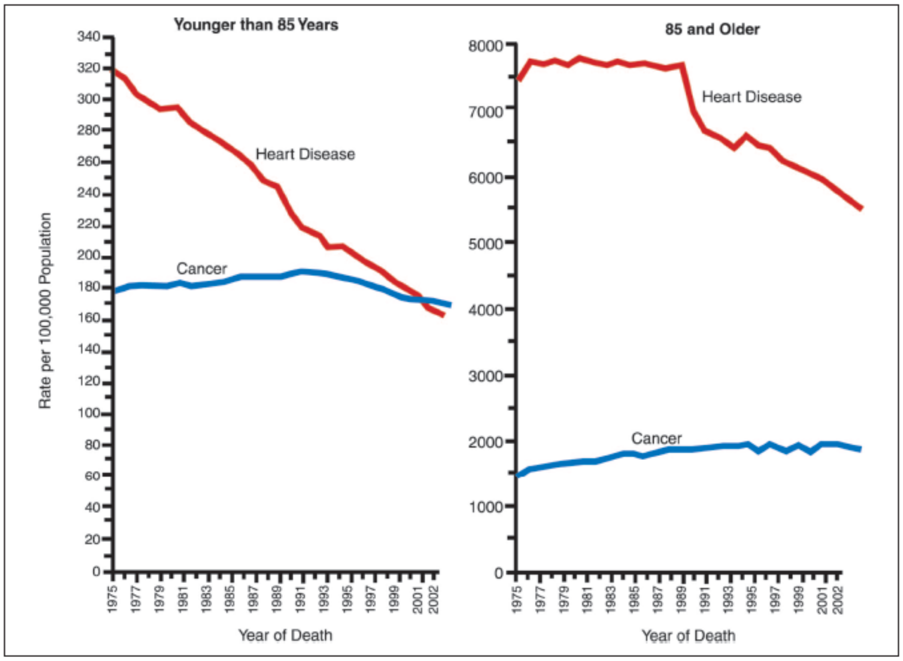

Figure1.2. Death rates from cancer and heart disease, US 1975-2002. [5]

The incidence and mortality rates for the top ten cancers for both men and women in the US are depicted in Figure 1.3. According to the NIH's National Cancer Institute (NCI), death rates decreased for 11 of the 15 most common cancers in men, but actually increased for prostate cancer between 1995 and 2003.[5] As demonstrated in Figure 1.3, it is currently estimated that prostate cancer accounts for a little less than one third of all new cancer cases in the US in men, with more than 218,000 new cases expected from 2007. Figure 1.4 reveals that while mortality rates due to prostate cancer have slowed recently, it still represents the second largest cause of cancer-related deaths in US males.

Estimated New Cases*

Males			Females		
Prostate	218,890	29%	Breast	178,480	26%
Lung & bronchus	114,760	15%	Lung & bronchus	98,620	15%
Colon & rectum	79,130	10%	Colon & rectum	74,630	11%
Urinary bladder	50,040	7%	Uterine corpus	39,080	6%
Non-Hodgkin lymphoma	34,200	4%	Non-Hodgkin lymphoma	28,990	4%
Melanoma of the skin	33,910	4%	Melanoma of the skin	26,030	4%
Kidney & renal pelvis	31,590	4%	Thyroid	25,480	4%
Leukemia	24,800	3%	Ovary	22,430	3%
Oral cavity & pharynx	24,180	3%	Kidney & renal pelvis	19,600	3%
Pancreas	18,830	2%	Leukemia	19,440	3%
All Sites	**766,860**	**100%**	**All Sites**	**678,060**	**100%**

Estimated Deaths

Males			Females		
Lung & bronchus	89,510	31%	Lung & bronchus	70,880	26%
Prostate	27,050	9%	Breast	40,460	15%
Colon & rectum	26,000	9%	Colon & rectum	26,180	10%
Pancreas	16,840	6%	Pancreas	16,530	6%
Leukemia	12,320	4%	Ovary	15,280	6%
Liver & intrahepatic bile duct	11,280	4%	Leukemia	9,470	4%
Esophagus	10,900	4%	Non-Hodgkin lymphoma	9,060	3%
Urinary bladder	9,630	3%	Uterine corpus	7,400	3%
Non-Hodgkin lymphoma	9,600	3%	Brain & other nervous system	5,590	2%
Kidney & renal pelvis	8,080	3%	Liver & intrahepatic bile duct	5,500	2%
All Sites	**289,550**	**100%**	**All Sites**	**270,100**	**100%**

Figure 1.3. Ten Leading Cancer Types for the Estimated New Cancer Cases and Deaths, by Sex, US, 2007.[5]

A further breakdown of the mortality rates for the top four occurring cancers is depicted in Figure 1.5. These four cancers represent more than half of the diagnosed cancers in the general population and nearly half of all mortality due to cancer. For all but lung cancer, diagnosis in the localized stage of development dramatically improves 5-year and 10-year survival rates towards nearly 100%, as shown in Figure 1.5. It is widely believed that a winning strategy to realizing this goal involves the detection of serum-level biomarkers (those evident in circulating blood) that are currently being discovered for various cancers through genomic and proteomic investigations [6].

The future of cancer diagnostics will therefore likely involve ultra-sensitive screening tools that identify multiple markers indicative of the earliest stages of cancer development. These markers have been difficult to find as they exist in extremely low concentrations in circulating blood. In order to make use of these discoveries at a clinical level, ultra-sensitive biosensors exhibiting high degrees of specificity will be required to identify these proteins in clinical samples (such as patient blood plasma or urine). A

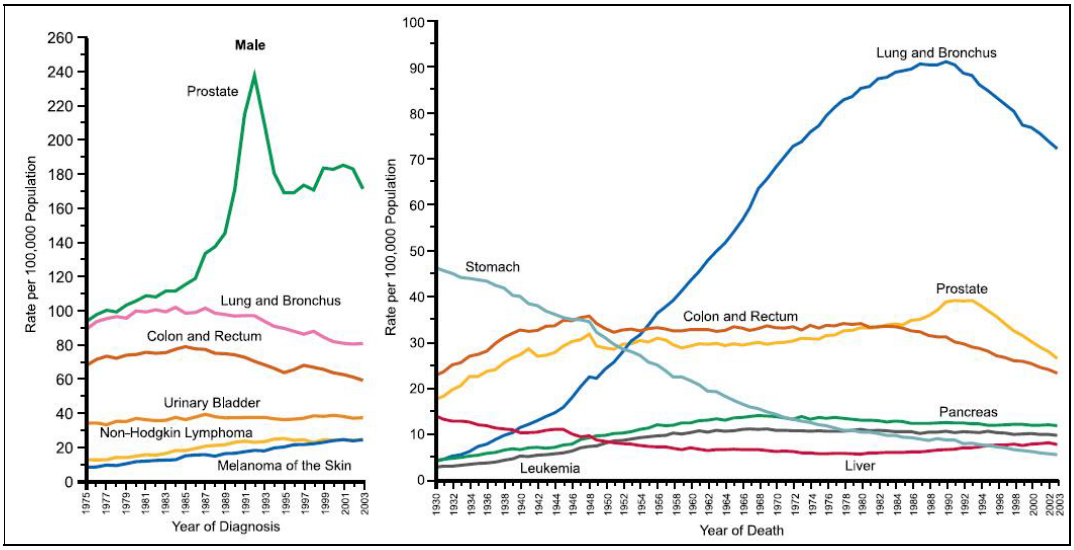

Figure 1.4. Annual-adjust cancer incidence (left) and death (right) rates from the U.S. among males for selected cancers [5].

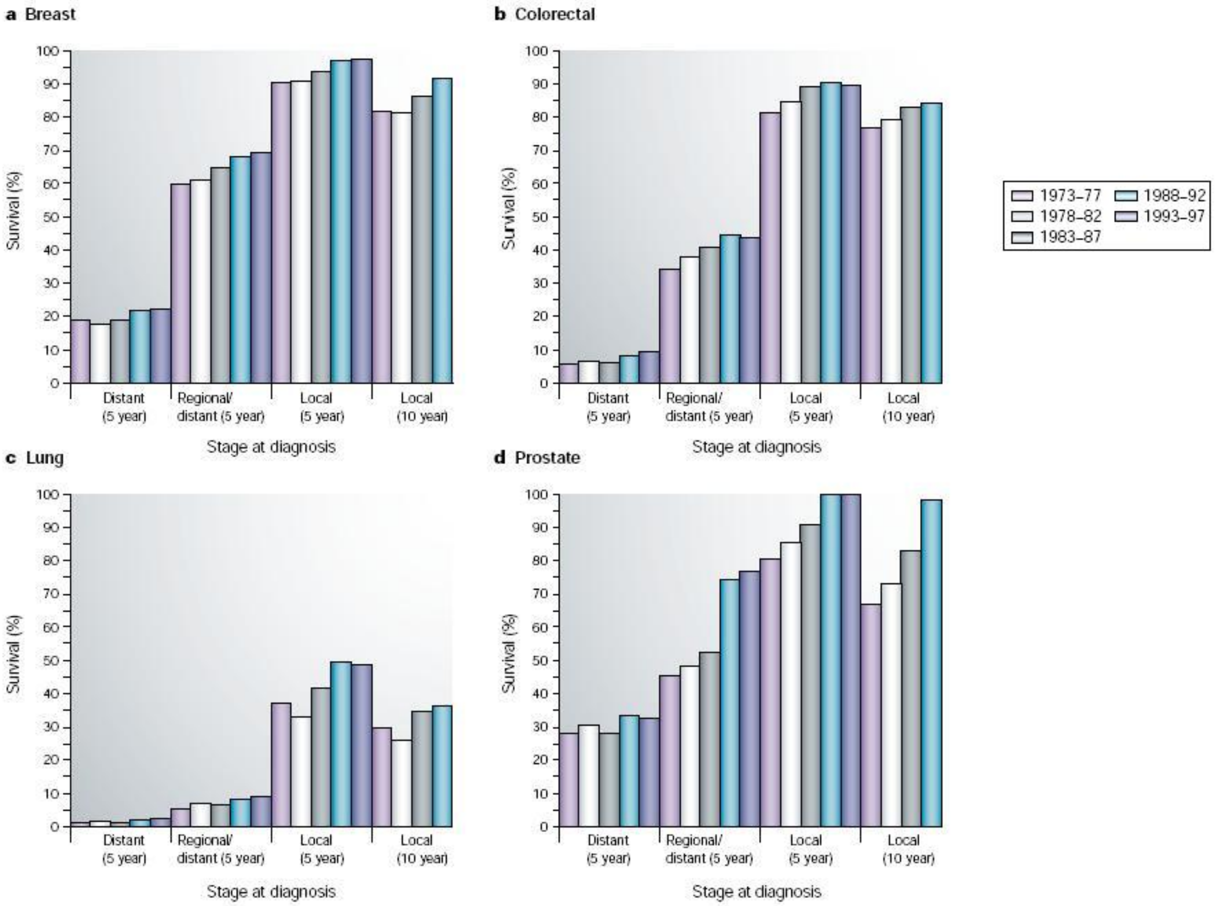

Figure 1.5. Relative survival (5 and 10 year) among selected cancers diagnosed with distant, regional or distant, or localized disease at the time of diagnosis [6].

general review of the cancer literature regarding the use of molecular markers quickly reveals that there is no known single marker sufficient for positive diagnosis of any cancer [9-11]. A sensing technology that identifies a multi-protein signature for diagnosis is most likely to minimize false positives and false negatives [9]. A sensor array incorporating high sensitivity and high specificity could have an impact at multiple levels including early detection screening, post-therapy monitoring, as well as on the proteomic discovery process.

The goal of this research is therefore to provide a tool for detecting multiple known targets in complex media at the earliest stages of neoplastic growth and proliferation. Prostate cancer represents an excellent test case as the early carcinogenesis and subsequent proliferation of this cancer are among the best understood in all of oncology. It is estimated that 91% of new cases of prostate cancer between 1995 and 2001 were diagnosed at local or regional stages of progression [5]. Not only does this indicate broad clinical understanding of prostate cancer, but it also indicates a wealth of tissue samples available for study at earlier stages of progression.

The most commonly used techniques in clinical laboratories for detecting specific proteins in very low concentration in complex media (such as blood or urine) are immunoassays. One of the most popular is the enzyme linked immunosorbent assay (ELISA) test. While there are many variants to the ELISA test, conventional ELISA's are considered to have a limit of detection on the order of ~ 1 ng/mL [12]. In its simplest form, conventional ELISA's involve significant preparation and then application of various reagents, each separated by washing steps, then processing with a microplate reader and final analysis. The entire procedure can take anywhere between several hours to a couple of days to perform. Overall, ELISA's are relatively expensive, time consuming and labor intensive processes requiring at least some training and a significant amount of practical experience to perform successfully. Desired improvements on ELISA capability would include label-free detection, near real-time response, greater sensitivity, and capacity for multiplexing. Emerging technologies such as optically-based biosensors [13] or marker-tagged nanoparticles [14] offer excellent alternatives for clinicians, but are currently expensive to produce.

At the outset of this research, the leading technology in label-free detection of protein interactions was surface plasmon resonance (SPR) based devices [15]. While many advancements have been made in the intervening years [13, 16, 17], including improved multiplexing capability, they still suffer from two significant limiting factors. The first is cost. SPR has gained broad use by clinical researchers of late, generating a significant commercial market for these sensors [16]. Significantly, however, the cost of a single SPR sensor is approximately $160 (Biacore's CM5 SPR sensor chip available through GE Healhcare), even in this more developed market. Note, this cost is simply for the transducer component of the overall sensor, and still requires both the monitoring electronic system and the application of appropriate capture agents. For multiple sensors used in a multiplexed system, the commensurate price rises rapidly. Furthermore, there is a limitation on how many channels can be introduced for multiplexed operation, based on the monitoring system being used. It is not feasible that these sensors could be utilized by the broader public for routine testing of multiple targets on a massive scale. The second limiting factor of the SPR system is that the sensitivity range is narrow and fixed by the precision of the detection mechanism.

The sensors I have proposed take advantage of advances made in the microelectronics industry allowing for fabrication of piezoelectric resonator-based sensors in an array package to provide multiplexed sensors at a much lower cost. A microelectronic mass-production facility could quite easily produce these sensor arrays and significantly take advantage of economies of scale and drive down the price as the market size increased. Another advantage of this approach comes from the fact that the detection limit of acoustic sensors is a function of their resonant frequency, which can be controlled by physical parameters of the resonator. As fabrication technology and capabilities continue to improve, the detection capabilities of these sensors should improve correspondingly.

The specific aims of this thesis research are therefore as follows:

1. To develop a bulk acoustic resonator device appropriate for application as a highly sensitive biosensor.
2. To develop an appropriate biosensor preparation procedure by immobilization of appropriate capture agents.
3. Demonstrate the functionality of these biosensors towards known cancer biomarkers.

CHAPTER 2

BACKGROUND & SIGNIFICANCE

To make clear what I am attempting to do, it is necessary to clearly explain the principles that I will be employing towards developing the proposed sensor and also describe how this work fits into the broader body of research regarding biosensor design and development. First, I will describe the principles of acoustic-based sensors, as opposed to electrochemical or optical transduction devices. As part of this discussion, I will include a discussion of how my work fits within the field of acoustic sensor device technology. Second, I will describe how acoustic wave devices can be employed toward biosensor applications and the potential advantages of using such a platform over alternative label-free detection methods. Finally, I will argue for importance of multiplexing and the development of a biomarker micro-array.

Principles of acoustic resonators

Acoustic wave resonators function by the excitation of the piezoelectric class of crystals due to an alternating electric field. That is to say, piezoelectric crystals have the capacity to launch and support a mechanical acoustic wave as the result of transducing energy from an excitatory RF electric field [18]. All crystals are classified into one of seven categories, based on their degrees of symmetry. The seven systems are in turn sub-divided into point groups, or classes, according to their symmetry with respect to a point. This yields thirty-two classes of crystal in total. Twenty-one of the thirty-two existing crystal classes exhibit a lack of centro-symmetry, or an inversion asymmetry. Of these twenty-one, all but one exhibit non-zero piezoelectric constants [19]. This piezoelectric crystal family of twenty is characterized by this inversion center, which form electrically neutral dipoles in their natural state. The crystal of interest for this research is zinc oxide (ZnO), which is a hexagonal *6mm* class crystal, and belongs to this piezoelectric family.

When an external stress is applied to a piezoelectric crystal, the symmetry is disturbed causing a charge asymmetry, resulting in an electric displacement across the material. This is the direct piezoelectric effect. The inverse piezoelectric effect, as the name implies, describes the strain of the material under an electric field due to the realignment of unit crystal dipoles in response to that field. Thus, an acoustic wave can be launched through the bulk of the material by exposing the crystals to an oscillating electric field. By matching the oscillation of the electric field to the physical parameters of the crystal that bounds the mechano-acoustic wave, a resonance condition is achieved in which the maximum amount of energy is being transduced into mechanical energy due to the favorable conditions.

The fundamental equations that describe the relationship between the electric dipole and external forces is described by the following constitutive relations:

$$\overline{T} = \overline{c} : \overline{S} - \overline{e} : \overline{E} \tag{2.1}$$

$$\overline{D} = \overline{\varepsilon} : \overline{E} + \overline{e} : \overline{S} \tag{2.2}$$

Note that equation (2.1) is an extension of Hooke's law in three dimensions, where T is stress, S is strain, c is the stiffness tensor. The second term in (2.1) represents the effect of piezoelectric stiffening under an electric field where E is the electric field and e is the piezoelectric coupling tensor. Equation (2.2) is Maxwell's definition for electric displacement, D, where ε is the permittivity tensor of the material and E is again the apparent electric field. Equation (2.2) is modified by the inverse piezoelectric strain component of the electric displacement formed by the product of the piezoelectric tensor, e, and the external strain, S. A more extensive treatment of the generation and propagation of acoustic waves in crystals can be found in Rosenbaum [20].

Propagation of an acoustic wave in a solid can take several forms, or modes. In general, these waves can be either longitudinal (particle displacement in parallel with the propagation direction), shear (particle displacement perpendicular to the wave propagation direction) or a combination of the two. For the purpose of developing a biosensor application, any resonator device used must employ an acoustic mode that exhibits particle displacement parallel to the surface of the device. This is necessary as any particle displacement not parallel to the surface would be readily absorbed by either the viscoelastic surface coating comprising the capture molecules necessary to functionalize the sensor, or by the liquid test media itself as compression waves.

Acoustic wave devices are broadly categorized by those that travel within the crystal bulk, known as bulk acoustic waves (BAW), or those that travel along the crystal surface, known as surface acoustic waves (SAW). This research will not investigate the shear-horizontal surface acoustic wave (SH-SAW) family of devices which have been applied in numerous studies towards sensing in a liquid phase environment [21-24]. The sensitivity of shear-mode resonator-based biosensors has been characterized by many, including Sauerbrey [25], Kanazawa [26, 27], and more recently Hunt [28], (and will be discussed in greater detail later in this chapter) but all agree that the sensitivity of these devices is proportional to a power of the fundamental resonant frequency, f_o.

The resonance frequency of a SAW device is controlled by a surface parameter of the electrode fabrication. SAW devices are created by depositing an electrode configuration called 'interdigitated trandsducers' (IDTs) onto the surface of an appropriately aligned polished crystal surface, as seen in Figure 2.1. The smaller the distance between "fingers" of the IDT exciting the surface acoustic wave, the higher the resonant frequency, as the transducer spacing defines the wavelength of the acoustic wave.

For bulk acoustic devices, the resonant frequency is a function of the thickness of the film. Piezoelectric crystal films can be deposited with extremely small thicknesses through a variety of liquid and vapor film deposition techniques [29]. In order to achieve ultra-high frequencies (e.g. GHz) of operation in a SAW device, extremely high resolution photolithography equipment is required, which is neither cheap nor widely

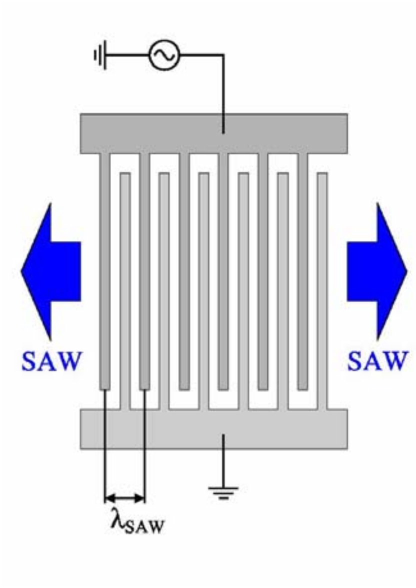

Figure 2.1. IDT electrode configuration commonly employed for fabrication of a SAW transducer. [Taken from www.sp.phy.cam.ac.uk]

available. For this reason, it is much simpler to achieve higher fundamental resonant frequencies in BAW devices than in SAW devices. For this reason, this research will focus on a BAW design.

Resonator Design

Piezoelectric ZnO thin films have most often been used in the past as high frequency filters for a multitude of telecommunications applications [30, 31]. Typically these devices are operated in the thickness-excited (TE) longitudinal mode in which the frequency can be tuned simply by varying the thickness of the ZnO thin film. Methods of excitation will be discussed in greater detail later in this chapter. When operated with an adjacent liquid medium, the longitudinal mode energy is dissipated, as described earlier, into the liquid as compression waves for devices utilizing waves that propagate at a velocity higher than the sound velocity in the liquid. This results in a highly reduced quality factor, *Q*, and poor mass resolution in a sensor application. *Q* is a common parameter used to characterize the strength of a resonator. Resonator *Q* is broadly defined as:

$$Q = \frac{2\pi \cdot \text{Energy Conserved per cycle}}{\text{Energy Dissipated per cycle}}$$

There exist many methods of estimating *Q*, which receives discussion by Rosenbaum [20]. As previously mentioned, acoustic waves can travel in a variety of modes. The thickness shear mode (TSM) is better suited for liquid sensing applications due to the shear particle displacement of the acoustic wave in the piezoelectric film. Since the adjacent liquid medium cannot effectively support a shear wave, very little energy is transferred into the liquid resulting in minimal damping of the acoustic wave.

The term ‘TSM resonator’ is often used interchangeably with quartz crystal microbalance (QCM). That is because the QCM is by far the most widely used resonator in commercial applications that operates in the TSM mode. QCMs are fabricated by taking thin slices at the appropriate angle from a single crystal bulk, as shown in Figure 2.2. Application of TSM resonators in biosensor applications are described in greater depth later in this chapter.

The sensitivity of acoustic waves in AT-cut quartz plates has been widely exploited with QCMs as gravimetric sensors in both vapor phase and in liquid phase sensing [32-35] which uses TE to excite the wave. It has been shown, however, that lateral field excitation (LFE) can also be used to excite the TSM wave in QCMs [36-39] and that the resulting device may be more sensitive to surface perturbations than the standard TE QCM for liquid-phase sensing applications [40-42]. The LFE configuration is demonstrated in Figure 2.3 below, in comparison to the TE configuration. The

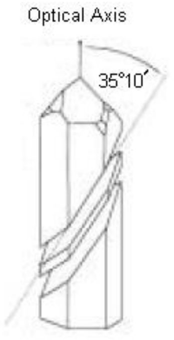

Figure 2.2. A quartz plate is cut at an angle of 35˚10' with respect to the optical axis to form AT-cut quartz suitable for QCM applications. A deviation of only 5' from this angle leads to a significant change in the temperature coefficient.[43]

advantages of LFE over TE liquid-phase applications are mainly attributed to the fact that in LFE, the electrodes that generate the electric field are not directly in the path of the acoustic wave, as in TE. Since the metal material that forms the electrode is a source of acoustic wave scattering and damping, its removal from the acoustic path results in higher *Q* values. Other advantages include increased stability at a given harmonic, and reduced aging of the crystal since the electrode is absent from the area of greatest vibrational motion [44]. For biosensor applications, removing the electrode from the acoustic path also means that biological molecules can be immobilized directly onto the region of highest particle displacement which should result in greater sensitivity of the sensor.

There are numerous disadvantages to using QCMs as biosensors, however. QCMs typically operate in the frequency range between 5-35 MHz. In AT-cut quartz plates, it is difficult to further increase the fundamental operating frequency because of its

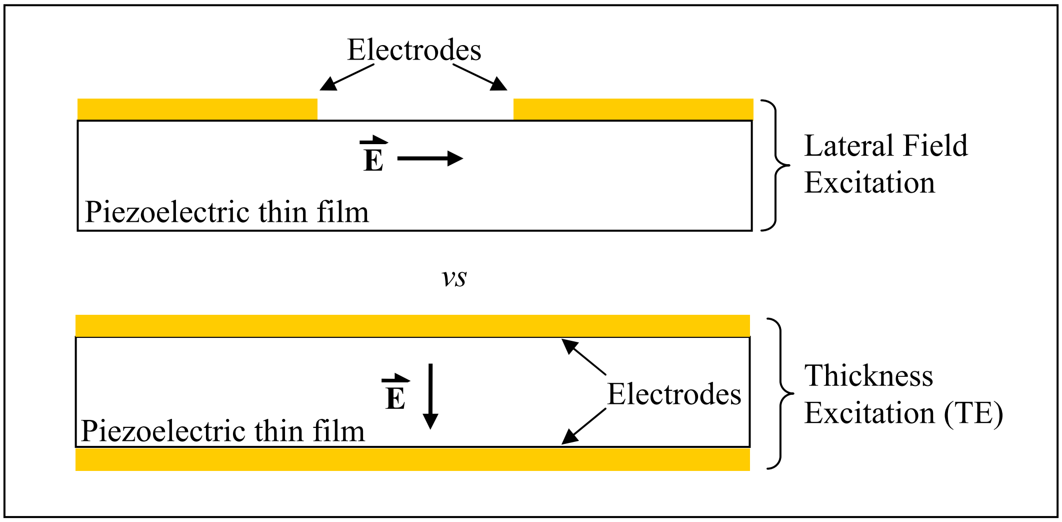

Figure 2.3. Lateral field excitation resonator configuration as compared with the more common thickness excitation configuration.

dependence on the thickness of the quartz plate. At very low thicknesses, the quartz plate becomes extremely fragile and is too difficult to handle. It is possible to achieve higher frequencies with the QCM by monitoring harmonic modes beyond the fundamental, but these become progressively diminished with increasing harmonic number [45, 46].

It is therefore necessary to develop a TSM resonator that can be easily fabricated in a robust design that can achieve higher frequencies of operation than the QCM. The first aim of this research is therefore to develop a thin film ZnO bulk resonator operating a TSM, which requires two fundamental criteria to be met. First is excitation of the TSM itself. One method of achieving this is LFE of *c*-axis oriented ZnO and involves an electrode configuration similar to the one seen in Figure 2.3. LFE of ZnO will be discussed in greater detail in Chapter 3. Second, a resonator requires that the acoustic wave be maintained in the crystal. A fundamental rule of mechanics is that acoustic energy has a preference to propagate through a denser media, with particles free to move and carry the wave. For that reason, it is often asserted that acoustic waves prefer to travel in media with a slower acoustic velocity. The acoustic velocity of a crystal film is described by

$$v_a = \sqrt{c_n / \rho_n} \tag{2.3}$$

where ρ_n is the film density and c_n is the appropriate stiffness parameter. A second fundamental rule is that high acoustic impedance mismatches between adjacent media encourage a high reflection response of an incident acoustic wave. Acoustic impedance can be described by [47]

$$Z_n = \sqrt{c_n \rho_n} \tag{2.4}$$

As air has very low stiffness and density compared to piezoelectric crystals, its affective acoustic impedance of zero. That is why a common technique for fabricating thin film bulk acoustic resonators (FBARs) requires the etching of an air barrier beneath the piezoelectric film. In this configuration, the vast majority of acoustic energy is reflected at each surface and remains within the piezoelectric crystal film.

This etching step is both difficult to achieve and requires an additional and expensive fabrication step. Furthermore, the films of ZnO necessary to produce the very high frequencies desirable for higher orders of sensitivity would cause these devices to be extremely delicate. The solution to this problem is to deposit the piezoelectric film onto a solid structure that mimics the acoustic impedance of air, which is referred to as a solidly mounted resonator (SMR). Newell first described the concept of SMRs in 1965 [48], in which an acoustic mirror (analogous to an optical Bragg reflector) is deposited beneath the piezoelectric crystal film, as shown in Figure 2.4. I employ this configuration in order to develop a design that is both robust and easy to fabricate.

Excitation of shear mode bulk waves in thin film ZnO have been reported as early as 1974 [49]. More recent success has been reported by Krishnaswamy, *et al.*, who attempted the growth of inclined *c*-axis oriented films coupled with an electrode pattern in which the electrodes are situated on opposing surfaces of the thin film to produce an electric field through the thickness [50]. The incline of the ZnO axis would thereby allow for excitation of the crystal orthogonal to the *c*-axis and stimulate a shear mode acoustic

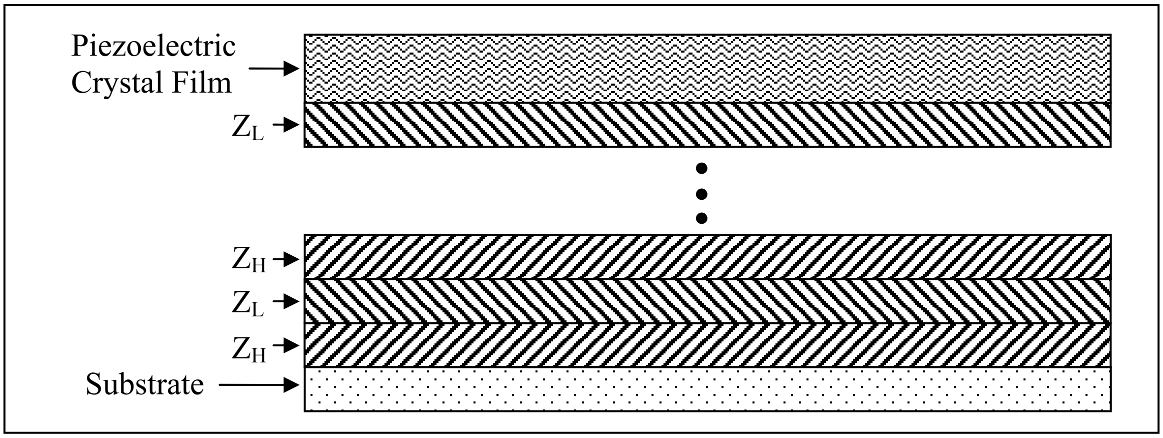

Figure 2.4. The solidly mounted resonator configuration (SMR) consisting of alternating layers of ¼-λ low and high acoustic impedance films.

wave. Wang and Lakin took a similar approach and had excellent success in fabricating oriented films with the *c*-axis of the hexagonal crystal oriented 40° to the substrate normal [51]. While their resonator quality factor, Q, and electro-mechanical coupling, K^2, were high, the operating frequency attempted was low (~293 MHz) and the fabrication procedure required bulk etching of the Si wafer to produce air-backed ZnO membrane resonators. More recently, Link *et al.* have revived the inclined ZnO growth research with the intent of developing ZnO TSM resonators for liquid phase sensing [52, 53]. Their device design is demonstrated in Figure 2.5. A shortcoming of the inclined ZnO growth method, in general, is that the thickness excitation requires that the electrodes be in the path of the acoustic wave. While it offers the benefit of a higher operating frequency than the QCM for sensing, it still suffers from the same pitfalls as the QCM because the electrodes are located in the area of highest sensitivity.

In a study by Woo Wai *et al.* focusing on non-inclined *c*-axis oriented ZnO, the TSM was excited through LFE [54]. The devices were fabricated through the use of a self-

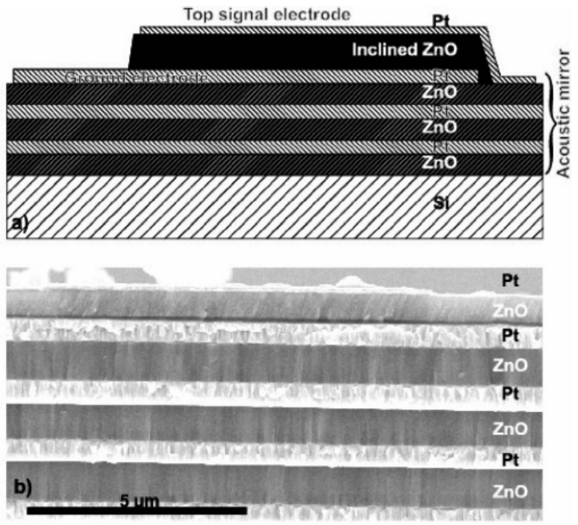

Figure 2.5. a) Schematic cross section and b) scanning electron microscopy of solidly mounted resonators. The upper ZnO film is *c*-axis inclined [53].

aligning process that involved ZnO liftoff and a spiral electrode structure spanning 2 mm in diameter. Operating close to 4.1 GHz, the devices illustrated the ability for ZnO FBARs to be operated at high frequencies with relative ease. An acoustic mirror was not implemented in the design, however, and the resonator Q was very low (roughly 35).

Acoustic velocity calculations made from the numbers given in the study yield ~3,280 m/s. Given that the acoustic velocity, v_a, of a resonator is defined by Equation (2.3), a theoretical estimation of ~2,841 m/s is calculated using single-crystal bulk stiffness properties of ZnO available in Auld [55]. This value is reasonable considering the polycrystalline variations in depositions of thin film ZnO.

Acoustic Biosensors

Acoustic resonators were first recognized as an appropriate platform for highly sensitive sensors in the 1950's. The mechanism for detection relies on the stable resonance of an acoustic wave in a fixed space. The physics of an acoustic wave propagating through a crystal, oscillating between opposing boundaries, is well understood and has been thoroughly characterized by Auld [55]. For sensor applications of acoustic resonators, the acoustic wave acts as a probe that indirectly queries the surfaces for changes in the boundary conditions. Perturbations of those boundary conditions results in a measurable frequency shift.

Sauerbrey was the first to observe that the resonance condition of a piezoelectric resonator was impacted by the loading of one surface. He worked to characterize the sensitivity of acoustic sensors using the QCM as part of his dissertation research in the late 1950's. One publication in particular is often cited in the literature in regard to acoustic sensors, in which Sauerbrey observes that the resonant frequency of the QCM shifts in accordance with the following [25]:

$$\Delta f = \frac{-2 f_o^2 \Delta m}{A\sqrt{\rho_q \mu_q}} \tag{2.5}$$

where f_o is the unloaded resonant frequency of the sensor, A is the acoustically active surface area, ρ_q is the crystal density, μ_q is the crystal stiffness, and m is the mass loading at the surface of the crystal. As can be seen from Equation (2.5), the shift in resonant frequency of the sensor is proportional to the change in mass at the surface boundary via a coefficient scaled by the square of the unloaded resonance frequency. The higher f_o, the more sensitive the resonator is to a corresponding mass loading at the surface.

The derivation of this equation requires assumptions that are not valid, however, for operation in a liquid environment or for loading of biological materials at the surface. One assumption, for example, is that the loaded mass must be a rigid film. As noted earlier, the acoustic waves have a propensity to travel in materials of higher acoustic impedance. For the case of a liquid film, there exists a decay length in which the shear acoustic wave propagates into the liquid film. This decay length, δ, is defined as

$$\delta = \sqrt{2\eta_L / \omega\rho_L} \tag{2.6}$$

where η_L is the viscosity of the liquid, and ρ_L the liquid density. For the case of a 5 MHz QCM resonator, the acoustic wave would travel 250 nm into water.

Kanazawa and Gordon were the first to address an appropriate description for acoustic resonators operating in a liquid, deriving the following relationship [26]:

$$\Delta f = -f_o^{3/2} \sqrt{\frac{\eta_L \rho_L}{\pi \rho_q \mu_q}} . \tag{2.7}$$

William Hunt, alternatively, approaches the entire relationship afresh, seeking “to go beyond the static Sauerbrey equation to a more dynamic equation” to more precisely define the change in boundary conditions as a description of the molecular recognition event [28]. Beginning with the complex reciprocity relation described by Auld [55], Hunt employs time-dependent perturbation theory to derive the following relation for frequency shifts experienced by the QCM in a biosensor application:

$$t\frac{\partial \Delta\omega}{\partial t} + \Delta\omega = \frac{\omega_u h_f}{\pi\sqrt{\rho_q \mu_q}}\left\{-\omega_u\left[\Delta\rho - \frac{\Delta\mu}{V_S^2}\right] + i\cdot\left[\frac{\Delta\rho}{\partial t} - \frac{1}{V_S^2}\cdot\frac{\Delta\mu}{\partial t}\right]\right\} \tag{2.8}$$

where ω_u is the unperturbed frequency (in radians), t is time, h_f is the height of the film, and V_S represents the acoustic shear wave velocity. If $\Delta\rho$ and $\Delta\mu$ were known, it would then be possible to solve (2.8) using the integrating factor method, which would yield:

$$\Delta\omega = \frac{1}{t}\left(\int^{t}\frac{\omega_u h_f}{\pi\sqrt{\rho_q \mu_q}}\left\{-\omega_u\left[\Delta\rho(\tau) - \frac{\Delta\mu(\tau)}{V_S^2}\right]\right\}d\tau + i\cdot\left[\Delta\rho(t) - \frac{\Delta\mu(t)}{V_S^2}\right] + C\right) \tag{2.9}$$

It must be noted that Hunt assumes a stress-free boundary in which no acoustic energy transfers into the adjacent liquid/air space beyond the biofilm. That is to say, $T\cdot\hat{n} = 0$. He acknowledges that this is not accurate, of course, but the assumption is required to simplify the derivation. Proceeding with this assumption and assuming that ω, ρ and μ do not vary with time, Equation (2.8) becomes

$$\Delta f = \frac{-2f_o^2 h_f}{\sqrt{\rho_q \mu_q}}\left[\Delta\rho - \frac{\Delta\mu}{V_S^2}\right]. \tag{2.10}$$

Note that Equation (2.10) has a striking similarity to the Sauerbrey Equation (2.5) with the exception that the frequency shift is now a function of both a change of mass loading at the surface as well as a change in the mechanical stiffness of the film. This has significance when the film consists of biological molecules that are known to undergo a conformational change upon binding a target. This provides both the opportunity that TSM resonators could have an enhanced detection capability and the cautionary note towards interpreting the meaning of collected data.

The work of Sauerbrey established the potential for acoustic wave devices as a viable sensor platform. QCMs became widely used because they demonstrated exceptional conservation of energy as a resonator, characterized by Q values of up to 70,000 and excellent frequency stability between 0-50˚C [47]. Breakthroughs in oscillator technology allowed Nomura and Okuhara in 1982 to demonstrate that these sensors could be employed in a bioanalytic capacity by operating them in liquids [56]. Since then, they have been employed quite extensively as biosensors [47], with several commercial QCM systems available today [45]. As mentioned earlier, QCMs are limited by the fact that films thin enough to reach the GHz range of operation are far too fragile to handle if cut from a single-crystal bulk and cannot be deposited onto a support substrate with the crystal texture required.

Sensor Arrays

As mentioned earlier, it is generally agreed that there is little chance that a single biomarker will be able to provide definitive evidence of cancer proliferation [57]. One of the most successful and widely used marker screening tests involves the diagnosis of prostate cancer (PCa) by measuring the serum concentration of prostate specific antigen (PSA) in conjunction with a digital rectal exam. There exists significant controversy over the use of PSA testing as a means of diagnosing PCa, predominantly due to the high false positive rate [58-62]. Extensive long-term studies (including such studies as the Prostate, Lung, Colorectal and Ovarian Screening Trial ff to be completed in 2015) begun in the 1990s have yet to provide conclusive evidence of the efficacy of the PSA screening test for those under 75. For individuals over 75, however, the US Preventive Services Task Force has already issued a recommendation against the regular practice of PSA screening. Given the average lifespan of males and taking into consideration the generally slow progression rate of PCa, this recommendation was made because the cancer itself tends to not have a significant impact on these individuals overall survival or quality of life. Taken together with high false positive rate of the PSA test itself, the negative psychological impacts of a positive diagnosis, and the trauma associated with available treatments, the negative impacts are considered to outweigh the benefits of screening [63]. This recommendation has understandably been met with some contention from clinicians, and as a result is likely to be considered as a suggestion rather than as a rule, by most. Obviously, a more definitive screening mechanism is required in general, that will allow for the quantification of multiple molecular targets.

It is further desirable to minimize false negatives and false positives. Sensor arrays allow for implementing redundancy in the system by preparing multiple sensors in the same array for the same target and thereby delivering enough data to employ statistical analysis of the results. For this reason, sensor arrays that can test for multiple targets simultaneously offer the most useful tool for an early detection system for cancer. A cursory search of the literature quickly reveals that many researchers are already pursuing sensor array systems rather than single sensor systems [31, 48, 55-63]. These array systems often include, however, delicate designs that are difficult and expensive to fabricate.

A recognition of the importance of this approach is exemplified by one of the primary initiatives of the NCI's Early Detection Cancer Network (EDRN), whose mission is "to make molecular diagnostics a reality [allowing for] individualized treatment for cancer patients." The initiative of interest is the identification of proteomic technologies that allow for rapid identification of cancer proliferation *signatures*. That is to say, the proliferation of a particular cancer is revealed by the quantification of multiple targets in a patient's sample. Their efforts have converged upon various protein and nucleic acid microarray technologies that allow for rapid screening and subsequent validation of new circulating biomarkers. Some of the technologies highlighted in their latest annual report include the LUMINEX Corporation's xMAP system and the nucleic acid programmable protein array (NAPPA) system from Harvard Medical School [64].

Acoustic biosensor research in the past has largely focused on the application of QCM devices [65, 66]. As is the case for most biosensors, these sensors are comprised of two fundamental components (described in Figure 1.1). The first being the base transducer device, or resonator, that excites and maintains a resonating acoustic wave in the piezoelectric crystal. The second component is the immobilization of appropriate capture agents at the surface of the crystal, thereby functionalizing the resonator as a biosensor. When a target molecules from the test medium interact or bind with the capture molecules, the boundary conditions are altered which in turn changes the resonance conditions for the acoustic wave. This is measured as a resonant frequency shift.

Theoretically, the sensitivity of an acoustic biosensor is directly related to the value of that resonant frequency, as discussed previously in this chapter. While QCM technology offers excellent detection capabilities, it is limited in several ways with respect to biosensor applications. The most significant limitations include the relatively low frequency of operation, as mentioned in Chapter 2, but also the relative difficulty in multiplexing the sensors due to their large size. Cost is also a drawback to QCM technology as the sensors are comprised of quartz plates which can be expensive to manufacture to the required specifications. SAW devices have provided several advantages in addressing many of the aforementioned criteria [65, 66], but mass fabrication tools still limit commercially available SAW devices to the sub-gigahertz (GHz) range of operation.

This research proposes an acoustic-based solution that meets all of the requirements proposed by Erickson, *et al* [57]. In summary, those requirements include sensitivity and specificity, multiplexing capability, and a reduction in measurement complexity and cost. The simple design is compatible with existing microelectronic fabrication processes that allow for cost-effective mass production, and has a very small footprint (< 5 mm^2). As mentioned earlier, with moderate spatial arrangement, one could easily fit as many as 1,000 arrays, each consisting of eight devices, onto a single 3-inch wafer. The design will also allow for expandable array configurations. The sensing mechanism involved is entirely electronic and occurs as the capture molecules bind their target. The sensors thereby provide a means of label-free, near real-time reporting with minimal electronic hardware.

CHAPTER 3

RESONATOR DESIGN & IMPLEMENTATION

The development of a novel microelectronic resonator requires two fundamental problems be solved. Primary is the identification of an appropriate material with the proper crystal orientation that will support the acoustic mode of interest. As identified in the previous chapter, the TSM is the mode of interest for the purpose of biosensor application. Further, a robust and low-cost design is desired, which will be achieved by pursuing a solidly mounted ZnO resonator configuration. This encompasses the second problem, which is the development of an appropriate acoustic mirror to reflect the acoustic energy back into the piezoelectric crystal. I will begin this chapter with a theoretical confirmation that *c*-axis oriented ZnO can support the desired TSM wave. I will then discuss the chosen resonator package design and derive a theoretical model for the desired acoustic mirror and subsequent implementation of the solidly mounted TSM thin film ZnO resonator. Finally, I will discuss efforts to improve the device design for the purpose of biosensor applications.

Thickness Shear Mode in ZnO

Propagation of an acoustic wave via piezoelectric excitation in a crystal bulk is described by the Christoffel equation:

$$k^2 \Gamma_{ij} v_j = \rho \omega^2 v_i \tag{3.1}$$

where k is the wave number defined as ω / v_a (or frequency/acoustic velocity), ρ is the density of the material, v_i and v_j are the particle polarization direction vectors, and Γ_{ij} is the piezoelectrically stiffened Christoffel matrix. Γ_{ij} is defined as,

$$\Gamma_{ij} = l_{iK}\left(c_{KL}^{E} + \frac{\left(e_{Kj}E_j\right)\left(E_i e_{iL}\right)}{E_i \varepsilon_{ij}^{S} E_j} \right) l_{Lj} \tag{3.2}$$

where E_n is the three dimensional electric field vector and the l_{iK} matrix describes the divergence of the acoustic wave propagation, taking the following form:

$$l_{iK} = \begin{bmatrix} l_x & 0 & 0 & 0 & l_z & l_y \\ 0 & l_y & 0 & l_z & 0 & l_x \\ 0 & 0 & l_z & l_y & l_x & 0 \end{bmatrix} . \tag{3.3}$$

In (3.3), the nonzero terms come from the propagation vector

$$\hat{\mathbf{l}} = l_x\hat{\mathbf{i}} + l_y\hat{\mathbf{j}} + l_z\hat{\mathbf{k}} . \tag{3.4}$$

The l_{Lj} matrix is simply the transpose of l_{iK}, and c_{KL}^{E} is the material stiffness tensor at a constant electric field rotated by the appropriate Euler angles. As mentioned above, the crystal orientation was confirmed by XRD to be a highly *c*-axis aligned *6mm* hexagonal ZnO crystal, so no Euler angle rotations need be applied. Further assuming wave propagation in the direction of the thickness of the film and also aligned with the substrate surface normal, the terms l_x and l_y go to zero and l_z can be assumed to be unity.

In order to generate a TSM wave in normally aligned *c*-axis oriented ZnO, it is necessary to use LFE of the ZnO bulk. As demonstrated in Figure 2.3, LFE involves co-planar electrodes generating an electric field parallel to the film surface, or laterally.

Given that the electric field has been maximized in the *x-y* plane, it can be assumed that E_z goes to zero (i.e. the electric field in the *z* direction) and the electric field parameters can be described as $E_x^2 + E_y^2 = 1$.

The standard stiffness tensor for the *6mm* class of hexagonal crystals is defined as

$$c = \begin{bmatrix} c_{11} & c_{12} & c_{13} & 0 & 0 & 0 \\ c_{12} & c_{11} & c_{13} & 0 & 0 & 0 \\ c_{13} & c_{13} & c_{33} & 0 & 0 & 0 \\ 0 & 0 & 0 & c_{44} & 0 & 0 \\ 0 & 0 & 0 & 0 & c_{44} & 0 \\ 0 & 0 & 0 & 0 & 0 & c_{66} \end{bmatrix} \qquad (3.5)$$

where the subscripts exhibit the abbreviated Einstein summation notation [20] that allows the true 9 x 9 stiffness tensor to be reduced via symmetry to the 6 x 6 in (3.5). The corresponding piezoelectric coupling tensor takes the form

$$e = \begin{bmatrix} 0 & 0 & 0 & 0 & e_{15} & 0 \\ 0 & 0 & 0 & e_{15} & 0 & 0 \\ e_{31} & e_{31} & e_{33} & 0 & 0 & 0 \end{bmatrix}. \qquad (3.6)$$

By defining the electric field *E* as

$$E_j = \begin{bmatrix} E_x \\ E_y \\ 0 \end{bmatrix} = E_i^T , \qquad (3.7)$$

it is now possible to solve for (3.2) symbolically, yielding the following solution to the Christoffel matrix:

$$\Gamma_{ij} = \begin{bmatrix} c_{44} + \frac{e_{15}E_x^2}{\varepsilon_{11}} & \frac{e_{15}^2 E_x E_y}{\varepsilon_{11}} & 0 \\ \frac{e_{15}^2 E_x E_y}{\varepsilon_{11}} & c_{44} + \frac{e_{15}E_y^2}{\varepsilon_{11}} & 0 \\ 0 & 0 & c_{33} \end{bmatrix}. \tag{3.8}$$

Substituting (3.8) into (3.1), we find that the Christoffel equation is a simple eigenvalue problem, where the corresponding eigenvalues and respective eigenvectors solutions are

$$x_1 = \begin{bmatrix} -E_y \\ E_x \\ 0 \end{bmatrix}, \lambda_1 = c_{44} \ , \ x_2 = \begin{bmatrix} E_x \\ E_y \\ 0 \end{bmatrix}, \lambda_2 = c_{44} + \frac{e_{15}^2}{\varepsilon_{11}} \ , \ x_3 = \begin{bmatrix} 0 \\ 0 \\ 0 \end{bmatrix}, \lambda_3 = c_{33} \ . \tag{3.9}$$

Each of the three eigenvectors, x_n, describes the particle displacement associated with an acoustic wave mode. The associated eigenvalues describe that mode's acoustic velocity, v_a, and direction. As can be seen, the only term that exhibits piezoelectric stiffening is the x_2 term, which indicates particle direction only in the *x-y* plane. The associated eigenvector, λ_2, describes shear wave propagation due to piezoelectric transduction in the *z*-direction through the c_{44} term. The acoustic velocity of this wave can thus be described by

$$v_a = \sqrt{\frac{c_{44} + \frac{e_{15}^2}{\varepsilon_{11}}}{\rho}} \ . \tag{3.10}$$

ZnO single-crystal bulk values taken from Auld [55] can be used for the terms in (3.10) in order to determine a theoretical velocity. This yields a shear wave velocity traveling in the thickness direction of 2,841 m/s in hexagonal *6mm* ZnO. It is important to stress that this value is ideal based on bulk single crystal values. Most ZnO thin films, including the films used for this research, are both polycrystalline and involve dopants that mitigate the conductive properties of pure ZnO. For these reasons, it is reasonable to assume that shear values will vary from the ideal velocity calculated above. Indeed, other investigators that have demonstrated TSM ZnO resonators have empirically determined values of 3,280 m/s [19], and 3,370 m/s [54]. It is worth noting that applying the appropriate stiffness values from Auld, a longitudinal wave traveling in the thickness direction should travel at 6,100 m/s, by comparison. This has been verified by numerous implementations of longitudinal wave FBAR devices [67-69], as well as those achieved in the very same lab in which this thesis research was accomplished [70, 71].

Thus I have demonstrated that the TSM is possible in *c*-axis oriented ZnO. It remains, therefore, to determine a device design that allows for growth of *c*-axis oriented ZnO films in a configuration that is both a robust and low cost implementation.

Solidly Mounted Resonator

Traditionally, FBARs are fabricated by etching the support layer upon which the piezoelectric film was deposited in order to create an air boundary on both the top and bottom of the piezoelectric film. Recall from Chapter 2 that acoustic energy prefers to travel in a medium where it travels slower, which is characterized by the mode acoustic velocity. More critical, however, is the magnitude of the impedance mismatch regarding the medium on either side of a boundary. As for electromagnetic waves, if the perceived acoustic impedance across a boundary is matched, the wave would pass through the boundary with practically no reflection. If a substantial impedance difference is perceived, however, then a substantial amount of the acoustic energy would be reflected. Theoretical estimation of the characteristic acoustic impedance of a material, Z_a, is often determined using the relation described in Equation (2.4). Using bulk properties for ZnO given by Auld [55], one can estimate the shear mode acoustic impedance of ZnO to be 15.53 kg/m^{2}s. Given the extremely low density and stiffness properties of air, one can reasonably assume that air has an effective acoustic impedance of zero. As described in Chapter 2, this low impedance boundary is necessary for containing the acoustic energy within the piezoelectric film. As I also explained in Chapter 2, the etching process required to accomplish this configuration is both often difficult to achieve (especially when ZnO is the piezoelectric film of interest) and does not accommodate the goal of producing a simple and cheap fabrication process.

For this reason, a solidly mounted resonator (SMR) configuration was chosen, as described in Figure 3.1. The SMR configuration was introduced by Newell [48], in which he describes the fabrication of an acoustic mirror below the piezoelectric film. The theory behind this configuration is similar to that of a Bragg reflector for reflecting optical waves, in which alternating materials of high and low impedance at ¼-wavelength thickness can mimic a zero acoustic impedance boundary at the piezoelectric layer.

The theory has been modeled by several using transmission line theory [72-74]. Ballato presents a networked transmission line model for piezoelectric acoustic wave excitation and propagation employing networked electromagnetic models of electro-elastic activity as perfect analogs of mechano-acoustic activity, both within the bulk at any point and also at the boundaries. According to Ballato, appropriate analogs from the electrical input impedance of multiple transmission lines in series (representing multiple material films adjacently layered on top of each other) are identical to the effective acoustic impedance of the overall structure and substrate. Ballato's electric circuit model is actually designed to model the coupling of electrical inputs to mechanical wave propagation through a piezoelectric bulk via transformers, but is entirely appropriate for modeling the propagation of mechanical waves in the non-piezoelectric films that make up the acoustic mirror. This model can be represented as the one shown in Figure 3.1.b. Ballato's model will be revisited later when discussing the resonator design.

From transmission line theory, we know that the characteristic electrical input impedance, Z_{in}, at a junction is given by [75]

$$Z_{in} = Z_o \left(\frac{Z_L + jZ_o \tan(kl)}{Z_o - jZ_L \tan(kl)} \right) \tag{3.11}$$

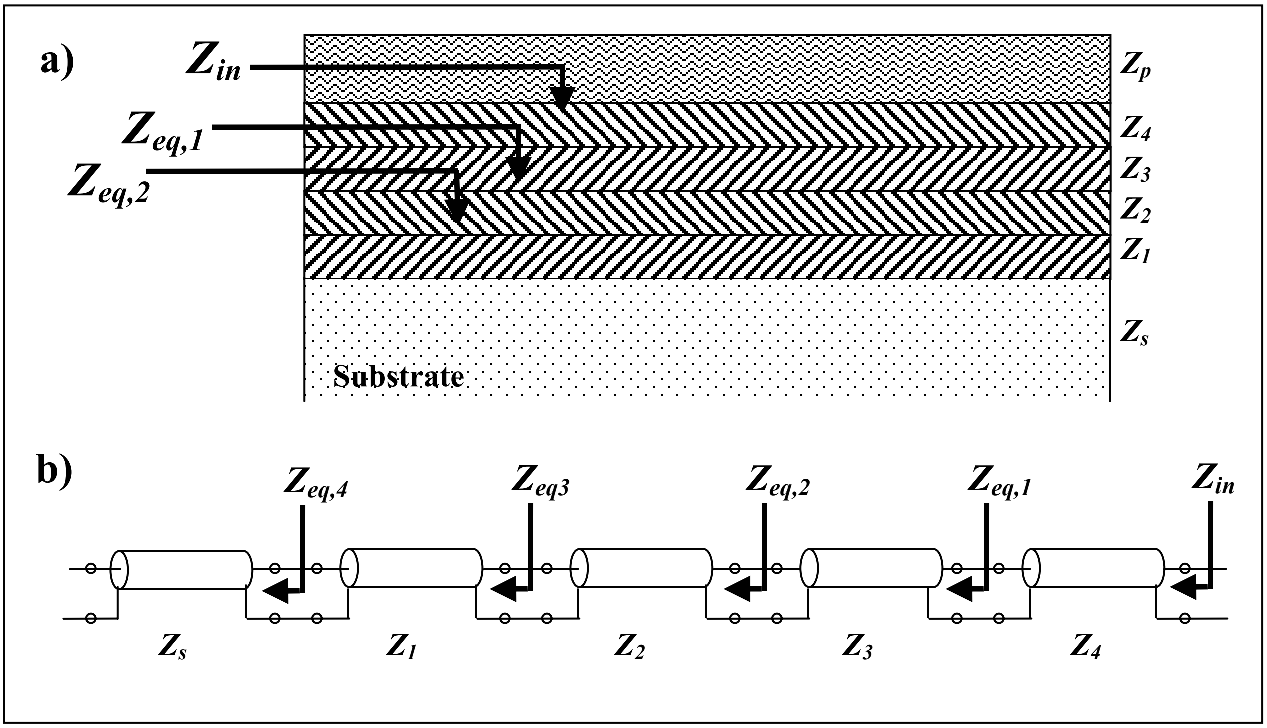

Figure 3.1. Schematic of a) the SMR configuration and b) the transmission line representation.

where k is the wave number, l is the length of the transmission line, Z_o is its characteristic impedance of the incident material, and Z_L is the apparent load impedance of the material beyond the boundary. In order to calculate the apparent acoustic impedance seen at the bottom boundary of the piezoelectric layer, shown in Figure 3.1 as Z_{in}, Equation (3.11) can be rewritten to estimate the effective impedance of the acoustic mirror and substrate as follows [76]

$$Z_{in} = Z_4\left(\frac{Z_{eq,1} + jZ_4\tan(kd)}{Z_4 + jZ_{eq,1}\tan(kd)}\right) \tag{3.12}$$

where d is the film thickness, Z_4 is the acoustic impedance of layer 4 and $Z_{eq,1}$ is calculated by

$$Z_{eq,1} = Z_3\left(\frac{Z_{eq,2} + jZ_3\tan(kd)}{Z_3 - jZ_{eq,2}\tan(kd)}\right). \tag{3.13}$$

This recursion is continued until all layers have been defined through to the substrate. This calculation is easily accomplished through the MATLAB script I created, which is presented in Appendix A.

Having implemented a script to model the mirror response, it was therefore easy to consider multiple material options for the mirror layers. Recall from Chapter 2 that alternating materials of high and low acoustic impedance yield a stronger reflection response. With that in mind, the materials considered are enlisted in Table 3.1, in which the acoustic impedances and shear velocities were calculated using Equations (2.3) and (2.4), respectively, and bulk values from Auld [55]. Note that the shear velocity is obviously required to determine the ¼-wavelength film thickness.

Material	**Vertical Shear Stiffness, c_{44} (10^{10} N/m^2)**	**Density (kg/m^3)**	**Velocity (m/s)**	**Impedance (kg/m^{2}s)**
ZnO	4.247	5680	2841	15.53×10^6
Fused SiO_2	3.12	2200	5132	11.3×10^6
Ta_2O_5*	5.69	8200	2634	21.6×10^6
$LiTaO_3$	9.4	7450	3552	26.5×10^6
Al_2O_3	14.5	3986	6031	24.0×10^6
W	15.2	19200	2814	54.0×10^6
Si	7.956	2332	5841	13.62×10^6

Table 3.1. Material options for use in the acoustic mirror. *Material properties for Ta_2O_5 were obtained from [77].

It is desirable to choose the material immediately adjacent to the piezoelectric ZnO to have a lower acoustic impedance, rather than a high one, as explained by Lakin, *et al* [31]. Multiple mirror pairings were considered and modeled using a center frequency of 2.0 GHz and 6 layers of alternating mirror materials, with the results demonstrated in Figure 3.2. As expected, the material pairing exhibiting the strongest degree of impedance mismatching demonstrated the most significant mirror response, though the responses shown in Figure 3.2 suggest that most of these mirror configurations should respond adequately when 6 layers are implemented.

Since Ta_2O_5 was on hand and demonstrated efficacy for previous designs for longitudinal devices [76], it was thought that this would work sufficiently for ZnO TSM devices. As is true for reflector gratings for SAW devices, the greater the number of gratings, the more efficient the reflector. Simulations were executed for various numbers of layers for alternating ¼-wavelength layers of fused silica (SiO_2) and Ta_2O_5. As can be

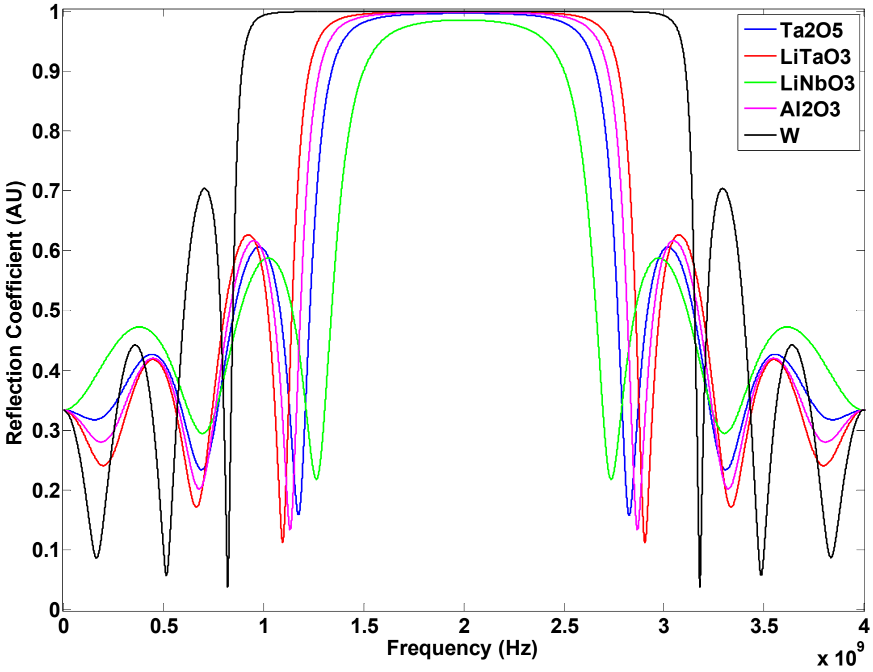

Figure 3.2. Modeled mirror reflection response from 0 to 4 GHz for multiple 6-layer mirror configurations.

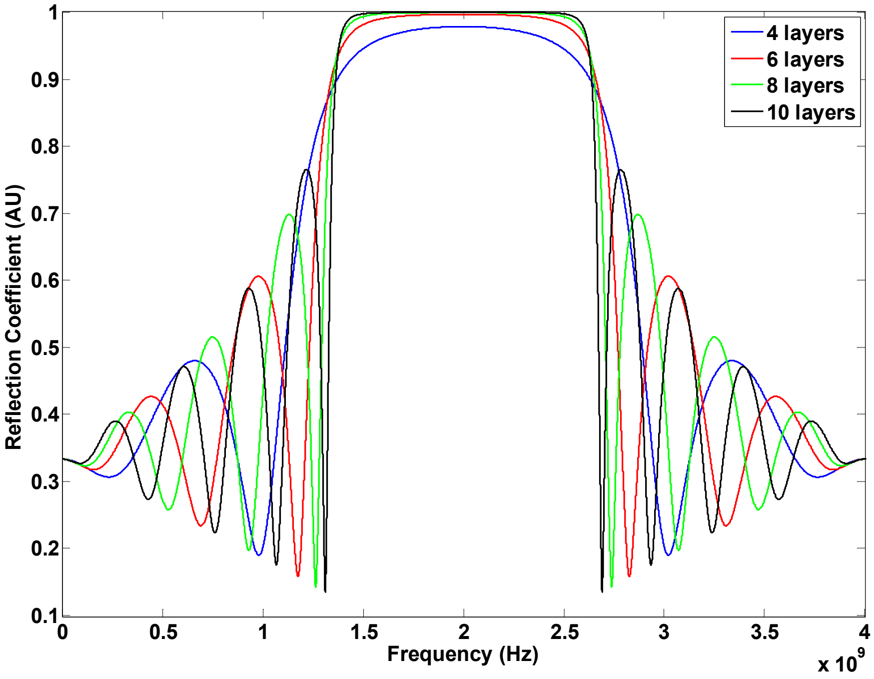

Figure 3.3. Modeled response of acoustic mirror using Ta_2O_5 and fused silica with 4, 6, 8 and 10 alternating layers at 1/4 wavelength thickness.

seen in Figure 3.3, significant improvement is demonstrated from 4 layers to 6 layers, with only slight improvement in efficiency from 6 layers to 8 layers (and practically no benefit extending to 10 layers). An important result of these simulations is broadband response of these mirror simulations. The reason this is advantageous is due to a significant shortcoming of RF sputtering thin films onto a substrate, which is the tendency for significant variation in film thickness. The parallel resonance frequency of a TSM BAW resonator is determined by

$$f_p = \frac{v_a}{2 \cdot d} \tag{3.14}$$

where d is the film thickness and v_a is the acoustic velocity. Significant variation in the film thickness will cause a commensurate variation in resonance frequency. The Unifilm PVD-300 sputtering system uses a patented deposition process that allows it to achieve 99.7% thickness uniformity across a three inch wafer. Even with this quality, a variation of 1% for a device intended to operate at 2 GHz would result in ± 215 MHz across the wafer. Therefore the broadband response of the mirror is desirable as it would accommodate these variations.

Simulations were also implemented with an odd number of mirror layers. The results of these simulations are shown in Figure 3.4. As can be seen, a notch feature appears at the center frequency where the desired resonance activity should be. This is expected due to the alternating nature of the low to high impedance clamped boundary versus the high to low impedance free boundary of the mirror [31]. Therefore odd layer implementations were not attempted.

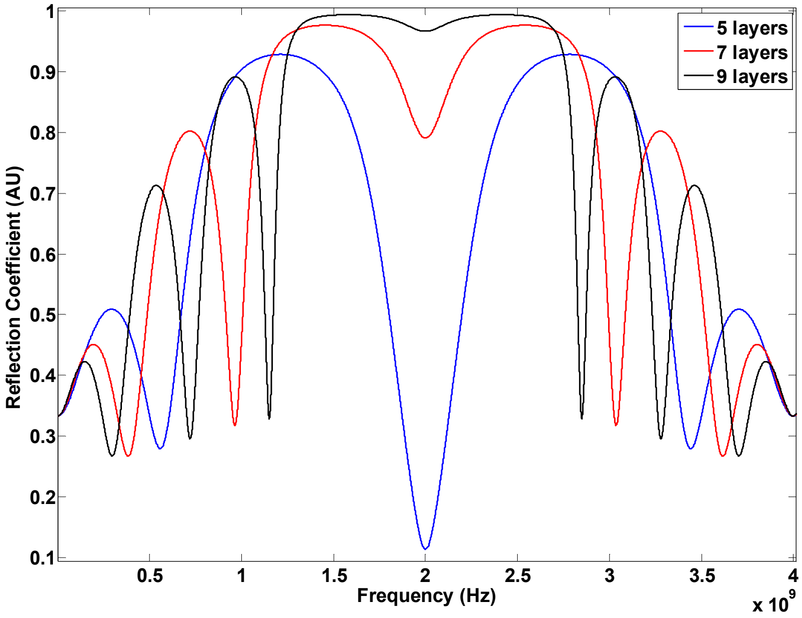

Figure 3.4. Modeled response of acoustic mirror using Ta_2O_5 and fused silica with 5, 7 and 9 alternating layers at ¼-wavelength thickness.

Deposition of *c*-Axis Oriented Thin Film ZnO

It is well known that ZnO can be deposited as a thin film through various methods, including chemical vapor deposition (CVD) [78, 79], metal-organic CVD [80-82], molecular beam epitaxy [83-85], electron beam (E-beam) evaporation [86], pulsed laser ablation [87], and the sol-gel method [88] to name but a few. Highly *c*-axis oriented films are consistently deposited, however, by means of RF magnetron sputtering [89-93]. RF magnetron sputtering involves the bombardment and energetic release of atoms, or sputtering, of a target material by an ion plasma beam. Magnetron sputtering is generally desired for slower deposition at lower vacuum levels which yields relatively well ordered crystal films with high uniformity. This method will be employed in this research for this reason and because of the compatibility of the method with existing low-cost commercial fabrication. The *c*-axis orientation is important for the implementation of the desired thickness shear mode, as I shall demonstrate later in this chapter.

Multiple investigations testing one or more parameters for optimizing RF magnetron sputtering of ZnO have been performed including RF power (stepped and constant) [93, 94], oxygen:argon ratio and pressure [90, 92, 95], surface roughness [91], substrate/electrode material [96], and substrate temperature [97]. Interestingly, in nearly all studies, researchers concluded that the parameter (or parameters) under investigation was the most important variable for the high *c*-axis orientation of sputtered ZnO. Gardeniers *et al*, report one of the more thorough examinations by testing a variety of factors, including substrate material, substrate temperature, RF power, and distance between the target and the substrate [89]. Indicative of the findings broadly in the literature, they conclude that all parameters have a significant impact on the quality of the ZnO film.

For the purpose of this research, a protocol for high quality *c*-axis oriented ZnO has been employed by a former member of the lab, Dr. Shawn Pinkett, in collaboration with Dr. Jerry Siebert. Dr. Pinkett achieves high *c*-axis oriented ZnO using the parameters outlined in Table 3.2, the derivation of which are fully treated in [76]. All films were sputtered using the Unifilm PVD-300 RF/DC sputtering system, which employs a moving platform for the substrate wafer, both spinning the wafer and moving it periodically beneath the plasma beam in an effort to achieve a highly uniform coating across the wafer.

Parameter	Value
Temperature	325ºC
Deposition Pressure	5.02 x 10^{-3} Torr
Argon:Oxygen ratio	97.5 : 2.5
RF Power	135 W
Distance from target to substrate	6.9”
Substrate material	<0 0 1> Silicon, mechanical grade

Table 3.2. Sputtering parameters used for deposition of highly *c*-axis oriented ZnO using the Unifilm PVD-300 sputtering system.

X-ray Diffraction Characterization

The crystallinity of thin films is often gauged by making X-ray diffraction (XRD) measurements of the film. Crystallinity describes the condition under which atoms are arranged in a regular pattern. Single-crystal films require that there is a smallest volume element that by repetition in three dimensions sufficiently describes the crystal. This is extremely difficult to achieve through conventional synthetic thin-film deposition methods, of course, so it is necessary to gauge the degree of ‘poly-crystallinity’ of a thin film in order to assess its quality. The measurements most often used for assessing thin films are the full width at half maximum (FWHM) of the θ–2θ scan and of the 2θ-ω rocking curve scan, in which Figure 3.5 describes the terms used. θ describes the angle of incidence from the target platform supporting the wafer while 2θ represents the angle from that incidence vector to the receiver device. ω is the term used to describe any tilt applied to the support platform. The θ–2θ scan varies the θ and 2θ angles and gives the diffraction angle peak revealing the predominant crystal orientation. The FWHM is a measure of the span of the reflection peak at half-maximum and the θ–2θ FWHM in particular is the parameter most often described in the literature to characterize the crystal

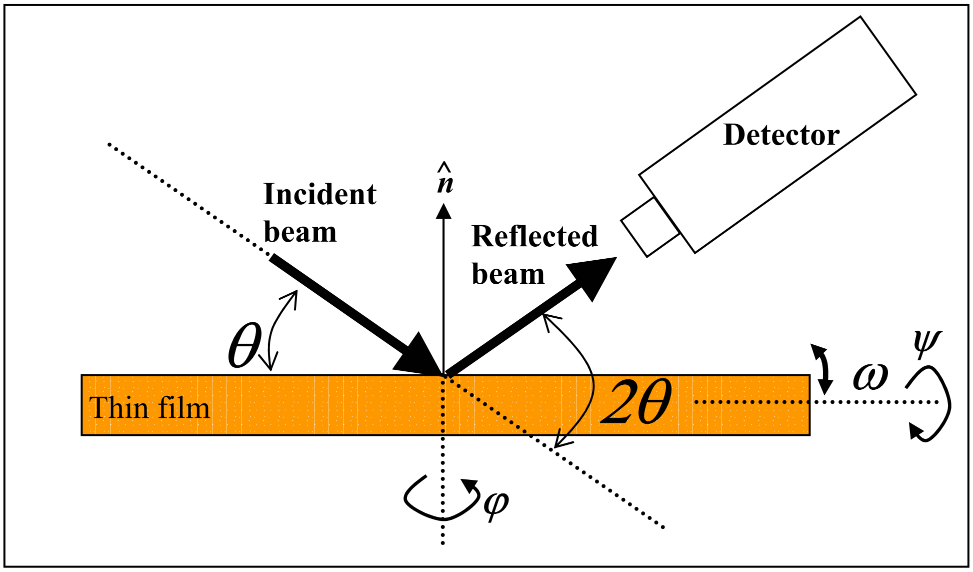

Figure 3.5. XRD for assesmment of thin film crystallinity.

uniformity of a thin film. The 2θ-ω rocking curve scan is generally considered a better assessment of the quality of the film [98] and involves varying ω at a fixed 2θ angle, which reveals a detailed structure of the peak being analyzed. Due to the prevalence of θ–2θ scans demonstrated in the literature, these were used for the purpose of this film characterization.

The films were characterized using a Philips X'Pert Materials Research Diffractometer using a hybrid mirror/monochromator incident optics and a ¼-degree receiving slit in the diffracted optics beam path. Considering that high c-axis orientation is a principle component of achieving the desired TSM resonator, it was decided that ZnO should be deposited on multiple substrates to find out how much of an impact the underlying substrate crystal structure would have on the epitaxial growth of ZnO. ZnO was deposited on DC sputtered W, RF sputtered Ta_2O_5, RF sputtered SiO_2, polished (1 0 0) silicon, polished (1 0 0) gallium arsenide (GaAs), and polished (0 0 1) sapphire (Al_2O_3). The first 3 surfaces were chosen due to their potential as components of the acoustic mirror, and the final three for general comparison purposes. The polished sapphire was of particular interest, as it is considered lattice matched to *c*-axis oriented ZnO and should yield the highest degree of orientation [89, 96]. By contrast, the polished GaAs is not lattice matched and should therefore yield a relatively lower degree of crystallinity. The results of these depositions are demonstrated in Figure 3.6 below. Note

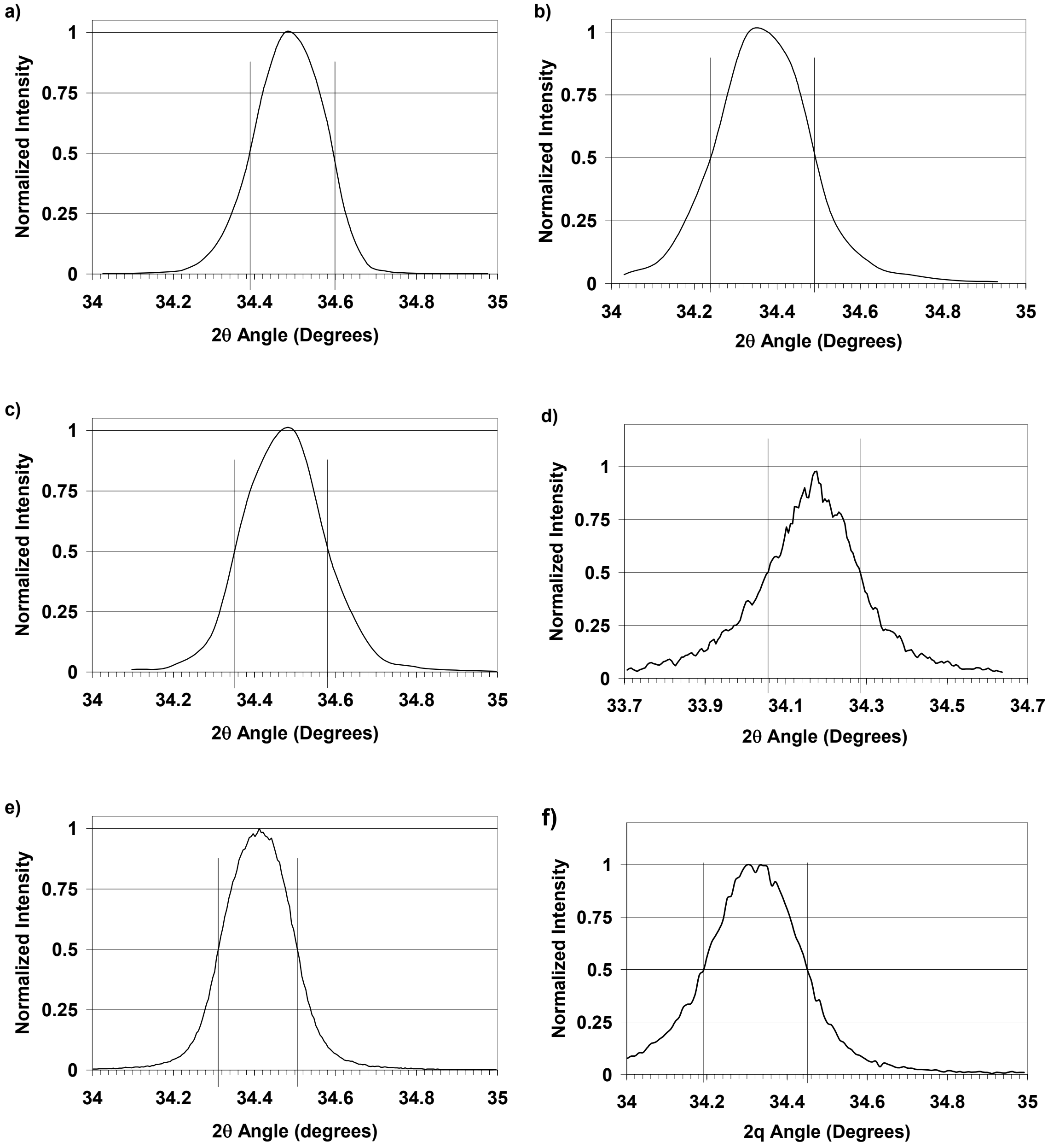

Figure 3.6. θ–2θ XRD scans of ZnO RF sputtered onto a) Sapphire, b) GaAs, c) Silicon, d) W, e) Ta_2O_5 and f) fused silica.

that results indicate that there was little variation in the quality of the ZnO film due to the substrate crystal. This gave me confidence that ZnO deposited using the protocol described in Table 3.2, would yield high crystallinity regardless of the substrate material. That is to say, the mirror surface material would not impact the ability of the ZnO film to support the desired TSM. The 2θ FWHM measurements for all substrate materials are summarized in Table 3.3. Incidentally, these results indicate *c*-axis oriented crystallinity on par with that reported by others referenced in this document [89, 90, 92-97].

Base Layer	**2θ FWHM**
Sapphire	0.20°
GaAs	0.25°
Si (1 0 0)	0.23°
W	0.24°
Ta_2O_5	0.20°
Fused Silica (SiO_2)	0.26°

Table 3.3. 2θ FWHM from XRD scan results of ZnO RF sputtered onto various surfaces.

From ZnO to Ta_2O_5

Figure B.1 demonstrates the initial SMR design for achieving the base transducer for my biosensor application. Many wafers were fabricated with multiple electrode configurations and mirror thicknesses attempted over a period of nearly 2 years before I finally discovered a resonance response using the parameters shown in Table 3.4. The majority of this time was spent on alternate electrode configurations and broad approaches to achieving the LFE design. The electrode configurations attempted over this time period are demonstrated in Appendix B. Note that the configuration that finally worked utilized an 8-layer mirror, consisting of SiO_2 as the low acoustic impedance material and Ta_2O_5 as the high acoustic impedance material, and ZnO as the piezoelectric crystal. Each layer was deposited via RF sputtering using the parameters described in Table 3.4. The electrodes were deposited by electron beam evaporation at a thickness of 1200 Å of Al with a 300 Å adhesion layer of Cr. Layer thicknesses were chosen to yield the 8-layer mirror response reflected in Figure 3.7. A SEM image of the profile of the fabricated device is shown in Figure 3.8, confirming the fabrication result was as intended.

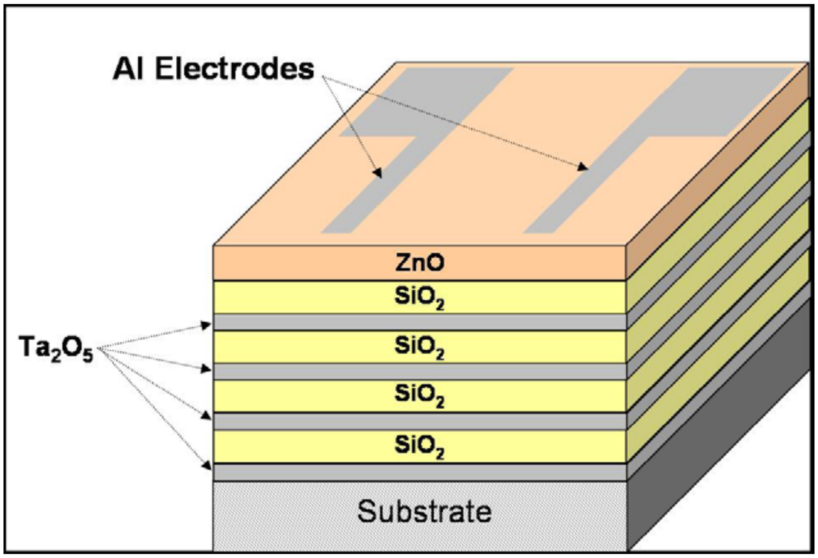

Figure 3.7. Initial ZnO SMR design.

Parameter	ZnO	Ta_2O_5	Fused Silica (SiO_2)
Layer Thickness	750 nm	450 nm	850 nm
Temperature	325ºC	Ambient	Ambient
Deposition Pressure	5.03 x 10^{-3} Torr	5.02 x 10^{-3} Torr	5.02 x 10^{-3} Torr
Argon:Oxygen ratio	97.5 : 2.5	97.5 : 2.5	98 : 2
Power	135 W @ 98 V	115 W @ 121 V	281 W @ ~58 V
Deposition Rate	400 Å/min	600 Å/min	300 Å/min
Distance from target to substrate	6.9”	6”	6”

Table 3.4. Deposition parameters for original device design.

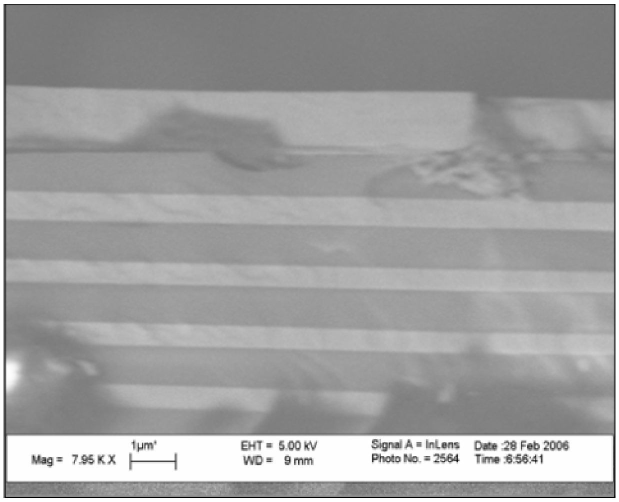

Figure 3.8. SEM image of profile of fabricated device, confirming output of fabrication to meet the design specifications.

Resonator performance was assessed using a Cascade Microtech 9000 probe station and Cascade Microtech ACP40/GSG-150 probes. Results were recorded with a HP8753C Network Analyzer equipped with an 85047A S-Parameter Test Set. The resonator is a one port device, so the measurements made are referred to as the reflection scattering parameters, or S_{11} response. The S_{11} response is a ratio of the reflected signal over the incident signal over a given frequency range. From the S_{11} data, it is in turn possible to obtain the impedance response of the resonator through the following transformation:

$$Z_{in}(f) = Z_o \frac{1 + S_{11}(f)}{1 - S_{11}(f)} \tag{3.15}$$

where Z_o is the load impedance (generally 50Ω). One-port S_{11} responses of each device are the first tests I perform on any fabricated resonator and give the best information regarding the resonance quality. Due to the parallel electrode configuration required for LFE and the semiconductor nature of ZnO, the scattering response should look like a simple capacitor, in which a relatively constant reflection of the incident signal is observed. As the frequency range is swept, there is a range in which the physical parameters of the thin film and the transduction properties of the piezoelectric crystal absorb the incident signal, transforming it into a mechano-acoustic wave that propagates through the bulk. At the resonance condition, a standing wave is achieved and a maximum transduction of electrical into mechanical energy is established. The narrower the frequency range, or band, of that transduction and the greater the overall absorption of the incident electromagnetic energy, the stronger the performance of the resonator. This is reflected in higher resonance quality factor, Q.

A typical S_{11} response for these initial resonators is shown in Figure 3.9.A below. As can be seen, the device exhibits a characteristic resonator reflection scattering response, albeit a relatively poor one, at around 1 GHz. These resonance conditions are deemed weak as the response band is very wide and the overall energy absorbance is relatively small. Figure 3.9.B and 3.9.C shows the conversion of the S_{11} response into the corresponding magnitude of the input impedance response, accomplished through the relationship described in Equation (3.15), and the Smith Chart of the complex reactance, respectively. It must be noted, however, that as this was the first resonance observed after nearly 2 years of experimentation with various configurations, I was still relatively excited about the breakthrough. I was surprised by the response, however, as the resonance observed would have meant the TSM wave launched in ZnO was resonating with an acoustic velocity of 1,980 m/s, much lower than the expected 2,840 m/s (see Chapter 2). I hypothesized that several possibilities existed at this point. These included the possibility that the dopants in the ZnO target material used for sputtering were substantially affecting either the density or stiffness of the sputtered film or that the physical properties of the mirror itself was not focused properly on the resulting acoustic

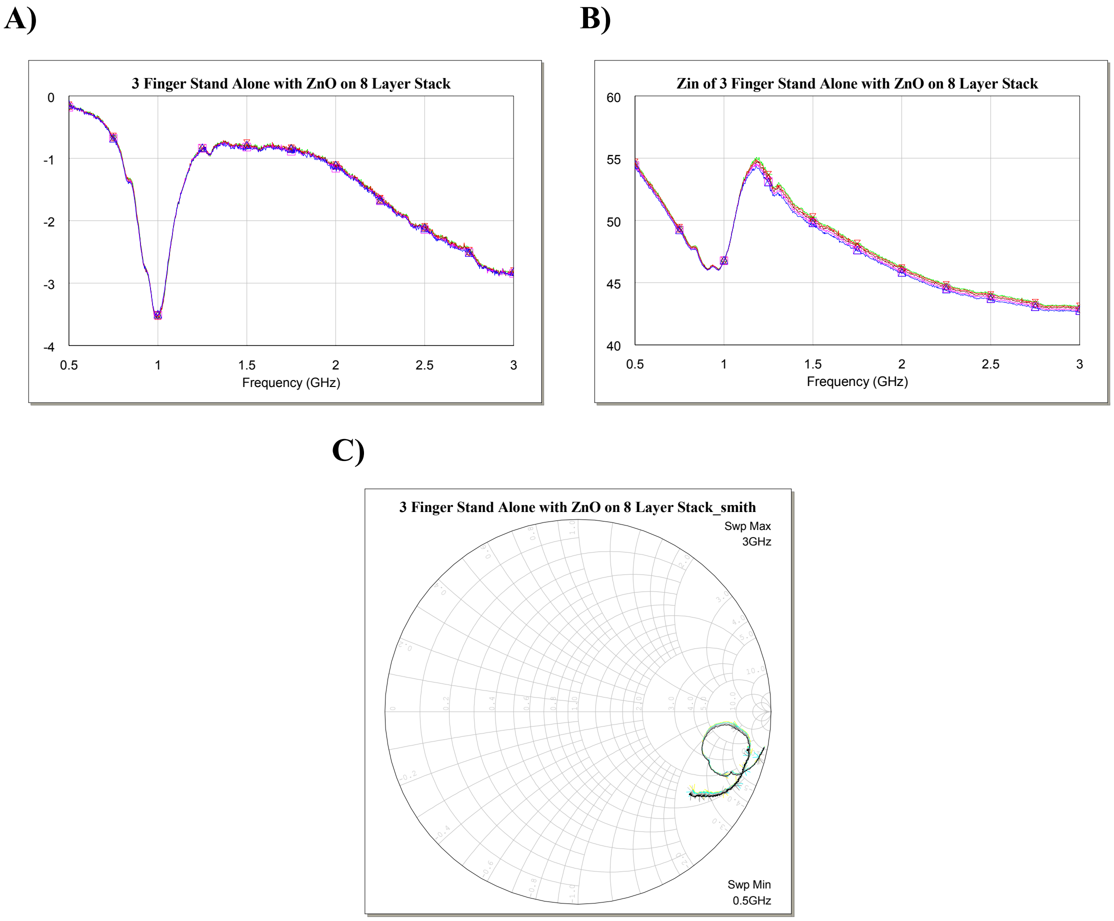

Figure 3.9. A) S_{11} response, B) $|Z_{in}|$ response, and C) Smith Chart showing typical responses for 8-layer mirror resonators with ZnO on top.

wave and may be scattering the energy.

My initial excitement at finding a resonance was substantially diminished when I fabricated a subsequent wafer with a substantially thinner layer of ZnO. Upon probing this next series of resonators with the probe station, I observed the exact same response as with the previous fabrication. Recall from Equation (3.14) that the resonance frequency of a bulk acoustic wave resonator device is determined directly by the thickness of the piezoelectric film. This led to yet another fabrication in which I fabricated electrodes directly onto the 8-layer mirror, in which fused silica was the top layer, and no ZnO was present. This wafer yielded the results shown in Figure 3.10 below. As can be seen, these

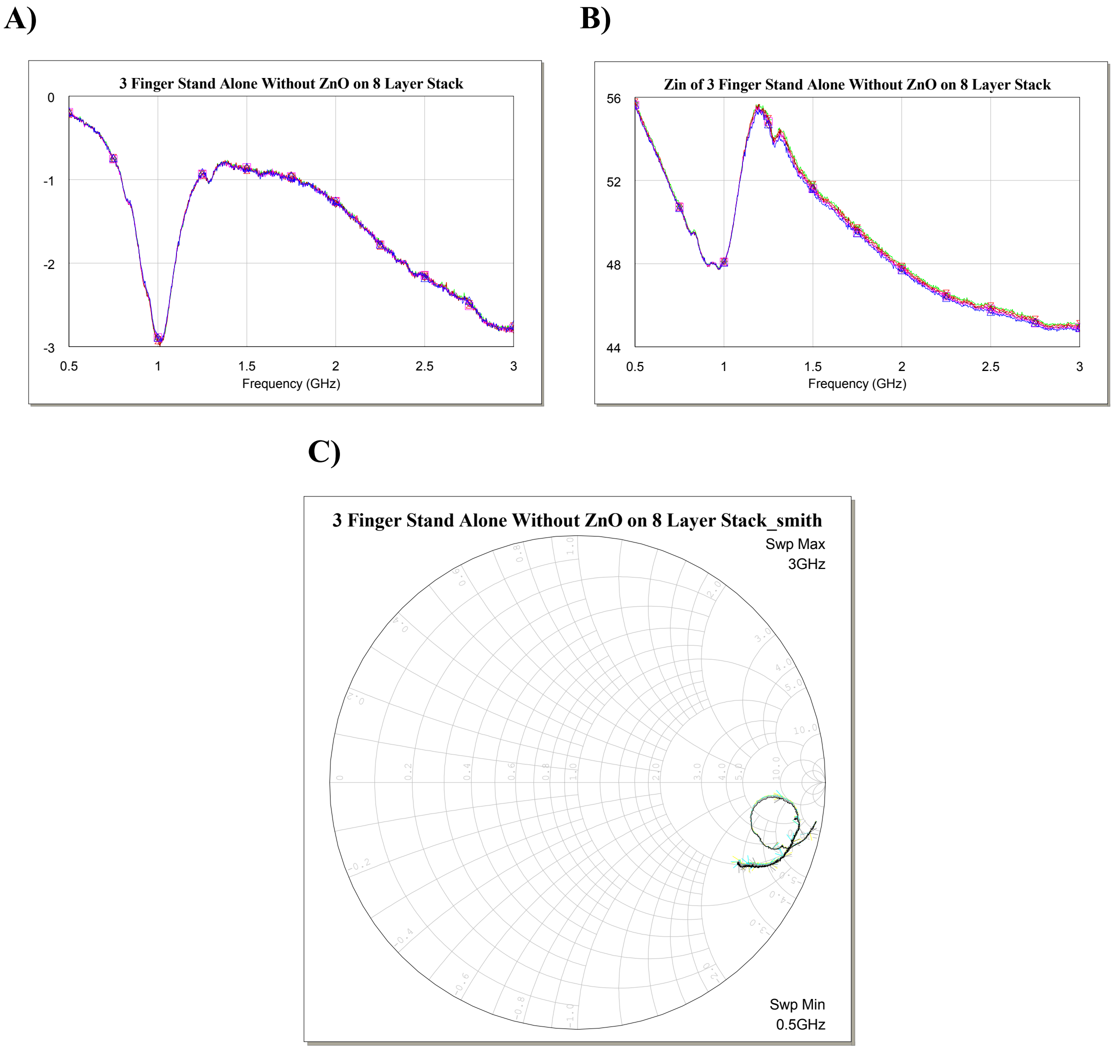

Figure 3.10. A) S_{11} response, B) $|Z_{in}|$ response, and C) Smith Chart showing typical responses for 8-layer mirror resonators ***without*** ZnO on top.

responses are remarkably similar to those shown in Figure 3.9, meaning the resonance had nothing to do with ZnO. At this point, it was thought that perhaps Ta_2O_5 could be piezoelectric and led to the investigation described in the following section.

The Case for Piezoelectric Ta_2O_5

Piezoelectric Ta_2O_5 have been employed for SAW devices [99-103]. Thin *x*-axis oriented monoclinic crystalline Ta_2O_5 films deposited by DC diode sputtering on fused quartz with *y*-directed SAW propagation has been successfully demonstrated [104, 105]. In another application, Ta_2O_5 films have been deposited as a loading layer on top of ST-cut quartz in an effort to optimize SH-SAW performance. At an optimal thickness, this layer was shown to improve K^2 and reduce insertion loss over devices without the film [106].

Despite the characterization of Ta_2O_5 for SAW applications, there has not been much investigation into bulk acoustic modes for piezoelectric Ta_2O_5 to date. I therefore decided to investigate the bulk acoustic properties of Ta_2O_5 in a thin film Ta_2O_5/SiO_2 stack deposited by RF magnetron sputtering. The motivation for this was to generate a resonator which exhibits the TSM of operation through LFE. For a surface-only mounted electrode configuration, the separation of the Ta_2O_5 layers by a SiO_2 layer might help to focus the electric field in a horizontal orientation through the Ta_2O_5 layer. For lateral field excitation applications, it was believed that this would help to improve the electrical coupling to a TSM mode.

A thin film 3-layer stack of alternating SiO_2 and Ta_2O_5 was deposited by RF magnetron sputtering using the Unifilm PVD-300 sputtering system. The layers were alternating fused silica (SiO_2) and Ta_2O_5, in which Ta_2O_5 was the first layer deposited onto a mechanical-grade Si (1 0 0) wafer. Electrodes were fabricated on top of the stack in the configuration shown in Figure 3.11. The sputtering parameters for the 3-layer alternating stack are provided in Table 3.4. The SiO_2 layer was determined to be approximately 750 nm thick while the Ta_2O_5 layers were approximately 450 nm thick. The final thicknesses of each layer were verified using SEM imaging, and can be seen in Figure 3.12 from a cross-sectional view. The SEM images were taken using a LEO 1530

Thermally-Assisted Field Emission Scanning Electron Microscope system. The electrodes were 150 nm of aluminum deposited on top of a seeding layer of 30 nm chromium using a CVC E-beam evaporator and standard photolithography process, outlined in Appendix C.

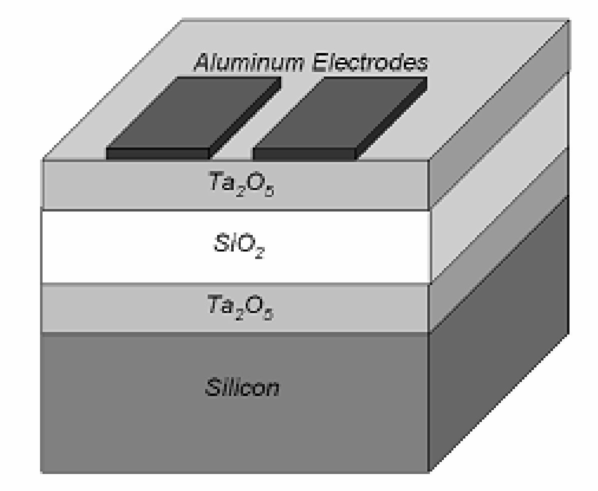

Figure 3.11. Device design for LFE of a piezoelectric Ta_2O_5 TSM resonator**.**

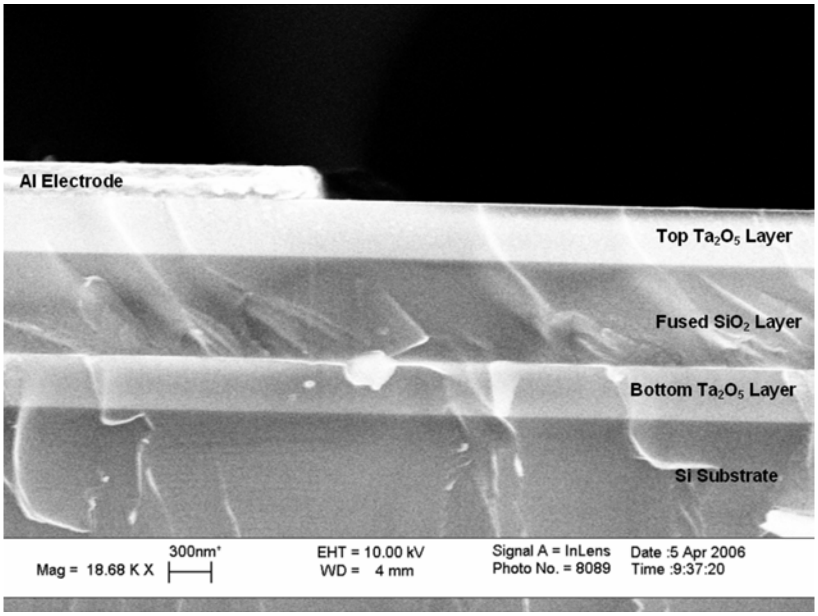

Figure 3.12. SEM image of profile of fabricated resonator.

The electrodes were designed such that the electric field created upon excitation would be perpendicular to the wafer surface normal. This laterally-oriented electric field was already found to excite the resonance shown in Figures 3.9 and 3.10. It was further believed at this point that this electrode configuration was exciting the TSM acoustic wave in the Ta_2O_5 (i.e. through LFE). It was therefore required to demonstrate that this was even theoretically possible.

X-ray Diffraction Characterization of Ta_2O_5

XRD data were taken on a Philips X'Pert Materials Research Diffractometer using a hybrid mirror/monochromator incident optics and a ¼-degree receiving slit in the diffracted optics beam path. Previous investigations with DC diode sputtering have found a significant variety in the growth of Ta_2O_5 crystals by altering the deposition parameters. A 2θ-ω scan of the film indicated a weak polycrystalline peak at ~26.4°, indicating an (11 0 1) orthorhombic *2mm* crystal orientation shown in Figure 3.13. The peak was found only after applying a 10° offset on ω to the wafer upon running the 2θ-ω scan, however, indicating the crystal must have grown offset from the normal of the substrate by that angle. The pole plot depicted in Figure 3.14 is a 2.5-D plot of the 4-pole symmetry about the φ axis with a 90° rotation on ψ for the radial axis. Three of the peaks in the pole plot are readily apparent. The fourth, however, while well above the noise floor, is a much smaller peak than the three other peaks. Other samples sputtered under the same condition required a tilt of ~12.3° for the [11 0 1] peak to be observed. This was found to be repeatable under the sputtering conditions given in Table 3.4. Using a reciprocal space diagram and powder diffraction X-ray tables, it was determined that if one assumes that

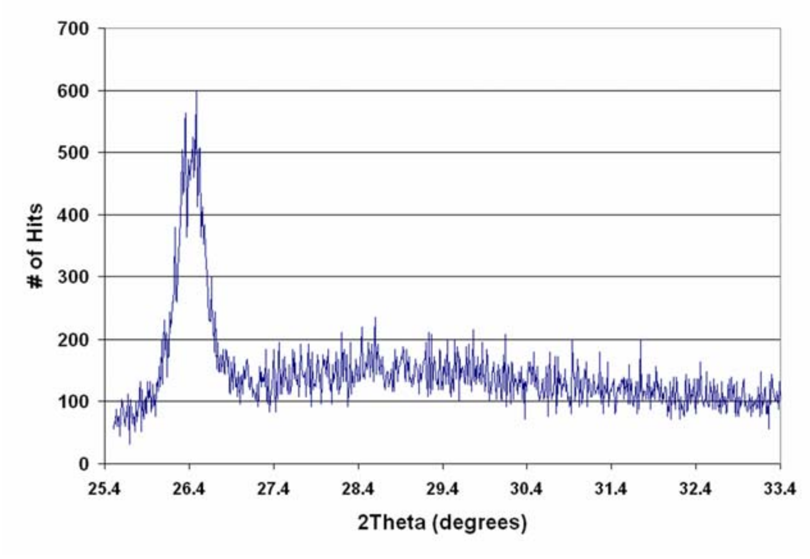

Figure 3.13. *2θ-ω* scan of 10º tilted Ta_2O_5

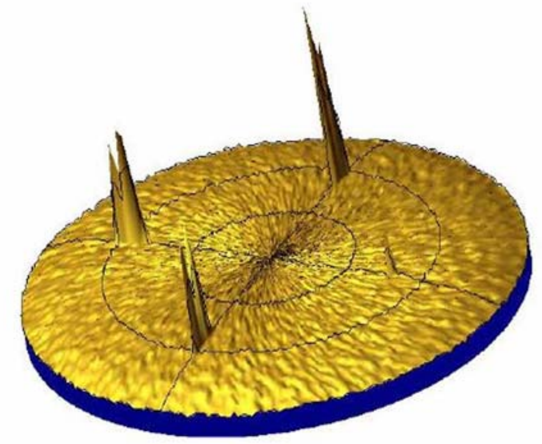

Figure 3.14. 2.5-D pole plot, or φ scan, of 4-pole symmetry**.** [Prepared by Dr. Walter Henderson]

the [17 0 1] axis is aligned parallel to the Si [1 0 0] axis, then the [11 01] axis is tilted approximately 10 degrees to the low angle side as was observed. If one assumes that the [19 0 1] is aligned to the Si, the tilt is ~12.3 degrees, which is the offset that was seen in some of the samples. Initially, these alignments do not seem to make much sense from an epitaxial alignment point of view, but after examining at the lattice constants, there may be a viable explanation. The orientation with the [17 0 1] ([19 0 1]) axis parallel to the Si [1 0 0] axis has an in-plane periodicity of 6.728 (6.628) Å. The ratio of this distance for the [17 0 1] ([19 0 1]) orientation to the Si [1 0 0] lattice constant, 5.43095 Å at room temp, is thus 5:4 (11:9 close to 6:5) within about 1%.

Compared to the values in the cases where the [1 0 0], [0 1 0], and [0 0 1] Ta_2O_5 directions are parallel to the Si [1 0 0] – 81:10, 7:5 and 7:8, respectively – it is likely that the proposed orientations are the most energetically favorable way for the Ta_2O_5 to achieve a harmonic or periodic lattice match on Si. In particular the elevation of the Ta_2O_5 [1 0 0] axis out of the interface plane seems to be strongly preferred. That axis with its large lattice constant is a difficult match to the underlying silicon, and the substrate therefore is a poor template for that potential orientation. The scans show that there is clearly an amorphous component as evidenced by the broad slowly, trailing hump at lower 2Θ angles, shown in Figure 3.13. However, the φ scans strongly suggests the presence of oriented, crystalline (likely polycrystalline) Ta_2O_5.

Thickness Shear Mode in Piezoelectric Ta_2O_5

Once the crystal orientation is known, it is possible to solve the Christoffel equation described in Equation (3.1) to find the modes of propagation in the bulk given a defined electrical excitation direction. We begin by considering the non-piezoelectric Christoffel equation, as provided in Equation (3.1) and (3.2). It is estimated that the oriented Ta_2O_5 films belong to a class of *2mm*. The orthorhombic system class *2mm* tensors are used in the calculations here because of the XRD results discussed above. All solutions to the Christoffel equation were implemented in MATLAB, using the code presented in Appendix E.

If the direction of propagation is chosen to be in the z direction, then l_x and l_y go to zero, and l_z becomes 1. The Euler angles are chosen such that the rotated system corresponds to the z-axis in the direction normal to the (17 0 1) plane and the x-axis can be chosen to be oriented in the plane parallel to (17 0 1) and in line with the electric field. Since there are different manners of describing Euler angles, I have chosen the one most familiar to us. In that system, ϕ corresponds to a counterclockwise rotation about the z-axis, θ corresponds to a counterclockwise rotation about the new y'-axis, and φ corresponds to a counterclockwise rotation about the new z''-axis. Under this convention, the Euler angles to describe a system in which the z-axis is normal to the (17 0 1) plane are $\phi = 0$, $\theta = 86.633^\circ$ and $\varphi = X$ where X is the angle corresponding to the direction of the electric field. Since our electrodes are fabricated on top of sputtered Ta_2O_5, X is arbitrary because the exact orientation of the electrodes in the x-y plane with respect to the crystal lattice is unknown. For simplicity, I will set $\varphi = 0$.

For the Ta_2O_5 stack structure described in Figure 3.11, the electric excitation is orthogonal to the wave propagation direction. Therefore, if the wave propagation is in the direction of the z-axis, the electric field is in the x-y plane. From the general solutions, it is possible to determine that the exact orientation of the electric field with respect to the crystal lattice is not as important here because it yields similar results.

Here I will describe the coupling and acoustic wave propagation for the purely x-axis oriented case since symbolically the solutions are much simpler than those for the odd-angle rotated case and will then attempt to explain how the (17 0 1) normal relates to this. First, the orthorhombic *2mm* tensors, obtained from Nakagawa, *et al* [20], were transformed such that the z-axis is normal to the (1 0 0) surface of Ta_2O_5. Then, the wave propagation is specified to be in the z direction of the transformed axes and the electric field in the direction of the x-axis. The symbolically solved Christoffel matrix comes out to be:

$$\begin{bmatrix} c_{55} & 0 & 0 \\ 0 & c_{66}+\dfrac{e_{36}^2}{\varepsilon_{33}} & 0 \\ 0 & 0 & c_{11} \end{bmatrix}$$

The eigenvalues of this matrix correspond to terms that can be used to solve for the acoustic velocity for each of the three wave propagation modes. Upon inspection, it is possible to see that only the y-directed particle displacement is piezoelectrically stiffened. This means that for an electric field in the horizontal plane, parallel to the surface, a shear wave will be generated with a propagation direction normal to the surface. No other component of the Christoffel matrix contains a stiffened term. Similarly, if I solve for the Christoffel matrix with an electric field designated along the y-axis of the crystal, the Christoffel matrix becomes

$$\begin{bmatrix} c_{55}+\dfrac{e_{25}^2}{\varepsilon_{22}} & 0 & 0 \\ 0 & c_{66} & 0 \\ 0 & 0 & c_{11} \end{bmatrix}$$

which shows that this time, the particle displacement is parallel to the surface, but normal to the electric field. The coefficients involved in the stiffness have changed, but this is as expected for an orthorhombic crystal. Therefore, one can imagine that an electric field oriented at some angle between the x and y axes of the transformed system would provide a particle displacement normal to the field in the x-y plane with a wave propagation direction oriented toward that of the *z*-axis. Indeed it does, but the symbolic eigenvectors of the solved Christoffel matrix are too complicated to show here, even in the simplest case of a 45° offset.

The above situation has been solved assuming strong crystal orientation toward (1 0 0). It has already been shown, however, that the deposited film exhibits a highly *poly*crystalline mix with a predominant orientation along (17 0 1). To accurately predict any resulting piezoelectric activity, one must rotate the tensors according to the appropriate Euler angles described above and then solve and interpret the resulting Christoffel matrix. For the case of an *x*-directed electric field, it can be demonstrated that the particle displacement for the longitudinal case and for the shear cases are not directly aligned with the *z* and *x* axes respectively. They also show no piezoelectric stiffening just as in the (1 0 0) case discussed above. Coupling is reflected, however, in the *y*-direction and the particle displacement is directly aligned with the *y*-axis, as expected. For the case of a *y*-directed electric field, on the other hand, no coupling for the *y*-directed particle displacement shear mode is seen because of the angle difference between the (17 0 1) and (1 0 0) faces. Piezoelectric coupling due to the *y*-directed field does occur, however, for the longitudinal and *x*-directed shear modes. Therefore, we can conjecture that most likely, the lateral excitation of the Ta_2O_5 consists of multiple directions of particle displacement and will depend upon the exact angle of the electric field with respect to the crystal orientation. I have shown, however, that a thickness directed shear wave theoretically can be excited in both (17 0 1) and (1 0 0) oriented Ta_2O_5 thin films.

Finite Element Modeling of Ta_2O_5 LFE SMR

In addition to the Christoffel matrix calculations, electrostatics finite element modeling of the system was carried out using the software package Comsol Multiphysics™. The motivation behind this was two-fold. First, it helped to clarify the orientation of the electric field in the Ta_2O_5 stack as generated from the electrodes. It must be confirmed that an electric field parallel to the surface does emerge in the regions of interest in order to verify the lateral excitation of the device. Secondly, by modeling the system, it is possible to look at the relative levels of electrical energy density within the stack layers. Figure 3.15, prepared by Dr. Corso, shows the electric field through the layered stack. The first and third layers are Ta_2O_5 sandwiching a layer of SiO_2. Below the stack is the (1 0 0) mechanical-grade silicon substrate wafer that the entire structure was fabricated upon.

The resulting simulation shows that the electric field is *much* denser in the Ta_2O_5 layers than in the SiO_2 and is fairly horizontal in the active area of interest in between the electrodes (indicated by the box). It appears that the electric field in the top Ta_2O_5 layer is

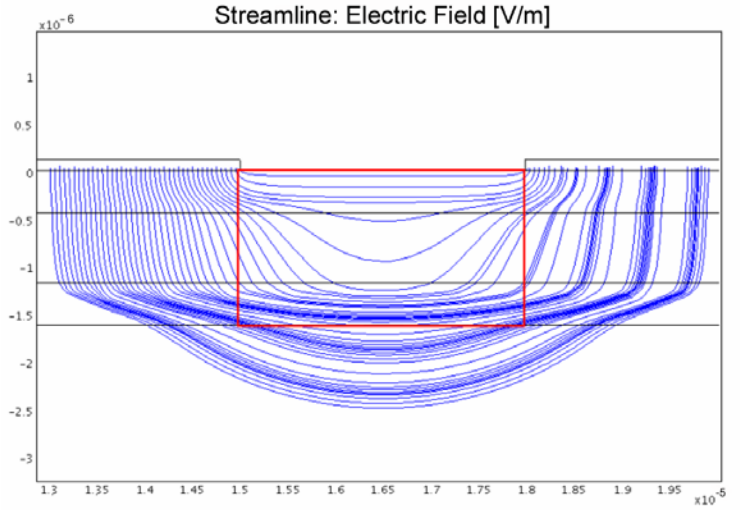

Figure 3.15. FEM plot of the electric field line orientation in active area (indicated by box). [Prepared by Dr. Christopher Corso]

relatively parallel to the surface. The permittivity of the SiO_2 is such that it draws the E-field more directly through to the subsequent layer. The permittivity of Ta_2O_5 then redirects the E-field in a manner parallel to the surface, which provides lateral excitation of the film. Figure 3.16 is an arrow plot where the size and direction of the arrow demonstrates the relative strength and orientation of the field in the stack. In the top Ta_2O_5 layer, the arrows within the active region are very well aligned. The electric field in the SiO_2 layer appears to have a more vertical component, especially towards the edge of the active area. The results from these simulations offer an independent confirmation that a lateral electrical excitation field exists in the Ta_2O_5 which substantiates the calculations made in the previous section. The finite element results also demonstrate the usefulness of the thin-film stack structure for electric field manipulation with regards to the piezoelectric films.

In order to calculate the energy density in the stack layers, finite element modeling was again utilized. The finite element simulation results in 2-D were extracted with each

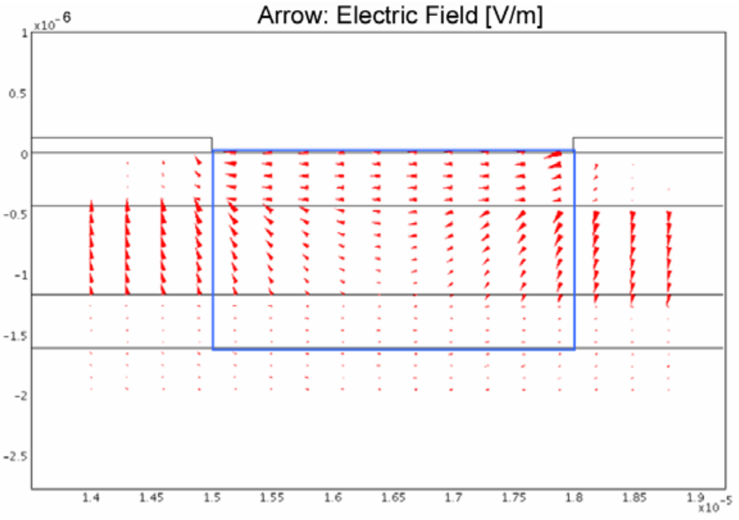

Figure 3.16. FEM arrow visualization of electric field orientation and relative strength. [Prepared by Dr. Christopher Corso]

point paired with a finite energy density. For each layer, the energy density values of all the points falling within the active area of interest of the layer were summed and divided by the total number of points to give the average energy density at a location within the active area. The totals were found and the ratio of the average energy density in the layer to the lowest average energy density in the stack was computed for each layer. The results are summarized in Table 3.5. From the data, it is apparent that the average energy density each Ta_2O_5 layer is greater than the corresponding average energy density of the SiO_2 layer directly above it. Clearly, there is some propensity for the electrical energy to migrate towards the Ta_2O_5 layers. This can be explained by the large relative dielectric permittivity of Ta_2O_5 which is approximately 19.5 in the *y*-axis direction [107] as compared to 3.8 for fused quartz [108]. Figure 3.17 shows a visualization of the energy density for the active area of the stack in between the electrodes. The lighter color corresponds to a higher energy density whereas the darker color corresponds to a lower energy density. It is clear from the image that the greatest energy density exists just at the edges of the electrodes in the top Ta_2O_5 layer. The layer contains a large amount of electrical energy density within the active region. This is important because the larger energy density allows for a better opportunity for coupling electrical energy into a mechanical wave. In the following layers a greater amount of energy density is contained in the Ta_2O_5 layer than in the SiO_2 layer which is desirable for the excitation of an acoustic wave in the Ta_2O_5.

Layer	**Average Energy Density Ratio**
Ta_2O_5 Layer 3	81.27:1
SiO_2 Layer 2	1.00:1
Ta_2O_5 Layer 1	1.82:1

Table 3.5. Average energy density for each layer. [Prepared by Dr. Christopher Corso]

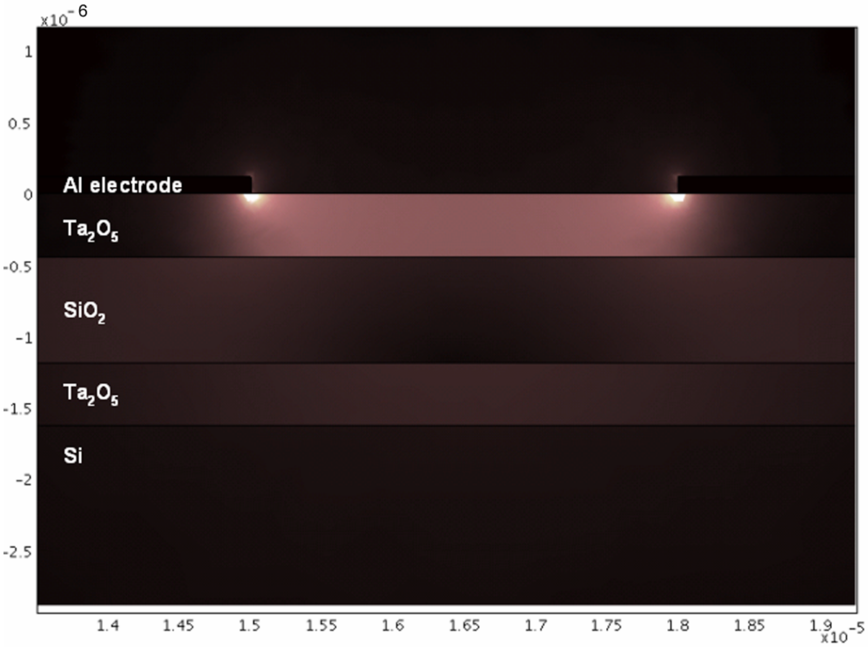

Figure 3.17. Visualization of electric energy density. [Prepared by Dr. Christopher Corso]

Ta_2O_5 Resonator Results

It was determined that the strongest resonance responses came from device arrays with the electrode configuration shown in Figure 3.18. RF probing of individual devices (i.e. those not fabricated as part of an array) yielded weaker resonance. Several regions of resonance regions were observed for each device around 450 MHz with the sharpest peak generally in the area of 525 MHz. As can be seen from a representative Smith Chart shown in Figure 3.19, multiple clear loop patterns emerge, indicative of resonance, are present. This response is typical of the response observed in a vast majority of the devices tested. The multiple peaks may be attributed to either the multiple layers of or the polycrystalline nature of the Ta_2O_5. From a sampling of 10 “good” devices, an average unloaded *Q* of these resonators is approximately 1,500, which is quite high

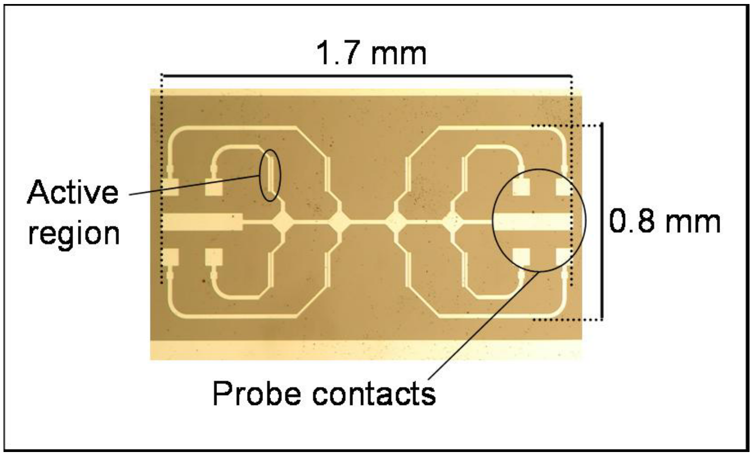

Figure 3.18. Electrode configuration used for results of Ta_2O_5 resonator tests.

Without the appropriate stiffness tensor quantities for the bulk material, it is difficult to derive the phase velocity value and thus the resonant frequency of a thickness shear wave for comparison with our results. However, in an attempt to further establish the existence of a thickness shear mode, a simple water test could be applied since water cannot support a shear wave but can support a longitudinal wave. If the acoustic activity

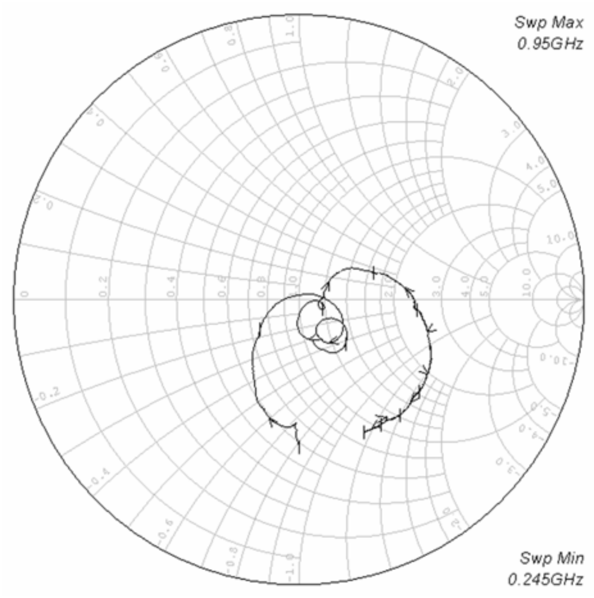

Figure 3.19. Smith Chart of Ta_2O_5 resonator array.

were longitudinal, application of de-ionized water at the surface would devastate the acoustic resonance observed in the device. Figure 3.20 below shows the response before (squares) and after (triangles) application of water to the surface. As can be seen, the water had no deleterious affects on the S_{11} suppression and a negative frequency shift occurred after water was observed of approximately 167 MHz. According to Sauerbrey [109], this response is to be expected from a TSM device, roughly described by Equation (2.5). It is reasonable to assume that the observed frequency shift could indicate a mass loading effect of the surface of the device by the de-ionized water. This further confirms the prediction made by analysis of the Christoffel solution that the resonance is a TSM wave. The response to the water test was shown to be repeatable across different device configurations in various locations about the wafer.

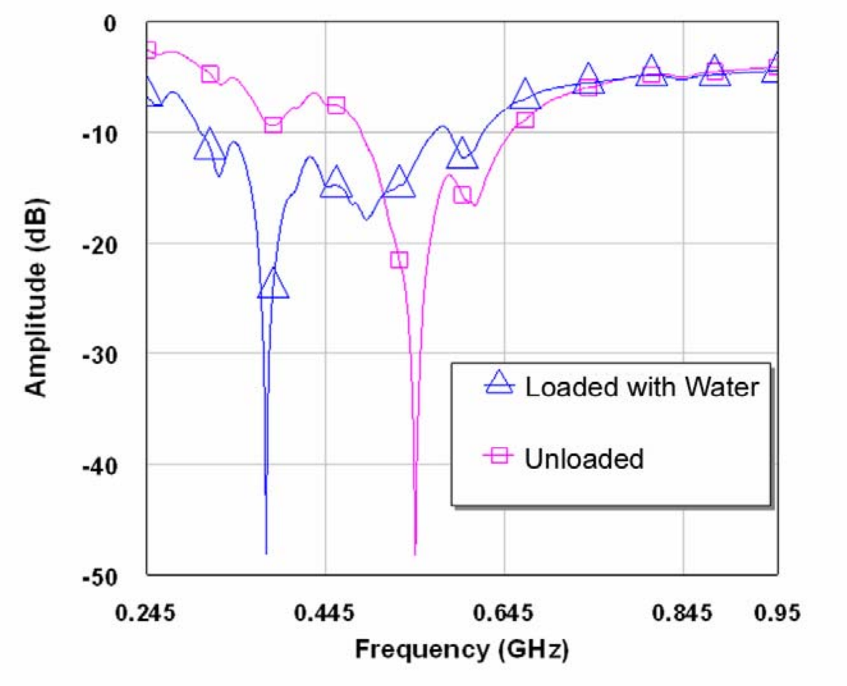

Figure 3.20. Frequency response representation of the S_{11} resonator response before and after water loading.

Not All Resonances are Acoustic

The next step, which should have been attempted before launching into the investigation described in the last section, involved an experiment in which the devices described in the previous section were repeated, but with films deposited at half the thickness. The results of these experiments again revealed results nearly identical to the previous results, in both quality and in frequency of response. As is described by Equation (3.14), acoustic resonance is directly determined by the film thickness. So this latest discovery confirms that not only does the resonance activity have nothing to do with piezoelectric ZnO, but that the resonance has nothing to do with piezoelectricity at all. In other words, the resonance observed through one-port S_{11} analysis was not acoustic in nature. Additional experiments in which the electrode traces were modified or cut in various locations revealed that the resonance was, in fact, purely electromagnetic in nature.

It was obvious at this point that these devices had limited, if any, usefulness as a biosensor. The lessons learned from this detour allowed for a more robust vetting of the resonators that were eventually developed for biosensor applications, however. These include a confirmation that the resonance observed from S_{11} responses are piezoelectric in nature and that the mode of propagation is assessed properly. It is not an entirely uncommon experience to review the published literature and come across reports in which thorough vetting of the observed phenomena were not performed.

From Ta_2O_5 back to ZnO

Given that piezoelectric Ta_2O_5 was not effective, it was decided that the original strategy of implementing a ZnO TSM SMR should be renewed. This time, however, the Ta_2O_5/SiO_2 mirror would not be used as it was thought to be insufficiently capable of reflecting the TSM wave. It was then determined that tungsten (W) and fused silica (SiO_2) might form an appropriate mirror for TSM acoustic waves resonating in a ZnO film, given the mirror predictions shown in Figure 3.2. W could also be deposited using the Unifilm PVD-300 Sputterer. A schematic of the new resonator design is shown in Figure 3.21.

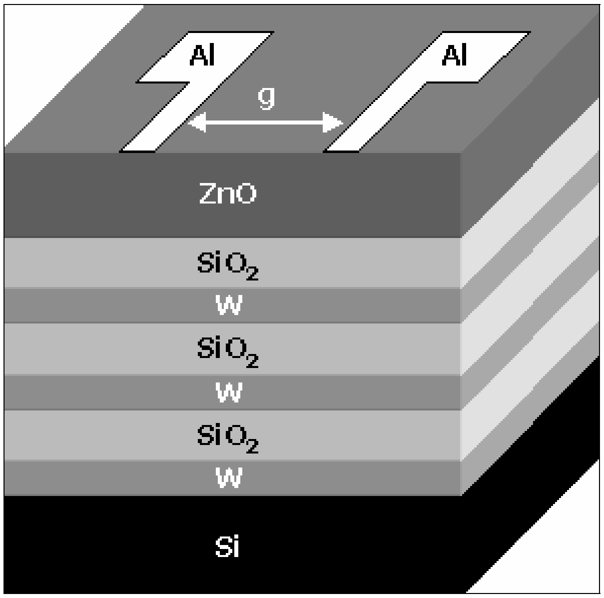

Figure 3.21. Design of ZnO SMR with alternating low acoustic impedance (SiO2) and high acoustic impedance (W) layers form a Bragg reflector.

Device Fabrication

As indicated above, all layers of the SMR were deposited using the Unifilm PVD-300 sputtering system. The deposition parameters for W and SiO_2 are outlined in Table 3.6. Recall that the deposition parameters for ZnO are described in Table 3.2. The thickness of each deposited layer was confirmed using a Leo 1530 thermally-assisted field emission (TFE) scanning electron microscope (SEM), shown in Figure 3.22. Layers understandably varied slightly across the 3” wafer, but were relatively uniform (<10% variation across the wafer). Layer thicknesses are described in Table 3.7, below. Given the material thicknesses measured, the acoustic mirror response was modeled using the model described in Figure 3.1. As can be seen from Figure 3.23, while not as smooth as I would prefer, the mirror should adequately reflect a TSM acoustic wave designed to resonate at 2.0 GHz.

Electrodes were deposited using a CVC E-beam evaporator onto the surface of the ZnO in various configurations consisting of a 30 nm layer of chromium (as a seeding/ adhesion layer) followed by 120 nm of aluminum. The electrodes were formed using a standard photolithography lift-off recipe, described in Appendix C. The various electrode configurations fabricated are shown in Figure 3.24, in which the ‘straight-finger’ geometries that yielded the best results are highlighted. Note that several dimensions of each electrode configuration were implemented in the mask design. Worth noting at this juncture is that very little difference was observed for operation of the TSM with respect to changes in the electrode width or gap spacing between electrodes. Some

Parameter	Tungsten (W)	Fused Silica (SiO_2)
Temperature	Ambient	Ambient
Deposition Pressure	5.00 x 10^{-3} Torr	5.02 x 10^{-3} Torr
Argon:Oxygen ratio	100 : 0	98 : 2
Power	121 A @ 135V	270 W @ ~40V
Distance from target to substrate	6”	7.1”
Substrate material	<0 0 1> Si - lyr 1 fused silica - all others	Sputtered <1 1 0> W

Table 3.6. Unifilm PVD-300 sputtering parameters for the deposition of W and fused silica to form the acoustic mirror.

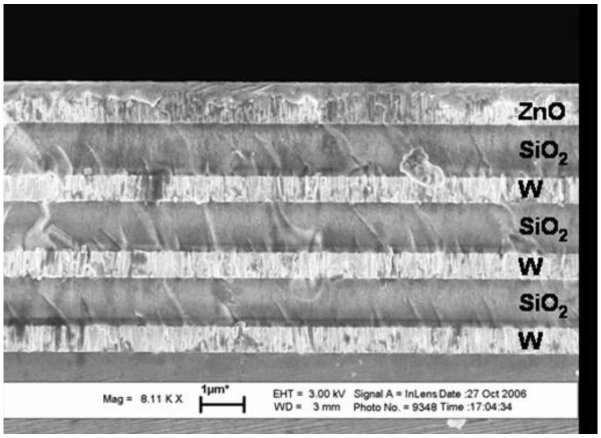

Figure 3.22. SEM image showing profile of fabricated SMR.

Material	Measured Thickness (nm)
Cr/Al Electrode	220
ZnO	710
SiO_2 (L6)	1220
W (L5)	596
SiO_2 (L4)	1206
W (L3)	596
SiO_2 (L2)	1141
W (L1)	596

Table 3.7. Material layer thickness as assessed by SEM

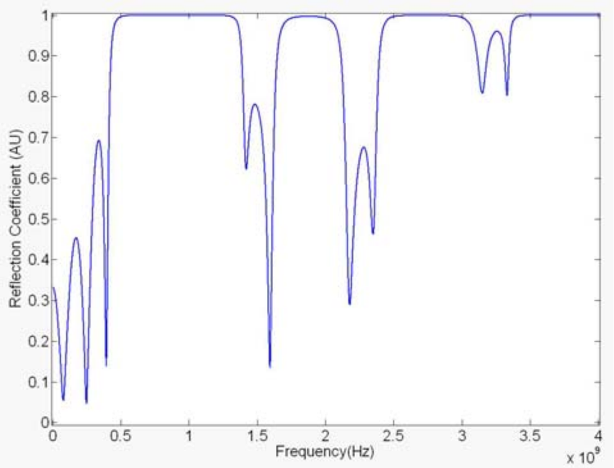

Figure 3.23. Model of mirror response given measured thickness values obtained by SEM for a 6 layer mirror consisting of W and SiO_2.

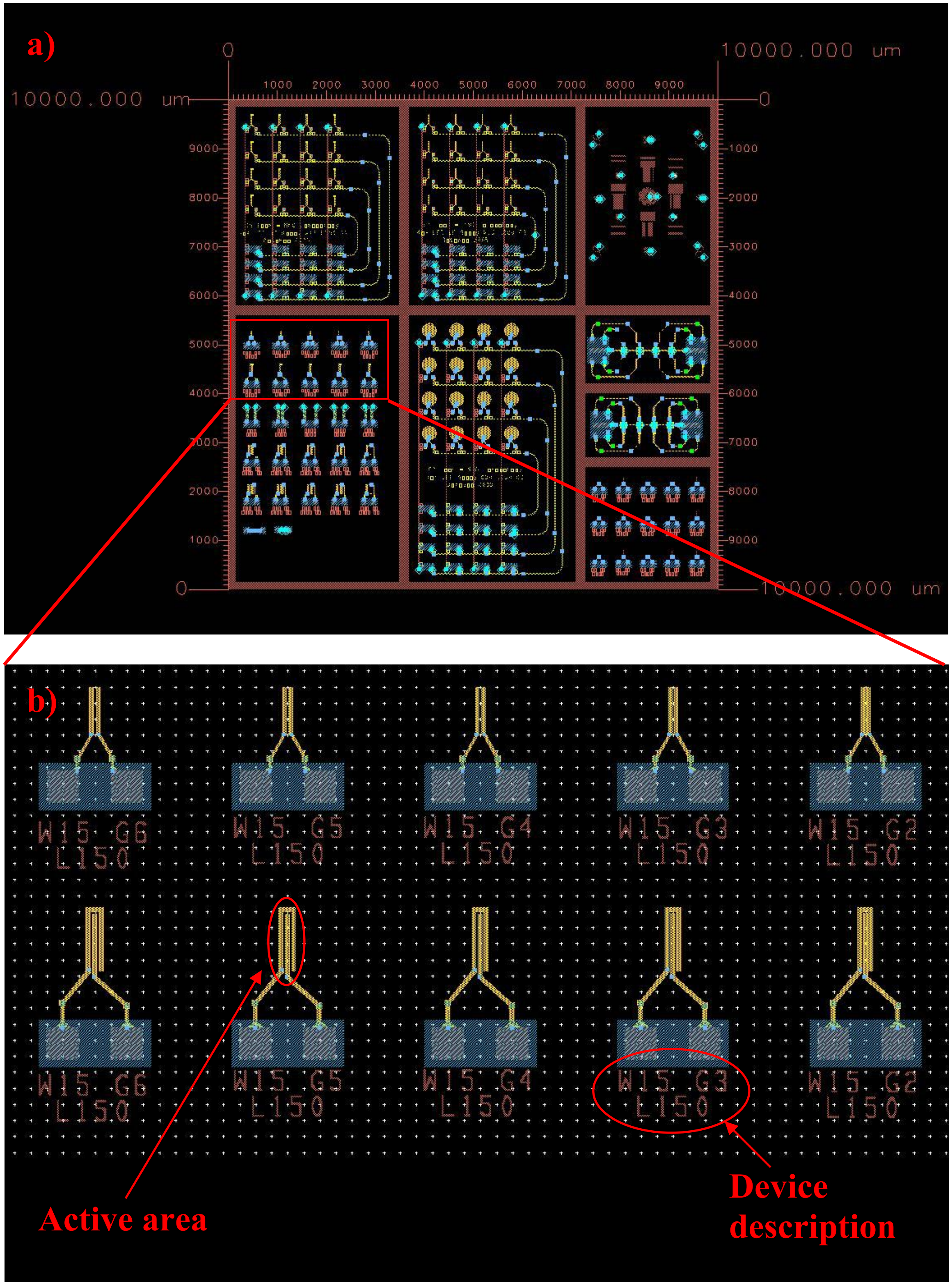

Figure 3.24. a) Electrode geometries fabricated in an effort to achieve LFE of TSM in ZnO with the enlarged image b) showing the 'straight-finger' geometries used to demonstrate high Q TSM devices. [Note: W15 – electrode width = 15μm, G3 – electrode gap 3μm, L150-electrode length=150μm]

differences were observed with later experiments with respect to the different geometries, a discussion of which is provided later in this chapter.

Figure 3.25 below demonstrates both a typical impedance response S_{11} response via a Smith chart and the corresponding magnitude of the impedance response converted using Equation (3.15). As described by Rosenbaum with regards to LFE devices, generally the admittance response, Y_{in}, rather than the impedance response, Z_{in}, is considered which takes the form [20]

$$Y_{in} = j\omega C_0 \cdot \left[1 - K^2 \frac{\tan\left({}^{kd}\!/_{2} \right)}{{}^{kd}\!/_{2}} \right] \tag{3.15}$$

where C_0 is the clamped capacitance of the parallel electrode configuration, K^2 is the piezoelectric coupling coefficient, k is the wave number described in (3.1), and d is the thickness of the piezoelectric film. This relation led to the development of the Butterworth-Van Dyke (BVD) equivalent circuit model, which is often used to represent

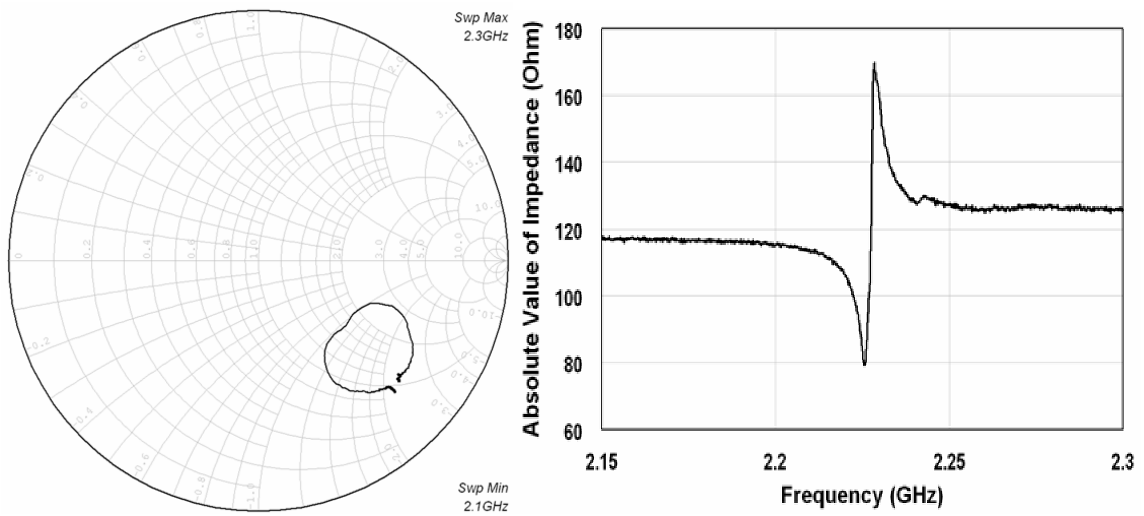

Figure 3.25. Typical magnitude of input impedance (left) and Smith chart of S_{11} response (right) of straight-finger LFE devices. Responses are typical of several thousand resonators fabricated and tested.

the resonance condition at and near resonance. The Ballato equivalent circuit model, briefly discussed earlier in this chapter, provides accuracy outside of the immediate region of resonance, but is a much more complicated circuit with analogs that are not as clearly drawn as with the BVD model. The BVD model, shown in Figure 3.26 [20], is slightly more useful for describing the physical phenomena of piezoelectric resonance and for simple modeling purposes.

From the impedance response described in Figure 3.25(right), note that there are two peaks of interest. The local maximum of the response represents the frequency at which the contributing capacitive and inductive impedances from the BVD model are maximally constructive, and is referred to as the parallel resonance, f_p. Alternatively, the local minimum of the impedance response represents the frequency at which the contributing capacitive and inductive impedances are maximally destructive, and the impedance approaches being purely resistive. This condition is called the series resonance, or f_s. Oscillator circuits can be designed to drive a crystal resonator at either of

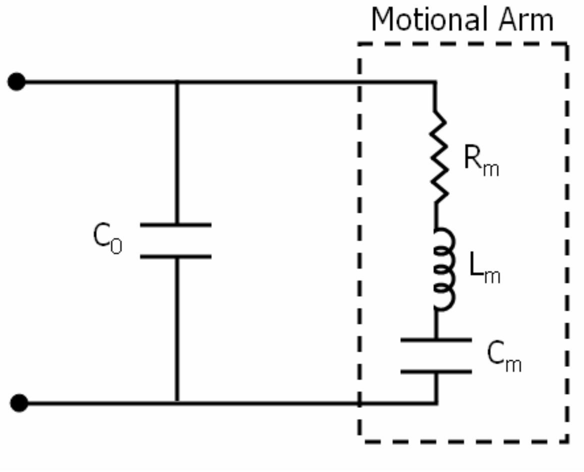

Figure 3.26. Butterworth-Van Dyke equivalent circuit model for piezoelectric resonance. The 'Motional Arm' represents the effective acoustic impedance near the resonance condition.

these conditions, but the parallel resonance is the most common, and is the one that I will focus on for this research.

It should be noted at this juncture that Q and K^2 are common metrics for assessing resonator performance. It is possible to estimate theoretical values for Q from material properties using the following formulae: [20]

$$Q = \frac{v_a^2 \rho}{\omega_r \eta} \tag{3.17}$$

where ω_r is the resonance frequency, and η is the relevant material viscosity, or sometimes as [55]

$$Q = \frac{c}{\omega_r \eta} \, . \tag{3.18}$$

It is similarly possible to estimate K^2 by [20]

$$K^2 = \frac{e^2}{c^E \varepsilon^S} \tag{3.19}$$

Obtaining single-crystal bulk values for ZnO from Auld [55], it is thereby theoretically possible to obtain K^2 values as high as 7%. Due to the fact that the viscosity tensor for ZnO has not been determined, it is not possible to obtain a theoretical Q value for these resonators at this juncture.

A summary of the S_{11} results for the ‘straight-finger’ devices, depicted in Figure 3.24.b, are provided in Table 3.7. The average unloaded Q of the parallel resonance, Q_p, was approximately 340 with a K^2 of approximately 0.4% (n = 30). The calculations used to assess Q and K^2 empirically from the S_{11} response are as follows: [20]

$$Q_p = \left(\frac{f_p}{2}\right)\frac{d\angle Z}{df_p} \tag{3.20}$$

$$K^2 = \left(\frac{\pi}{2}\right)^2 \frac{f_p - f_s}{f_p} \tag{3.21}$$

where f_p is the parallel resonance frequency and $\angle Z$ is the phase of the impedance response of the resonator. Note that the Q_s of the series resonance can be similarly calculated replacing f_p with f_s in Equation (3.20). Note that Q is also commonly estimated by taking a FWHM measurement from the relevant peak from the magnitude of the impedance response, as is done by the HP8753C Network Analyzer.

Immediately noticeable from the results summarized in Table 3.7 is the relatively low K^2 value, given the potential of 7% calculated earlier. From Equation (3.21), we find that K^2 is approximated by the frequency separation of the series resonance and the parallel resonance peaks from the magnitude of the input impedance response. Given the relationship described, the greater the frequency separation between f_s and f_p, the greater K^2. Without a corresponding increase in the magnitude of the f_p peak, however, then there must be a decrease in resonator Q due to the expansion of the width of the peak at half-maximum caused by the wider frequency spread.

Parameter	Average [Std Err]	Maximum
f_p	2.213 GHz [± 1.8 MHz]	2.227 GHz
Q_p	342 [± 19.9]	553
K^2	0.44 % [± 0.03 %]	0.88 %

Table 3.7. Summary of LFE of TSM in ZnO SMR using first successful device design (Figure 3.10). [n=30]

As a comparison, the QCM is widely attributed with having extremely high resonator *Q* (>60,000 at 10 MHz [109]), yet only exhibits k_t^2 of 0.5%. Note that for TE devices the coupling coefficient is represented as k_t^2, whereas LFE devices are described using K^2, as discussed by Rosenbaum. The two are related by [20]

$$k_t^2 = \frac{K^2}{K^2 + 1}. \tag{3.21}$$

Given that the operation of an acoustic biosensor involves the ability to resolve shifts in the resonance condition in response to a perturbation of the boundary conditions at one surface, it is felt that particular focus must be concentrated on optimization of resonator *Q* at the expense of K^2 in order to develop the most effective device for biosensor applications. Anecdotal evidence of superiority of *Q* as a key parameter for sensor application is the extensive and successful use of the QCMs which, as stated, exhibits high *Q* and very low k_t^2.

Confirmation of TSM

Before optimization of the device design can be undertaken, two central points must be confirmed regarding the device operation. As demonstrated by the investigation of Ta_2O_5, it is easy to misinterpret the collected results and make erroneous conclusions about the observed phenomena. In order to confirm that the devices were in fact operating the TSM acoustic wave in the ZnO film, a series of experiments were performed.

The first issue to be resolved is that the device exhibits changes in frequency in response to changing piezoelectric film thickness, confirming the resonance as an acoustic phenomenon. Further that the extracted acoustic wave velocity corresponds with the predicted theoretical values derived for single-crystal bulk ZnO described previously. Films were deposited in three different thicknesses onto the same mirror, of 660 nm, 710 nm, and 790 nm. The thicknesses were confirmed using the Leo 1530 TFE-SEM and the results are summarized in Table 3.8. As the data confirms, the observed resonance is indeed an acoustic wave and the wave velocity is very close to the predicted value of 2,841 m/s. Furthermore, the acoustic velocities extracted agree closely with the results of comparable studies [19, 51-53].

The second issue that must be confirmed is that the wave demonstrates shear particle displacement to the surface. Without access to a tool for physically imaging this parameter, a simple water drop test was implemented to demonstrate this. If the acoustic wave consisted of any longitudinal component, this should readily be transferred into the liquid medium as a compression wave. While the shear wave does exhibit some penetration into the liquid medium, as described by Kanazawa and Gordon [27], the majority of the acoustic energy should reflect back into the piezoelectric crystal. Figure 3.27 represents a typical result of depositing 20 μL of deionized water (DI H_2O) onto the

Measured ZnO Thickness (nm)	**f_o (GHz)**	**Extracted Acoustic Velocity (m/s)**
790	2.0	3,160
710	2.2	3,130
660	2.35	3,100

Table 3.8. Summary of observations of TSM resonance due to different ZnO film thicknesses deposited onto the same acoustic mirror.

device surface, as observed through the S_{11} response. Some deterioration of the resonance was observed resulting in lowering of the Q factor, which is due to the slight energy absorption into the liquid described above. Worth noting is that a more dramatic effect is observed when DI H_2O is deposited onto the surface of a QCM. Figure 3.28 provides a demonstration of that effect for comparison purposes. Note that both resonators exhibit a negative frequency shift upon introduction of water in addition to the spreading and loss of some of the acoustic energy. The frequency shift represents a mass-loading event at the surface. With significantly larger surface area and more water deposited on the surface, the QCM (f_p = ~10 MHz) only reflected a 2.5 kHz frequency shift, while the ZnO SMR (f_p = ~2.0 GHz) shifted by 11.3 MHz. This is consistent with the argument made in Chapter 2 claiming the sensitivity of the sensor to be directly proportional to a power of the resonant frequency.

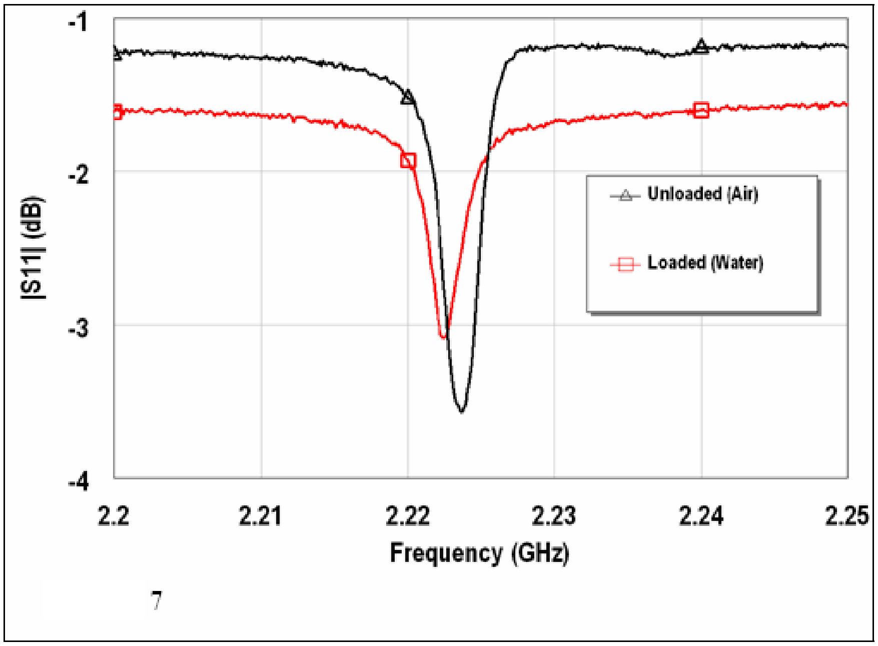

Figure 3.27. Frequency shift observed in S_{11} measurement in response to loading the ZnO SMR surface with deionized H_2O.

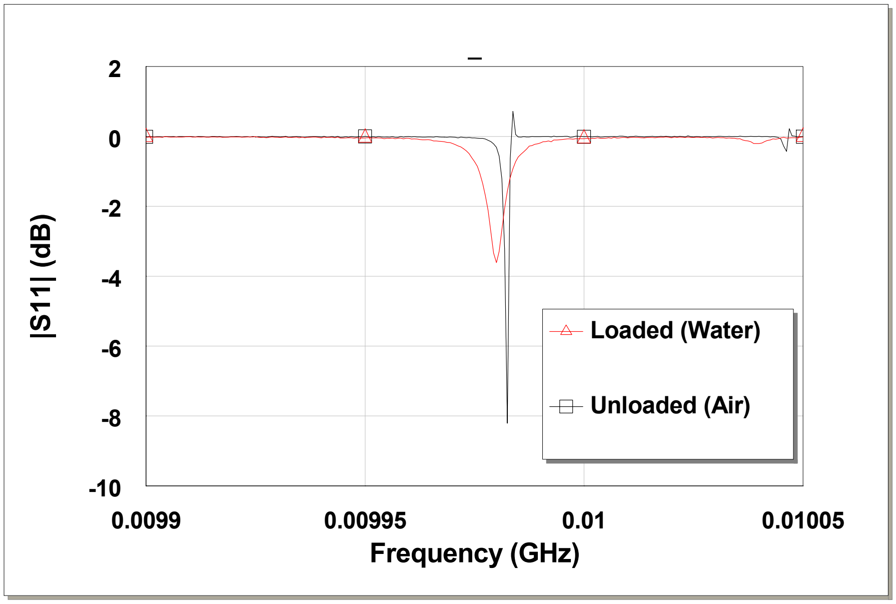

Figure 3.28. Frequency shift observed in S_{11} measurement in response to loading the QCM surface with deionized H_2O

It must be mentioned that several resonance peaks were observed from the broader band S_{11} responses. Two of the stronger resonance peaks were observed at~6,000 m/s and also at ~4,800 m/s. The 4,800 m/s peak was of particular interest as it dampened very little upon presentation of DI H_2O at the device surface. The peak was of significant interest because of its higher Q, yielding high potential for biosensor applications. It is strongly suggested that this resonance be further investigated for such an application. Table 3.7 summarizes the observations of this resonance activity.

Parameter	Average [Std Err]	Maximum
f_p	3.424 GHz [± 6.1 MHz]	3.467 GHz
Q_p	562[± 30.55]	744
K^2	0.23 % [± 0.05 %]	0.27 %

Table 3.7. Summary of LFE of 4,800 m/s resonance in ZnO SMR using device design shown in Figure 3.10. [n=29]

Resonator Testing

Due to the difficulty of fabrication and various issues regarding spurious resonance activity, it was decided that a new electrode configuration was required that balanced the electromagnetic field incident on the piezoelectric film. There was also reason to believe that a superior resonator could be achieved by fabricating a device in which the gap size between electrodes was significantly larger than the piezoelectric film thickness, as described by Rosenbaum as preferable for LFE [20]. The new design was accomplished by implementing a more symmetric electrode design that surrounded the signal electrode with ground electrodes, rather than establishing the ground on a single side as seen in Figure 3.24. The two electrode geometries were then implemented with various electrode widths and gap sizes for each configuration.

A total of eight different electrode configurations were tested using the two electrode shapes depicted in Figure 3.29. Devices were evaluated based on quality factor, Q, and coupling coefficient, K^2, as calculated from the S_{11} response of each device. Results obtained from ANOVA demonstrate that a statistically significant gap ($p < 0.01$) emerges between the performance of the circular shaped devices (Figure 3.28, left) and the straight electrode devices (Figure 3.28, right) when analyzing their K^2 and Q results. It is evident that the average Q is higher for the straight electrode configuration while the effective K^2 is lower. One possible explanation for this is that the circular electrode configuration has a larger surface area over which excitation of the crystal occurs.

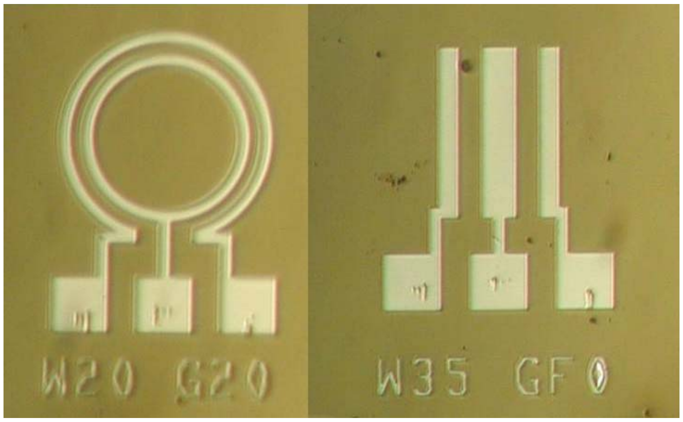

Figure 3.29. New electrode design exhibiting greater symmetry and larger electode gap widths. [Note: W20 - electrode width = 20mm; GF0 - electrode gap = 40 mm]

Therefore, the coupling of the electric field to the crystal over grain boundaries and crystal non-uniformities is more efficient overall while the added mass of the larger electrodes acts to reduce the *Q*. These results are summarized in Table 3.8 and Figure 3.30.

As indicated by the strong correlation between devices G & H, it is readily apparent from the data that the electrode widths fabricated had no statistically significant impact on the device performance as assessed by *Q* and K^2. One would hypothesize that greater distribution of the electric field from a *constant power* source to the piezoelectric crystal would result in a more distributed and efficient coupling of electrical energy into acoustic wave energy. Since *Q* is a ratio of energy conserved to energy dissipated per cycle, it would seem that the *Q* factor should improve as a reflection of this. It was surprising that the size of the gap between electrodes had no clear functional relationship with the device performance. Gap size does have some impact, however, as can be seen from device D in Table 3.8. Compared with the other straight electrode configurations, the 10 µm gap exhibits a significantly lower *Q* and higher K^2, on average. It appears that beyond a particular threshold between 10 µm and 20 µm between straight electrodes, there was a

Device	Shape	Electrode width (μm)	Electrode Gap (μm)	# Tested	Average *Q*	Average K^2
A	Circular	20	10	92	198	0.86%
B	Circular	20	20	72	195	0.87%
C	Circular	20	40	70	192	0.86%
D	Straight	20	10	69	198	0.84%
E	Straight	35	20	74	217	0.78%
F	Straight	35	40	98	206	0.77%
G	Straight	20	50	25	220	0.74%
H	Straight	35	50	44	221	0.73%

Table 3.8. Assessment of device performance of tested resonators from analysis of collected S_{11} parameters.

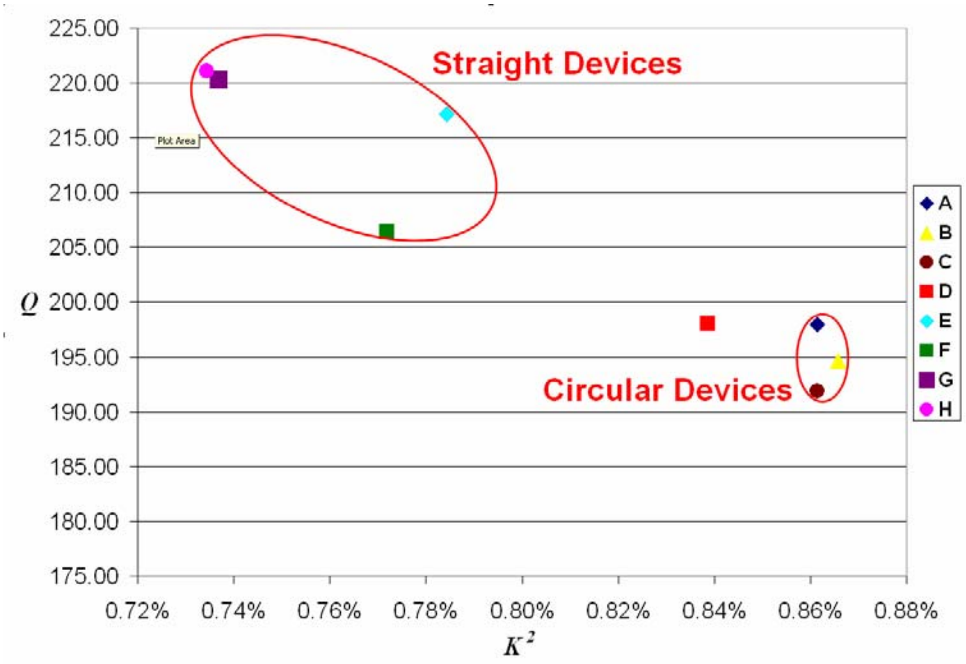

Figure 3.30. Comparison of various electrode configurations using *Q* and K^2. Note, results represent the assessment of over 500 devices fabricated and tested.

notable improvement in *Q*. No clear pattern emerges beyond this, however, for the ranges tested.

Having determined that the straight electrode configuration yielded higher *Q* devices, which has been identified as the desired parameter, 8-element arrays of these devices were fabricated in order to verify that the resonator design displayed in Figure 3.28 (left) performed as well in the array configuration as individual devices. That is to say, to confirm that the array structure did not bear any beneficial nor detrimental effects on the resonator's performance. Sampling more than 150 arrayed devices similar to those seen in Figure 3.31 showed that there in fact was a statistically significant difference in device performance. Note that tests were performed on both arrayed circular electrodes as well as straight finger electrodes. As in the isolated individual devices, the Q of the straight finger devices outperformed the circular devices. There was a significant deterioration in performance, however, from incorporation into array configurations. All of these arrays are demonstrated in Appendix B, and are similar to the array demonstrated in Figure 3.31, below. Results are summarized in Table 3.9. A 30% decrease in Q and a 15% decrease in K^2 was observed for straight finger devices with a 20 μm gap fabricated in the array configuration versus the isolated configuration. For devices fabricated into 8-element arrays with a 50 μm gap, again a decrease of 28% was observed in Q but only a 8% decrease in K^2. Note that the trade-off between Q and K^2 is still evident in these devices. One explanation for the decrease in performance is the addition of a significant amount of metal surrounding the active devices for bonding pads and ground-bus connections. The added mass from the electrodes provide a lossy material at the surface boundary which can act to scatter the acoustic energy. In addition, the different electrode configuration itself is likely to have altered the electric field from the isolated configuration, contributing to a change in the resonator performance. I felt that the results

Array	**Electrode Shape**	**Electrode width (μm)**	**Electrode Gap (μm)**	**# Tested**	**Average Q**	**Average K^2**
1	Circular	20	10	46	133	0.83%
2	Circular	20	40	32	121	0.83%
3	Straight	35	20	63	150	0.66%
4	Straight	35	50	23	159	0.67%

Table 3.9. Assessment of arrayed device performance of tested resonators from analysis of S_{11} response.

were still good enough to proceed, however, with sensor testing.

Biosensor Compatibility

As this is a novel resonator design implementation, it is important to characterize the general stability of the TSM acoustic wave in the thin film ZnO SMR. First, it was important to confirm that the resonance itself is stable and does not vary over time. An experiment was conducted holding the resonator fixed at 25ºC while constantly driving the resonator at 1 mW using a HP 8753C Network Analyzer. Devices were probed using Cascade Microtech ACP40 GSG-150 probes. It was found that the resonator was more than suitably stable, exhibiting a 0.01% shift (32 kHz) after 3 hours of constant resonance. The results are depicted in Figure 3.32.

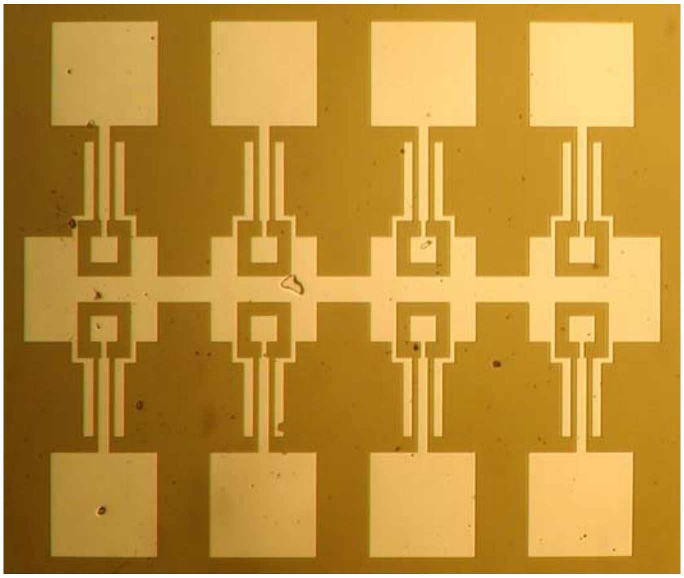

Figure 3.31. Digital image of fabricated 8-device array. Device is designed for probing with Cascade Microtech ACP40 probes and with pads large enough for subsequent wire bonding. (occupies 2.0 mm x 2.4 mm space)

A second parameter commonly investigated relates to the resonators susceptibility to varying temperatures. The parameter often investigated regarding this susceptibility is the temperature coefficient of resonant frequency (TCF), which is defined as

$$TC(f_x) = \frac{df_x}{dT} \cdot \frac{1}{f_{x,RT}} \tag{3.22}$$

where T is the temperature, f_x is the relevant resonant frequency and RT represents room temperature (25°C). The temperature was varied from 25°C up to 175°C in increments of 25°C and the resonant frequency was measured after the system was allowed to stabilize at each temperature point for at least 10 minutes. The results yielded an empirically derived TCF for the series and parallel resonance of +24.6 ppm/°C and +25.6 ppm/°C,

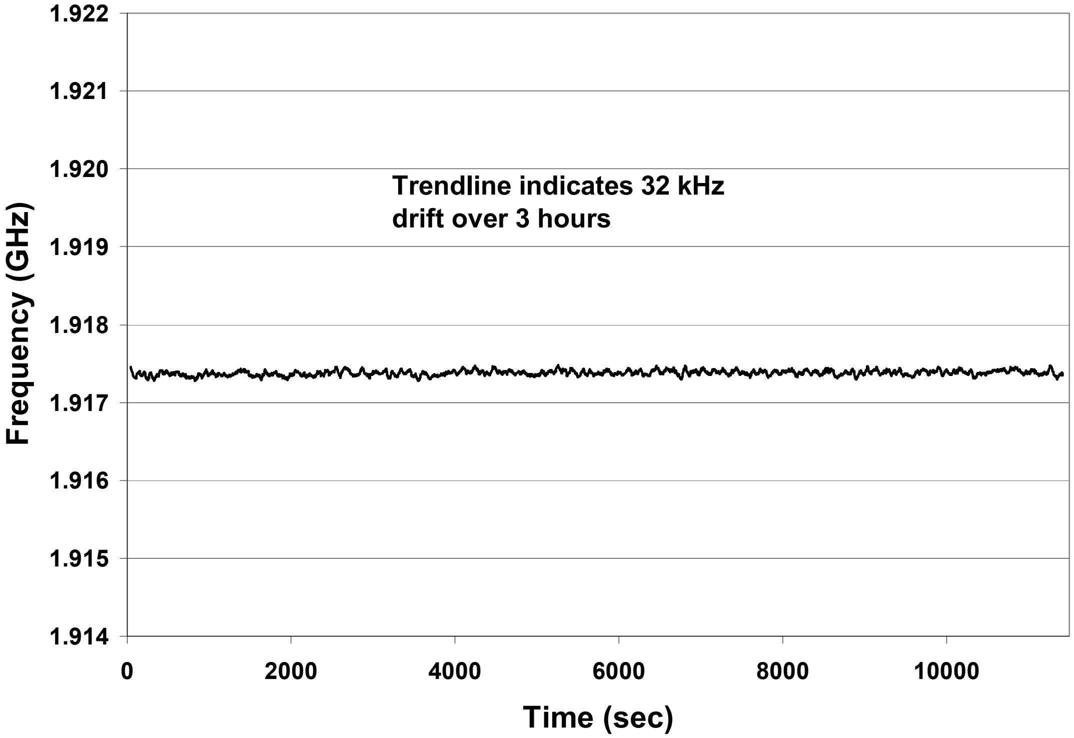

Figure 3.32. Parallel resonance frequency plotted against time demonstrating stability of resonance over a three hour time period, at a constant 25ºC.

respectively. Note that these are considered relatively low TCF values, suggesting these devices are appropriate for sensor applications. These results are demonstrated in Figure 3.33. This experiment was conducted 3 times with identical results.

The susceptibility of device *Q* and K^2 was also investigated to confirm no degradation in the quality of the resonance itself with increasing temperature. It was found that the K^2 remained very stable over the temperature range tested, varying by only 0.1% over the 155°C range. The *Q* drift of the resonator was slightly more significant, varying by roughly 42% over the 155°C temperature range. For application in a bench-top biosensor application in which testing is likely to occur at or near room temperature, the *Q* remained stable enough to consider negligible exhibiting an average shift of 0.28/°C

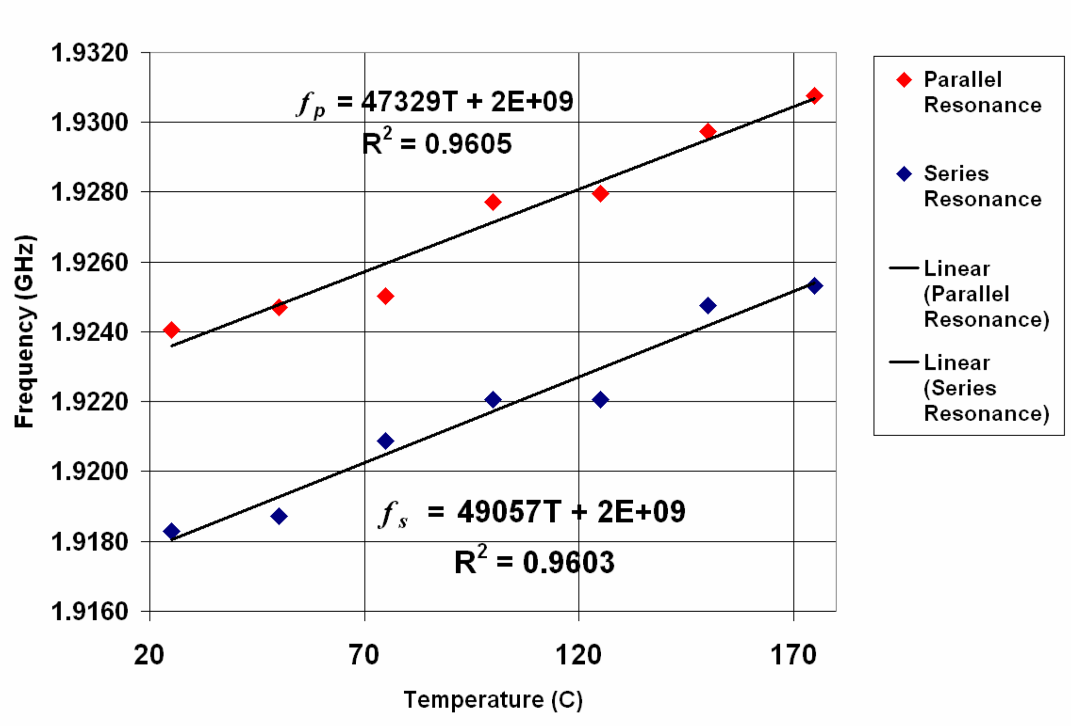

Figure 3.33. Frequency drift of parallel and series resonance frequencies with increasing temperature.

(<0.2% per degree). The results for the temperature stability of Q and K^2 are summarized in Figure 3.34 and 3.35, respectively.

When designing sensors for use with physiological samples, it is important to assess the sensor's performance under varying sample conductivity conditions. Hu *et al.* characterized the effects of sample conductivity on QCMs employing LFE rather than the typical TE for biosensor applications [110]. I determined that a similar investigation of the characteristics of the TSM in ZnO was sufficient to investigate this.

Considering the goal of employing these resonators in biosensor applications with biological fluid samples, the resonators were tested over a range of sample conductivities. Biological fluids are filled with electrolytes, which imbue the fluid they are in with conductive properties. It is common in the literature to see 0.9% NaCl in DI H_2O described as an equivalent salinity to blood. Therefore, I loaded the surface with 0.0% to 0.9% wt/vol of NaCl in DI H_2O. Saline solutions were prepared using 99.5% NaCl (Sigma) and HPLC-grade deionized H_2O (Burdick & Jackson) and mixed for at least 30 seconds on a mini vortexer (VWR Scientific Products). The devices were tested using the equipment described earlier in this chapter. In addition, a laptop computer running a custom LABVIEW program for tracking the resonance frequency of the device under test was employed [111]. The device arrays were exposed to the saline solutions by hand pipetting ~1 μl directly onto the resonator array surface while being probed.

Results indicate that the magnitude of resonator frequency shift varied little in relation to loading with pure water alone, as indicated in Figure 3.36. As can be seen, the percentage of frequency shift with increasing sample conductivity was less significant than the increasing noise level. These devices are not ultra high Q, as QCM devices are,

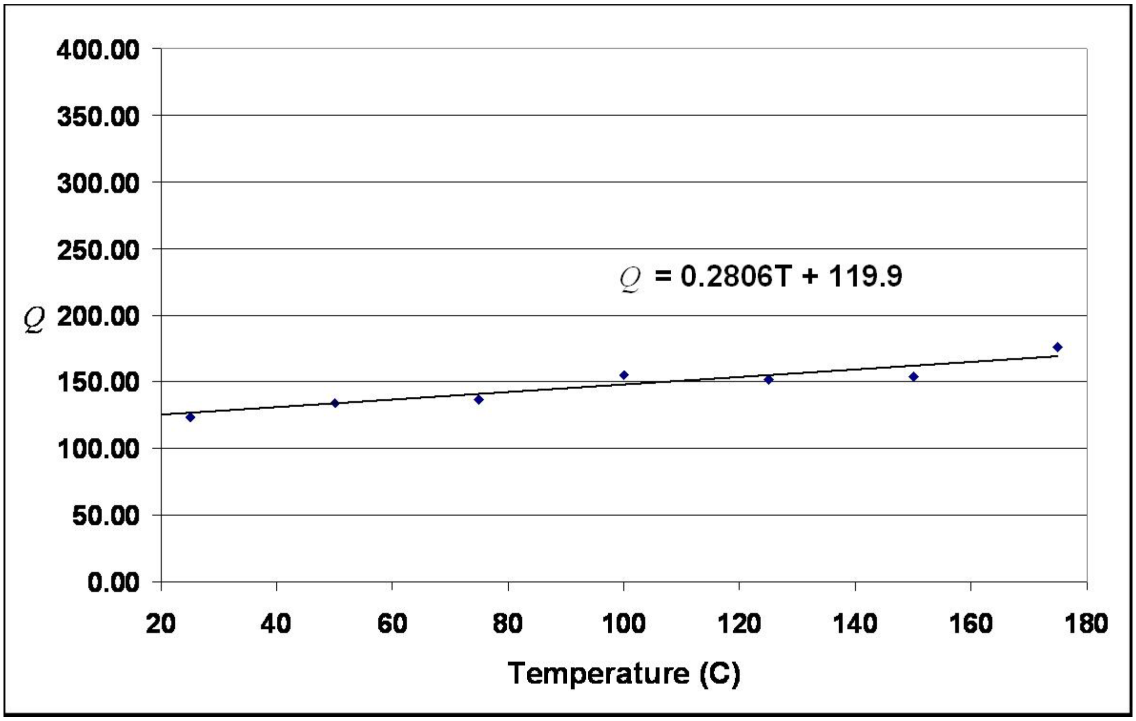

Figure 3.34. Susceptibility of resonator Q to changes in operating temperature from 25°C to 175°C.

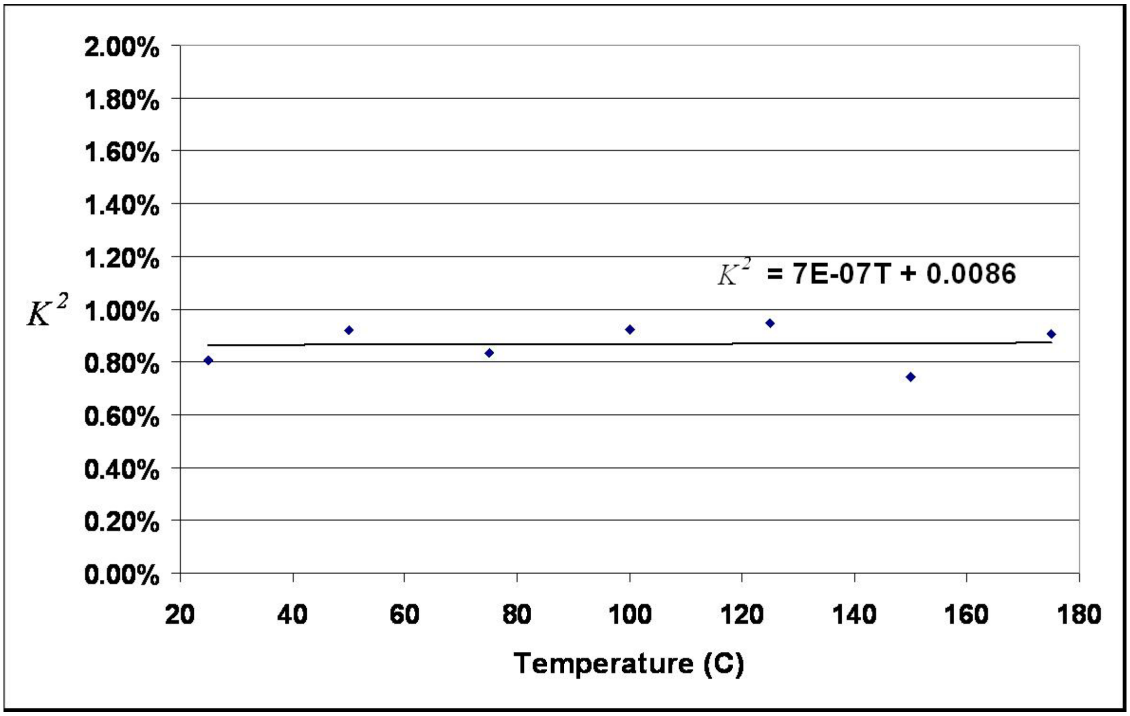

Figure 3.35. Susceptibility of resonator K^2 to changes in operating temperature from 25°C to 175°C

so the resonance peak is still slightly broad. Incidental high-frequency fluctuations in the reflection parameters will cause the parallel resonance monitor to register a shift if frequency, though the broad peak does not actually shift. The error bars in Figure 3.36 indicate the measured variance due to these incidental fluctuations. A further indicator of this can be seen in Figure 3.37, which demonstrates the results of a typical experiment when a 0.9% saline sample is deposited on the device surface then subsequently washed with DI H_2O. Figure 3.38 is provided as a comparison of the relatively lower levels of noise observed with DI H_2O alone.

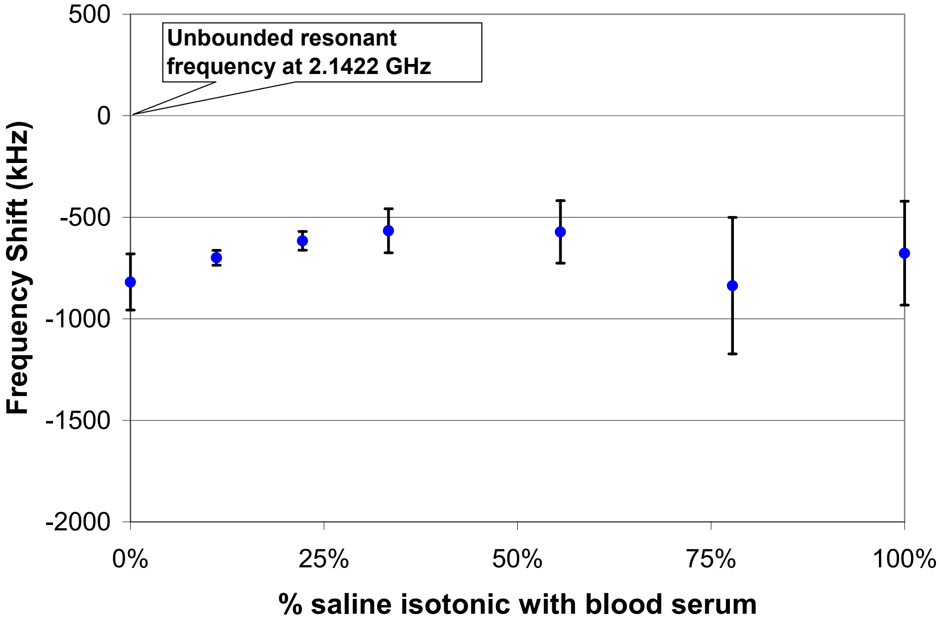

Figure 3.36. Typical experiment demonstrating change in parallel resonance frequency with increasing saline concentration on the surface of the resonator.

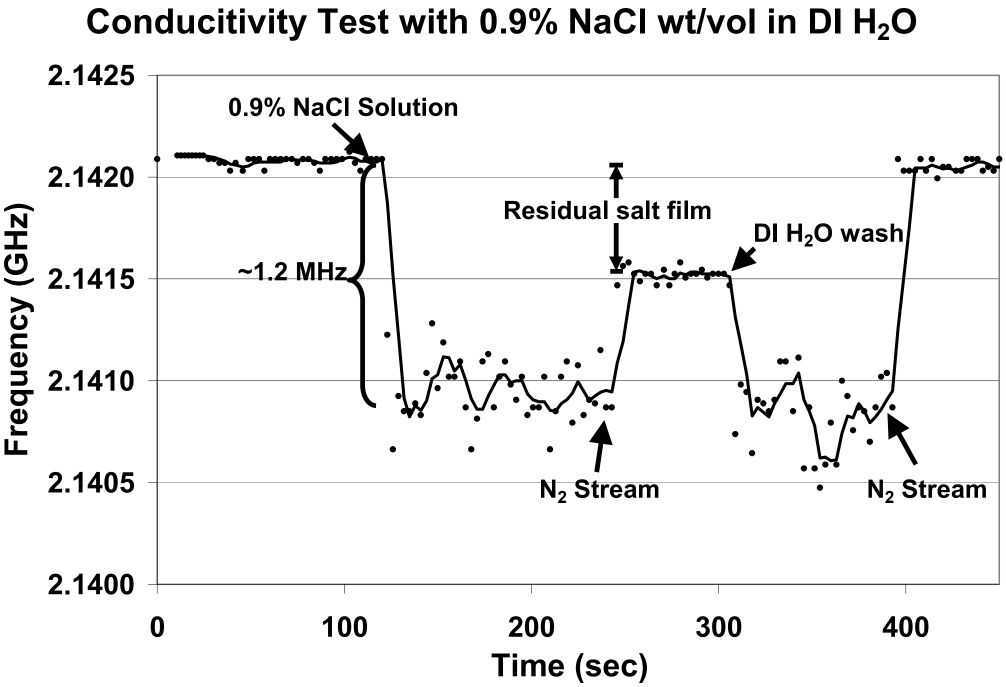

Figure 3.37. Demonstration of a typical conductivity experiment with 0.9% NaCl in DI H_2O.

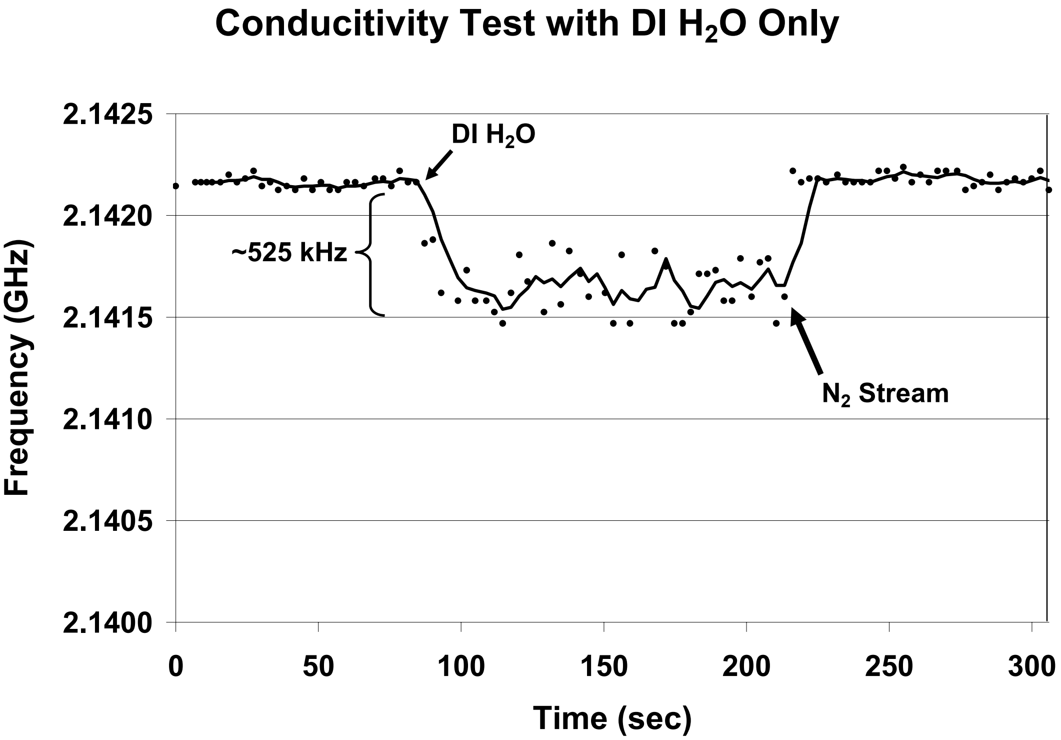

Figure 3.38. Demonstration of a typical conductivity experiment with 0.0% NaCl in DI H_2O.

CHAPTER 4

SENSOR FUNCTIONALIZATION

In order to functionalize the resonators developed through Chapter 3 for biosensor applications, it is necessary to create conditions at the surface of the piezoelectric layer that execute a molecular recognition capability for a specific target. This often requires a surface chemistry protocol involving the immobilization of an appropriate capture agent at the surface of the device that in turn has a high degree of specificity for a single target molecule. In this chapter I will discuss the selection of appropriate capture agents and the development of an appropriate protocol for immobilization of those capture molecules on the surface of my resonators. The use of a reference sensor as a control is absolutely critical for this protocol. Reference sensors functionalized with capture molecules specific to a target absent from the test media help guarantee that any frequency shift of the test sensor is due to binding of the intended target and not to non-specific binding or other changes in the surface. This argument can be made because both the test sensor and the reference sensor have received identical functionalization treatments with similar capture molecules and exposed to the same test medium. Any difference in behavior observed in the two sensors can be attributed to binding of the test sensor to target molecules in the liquid sample under test.

Recall that acoustic wave biosensors function by detecting changes in the path over which the propagating wave travels (see Chapter 3). As with most types of biosensors, the ability to obtain repeatable results from an acoustic sensor, especially one with potential for extremely high sensitivity, is related to the repeatability of the prepared surface layer, or biolayer, which executes the function of molecular recognition. A requirement for any high precision biosensor is that the output signal, or device response, be repeatable given multiple identical samples and on different sensor elements prepared in the same manner. Therefore controlled, reproducible immobilization of appropriate capture molecules to functionalize the device is necessary to preclude device to device signal variations. In assessing the quality of the various biolayer protocols attempted in this research, therefore, it is critical to qualify both the uniformity and repeatability of the biolayer.

Capture Molecule Selection

There are a myriad of capture agents that have been employed to functionalize transducers of various types into biosensors since the first biosensor was developed by Updike and Hicks in 1967 [112]. These include oligonucleotides, receptor proteins, enzymes, antibodies, synthesized polypeptides and lectins [113]. For the purposes of our specific applications, recall that we desire keeping interactions close to the surface so as to maximize the device sensitivity. For that reason, there is no need to consider capture agents larger than these. With the exception of glucose sensors, the most commonly employed capture agents are antibodies (Ab) [113]. To an increasing degree, however, biosensor developers are looking more towards various oligonucleotide structures, such as aptamers, for various reasons discussed later in this chapter. Recalling the goals of this biosensor research, it is a high priority to establish a biosensor with high specificity and selectivity. Of the capture agents reviewed for this research, antibodies and aptamers top the list for high affinity for their target analytes. A secondary priority is the ease of fabrication and potentially low cost of production. Given these criteria, I will consider both options and how well they would work for our application.

Antibodies

As mentioned, antibodies are one of the most commonly employed capture agents for biosensor applications. Ab’s, or immunoglobulins (Ig’s), are produced by all vertebrates as an essential component of their immune system. These molecules exhibit specific molecular recognition capability, determined through a complex evolutionary refinement process [12]. They are produced by the B cells of all placental animals in five isoforms, including the pentamer IgM, the dimer IgA, and the monomers IgD, IgE, and IgG. Among these, the IgG molecule is most widely used because it is by far the most abundantly produced and exhibits the greatest stability (generally lives 4 to 10 times longer than the other isoforms in plasma) [12].

The IgG molecule is a 150 kDa protein made up of two “heavy chain” segments (446 amino acids in length) and two “light chain” segments (214 amino acids in length) and comes in four subclasses. The four subclasses are categorized based on minor structural differences of the heavy chain, mostly accounting for the location of Cystine residues. The general monomer structure is demonstrated in Figure 4.1 below. The binding domain is located at the two amino-terminals of the structure and exhibit excellent specificity and affinity for their targets. The binding mechanism is controlled by both the variable amino acid residues that make up the binding pocket and the ‘hinging’ action of the di-sulfide bonds holding the heavy and light chains together. Taken together, IgG_1 molecules (the most abundant IgG subclass) have reported extraordinary affinity ($K_a > 10^{10}$ M^{-1}) [114].

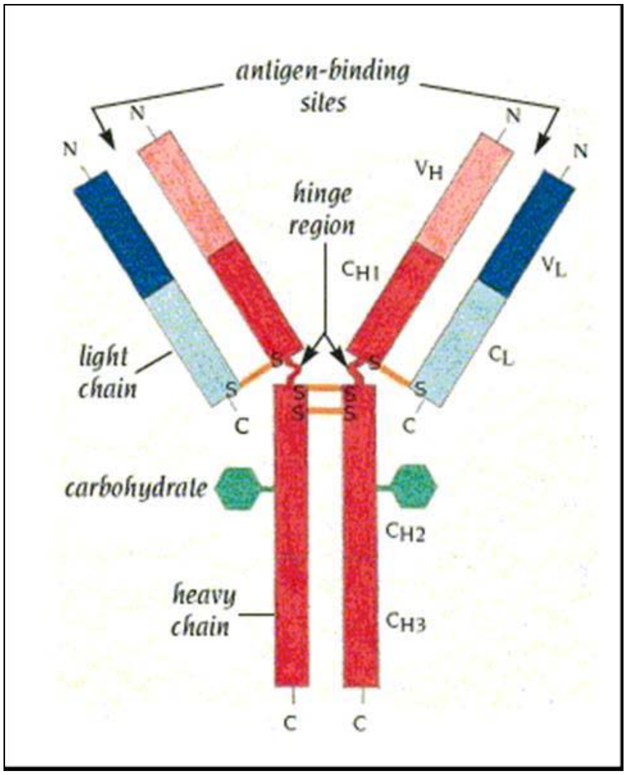

Figure 4.1. Secondary structure of the IgG monomer with individual regions identified [115].

Another attractive component of using IgG antibodies is the wide array of surface chemistry protocols for immobilizing the molecules in a functional manner on various surfaces. Recall the binding domain is located at the amino-terminals of the protein as indicated in Figure 4.1. For use as a capture agent attached to the surface of a transducer, the molecule must therefore be immobilized nearer the carboxyl-terminal (the region described as the F_c portion of the Ab, or crystallizable fragment) in order to maintain functionality as a capture agent. It is further desirable to achieve a covalent (or stronger) bond between the antibody and the device surface, so as to achieve a more generally stable sensor configuration. All protocols that I have encountered to date achieve this with the IgG molecule by covalent binding of an acid head group to an available amine terminated residue on the antibody. The F_c portion of the antibody exhibits a relatively rich population of available lysine residues, as indicated by the highlighted regions in Figure 4.2 below [116]. There are 18 Lysine residues and 5 Arginine residues in each of the two 220 amino acid length segments of the heavy chain within the F_c portion of the antibody.

Most of the work regarding covalently binding IgG molecules to *oxide* surfaces in an effort to functionalize them has focused on the use of quartz (SiO_2). Hydroxyl groups at the surface of an oxide provide sites for reaction with cross-linking molecules to form covalent bonds [117]. One of the more common methods for functionalizing SiO_2 surfaces involves the use of organosilanes. Success with immobilizing antibodies on SiO_2

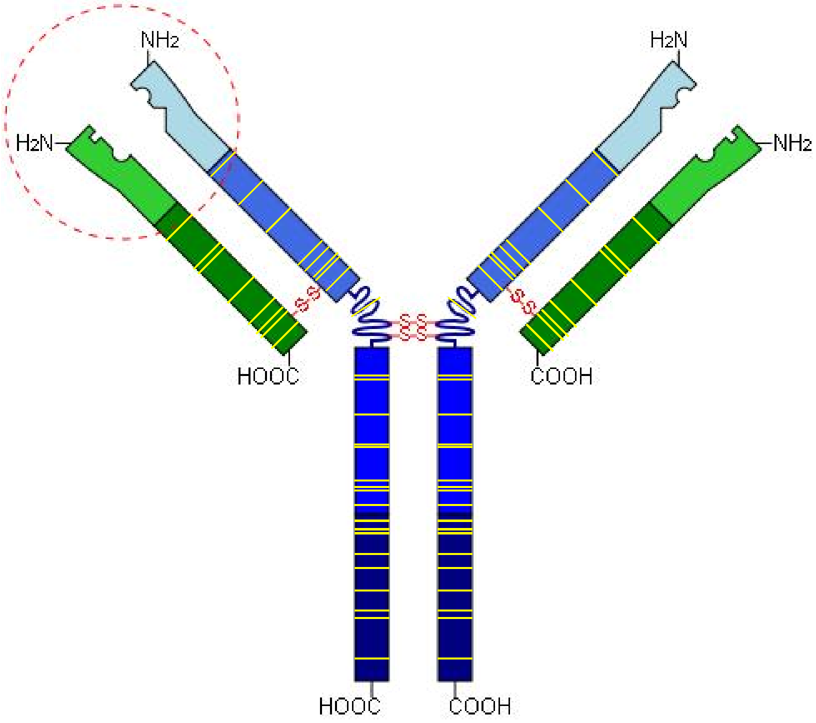

Figure 4.2. IgG molecule with approximate location of Lysine residue highlighted.

surfaces has been shown using amine- and thiol-terminal silanes such as 3-mercaptopropyl-trimethoxy-silane (MTS) with a variety of heterobifunctional crosslinkers, such as N-γ- maleimido-butyryloxy succinimide ester (GMBS) [117, 118]. Other work in modifying SiO_2 surfaces has focused on forming self-assembled monolayers (SAMs) using epoxysilanes [119, 120]. The great advantage of using an epoxysilane such as (3-glycidoxypropyl) trimethoxy-silane (GPS) for forming SAMs on oxide surfaces is that it eliminates the need for a secondary crosslinker between the silane molecule and target antibodies. The exposed epoxy groups react readily with amine groups. Given that hydroxyl groups are also available at the surface of planar ZnO, it is thought that some of these techniques may be employed.

Despite the amount of research that has been performed on various oxides, including SiO_2, there have actually been relatively few studies involving the functionalization of planar ZnO surfaces. One study reports the use of 3-aminopropyl-triethoxy-silane (APS), which is an amine-terminated silane, to covalently bind Interleukin-6 to the surface of device-quality ZnO films [121]. APS is used as the primary crosslinker, followed by glutaraldehyde as a secondary homobifunctional crosslinker to bind the protein, Interleukin-6. A major drawback with the use of glutaraldehyde, however, is that it binds to other gluteraldehyde and is known to form large polymer conglomerates which may bind many residues and form large multiprotein complexes [117]. My own early attempts at functionalizing planar ZnO using APS and glutaraldehyde yielded surfaces that indicated this was in fact occurring in my own preliminary trials. This study does demonstrate, however, that silane chemistries can be applied to the surface of ZnO.

There are many disadvantages to using antibodies for capture agent applications, of course. For one, the production of monoclonal antibodies for sensor and immunoassay applications is generally achieved through the Hybridoma Technique. This protocol involves the generation of lymphocytes due to the immune response of an infected vertebrate and isolation and extraction of these cells. The cells are then fused with myeloma cells, thereby forming hybridoma cells, that are then allowed to produce monoclonal antibodies (mAb’s) indefinitely in cell culture. The protocol is demonstrated in Figure 4.3 below. Hybridomas are both laborious and expensive to produce and can

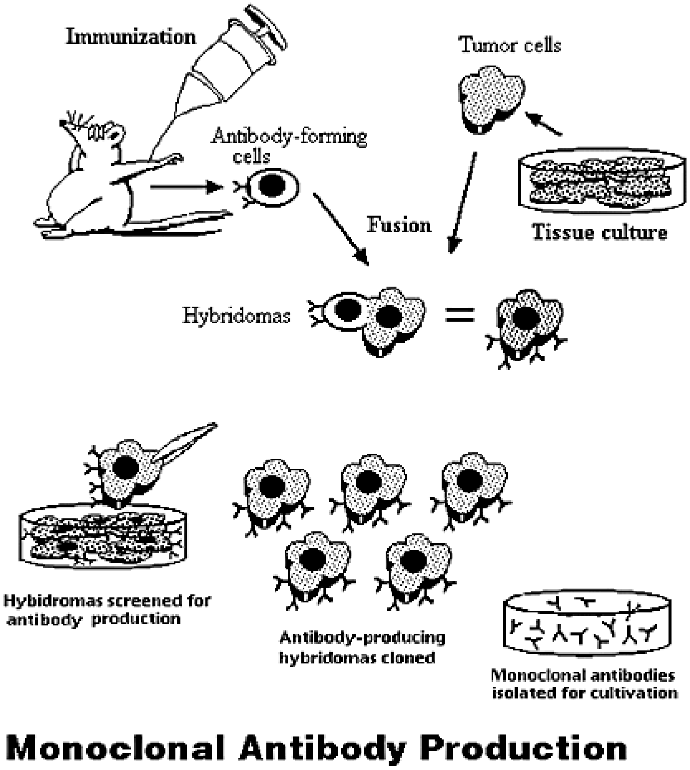

Figure 4.3. The *Hybridoma Technique* is the predominant method for generating monoclonal antibodies for commercial and laboratory applications. [Taken 09/04/2008 from **http://www.accessexcellence.org/RC/VL/GG/monoclonal.php**]

often prove restrictive. It is obviously difficult to create Ab's using this process for toxins or for targets which do not elicit an immune response. Additionally, mAb's tend to vary from batch to batch [122]. It is also impossible to generate mAb's for targets under non-physiological conditions. These proteins are also sensitive to temperature and pH changes, and denaturation of the molecule is irreversible. Finally, Ab's are relatively large (150 kDa) and difficult to immobilize on various surfaces in such a way that ensures its binding capacity for its target.

Aptamers

As previously mentioned, aptamers are oligonucleotide sequences that can selectively, and with high affinity, bind a target ligand. Both RNA and DNA strands can fold into a plethora of well-defined secondary and tertiary conformations for a given sequence, which is the basis for using them as binding agents for a wide variety of molecular targets. Aptamer have been found to undergo significant conformational changes upon binding with its target ligand, generally yielding a new complex in which the aptamer becomes imbedded in the tertiary structure of the target ligand [123]. Selection of the appropriate oligonucleotide sequence represents the crux of determining appropriate aptamers for different target ligand.

The first *in vitro* selection of RNA was accomplished in 1974 by Sol Spiegelman [124]. It was only after the development of polymerase chain reaction (PCR), however, that it became reasonable to more generally search for appropriate aptamer species for known target ligands [125]. So ripe was the field for such a breakthrough, that three separate groups (two within the same month) developed a similar process, exclusive of one another, for aptamer selection [126-128]. The process developed for aptamer selection is now referred to as the Systematic Evolution of Ligands by EXponential enrichment (SELEX) process. This process is described in Figure 4.4 below. The SELEX process is essentially a technique for reviewing extraordinarily large combinatorial libraries (most systems start with a DNA library containing 10^{14} to 10^{15} individual and distinct molecules) through an iterative process allowing for *in vitro* selection and subsequent amplification of selected oligonucleotides. The process is repeated as many times as necessary to determine the best oligonucleotide for a given target, for degree of specificity (rejecting candidates that bind structural analogs), and for maintained activity in desired environmental conditions. Early implementation of the SELEX process would take as long as two days to accomplish a single round. Given that between 8 to 15 rounds are necessary to yield an acceptable aptamer candidate, the overall process would take the better part of 2-3 months of constant refinement [122]. Vast improvements in instrumentation automation and understanding of individual step sensitivities has shortened the time of each round to less than 2 hours, yielding final candidates in less than 2 days [129].

The use of aptamers as capture agents in biosensor applications has the following advantages [122]:

- Large number of thermodynamically stable structural variants vs. peptides of equal length
- No known structure for which aptamers cannot be made to bind to
- Specificity and affinity to match and, in some cases, surpass antibodies
- Can use DNA microarray spotting technology to immobilize defined densities in precise locations on a large scale

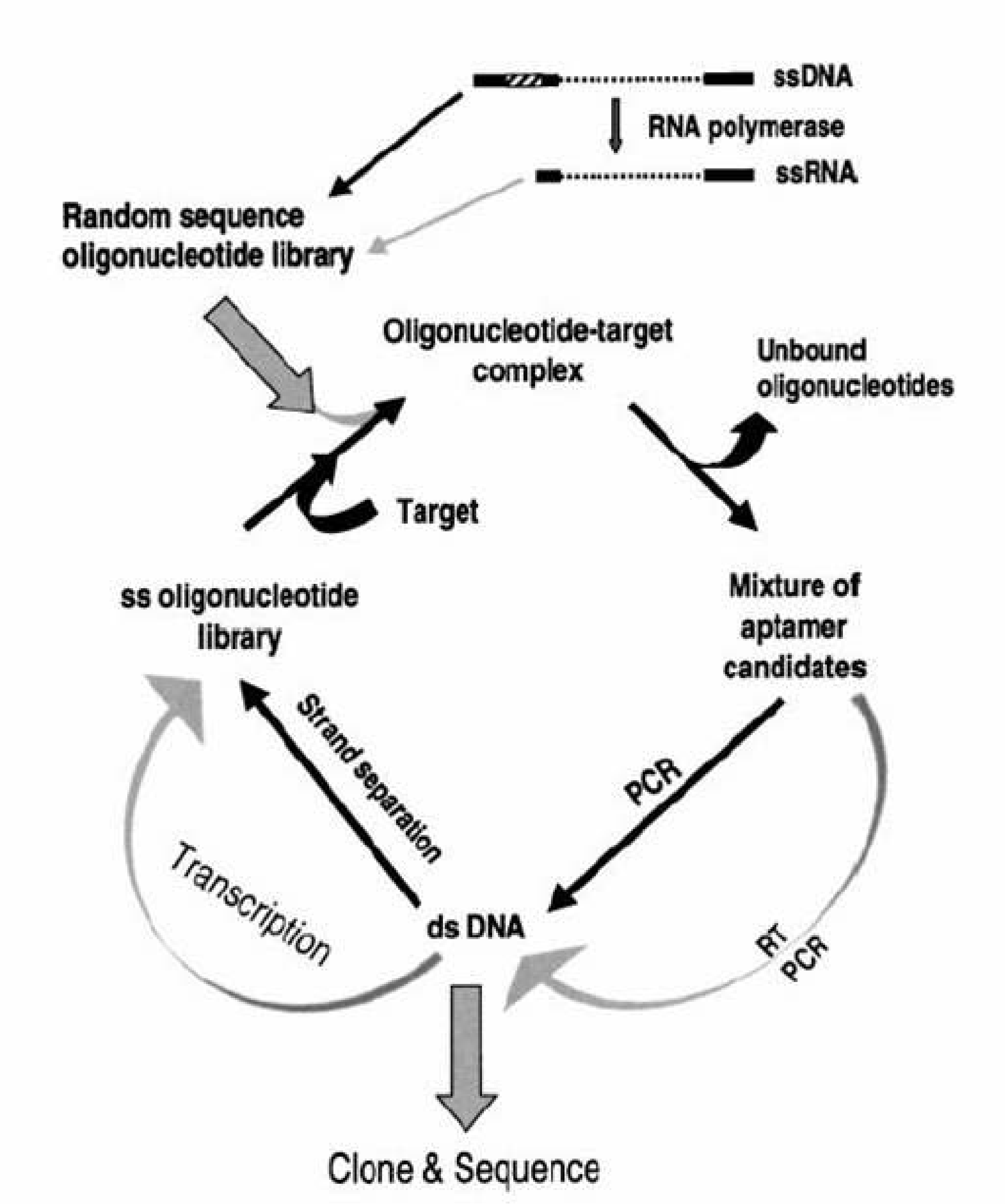

Figure 4.4. Systematic evolution of ligands by exponential enrichment (SELEX) process.

- Selected species can easily be modified to improve affinity and specificity (unlike Ab's) as well as to improve robustness in various environments
- Aptamers are much lighter and smaller, thereby capable of forming denser layers and being closer to the "sensing" surface

- Generation and selection is performed *in vitro*
    - Can function in non-physiological conditions
    - Selection conditions can be manipulated, allowing kinetic parameters to likewise change on demand
- Can be used for toxins or other targets that do not elicit an immune response
- Little to no batch-to-batch variation
- Reporter molecules (eg. radio-labeling) and other modifications can be arbitrarily bound at precise locations, increasing capability and variability
- Denaturation is reversible
- Long shelf-life under adverse conditions
- Can bind target proteins irreversibly, if desired
- Rapid automated selection process for aptamer isolation
- Oligonucleotide clones are cheap and easy to mass produce

The Decision to Use Antibodies

With regards to applications specific to this research, there are two attributes in particular that make aptamers especially attractive. First, it becomes possible to fabricate sensors with re-usable surfaces. Aptamers can be made to release target upon exposure to extreme heat, salt, or chelating agents [130-132]. Second, aptamers are easily immobilized on nearly any surface with controllable densities [132]. Given the limited investigation of covalently binding capture molecules to the surface of planar ZnO, this becomes an obvious advantage.

There are disadvantages, as well, to using aptamers. First of all, they are generally not commercially available for many targets. In order to obtain aptamers for any particular target, one would most likely have to partner with a laboratory that has the time and inclination to collaborate. Georgia Tech does not have such a laboratory, so any collaboration would likely need to be conducted remotely. Secondly, nucleic acids are notoriously difficult to deal with and would likely require significant expertise in biochemistry in order to manipulate for a novel application. While I have a confidant grasp of the fundamentals of biochemistry, a parallel doctoral-level pursuit in the field would be neither feasible nor appropriate. Finally, the application itself of a new aptamer species to a previously un-investigated planar surface is entirely novel, and would require a greater investment in time and resources than pursuit of a more conventional approach.

Given the already significant challenges of the goals of this thesis research, it is unlikely that this would be the more expeditious solution to the dilemma of functionalizing the surface of my biosensor. Suffice it to say that there is extraordinary potential in the use of aptamer technology as the capture mechanism for biosensor applications. It is strongly felt by this researcher that due to advantages such as size, overall stability, and the potential for reuse of each sensor, that aptamers will likely play a significant role in the ultimate development of this and other biosensor technologies.

I have therefore determined that because of the prevalence of existing immobilization techniques and relative ease of procurement, Ab’s should be used as the appropriate capture agent for functionalization of these biosensors. It must be repeated that this approach still has drawbacks, such as being relatively costly for mass production, slow development times, and the relatively large size of each molecule, to name a few. This approach still accomplishes the proof of concept for this sensor technology. In the future, it will likely be more interesting to pursue aptamers and other molecules that offer means of skirting these drawbacks. Given our capture agent selection and device function, we can therefore identify the biosensor being developed as a label-free immunosensor array.

Surface Preparation Protocol

As mentioned above, a critical aspect for the development of label-free immunosensors is the employment of *highly uniform* and *repeatable* antibody immobilization techniques. As previously discussed, silane chemistries offer a strong possibility for successfully immobilizing Ab's on the surface of our ZnO in a covalent manner. A review of the literature identifies two different molecules appropriate for such a purpose. They are (3-glycidyloxypropyl) trimethoxysilane (GPS), and (3-mercaptopropyl) trimethoxysilane (MTS) for the immobilization of IgG Ab's. In order to assess the chemical modification of the ZnO surface, I employed water contact angle measurements, atomic force microscopy (AFM), and fluorescence microscopy.

To provide visual confirmation of the density and uniformity of antibody immobilization, fluorescently labeled IgG antibodies are employed for each protocol. Over the course of the investigation, I found fluorescence microscopy to yield the most relevant information for assessing the surface coating uniformity and repeatability. The ultimate test of functionality is assessed by using the prepared devices in a basic sensor experiment. Publication of these findings can be found in [133].

ZnO Preparation

ZnO samples were prepared by depositing 500 nm of ZnO onto 3” (1 0 0) silicon wafers (University Wafer) by RF magnetron sputtering using the Unifilm PVD-300 sputtering system. The wafers were diced into 1 cm × 1 cm squares for the surface functionalization experiments. Prior to surface functionalization, the ZnO samples were sonicated in acetone for 5 minutes in an ultrasonic bath before being cleaned using an ion beam mill. The samples were milled in a 20% oxygen / 80% argon atmosphere for 5 minutes with a beam current of 9 mA at 50 VDC. This was done to remove any adsorbed chemical species from the surface and to provide a reactive surface for the silane to bind. It is important to note that the milling procedure was found to be absolutely critical to preparing highly repeatable and highly uniform surfaces. Without this step, all protocols attempted yielded relatively poor results.

Surface Modification

The silane solutions for treating the ZnO samples were prepared under a nitrogen atmosphere. The solutions prepared were a 4% solution by volume of MTS (Fluka) in dry toluene (Sigma) and a 4% solution of GPS (Sigma) in dry toluene. Immediately following the ion milling procedure to clean the ZnO surface, samples were placed in vials containing 2 mL of the silane, sealed in a centrifuge tube (VWR), and placed in a nitrogen environment for 24 hours. The samples were then removed from the vials and rinsed with ethanol followed by sonication for 5 minutes in ethanol (95%, Sigma). The samples were then dried with a stream of N_2 gas. Samples treated with the 4% MTS were then placed in vials containing 2 mL of 2 mM GMBS (Fluka) in ethanol and sealed for 24 hours. Following sonication in ethanol, GPS coated samples were immediately treated with the protocol described in the next section. The MTS+GMBS coated samples were removed from the GMBS solution and sonicated in ethanol for 5 minutes. With the crosslinkers attached, the surfaces are now considered activated.

Covalent Antibody Attachment

The activated surfaces were treated with 548 nm Alexa-Fluor labeled Goat anti-rabbit IgG antibodies (Invitrogen). 25 μL of a 200 μg/mL solution of the fluorescently labeled antibodies in PBS buffer (pH 7.4) was pipetted onto the surface of the samples. The antibody solution was incubated for 2 hours in an opaque GelPak™ container (Fisher) in a nitrogen environment at room temperature. After incubation with the Ab solution, each substrate was rinsed with aliquots of PBS buffer followed by rinsing with a light stream of ultra-pure water (Burdick & Jackson) to remove any unbound antibodies from the surface. Control samples for testing simple antibody adsorption directly to the ZnO surface were also prepared by incubating ion etched ZnO samples with the antibody solution for 2 hours.

Based on previously described mechanisms [117, 121, 134], a summary of the reactions for covalently attaching antibodies to the ZnO surface is shown in Figure 4.5. Deposition of the silanes is achieved through reaction of the head groups with hydroxyl groups at the ZnO surface. The thiol group on the MTS molecules react with the maleimide region of the secondary crosslinker GMBS in organic solvent. This reaction leaves the succinimide residue of the GMBS available for antibody attachment. The succinimide residue then binds to an available amino group of the antibody to form a covalent bond between the antibody and the ZnO surface. It has been shown that antibodies immobilized using this approach still maintain a significant amount of activity,

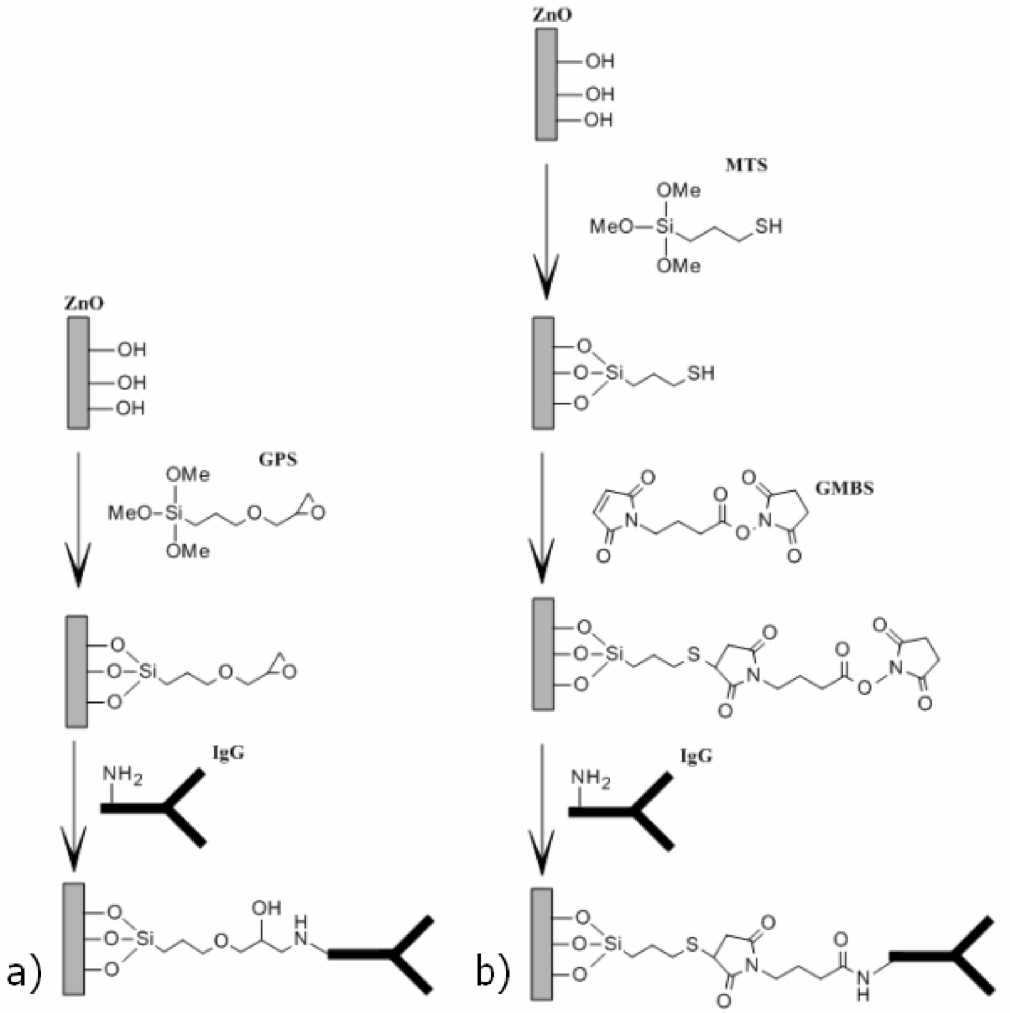

Figure 4.5. The proposed immobilization scheme for covalent attachment of IgG antibodies to the surface of sputtered ZnO using a) GPS and b) MTS + GMBS as silane-based crosslinkers.

albeit less than with oriented immobilization techniques such as those that target the carbohydrate group on the F_c region of the IgG antibody [118]. However, the ease and simplicity of the immobilization protocols studied here make them more suitable for biosensor applications than oriented immobilization techniques which often require numerous steps, harsh experimental conditions, and high antibody losses prior to immobilization.

Surface Protocol Results

Water Contact Angle Measurements

Water contact angle measurements were performed using an SEO Phoenix 150 Contact Angle Analyzer. The contact angles for each of the surface treatments were evaluated by averaging the contact angles from at least five separate measurements for each surface treatment, in which at least two surfaces for each protocol, following reaction with the silane. The silanized samples were measured and compared to a control sample consisting of ZnO with no surface treatments other than ion etching to clean the surface of any adsorbed species and sonication in ethanol to simulate the rinse process.

The results from the water contact angle (WCA) measurements after the samples were coated with the silanes indicate that the average WCA for each of the crosslinkers were greater than the WCA of the control, indicating an increase in surface hydrophobicity. The results are summarized in Table 4.1 below. Samples coated with MTS had an average water contact angle of 77° which were statistically different than the untreated ZnO (control) case which exhibited a water contact angle of 72°. The contact angle results for surfaces coated with MTS seem to agree well with previous WCA investigations of dithiol self-assembled monolayers on gold which were reported to be approximately 83.5° on average [135]. The WCA measurements performed with the 4% GPS solutions also suggest that the surface is being chemically modified. These samples yielded a significant increase in average WCA to 80º. An interesting phenomenon was observed for samples coated with GPS, however. Immediately after the water droplet is placed onto the sample surface, it was observed that the WCA is much higher than the control case indicating that the surface is hydrophobic. However, the WCA changes as a function of time in a manner that seems to be unrelated to evaporation phenomena. The WCA value of 80° was averaged from measurements taken immediately after the drop was placed on the surface. After a period of 20 to 30 seconds, the WCA drops by about 5-7 degrees and then stabilizes. One possible explanation for this phenomenon is that the water droplets react with the exposed epoxy groups, hydrolyzing the ring to form surface hydroxyl groups which would result in increased hydrophillicity.

Surface Treatment	Avg. WCA (degrees)
Untreated ZnO	**72 ± 2**
GPS	**80 ± 5**
MTS	**77 ± 1**

Table 4.1. Water contact angle measurements for surface treatments applied. (n = 10 for each case)

Atomic Force Microscopy Measurements

AFM was used for monitoring the morphological changes at the surface that result from coating the surface with the crosslinkers and subsequent immobilization of antibodies. AFM was considered an appropriate instrument for assessing morphological changes at the surface as it is capable of measuring features with extremely high resolution (on the order or a few nanometers) and can do so at atmospheric pressure. This is important as the surface will contain antibodies, which would denature at the pressure and temperature required for vacuum systems such as SEM. Further, the measurement mechanism is roughly passive, when operated in tapping mode, as opposed to the significantly invasive (and potentially destructive) mechanisms that employ X-ray or electron beam modalities. Figure 4.6 shows typical stepwise AFM scans for each surface after treatment with the crosslinkers and antibody solution, with surface roughness measurements summarized in Table 4.2.

A Digital Instruments (DI) 3000 AFM was used in tapping mode to measure the following: bare ZnO samples; samples after treatment with MTS+GMBS and GPS, respectively; and finally, samples after treatment with the crosslinkers + antibody solution. AFM probe tips were obtained from Veeco Instruments (FESP). Multiple scans

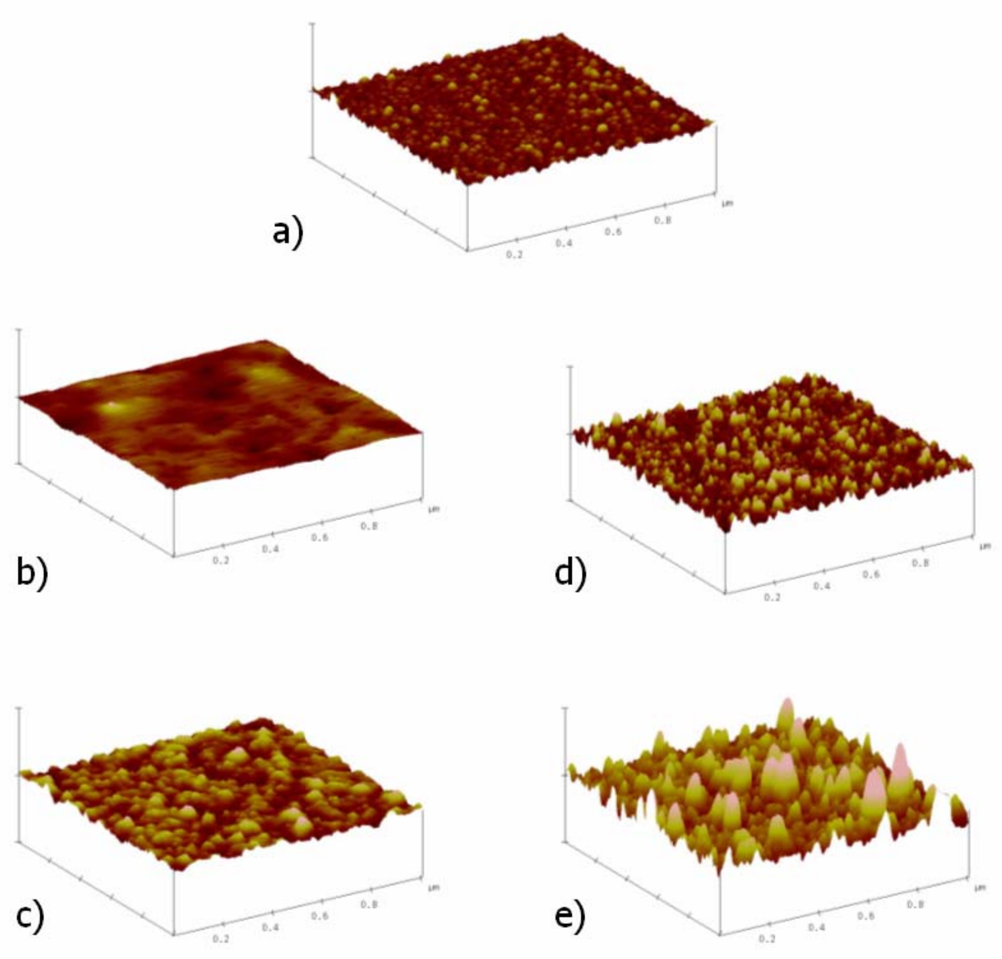

Figure 4.6. AFM topographical scans of a) the untreated ZnO surface and samples treated with b) GPS, c) GPS + Ab, d) MTS + GMBS, and e) MTS + GMBS + Ab. Scans are 1 µm x 1 µm with a vertical scale maximum of 65.0 nm.

Surface Treatment	n	Roughness (nm)	Avg. Particle Height (nm)	Avg. Particle Diameter (nm)
Untreated ZnO	**4**	**2.2 ± 0.1**	**2.8 ± 0.4**	**43.4 ± 4.6**
GPS	**3**	**1.5 ± 0.4**	**2.9 ± 0.6**	**54.3 ± 5.9**
MTS	**5**	**2.4 ± 0.1**	**3.0 ± 0.4**	**43.8 ± 7.1**
MTS + GMBS	**5**	**4.3 ± 0.1**	**6.6 ± 0.9**	**40.8 ± 3.0**

Table 4.2. AFM surface analysis for each stage of both surface treatments.

of each sample were taken to across each 1 cm × 1 cm sample and scans were taken on multiple samples. The scans were evaluated for surface roughness and overall average particle height and diameter using the DI Nanoscope software.

Note Figure 4.6.a demonstrates the characteristic cobblestone appearance of the surface of the untreated control ZnO sample, with round grains that have fairly well defined boundaries. For the bare ZnO case, the mean surface roughness is approximately 2.8 (± 0.4) nm while the particle height is 3.05 (± 0.5) nm. The characteristic AFM scan of the surface after silanization with GPS in Figure 4.6.b shows a surface that is morphologically different from that of the controlled case. The average surface roughness decreases on average by 42% to 1.2 (± 0.3) nm. This implies an overall smoothening of the surface which is similarly suggested by the appearance of the scan. One possible explanation is that the GPS molecules have been deposited into the gaps in-between the grains to fill some of the grain boundaries. The results were observed at many locations across any single chip, and from chip to chip. After incubation with the antibody solution, the GPS+Ab treated surface has an increased surface roughness on average to 2.0 (± 0.1) nm with an average particle height of 3.3 (± 0.8) nm which indicates that the surface is being modified, statistically after treatment with the antibody solution. A typical scan is shown in Figure 4.6.c. These results offer strong evidence that either antibodies were successfully immobilized on the surface due to this protocol or that the exposure of the GPS coated surface was morphologically altered upon exposure to the antibody solution.

The AFM scans of the samples treated with MTS+GMBS in Figure 4.6.d show significant differences in the surface morphology as compared to the GPS. Rather than a decrease in surface roughness, we see an increase in surface roughness to 3.7 (± 0.7) after treatment with MTS+GMBS. The average particle height for the MTS+GMBS treated samples was increased to 6.8 (± 0.4) nm indicating an increase in particle size due to deposition of the MTS+GMBS. Figure 3.2.e clearly shows the subsequent treatment with the antibody solution yields particles on the surface that have a significantly larger average height 13.7 (± 0.3) nm which is indicative of the immobilization of the antibodies to the surface. The data from these scans along with the WCA measurements provide confidence that the surface is being chemically modified and that the surfaces are morphologically modified after treatment with the antibody solution.

Confocal Microscopy

While the AFM scans offered significant evidence suggesting that the surfaces were being altered morphologically, they did not offer conclusive evidence that antibodies were immobilized on the surface. These scans were also unable to demonstrate uniform distribution of immobilized antibodies. I decided that an additional analysis was required in order to confirm the presence of antibodies and assess the degree of density and uniformity of any antibody immobilization. The antibody conjugation reaction was executed using both GPS and MTS+GMBS onto ZnO samples similar to those prepared for the AFM scans. The devices were then dried with a stream of N_2 gas and fixed to a glass slide in preparation for confocal microscopy analysis. A Zeiss Laser Scanning Microscope 510 equipped with a HeNe laser (543 nm excitation) was used to visualize the distribution and intensity of the fluorescently labeled antibodies. Each sample was viewed at 10× and 40× magnification and images were taken at random locations throughout the area of antibody deposition. Control samples were prepared and analyzed for comparison between fluorescence due to antibody coverage and fluorescence to due background noise. Rather than incubation with the 200 μg/mL antibody in PBS, the control samples were treated with the full crosslinking protocol then incubated with 25 uL of 5 mM azide in PBS to replicate the solution containing the Alexa-Fluor labeled antibodies. Therefore, the only difference between the control and target samples is the presence of antibodies. To quantify the fluorescence for each surface treatment, the detector gain was fixed at a constant value and images were taken for all of the samples. The RGB luminance intensity signal was collected for each pixel in 0.03 mm^2 areas across the samples. The average fluorescence intensity was calculated by taking the mean pixel luminance intensity for each 0.03 mm^2 area and averaging the values over at least 25 measurements.

While the AFM scans clearly indicate that the surfaces are being modified with the surface treatment, fluorescence microscopy was employed to provide more information about antibody surface coverage density and uniformity. Prior studies characterizing antibody immobilization techniques have generated a variety of methods for analyzing the amount of antibodies bound to the surface of a material [117, 118, 134]. As acoustic biosensors become increasingly more compact, the antibody immobilization surface coverage becomes increasingly more important. It is necessary to compare the surface treatments quantitatively, which is most effectively demonstrated in this study through an analysis of the fluorescence images due to fluorophor-labeled IgG molecules. Example images of typical responses for each surface treatment are demonstrated in Figure 4.7.

Figure 4.8 shows a comparison of the average fluorescence intensity (luminescence) for the two silane immobilization methods versus the untreated bare ZnO sample. Each scan includes the average fluorescent intensities accounted for by the control samples, which serve as an estimation of the combined background fluorescence from the ZnO, the crosslinker molecules (for the GPS and MTS+GMBS treated chips), and the PBS buffer. The average intensity was found to be highest overall for the MTS+GMBS+Ab samples as compared to the GPS+Ab and the bare ZnO. The fluorescence evident from the bare ZnO sample treated with antibodies above the control can be attributed to a small amount

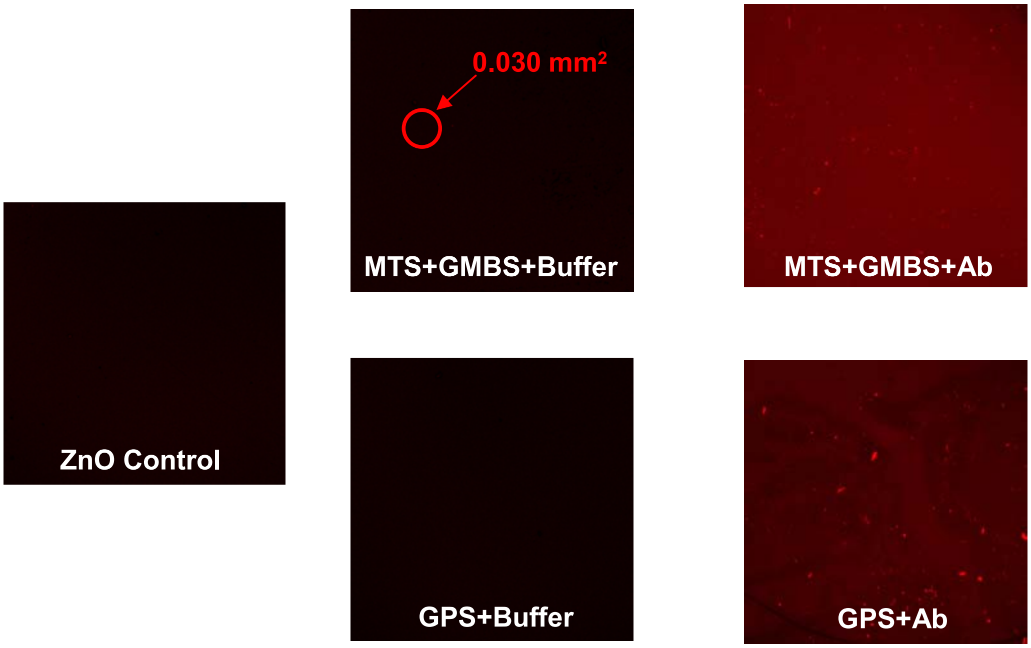

Figure 4.7. Typical confocal laser scanning microscope images upon HeNe excitation for different surface chemistry protocols.

of antibody adsorption to the surface of the ZnO in the absence of crosslinking molecules.

Statistically, the fluorescence of the samples treated with the MTS+GMBS+Ab were on average about 21% higher than the samples treated with GPS+Ab. Since variation of the fluorescence within a region of constant size can be attributed to the amount of fluorophor present, these results indicate a highly repeatable increased antibody surface coverage with the MTS over the GPS. The MTS fluorescence as compared to the untreated ZnO case indicates roughly a three-fold increase of average fluorescent intensity. The uniformity of the fluorescence is quite high as is illustrated by a relatively low standard deviation over 25 separate measurements across the sample. I also found

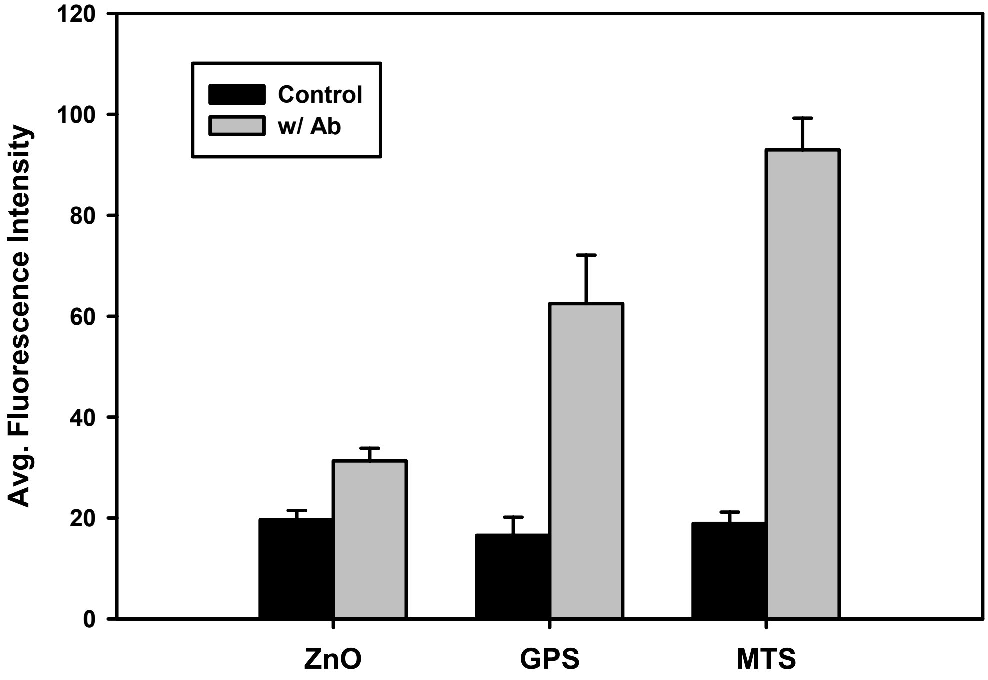

Figure 4.8. Average fluorescence intensity for each surface treatment after incubation with antibodies versus incubation with buffer [Error bars = Std. Error]. [n = 25 for each of the 6 cases shown]

the results to be repeatable from sample to sample which also indicates robustness in the protocol with each of these surface treatments.

CHAPTER 5

BIOSENSOR IMPLEMENTATION AND TESTING

The foundational components of my novel acoustic wave, label-free, immunosensor microarray have now been developed. It is therefore appropriate to apply these sensors towards cancer-relevant biomarker detection. The testing was broken up into two approaches. First, in assessing the potential sensitivity of the sensors, a dose response curve was generated for increasing concentrations of recombinant mesothelin-Fc protein in buffer. Positive indications from these experiments allowed me to pursue the application of these devices towards targets in more physiologically relevant media. The immunosensor microarrays were therefore prepared for detection of PSA in conditioned medium from a LNCaP prostate cancer cell line. The eight-device sensor arrays described in Chapter 3, designed to operate at ~2 GHz, were used for these experiments. In this chapter, I will describe specific needs for cancer detection in general and the relevancy of the two markers chosen. I will then describe the outcomes of both experimental goals.

Designing a Sensor for Early Cancer Detection

Advances in the understanding of carcinogenesis and tumor development are moving slowly towards developing a *complete* understanding of the etiology of various carcinogenic mechanisms. One extraordinary byproduct of this broad investigation is the discovery of new potential molecular targets, or biomarkers, for identifying malignancies at the earliest stages of development. It is often remarked that what is required to accelerate this discovery process is a tool for high content screening of complex tissue samples [48, 123]. An ideal biomarker would obviously be a target that could be measured at detectable levels in peripheral blood, can clearly separate benign conditions from malignant disease, and whose levels would provide information for disease proliferation, or staging. Since it is very unlikely that such a marker exists for any condition, it is further necessary to develop a system that can efficiently screen for multiple targets. As discussed in Chapter 2 of this manuscript, a biosensor array is an appropriate way to approach high content screening capability and make use of these discoveries.

As indicated in Chapter 2, it is entirely unlikely that quantification of a single marker from patient tissue will satisfy the criteria for making diagnostic decisions with high-confidence. Some of the difficulties with using PSA for such a decision making tool has already been discussed, and will be covered further later in this chapter. It is already common therapeutic practice, however, to employ tools such as nomograms for making decisions regarding the treatment of cancer patients. Nomograms provide risk assessments for patients considering various therapeutic options based on a number of critical measurements specific to that individual compared with the outcomes of hundreds (if not thousands) of past patients that presented with similar conditions. The Body Mass Index (BMI) is one of the most commonly known nomograms. For prostate cancer patients, two nomograms in particular are widely used for assessing treatment options: the Partin Tables (developed at Johns Hopkins Hospital) and the Kattan Tables (developed at the Memorial Sloan-Kettering Cancer Center) [124-127]. Both nomograms require information such as Gleason score, PSA-related activity, and tumor staging.

Any tool developed for achieving HCS is likely to be applicable for post-therapeutic monitoring as well as clinical diagnosis and early detection. Since clinicians are already familiar and comfortable with the use of nomograms, information resulting from HCS tests can quickly be incorporated into the nomogram's algorithm. It is conceivable that extensive use of HCS biosensors coupled with significant elucidation of the proteome of various cancer proliferations could be entirely sufficient for early detection, tumor staging, treatment selection and appropriate continuous monitoring.

As mentioned in Chapter 2, a broad effort to develop biosensors that provide label-free detection of clinically relevant biomarkers is underway. Recent approaches in the development of biosensor array systems have made use of various optical [136-138], electrical [139, 140], and piezoelectric [57, 141, 142] transduction mechanisms, to name a few. Some of the efforts regarding the challenges associated with an acoustics-based tool for such a sensor array have been discussed in Chapter 2.

This research presents an acoustic-based solution that meets all of the requirements proposed by Erickson, *et al* [57], which includes significant sensitivity and specificity, multiplexing capacity, and reduced complexity and cost of fabrication. Here, I engage in a preliminary investigation of the potential of these devices as biosensors towards the following clinically relevant cancer biomarkers: human recombinant mesothelin-Fc fusion protein and prostate specific antigen (PSA).

Selected Cancer Biomarkers

Mesothelin

Mesothelin is a 40 kDa cell-bound surface glycoprotein found abundantly on normal mesothelial cells of the pleura, pericardium and peritoneum [143]. Mesothelial cells are flat in shape and are responsible for regulating the transport of cells and molecules into and out of the peritoneal cavity. Translation of the gene encoding mesothelin first yields a 71 kDa pre-cursor protein, which is subsequently split into a 31 kDa protein called megakaryocyte potentiating factor (MPF) and the 40 kDa mesothelin protein. Early investigations suggested that mesothelin played a role in cell adhesion[144], though subsequent work has called that into question [145]. Over-expression of mesothelin has been associated with several cancers including ovarian, lung, pancreatic, mesotheliomas, and squamous cell carcinomas [143, 144, 146-149]. The function of mesothelin remains largely unknown, but with regards to carcinogenesis, mesothelin is credited as playing a tumor differentiation function [150]. It has been shown that mesothelin should remain below 9 ng/mL in serum for healthy individuals and above 25 ng/mL for patients with advanced stage mesothelioma [151].

Prostate Specific Antigen

PSA is a 31 kDa glycoprotein, initially thought to be exclusively produced by the prostate gland [152]. Ironically, prostate specific antigen has since been found not to be specific to the prostate and has been discovered in low concentrations in the endometrium, normal breast tissue, breast tumors, breast milk, female serum, adrenal neoplasms and renal cell carcinomas [153]. PSA is a kallikrein-related serine protease responsible for the liquefaction of the seminal coagulum during ejaculation to aid in semen motility [152]. The protein proved to be an appropriate forensic semen marker for rape cases and other criminal investigations in the late 1970's [152].

PSA has been employed as a key biomarker for prostate cancer diagnosis since the mid 1980's and is one of the only U.S. Food and Drug Administration (USFDA) approved markers for the diagnosis of cancer [154]. PSA testing coupled with the digital rectal exam (DRE) has an extensive history as the standard practice for diagnosis of prostate cancer in the U.S. [155]. PSA replaced prostatic acid phosphatase (PAP) as a marker for PCa diagnosis because of improved sensitivity [154]. 90% of apparently healthy men maintain a serum PSA level below 2.0 ng/mL and the generally accepted lower cut-off for a positive diagnosis is 4.0 ng/mL. That being said, malignant cases of PCa are certainly found among a small population of men with PSA levels below 2.0 ng/mL and there are also men with benign conditions with PSA levels above 4.0 ng/mL [154].

As indicated in Chapter 2, diagnosis of PCa from serum concentration of PSA has generated a significant amount of controversy that has persisted for more than a decade [58-60]. For men with PSA levels between 2.5 to 4.0 ng/mL, it is difficult to discern PCa from benign prostatic hyperplasia (BPH), and often leads to many unnecessary biopsies [156]. BPH is a relatively common condition experienced by roughly half of all men over 50 years of age [157], which similarly results in increased concentrations of serum-level PSA. As a result of this range of low specificity, a significant amount of work has been done to investigate alternate means of interpreting the results of PSA screening. Several practices have developed including measuring PSA velocity [158-160], the ratio of free to complexed PSA [152, 153], age-adjusted PSA [161], PSA density [162, 163] and several others. The use of PSA velocity has emerged as more commonly used in clinical practice and refers to the time it takes to double ones serum concentration of PSA. PSA velocity is described as offering reasonably improved sensitivity for patients whose PSA levels fall below 4.0 ng/mL [147, 149].

Suffice it to say that PSA falls short of exhibiting the traits of an ideal cancer marker. More recent investigations have revealed alternative serum-level biomarkers that could offer greater specificity for PCa detection beyond PSA. These include early prostate cancer antigen (EPCA-2) [164], prostate stem-cell antigen (PSCA) [165, 166], α-methylacl coenzyme-A racemase (AMACR) [167], methylated glutathione *S*-transferase π gene (GSTP-1) [168-170], prostate cancer antigen 3 (PCA3) [171, 172], human kallikrein 2 (HK2) [173, 174] and Hepsin [175, 176]. EPCA-2 has emerged as one of the more promising candidates [177], discovered by a proteomic screening of 385 serum samples at the Brady Urological Institute at Johns Hopkins Hospital by Leman, *et al.*

The strength of any given biomarker is commonly assessed through receiver operator characteristic (ROC) curves. This measurement plots sensitivity vs (1 – specificity) in regards to the strength of the marker in diagnosing the condition in question. Sensitivity, in this case, describes the probability that the marker is a positive identifier of the pathology in question, or true positive. (1-specificity) refers to the probability that presence of the marker is not an identifier of an alternate condition, or a false positive. Another common metric used for comparing the strength of different markers is the calculation of the area under the curve (AUC) of the ROC curve. The ideal ROC curve would appear as a step function, indicating perfect specificity per level of detection regardless of the acceptable false positive rate that comes with that concentration. The ideal ROC curve would yield an AUC of 1.0.

Leman *et al* generated ROC curves for both EPCA-2 and total PSA in distinguishing individuals with either PCa or BPH (Figure 5.1.A) and in distinguishing individuals with organ-confined (OC) and non-organ-confined (NOC) disease (Figure 5.1.B). As can be seen, for nearly all levels of acceptable false positive rates, EPCA-2 offers greater sensitivity for PCa. Figure 2 further demonstrates the ability of this marker in distinguishing PCa from various alternative conditions. Overall, using the cut-off

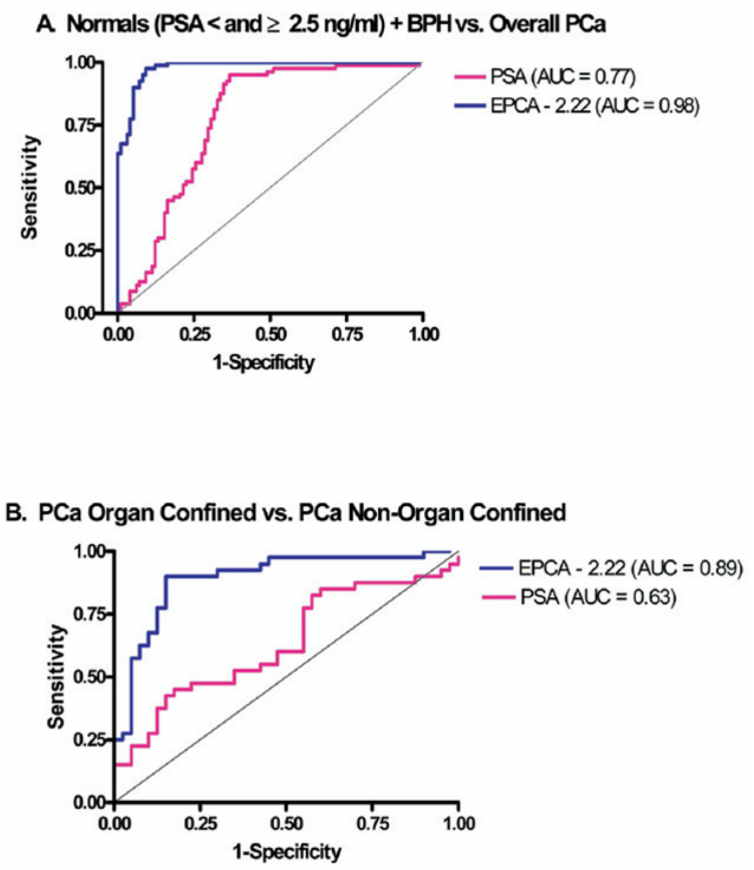

Figure 5.1. ROC curves for EPCA-2 and PSA in separating (A) healthy men with BPH from those with PCa and (B) distinguishing those with OC from those with NOC disease (80 patients with prostate cancer selected according to their OC or NOC disease status) [164].

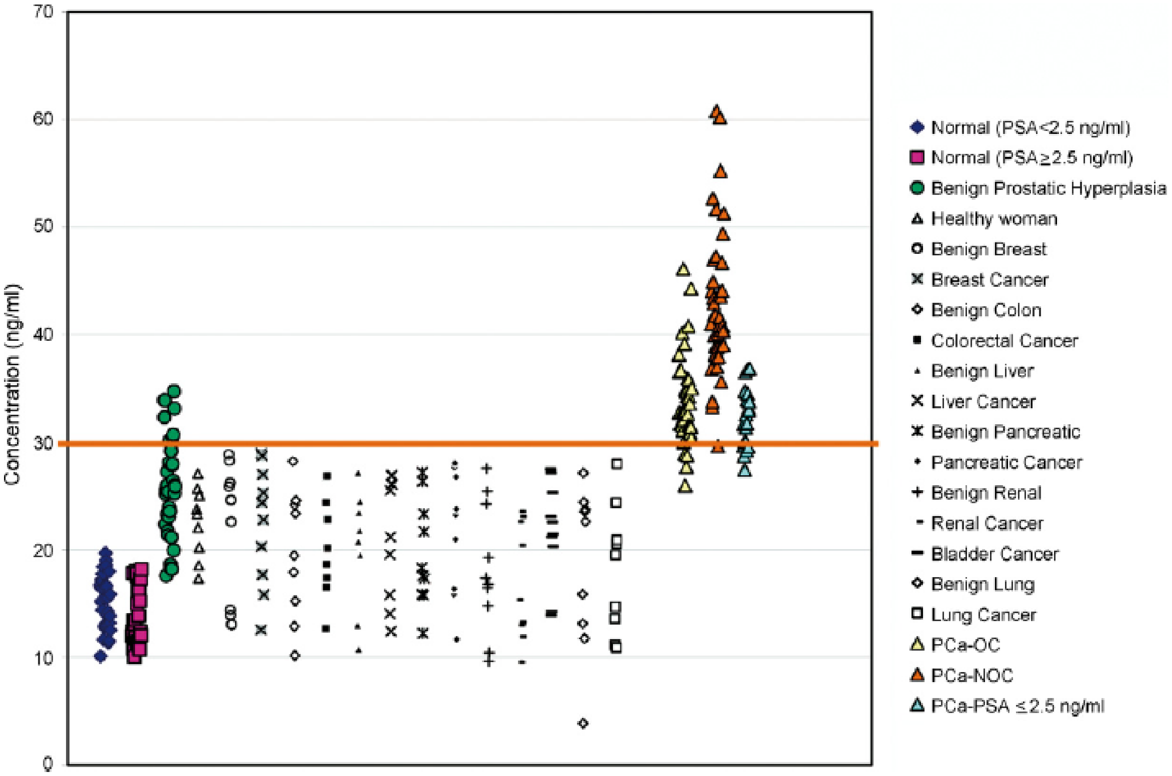

Figure 5.2. Serum analysis of EPCA-2 in study populations. Total of 330 serum samples screened for EPCA-2. Indirect ELISA's showed that EPCA-2 has a cutoff of 30 ng/mL or greater at estimated concentration. Cutoff represented by red line across graph [164].

concentration of 30 ng/mL, EPCA-2 assays were found to demonstrate 92% specificity and 94% sensitivity for individuals with PCa (AUC = 0.89). PSA demonstrated an overall specificity among the same population of only 65% (AUC = 0.62) [164].

Sensor Preparation

As mentioned in the introduction to this chapter, the goal is to assess both the sensitivity and specificity of the sensor design. A dose response curve is generated to assess the sensitivity of the sensor using varying concentrations of purified recombinant mesothelin-F_c in buffer. To test device specificity, sensor testing was performed to identify the presence of PSA in LNCaP, a prostate cancer cell line, conditioned medium. Recognition elements for fluoroscein isothiocyanate (FITC) were used as the negative control, as no FITC is present in LNCaP conditioned medium (CM). As a secondary validation of the PSA results, a commercially available immunoassay kit was also employed to quantify the level of PSA in the LNCaP CM.

Resonator arrays were fabricated as described in Chapter 3. Device operation and subsequent sensor testing was accomplished using a HP 8753 C Network Analyzer, equipped with a S-parameter test set and a Cascade Microtech 9000 Probe Station with a temperature control chuck. Devices were probed using Cascade Microtech ACP40 GSG-150 probes.

IgG antibodies were covalently attached to the surface of the ZnO piezoelectric film using the functionalization protocol described in Chapter 4 and summarized in Appendix D. In short, the protocol employs mercaptopropyl-trimethoxy silane (MTS) as a primary crosslinker to the ZnO surface, followed by N-γ-maleimido butyryloxy-succinimide ester (GMBS) as a secondary crosslinker to covalently bind IgG molecules at the F_c fragment to the device surface. The protocol is described by Figure 8. MB Anti-mesothelin mAb were obtained from Dr. Ira Pastan at the NCI and are described in [178]. All other mAb were obtained from Santa Cruz Biotechnology, Inc [anti-FITC (sc-69871) and anti-tPSA (sc-52170)]. Anti-tPSA, or total PSA, refers to an antibody specific to both complexed and free PSA.

Sensitivity Assessment

Sensitivity testing was executed by preparing sensors to target mesothelin and applying them to varying concentrations of recombinant mesothelin-Fc protein in PBS. Purified recombinant mesothelin-Fc protein in buffer was obtained from Dr. Ira Pastan at the NCI. Serial dilutions were prepared using PBS (pH 7.38) to create concentrations of 1 ng/mL, 10 ng/mL, 100 ng/mL, 10 μg/mL, and 50 μg/mL. The functionalization protocol was performed with anti-mesothelin "MB" polyclonal IgG antibodies also supplied by Dr. Pastan on five separate 8-device arrays. 30 μL of each concentration of the purified protein solution was then deposited on the surface of each sensor array and allowed to incubate at room temperature for 20 minutes. After the incubation period, devices were rinsed with PBS buffer then DI water then dried with a N_2 stream prior to measurement. S_{11} scattering responses for each device of each array were collected both prior to exposure to mesothelin solutions and again after the 20 minute incubation time.

Individual devices are measured both before and after exposure to the liquid sample under test. Scattering responses are converted to impedance values using equation (3.15). The peak of the magnitude of the impedance response represents the condition of parallel resonance, as described in Chapter 3, which is an easily monitored condition. An example of the frequency shift observed after exposure to the sample is depicted in Figure 5.3.

Figure 5.4 shows the device detection with increasing frequency shifts in response to increasing sample concentrations, returning a 195 kHz shift for the 50 mg/mL concentration and 29 kHz shift for the 1 ng/mL concentration. It is important to put the magnitude of these shifts in context. Prior investigations using QCMs (see Figure 5.5) as

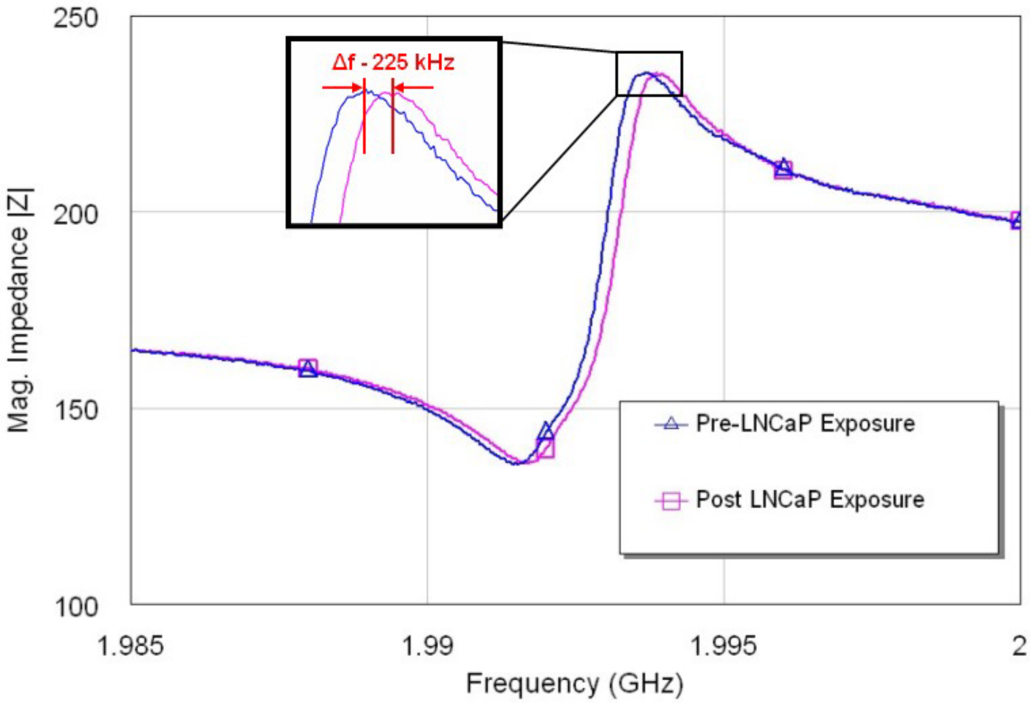

Figure 5.3. Typical impedance response of single sensor device showing response before (Δ) and after (□) exposure to the liquid sample under test. The peak of each curve represents the condition of parallel resonance.

the sensor for detection of a known target (sonic hedgehog, SHH) in the same LNCaP CM yielded only an 80 Hz frequency shift due to ~3 ng/mL concentration [179].

The actual concentration of SHH was determined by ELISA to be 0.2 ng for 70 μL of sample, or ~3 ng/mL [179]. At the lower concentrations, I observed frequency shifts almost 400 times greater in magnitude. This demonstrates an exceptional capability regarding *potential* limit of detection but cannot be directly compared due to the difference in targets and antibody affinities etc. Further device optimization will no doubt improve the sensitivity. Currently, however, the devices were clearly capable of broadly distinguishing increasing concentrations. Obviously the device response slows below 100 ng/mL, which indicates that more work must be done to reconcile overall mass resolution.

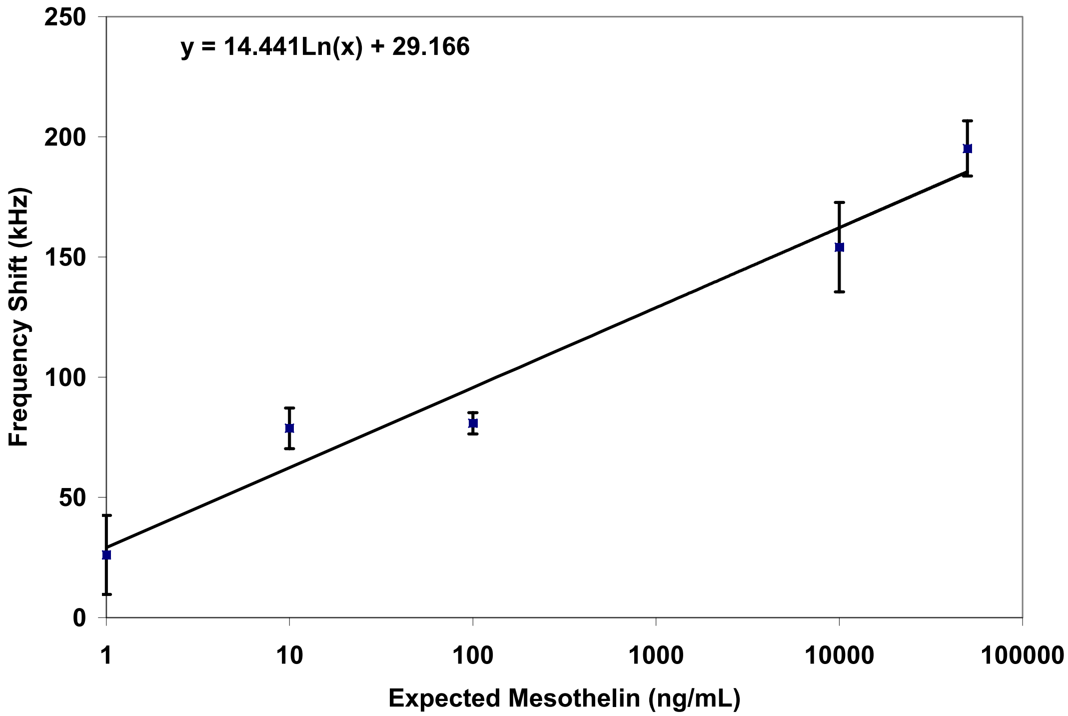

Figure 5.4. Dose response curve due to varying concentrations of purified recombinant mesothelin-F_c in PBS buffer (pH = 7.38). n = 8 for each case above. [Error bars represent standard error ($\sigma/\sqrt{n}$)]

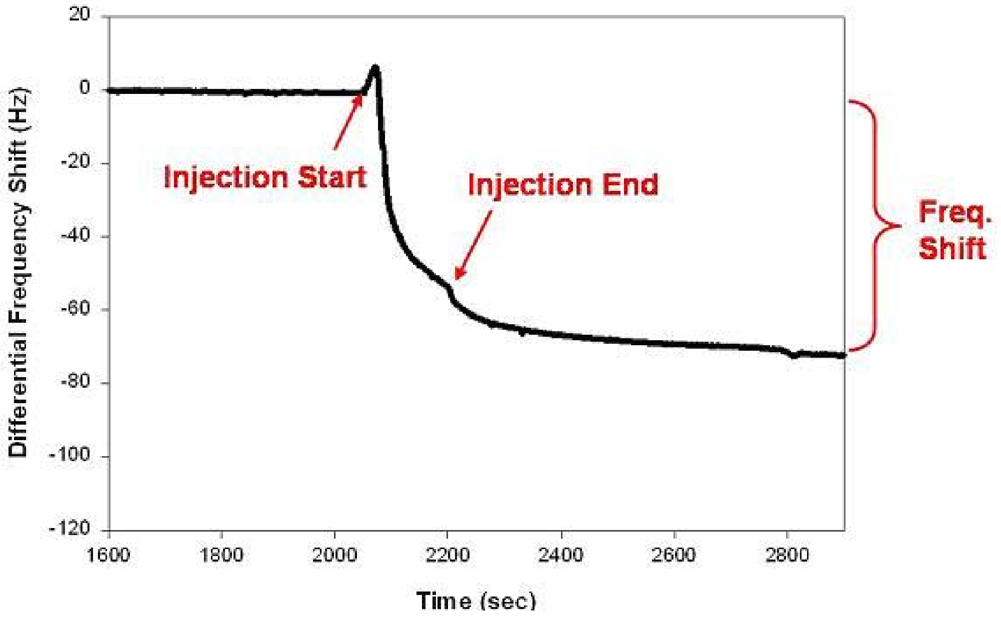

Figure 5.5. QCM sensor detection yields 80 Hz shift due to 3 ng/mL concentration of mesothelin in sample. While non-specific binding could compound the results, a control FITC antibody was used to subtract background binding [179].

A control experiment was performed using buffer solution of 10 μg/mL of recombinant mesothelin-F_c with a sensor array coated with anti-mesothelin and a separate sensor array coated with anti-FITC. The results are summarized in Figure 5.6. While the anti-mesothelin coated devices clearly indicate positive detection of the target protein over the anti-FITC coated devices, using analysis of variance I found that there was statistically little difference between the frequency shift associated with exposure of the anti-mesothelin devices to the 1.0 ng/mL solution and the anti-FITC control sensor ($p = 0.409$). As a result, no further testing was performed below 1 ng/mL because I determined this to be below the limit of detection for statistically significant differentiation from the reference.

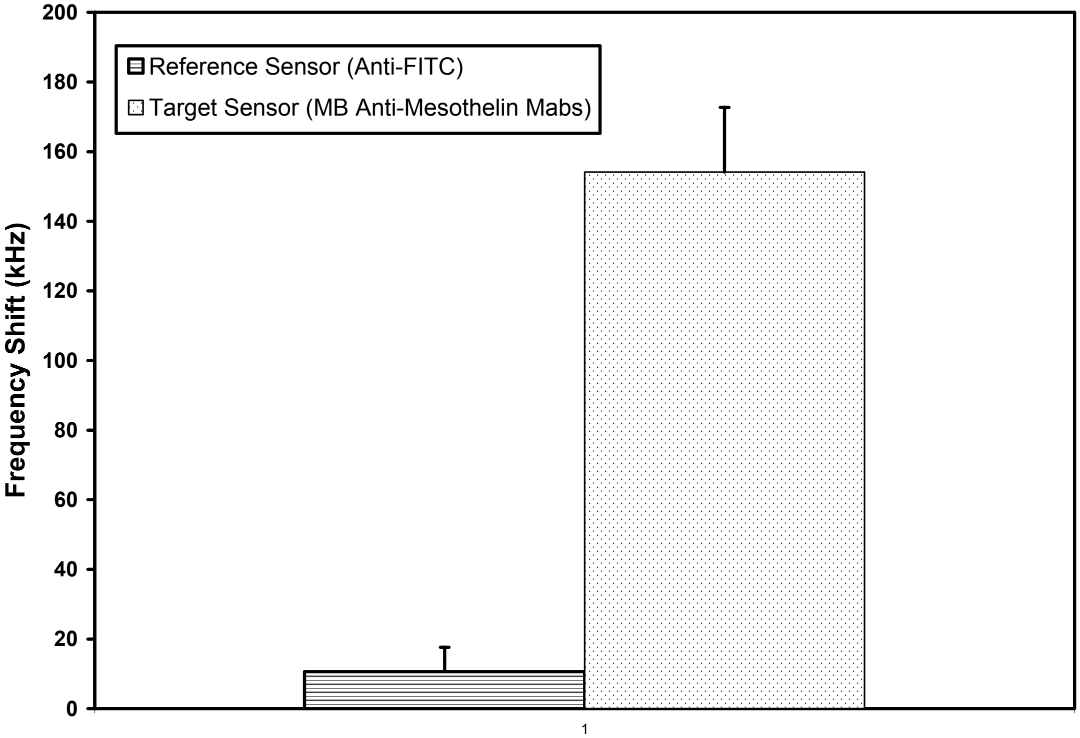

Figure 5.6. Control experiment depicting average frequency shift observed by a reference sensor (coated with anti-FITC, $n = 4$) and a target sensor (coated with anti-mesothelin, $n = 6$) after exposure to a purified solution of 10 μg/mL of recombinant mesothelin-Fc in PBS buffer. [Error bars represent standard error ($\sigma/\sqrt{n}$)]

It must be noted that sensor sensitivity is often defined as the slope of the sensor response curve to varying loads [180]. A traditional approach to determining this with gravimetric sensors is to deposit a known amount of mass on the sensor surface and measure the frequency shift. This is not plausible with biological samples, however, so a more useful method is to describe the overall sensitivity trends displayed under the given test conditions. As can be seen from Figure 1, the active region makes up only a very small portion of the total area of the array, all of which is exposed to the LSUT. Note that the vast majority of the device footprint is inactive, which includes the electrodes themselves. Deposition of the 30 μL sample more than covers the entire array. Future investigations should involve the development of an appropriate micro-fluidic flow cell which can limit the exposure to only the active resonance area of the sensor array to the LSUT, thereby making a sensitivity determination more reasonable. For this reason, I made an attempt to describe the overall sensitivity trends displayed under the given test conditions.

Specificity Assessment

LNCaP CM was obtained from Dr. Milton Datta at the Winship Cancer Institute at Emory University. LNCaP CM was obtained from exponentially growing LNCaP cells in RPMI-1640 medium, which was supplemented with 10% fetal calf serum, 4500 mg/L glucose, 1mM sodium pyruvate, 10 mM HEPES, 2 mM glutamine, and 15 mg/L sodium bicarbonate. The CM is therefore considered a sufficiently “noisy” environment for preliminary testing of device selectivity because it contains many proteins and other molecules from the cells. The functionalization protocol was performed with anti-FITC and anti-tPSA each on a separate 8-device array. Anti-FITC is employed as a negative control, targeting a molecule not to be found in CM. As a secondary control (marked ‘Control’ during the experiment), the functionalization protocol was performed on a set of devices but the final step of incubation with some antibody solution was replaced with incubation with plain PBS. 30 μL of LNCaP CM was then deposited on the surface of each functionalized sensor array and allowed to incubate at room temperature for 20 minutes. After the incubation period, devices were rinsed with aliquots of PBS buffer then a light stream of DI H_2O then dried with a N_2 stream for measurement. S_{11} scattering responses of each device of each array were collected both prior to exposure to LNCaP CM and again after the 20 minute incubation period.

The results of testing multiple sensor arrays for our two targets are summarized in Figure 5.7. It is clear that the devices could distinguish the presence of PSA, though not as clearly as would be desired ($p = 0.139$). It is expected that due to the extensive molecular diversity of the LSUT, a significant degree of non-specific binding is likely occurring. This is demonstrated by the 70 kHz (on average) shift from the Control sensors, having the crosslinking molecules but no antibodies attached to the surface, as compared with the 49 kHz shift (on average) from the FITC-targeted negative control sensors exposed to CM.

A commercially-obtained enzyme-linked immunoassay (EIA) kit for PSA (Biocheck, Inc: BS-1019) was used to independently determine the concentration of PSA in the LNCaP CM. The protocol was followed as described by the manufacturer using n=3 for control standards and blank wells and n=6 for the LNCaP CM wells. LNCaP CM was

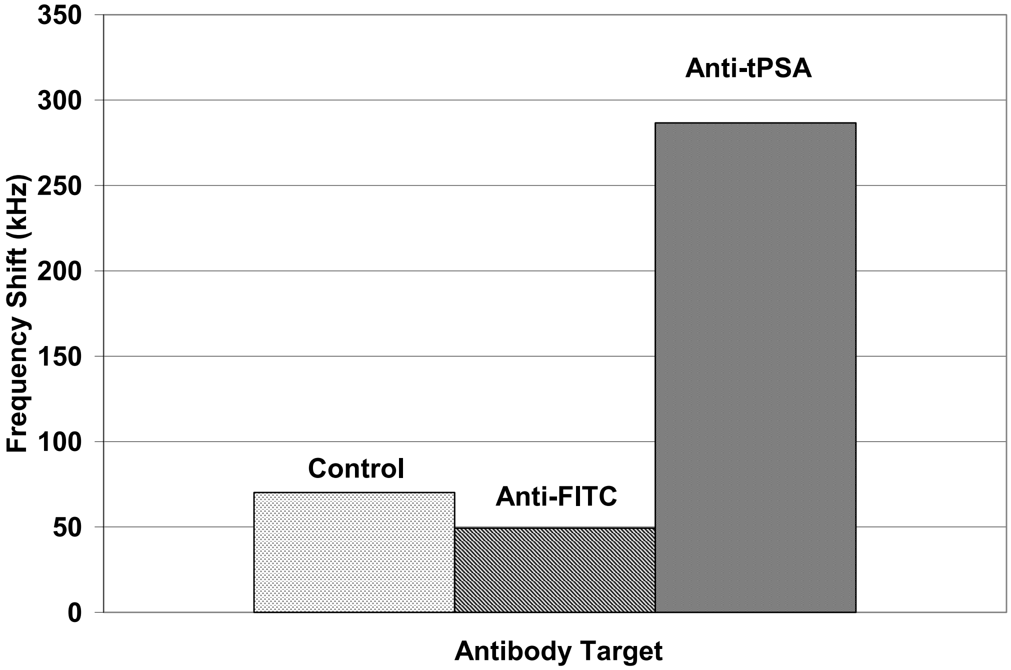

Figure 5.7. Comparison of the average frequency shift observed by sensors coated without antibodies (Control) [n=48], with anti-FITC (negative control) [n=44], and anti-tPSA [n=45] after 20 minute incubation with LNCaP CM.

diluted to 1:7 and 1:15 in PBS buffer. The results of the EIA are demonstrated in Figure 5.8 below. A commercially available EIA kit for PSA (total) was used to determine the actual concentration of PSA in the LNCaP conditioned medium. The results indicated the concentration of PSA to be roughly 950 ng/mL.

Given this very high concentration of our target, it is obvious that the sensor behaves differently given the "noise" of this testing environment. As stated at the beginning of this chapter, it was my goal to obtain preliminary results regarding the application of this sensor in a physiologically relevant medium. While the sensors are capable of distinguishing activity due to the appropriate target from control cases, they provide very little information regarding relative concentration. The testing protocol as it exists allows for many variables that must be controlled for, much of which can be solved with the development of an appropriate flow cell. Some of the variables I am referring to include

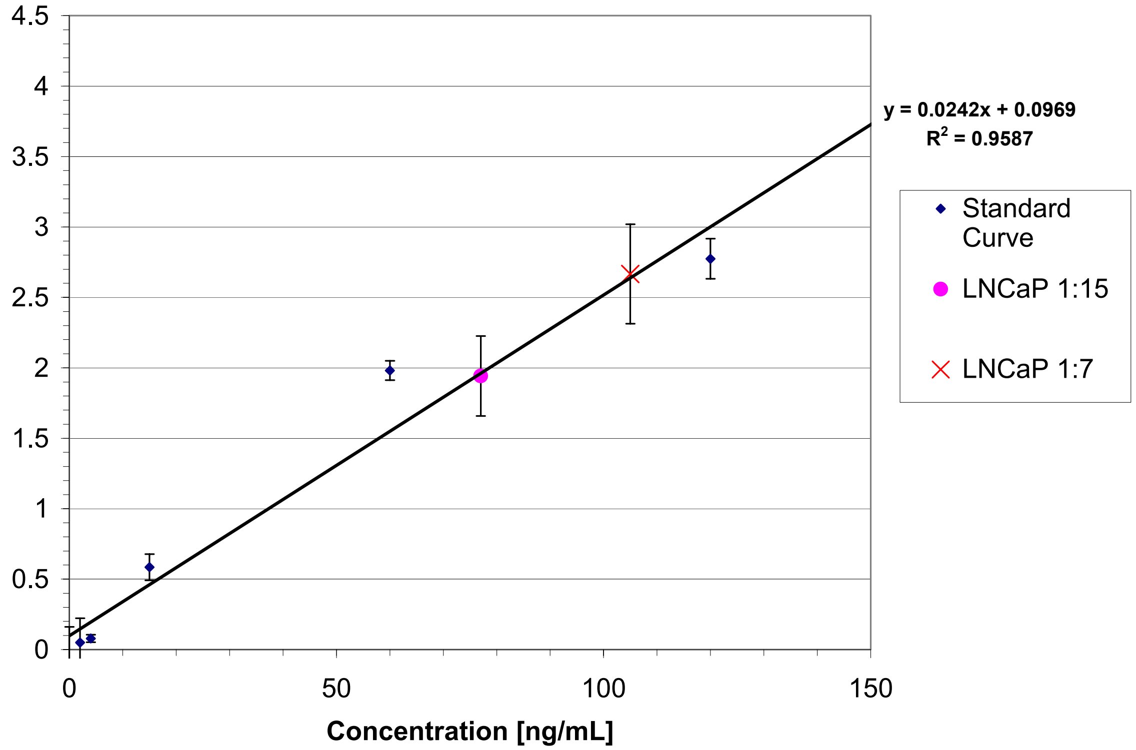

Figure 5.8. ELISA results for total PSA found in LNCaP conditioned medium using Biocheck, Inc BS-1019. (n = 3 for all standards, n = 6 for test samples)

varying distributed stress due to the application of the testing probes, drying of the surface environment, and uncontrolled exposure volumes are the most obvious.

Preliminary Packaging

I have taken steps towards developing a packaging system we are calling the AcµRay^{TM} (Acoustic Micro-Array, pronounced – ak′ ū rā) that introduces controls for the variables I have listed above. The AcuRay^{TM} system involves the development of two printed circuit boards (PCB), fabricated by Express PCB, which includes fixed electrical connections to each device, a fixed volume flow cell, and connectivity to an appropriate network analyzer for monitoring. The package is shown in Figure 5.9 and is made up of a disposable array sensor board and a RF switch board. In order to achieve the fixed electrical connections, the electrode array needed to be redesigned in order to make connections with the disposable array sensor PCB board. Connections for each device were established by fusing electrodes from the fabricated sensor chip to the electrodes of the test board using conductive epoxy. A jig was developed (see Figure 5.10) to properly align the chip with the disposable PCB board and press the two pieces together while the conductive epoxy was allowed to set. Note that the test board also housed the liquid sample space that would expose the sensor surface to the liquid sample (Figure 5.9). It was envisioned that a flow cell could be attached to the sensor board here. Once set, the

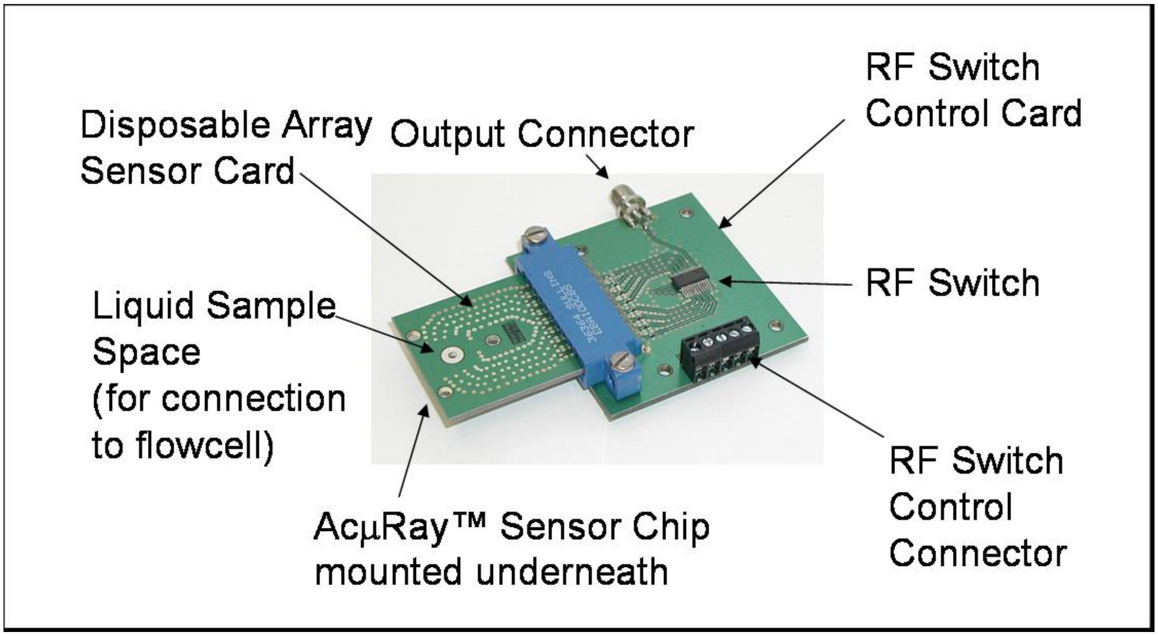

Figure 5.9. AcµRay$^{\text{TM}}$ System consisting of disposable array sensor card and RF switch card with appropriate connections.

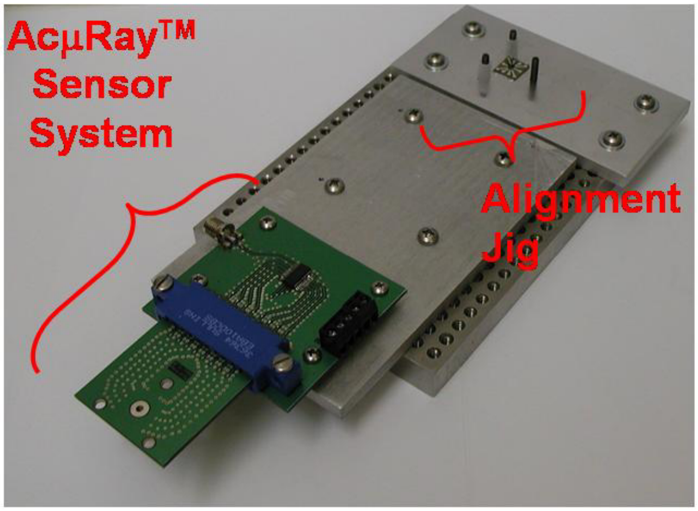

Figure 5.10. AcμRay^{TM} sensor system, including alignment jig for loading sensor chips onto disposable sensor array board.

sensor board was connected via a PC card connector to the RF switch board. The RF switch board includes a SP8T RF rapid switching integrated circuit (IC) from Hittite Microwave Corporation (HMC253QS24). The switching IC was set up to be controlled by a computer via a National Instruments test controller (NI USB-6008). Once the network analyzer was connected the to the output of the sensor array via the SMA connector shown in Figure 5.9, the responses of each device could be obtained periodically as controlled by the RF switch.

CHAPTER 6

CONCLUSION

Over the course of this research, I have developed the fundamental components of a biosensor designed to meet the following specific aims:

1. A bulk acoustic resonator device appropriate for application as a highly sensitive biosensor.
2. An appropriate biosensor preparation procedure by immobilization of appropriate capture agents.
3. Demonstration of the functionality of these biosensors towards known cancer biomarkers.

The sensor was comprised of two fundamental components outlined in aims 1 and 2. The first is a transducer element capable of monitoring its environment for extremely small perturbations. The second is the functionalization of the transducer as a biosensor by preparing its surface for high specificity for a particular target.

To implement the transducer, a solidly mounted resonator consisting of alternating layers of W and SiO_2 were grown on a p-doped <1 0 0> Si substrates with ZnO as the active piezoelectric layer at the surface. More than a thousand successful devices have been fabricated and tested after an investigation that included the fabrications of several tens of thousands of test devices. The acoustic mirror was designed to have a reflection coefficient closest to unity near the frequency of operation. The acoustic mirror frequency response was simulated to provide assurance of the frequency range coverage given a fixed number of alternating pairs of W and SiO_2. Finite element modeling was also performed to predict the electric field of an electrode configuration consisting of two long electrodes positioned on the top of the ZnO with a gap between them. Simulations showed that the electric field within the gap between the electrodes was primarily laterally oriented while the electric field directly beneath the electrodes was shown to be reduced in magnitude with an orientation normal to the surface of the ZnO.

To verify the thickness shear mode operation of the devices, I investigated the experimentally extracted acoustic velocity and the effects of water loading on the resonance. Without these tests it is difficult to adequately determine that a resonance is necessarily TSM. I have presented evidence of a TSM wave through exposure of the device to deionized water, comparison of extracted acoustic velocity with theoretical acoustic velocity, and varying the piezoelectric film thickness to yield respective changes in the frequency response.

I have further provided an investigation of two antibody immobilization techniques on planar ZnO surfaces. Several hundred surfaces were analyzed using water contact angle measurements, atomic force microscopy, and fluorescence microscopy to determine the surface characteristics and antibody surface coverage. I found that protocols employing both GPS and MTS are effective in immobilizing antibodies to the ZnO surface, but that MTS offers greater surface coverage, on average. The protocols yielded uniform and repeatable surface coverage using both methods which are necessary requirements for biosensor functionalization. Functionalization of crystalline ZnO surfaces is becoming an increasingly important topic as new biosensor platforms are being developed with this material. It was concluded that the MTS protocol offered superior results for functionalizing ZnO-based sensors due to the fact that it is a commercially available chemical and provides high antibody surface coverage with good uniformity.

I have further demonstrated here results for a novel acoustic biosensor system that exhibits all the qualities required for advances in proteomics research. Specifically, this system offers the potential for extraordinary sensitivity due to its operation in the several GHz range. Given frequency shifts in the tens of kHz for a few ng/mL levels of detection, improvement in general noise levels offers the potential to achieve several orders of magnitude improvement on the limit of detection. Further, the system is a simple array design that can be mass produced with existing industrial microelectronic fabrication equipment to reduce manufacturing costs and allow for real-time multiplexed sensor reporting. This last point has obvious molecular micro-array implications which provide the capability of implementing testing redundancy (reducing false positives and false negatives) as well as rapid multi-target monitoring.

Any sensor platform of high sensitivity must additionally consider that false positives and false negatives significantly hamper the ability to employ such devices for research much less for patient diagnosis. A sensor array technology allows for monitoring of multiple sensors simultaneously which offers both replications of each measurement as well as the capability to identify a multi-protein signature. This is the strongest approach for minimizing false positives and false negatives. The development of such a system could have an impact at multiple levels including proteomic research, post-therapeutic and eventually early detection screening.

As mentioned at the beginning of this dissertation, the findings of this research have led to the following:

- 4 peer-reviewed professional publications
    - 2 first-authored
- 3 conference presentations
- 6 conference posters

Beyond publication of this research in the aforementioned professional journals and conferences, aspects of this research have also been independently selected for circulation by mass media. The American Association for Cancer Research (AACR) independently selected my abstract for a press release to promote the September 2007 Conference on Molecular Diagnostics and Cancer Therapeutic Development, presented in Appendix F. This was picked up by various news organizations, including CNN's Sanjay Gupta, US News & World Report, Forbes, WebMD, Medicine.net, CBC News, various NBC and CBS news affiliates, HealthCentral.com, ScienceDaily, PhysOrg.com, Dentalplans.com and Health Scout. Links for these are also copied in Appendix F. The work was also highlighted in the April 17, 2008, broadcast of CNN's *Next Big Thing*, with Miles O'Brien.

Beyond the outputs of this research, I have also acquired a great deal of practical knowledge peripheral to the field of study. This thesis work would not have been possible without gaining proficiency with the following equipment:

- Scanning electron microscopy (Leo 1530, Leo 1550, Zeiss Ultra60, Hitachi S800)
- Atomic force microscopy (DI 3000)
- X-Ray Diffraction
- Laser Scanning Microscopy (Zeiss LSM 510)
- Wafer probing (Cascade Microtech 9000)

- Microfabrication
    - Photomask design (ADS)
    - Plasma vapor deposition (Unifilm PVD 300)
    - Electron beam evaporation (CVC)
    - Photolithography
    - Ion beam milling
    - Step Profilometer (Tencor Alpha-Step)
    - Wafer dicing
- Immunoassay protocols (ELISA)

and the following software programs:

- Applied Wave Research – Microwave Office (SPICE-based circuit modeling program)
- Advanced Design System (CAD program)
- Cascade Microtech WinCal Software
- MATLAB

Not only was proficiency required for the use of much of the microfabrication equipment, but the Microelectronic Acoustics Group owns and maintains its own fabrication equipment. It would not be an exaggeration to say that at least 15% of all the time spent in the laboratory for this doctoral program was spent on maintaining, modifying and often repairing this equipment. The Unifilm PVD-300, in particular, is a relatively complicated piece of equipment, comprised of more than 15 constantly degrading units including the vacuum chamber itself. I was exclusively in charge of maintaining this instrument for the entirety of my dissertation program, which underwent constant maintenance and had a massive breakdown at least once a year, on average. In addition to the Unifilm, I was similarly in charge of monitoring and repairing the CVC E-beam evaporator system, the Karl Suss MJB3 Mask Aligner system, and various other pieces of equipment. This is in addition to the ordinary complexities and intricacies associated with using core facilities such as the AFM and the Confocal LSM.

Over the course of this thesis work, I have developed several novel contributions to the field of biosensor microarrays. As summarized in the introduction of this manuscript, they include the following:

1. The development of a novel thickness shear mode bulk acoustic resonator utilizing ZnO;
2. The novel application of an appropriate surface chemistry protocol for functionalization of planar ZnO with monoclonal antibodies;
3. Implementation of these sensors toward detection of clinically relevant cancer biomarkers.

APPENDIX A: MATLAB CODE – MIRROR SIMULATION

```
% mirror.m
% written by Anthony Dickherber, January 2004

%Set frequency range
f = 0:12e4:6e9;
w = 2*pi*f;

NumLayers = 6;
d = zeros(1:6);

%as given by page 56...unknown calculation/derivation/source
%Z0 is the substrate material (Si), Z(odd) is the high acoustic
impedance

%material and Z(even) is the low acoustic impedance material
%NOTE: Impedances are normalized by the active area of the device
Z0 = .5;   %Si Substrate Z=0.5
%ZH = .7837;   %AlN is 1.0672
%ZL = .4549;   %SiO2 is 0.4183

CenterFreqofInterest = 2e9;

%material parameters for high and low acoustic impedance materials
rhoo = 2332;    %bulk Si density, from Auld
rhoL = 2200;     %density SiO2 = 2200 (fused silica from Auld)

%rhoH = 8200;     %Ta2O5, from Shawn's thesis
%rhoH = 7450;     %for LiTaO3
%rhoH = 4700;     %for LiNbO3
%rhoH = 3986;     %for Al2O3
rhoH = 19200;   %for W (from Auld)

C44o = 7.956e10; %c44 for Si (from Auld)
C44L = 3.12e10; %c44 for SiO2 (fused silica from Auld)

%C44H = 5.69e10;  %c44 for Ta2O5
%C44H = 9.4e10;    %c44 for LiTaO3
%C44H = 6.0e10;   %c44 for LiNbO3
%C44H = 14.5e10;  %c44 for Al2O3
C44H = 13.4e10;   %c44 for W  (crystalline from Auld)

%Calculate the normalization factor for impedance values
Ro = sqrt(rhoo*C44o);
NormFact = Ro/Z0;

%normalize impedance values of low and high impedance materials
ZH = sqrt(rhoH*C44H)/NormFact;
ZL = sqrt(rhoL*C44L)/NormFact;

%using the values for stiffness coeff. and density on page 62
VH = sqrt(C44H/rhoH);      %[m/s]
```

```
VL = sqrt(C44L/rhoL);     %[m/s]

%define thicknesses found on page 98 of thesis (lambda/4)
dH = 1/4*(VH/CenterFreqofInterest) %[m]
dL = 1/4*(VL/CenterFreqofInterest) %[m]

%calculate wave number for both regions
kH = w/VH;
kL = w/VL;

%Set up the Impedance matrix
Zeq = zeros(NumLayers-1,length(f));

%calculate equivalent impedance of stack shown on page 56 figure 3.8
%using equation 3.11 found on page 55 of Shawn's thesis

%Calculate impedance for first layer due to Z0
if mod(NumLayers,2)>0
    Zeq(1,:) = ZL*((Z0 + i*ZL.*tan(kL*d(1)))./(ZL +
i*Z0.*tan(kL*d(1))));
    disp('1 Low')
else
    Zeq(1,:) = ZH*((Z0 + i*ZH*tan(kH*d(1)))./(ZH + i*Z0*tan(kH*d(1))));
    disp('1 High')
end

%Calculate impedance for the rest of the layers
for n = 2:(NumLayers-1)
    if mod(n,2) > 0
        Zeq(n,:) = ZH*((Zeq(n-1,:) + i*ZH*tan(kH.*dH))./(ZH + i.*Zeq(n-
1,:).*tan(kH.*dH)));
        disp('High')
    else
        Zeq(n,:) = ZL*((Zeq(n-1,:)+i*ZL*tan(kL*dL))./(ZL+i.*Zeq(n-
1,:).*tan(kL*dL)));
        disp('Low')
    end
end

%Zeq(2,:) =
ZL*((Zeq(1,:)+i*ZL*tan(kL*dL))./(ZL+i.*Zeq(1,:).*tan(kL*dL)));
%Zeq(3,:) =
ZH*((Zeq(2,:)+i*ZH*tan(kH*dH))./(ZH+i.*Zeq(2,:).*tan(kH*dH)));

Zin = ZL*((Zeq(NumLayers-1,:) + i*ZL.*tan(kL*d(6)))./(ZL +
i*Zeq(NumLayers-1,:).*tan(kL*d(6))));

S11 = (Zin-1)./(Zin+1);

plot(f,abs(S11))
```

APPENDIX B: ELECTRODE CONFIGURATIONS IMPLEMENTED

Four mask designs were required to reach the electrode design implemented as a biosensor. These are referred to as LFE0, LFE1, LFE2 and LFE3. A final LFE4 mask has been implemented for use with the AcμRay System^{TM}, though testing is still on-going regarding this configuration. Provided in this appendix is a full record of all electrode geometries tried.

LFE0

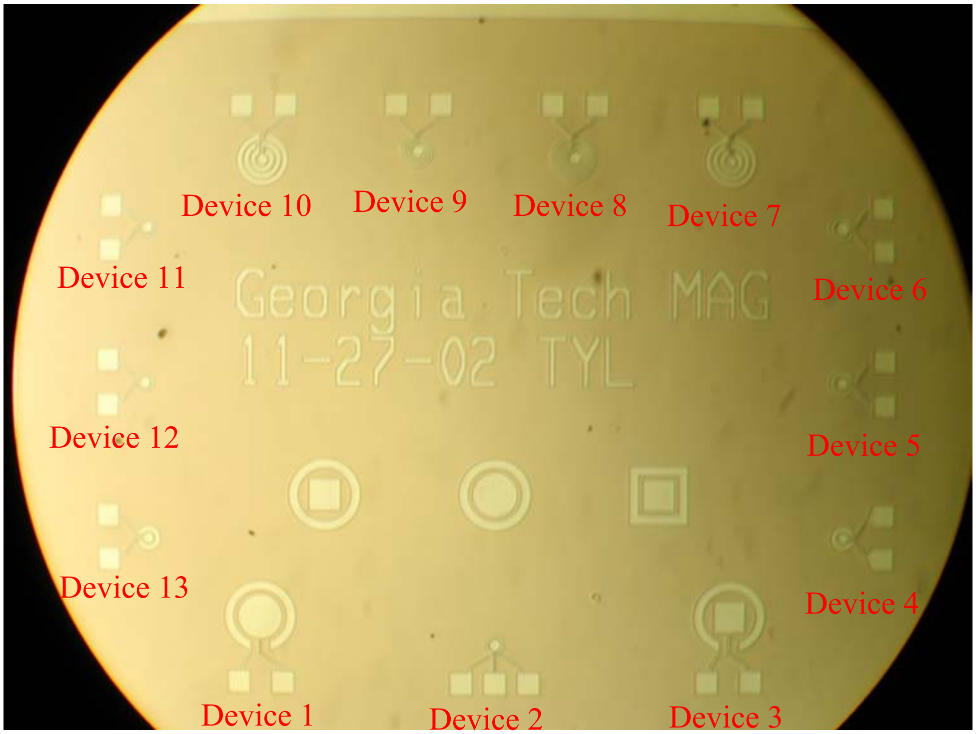

Figure 1. LFE 0 Die, measuring 4mm x 5mm and containing 13 electrode configurations for LFE. Mask designed to fit 204 dice per 3" wafer.

Device 1

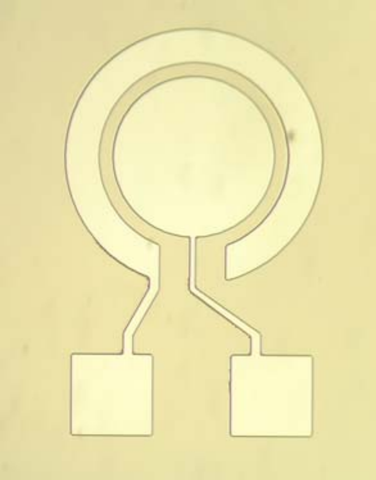

Outer Diameter: 325 μm
Inner Diameter: 240 μm
Center Diameter: 205 μm
Outer Gap: 84 μm
Lead width: 6 μm

Device 2

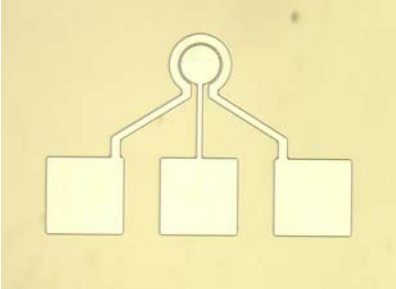

Outer Diameter: 82 μm
Inner Diameter: 60 μm
Center Diameter: 50 μm
Outer Gap: 25 μm

Device 3

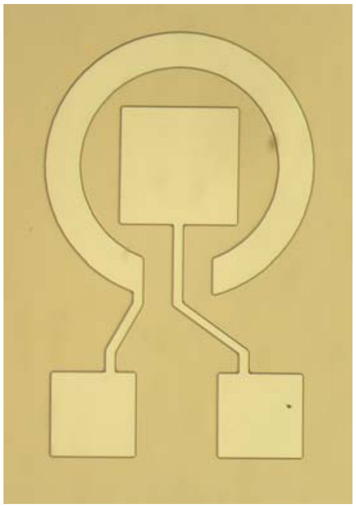

Outer Diameter: 325 μm
Inner Diameter: 240 μm
Square Width: 144 μm
Outer Gap: 85 μm
Lead Width: 6 μm

Device 4

Outer Diameter: 112.5 µm
Inner Diameter: 58.75 µm
Center Diameter: 51 µm
Outer Gap: 28.75 µm
Lead Width: 6 µm

Device 5

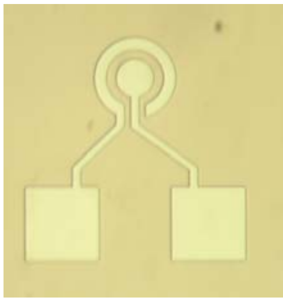

Outer Diameter: 112.5 µm
Inner Diameter: 78.75 µm
Center Diameter: 52.5 µm
Outer Gap: 28.75 µm
Lead Width: 6 µm

Device 6

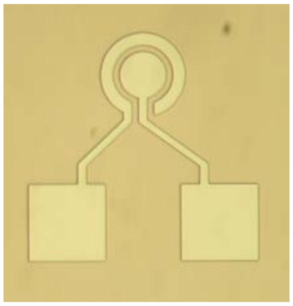

Outer Diameter: 112.5 µm
Inner Diameter: 80 µm
Center Diameter: 62 µm
Outer Gap: 28.75 µm
Lead Width: 6 µm

Device 7

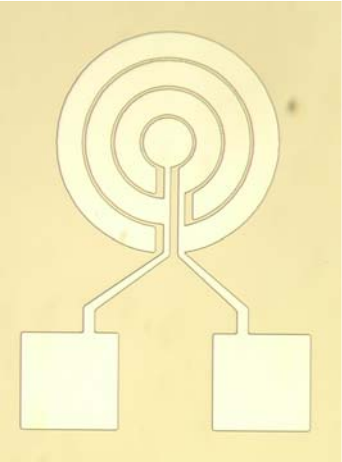

4 Outer Diameter: 206 µm
4 Inner Diameter: 180 µm
3 Outer Diameter: 163 µm
3 Inner Diameter: 120 µm
2 Outer Diameter: 112 µm
2 Inner Diameter: 58.75 µm
1 Diameter: 52.5 µm
Lead Gap: 7.5 µm
End Gap: 6 µm
Lead Width: 6 µm

Device 8

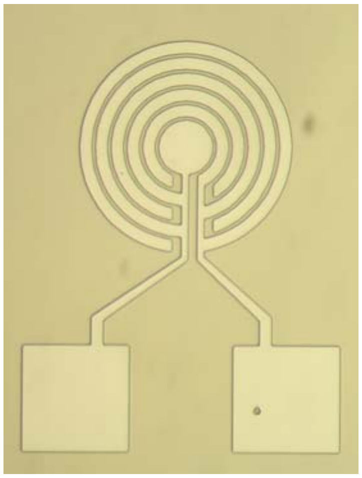

6 Outer Diameter: 205 µm
6 Inner Diameter: 180 µm
5 Outer Diameter: 170 µm
5 Inner Diameter: 150 µm
4 Outer Diameter: 140 µm
4 Inner Diameter: 120 µm
3 Outer Diameter: 110 µm
3 Inner Diameter: 90 µm
2 Outer Diameter: 80 µm
2 Inner Diameter: 60 µm
1 Diameter: 50 µm
Lead Gap: 10 µm
End Gap: 10 µm
Lead Width: 6 µm

Device 9

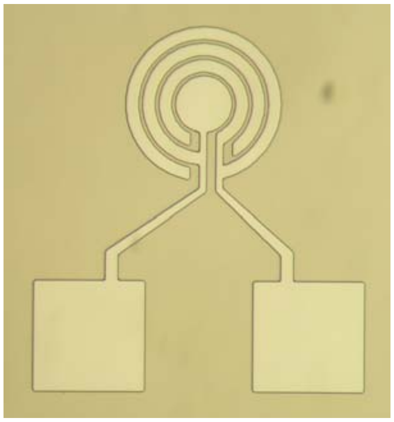

4 Outer Diameter: 142 µm
4 Inner Diameter: 120 µm
3 Outer Diameter: 110 µm
3 Inner Diameter: 90 µm
2 Outer Diameter: 80 µm
2 Inner Diameter: 60 µm
1 Diameter: 50 µm
Lead Gap: 10 µm
End Gap: 8 µm
Lead Width: 6 µm

Device 10

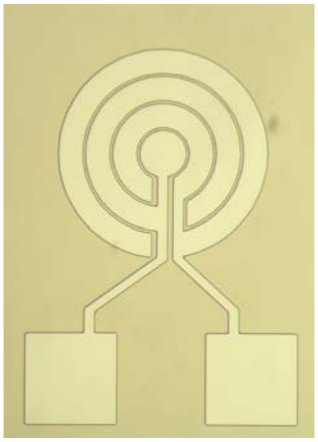

4 Outer Diameter: 230 µm
4 Inner Diameter: 180 µm
3 Outer Diameter: 172 µm
3 Inner Diameter: 120 µm
2 Outer Diameter: 112 µm
2 Inner Diameter: 60 µm
1 Diameter: 52 µm
Lead Gap: 6 µm
End Gap: 6 µm
Lead Width: 12 µm

Device 11

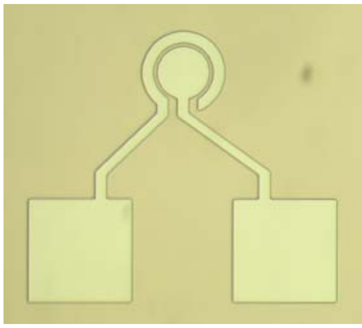

Outer Diameter: 82 µm
Inner Diameter: 60 µm
Center Diameter: 50 µm
Outer Gap: 28 µm
Lead Width: 10 µm

Device 12

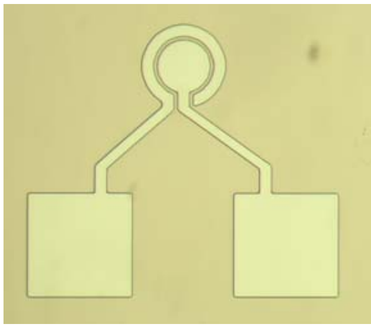

Outer Diameter: 82 µm
Inner Diameter: 60 µm
Center Diameter: 50 µm
Outer Gap: 20 µm
Lead Width: 10 µm

Device 13

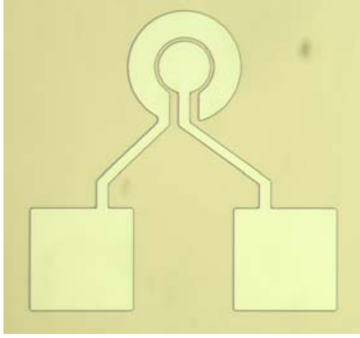

Outer Diameter: 104 µm
Inner Diameter: 60 µm
Center Diameter: 50 µm
Outer Gap: 28 µm
Lead Width: 10 µm

LFE1

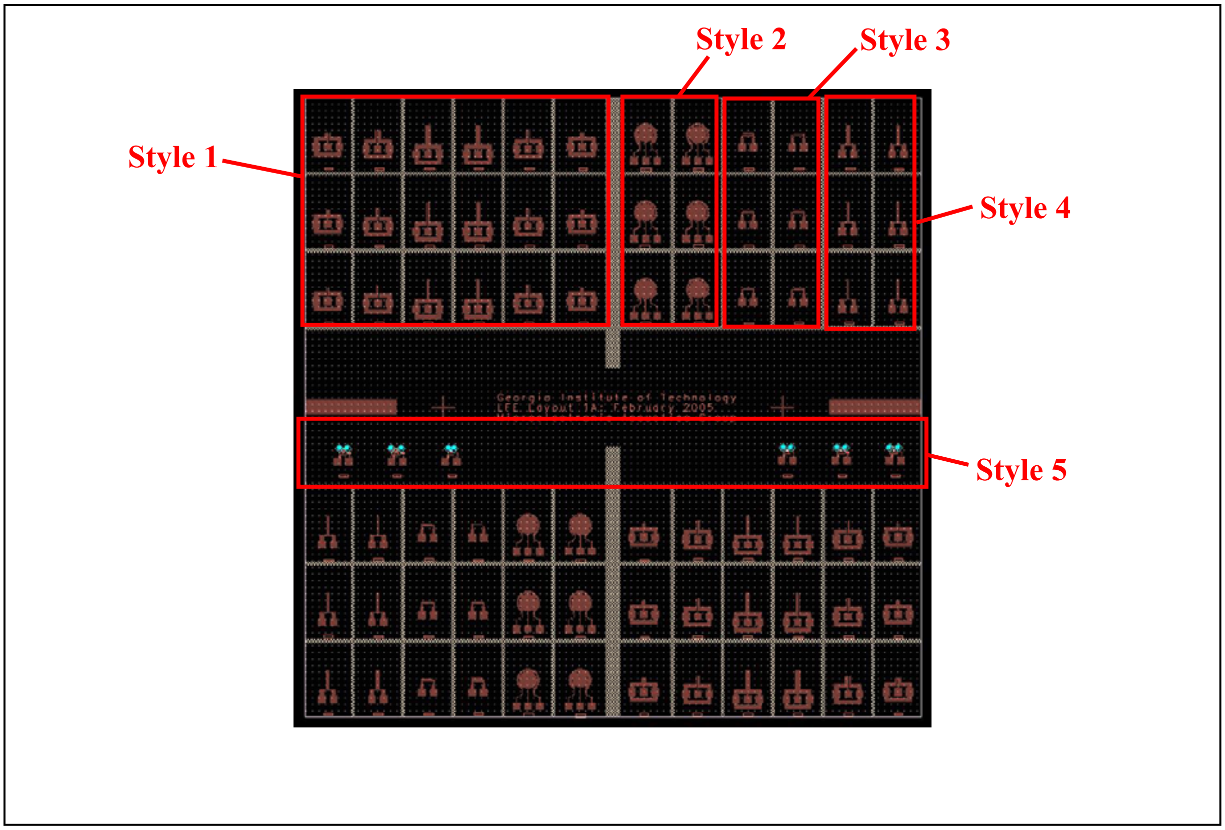

Figure 2. LFE I Die which includes 42 different electrode configurations that could be superimposed to form a 2-layer electrode configuration for more efficient LFE. Die measures 10 mm x 10 mm, arranged to fit 36 dice per photo-mask.

Style 1

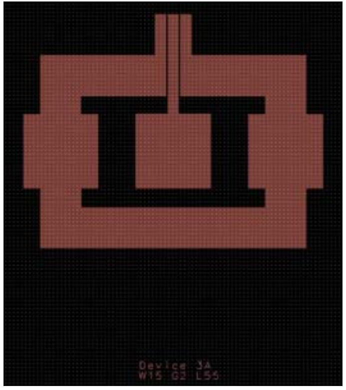

Electrode width = 10, 15, 25 μm
Electrode gap = 2, 3, 4, 5 μm
Electrode length = 55, 110, 250 μm

Style 2

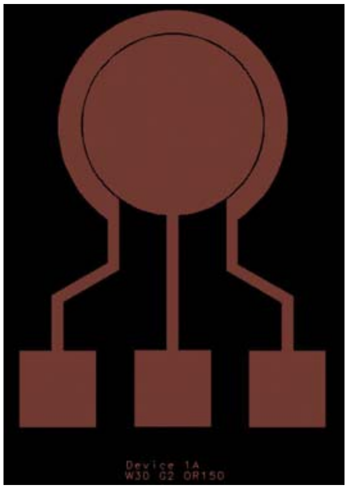

Outer electrode width (Signal) = 20, 30, 50 μm
Outer electrode diameter = 150 μm
Electrode Gap = 2, 3, 4, 5 μm

Style 3

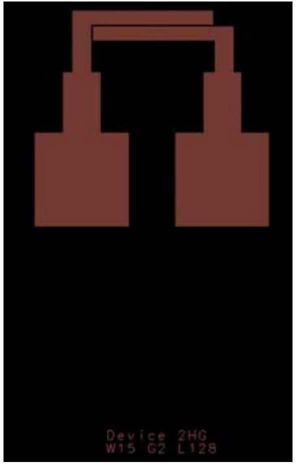

Electrode Width = 15 μm
Electrode Gap = 2, 3, 5 μm
Electrode Length = 128 μm

Style 4

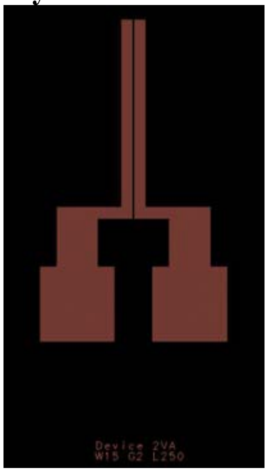

Electrode width = 15 μm
Electrode gap = 2, 3, 5 μm
Electrode length = 250 μm

Style 5

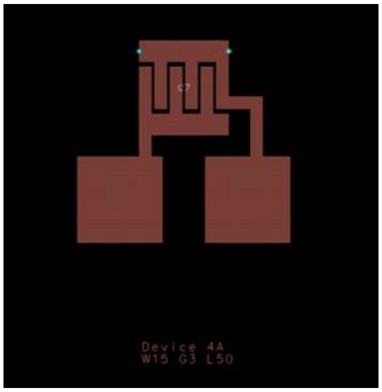

Electrode width = 10, 15, 20, 25 µm
Electrode gap = 2, 3, 4, 5 µm
Electrode length = 50, 150 µm
# of finger pairs = 3, 5

LFE2

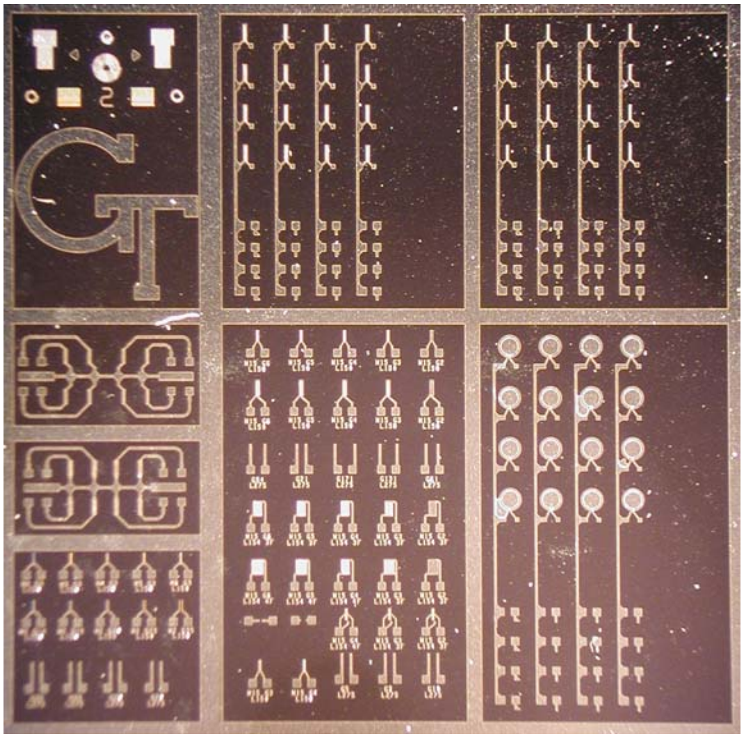

Figure 3. LFE II Die which includes 45 individual electrode configurations and 5 arrayed electrode configurations accounting for an additional 64 devices. Die measures 10 mm x 10 mm, arranged to fit 36 dice per photo-mask.

2-Finger

Electrode width = 15 μm
Electrode gap = 2, 3, 4, 5, 6 μm
Electrode length = 150 μm

3-Finger

Electrode width = 15 μm
Electrode gap = 2, 3, 4, 5, 6 μm
Electrode length = 150 μm

IDT Electrode

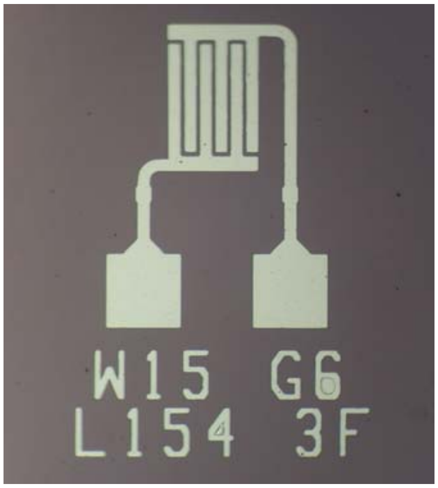

Both 3- and 4-pair IDTs
Electrode width = 15 μm
Electrode gap = 2, 3, 4, 5, 6 μm
Electrode length = 150 μm

Thin 2-Finger

Electrode width = 2, 3, 4, 5 µm
Electrode gap = 3, 10, 15, 20, 25, 35 µm
Electrode length = 150 µm

Slab Electrode

Electrode width = 25 µm
Electrode gap = 3, 5, 10, 21, 61, 94, 131, 171 µm
Electrode length = 275 µm

8-Device Array

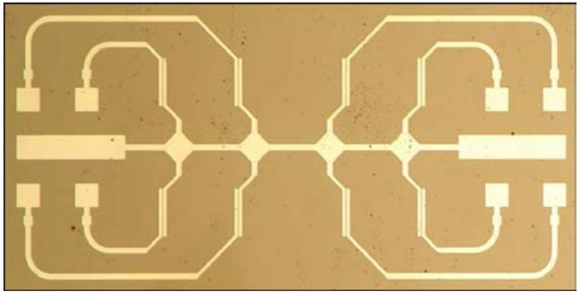

Both 2- and 3-Finger Design
Electrode width = 15 µm
Electrode gap = 3 µm
Electrode length = 150 µm

LFE3

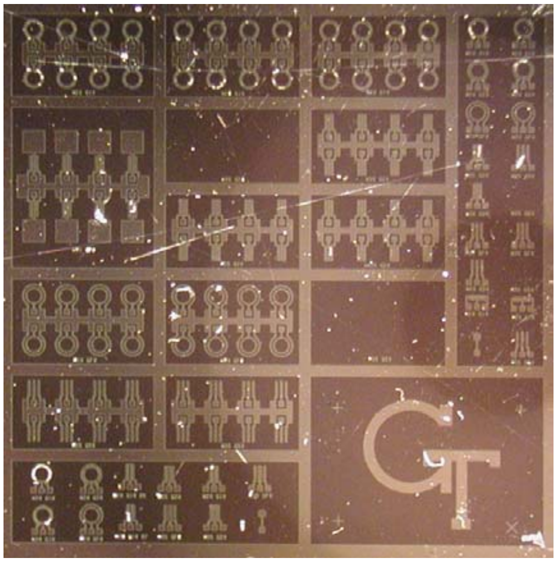

Figure 4. LFE III Die comprising 26 individual devices and 11 8-device arrays. Die measures 10 mm x 10 mm and is arranged to fit 36 die per 3-inch wafer on photo-mask.

Style 1

Electrode Width = 10, 20 μm
Electrode Gap = 10, 20, 40 μm

Style 2

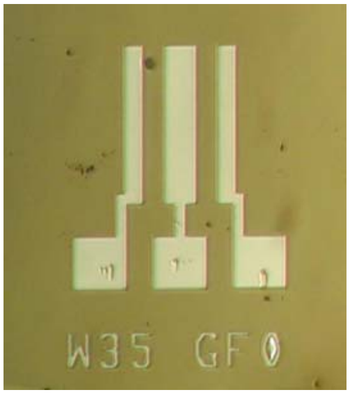

Electrode Width = 20, 35 μm
Electrode Gap = 10, 20, 40, 50 μm

Style 3

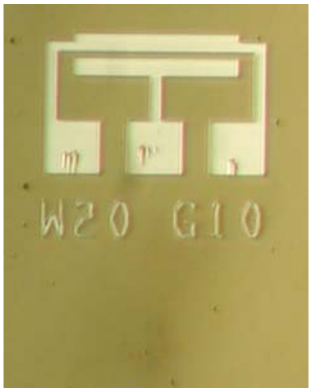

Electrode Width = 20 μm
Electrode Gap = 10 μm

Array Style 1

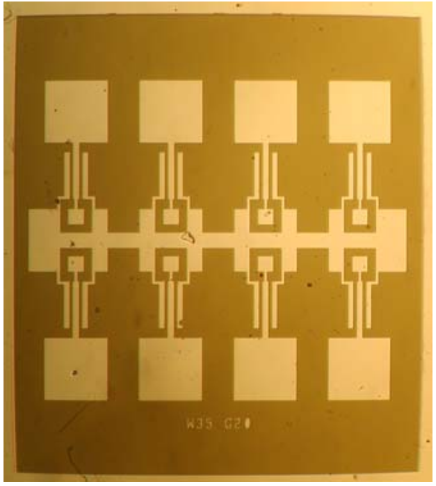

Electrode Width = 35 μm
Electrode Gap = 20 μm
Large squares are surfaces for subsequent wire-bonding

Array Style 2

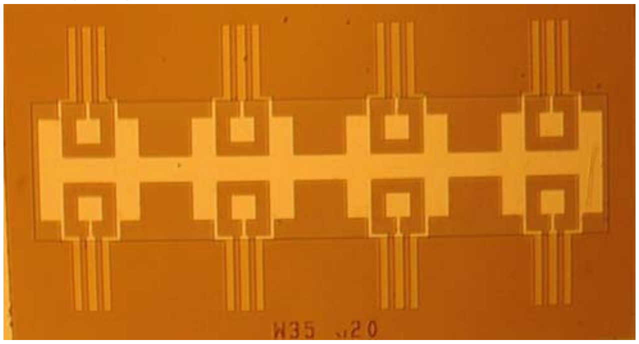

Electrode Width = 35 μm
Electrode Gap = 20, 50 μm

Array Style 3

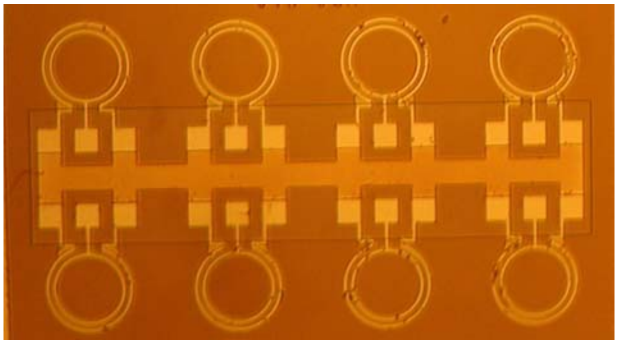

Electrode Width = 20 µm
Electrode Gap = 10, 40 µm

LFE4

4-Device Array

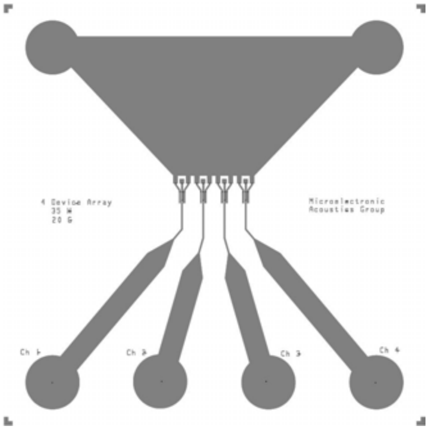

3-Finger Design
Electrode width = 35 µm
Electrode gap = 20 µm
Overall area = 10 mm x 10 mm

8-Device Array

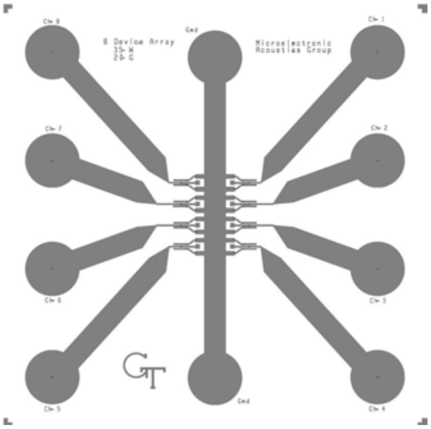

3-Finger Design
Electrode width = 35 µm
Electrode gap = 20 µm
Overall area = 10 mm x 10 mm

APPENDIX C: PHOTOLITHOGRAPHY PROCEDURE

The following materials were used for the photolithography process outlined below:

1. Laurell Technologies Corporation Model WS-200-4NPP Spin Coater
2. Karl Suss MJB3 Mask Aligner
3. Thermolyne Type 1900 Hot Plate

Photolithography Procedure:

1. Rinse the wafer with the following: TCE (Trichloroethylene), Acetone, Methanol, Isopropanol, DI H_2O.
2. Blow both sides dry with N_2 gas stream to remove moisture
3. Warm wafer on a heater plate for ~ 1 minute over 100ºC to remove all moisture
4. Load wafer on vacuum chuck of spin coater. Dispense enough 98% HMDS by pipette to cover entire wafer. Spin the wafer with 98% HMDS at 4000 rpm for 30 seconds at maximum acceleration.
5. Soft bake the wafer immediately on hot plate at ~ 180 C for 30 seconds.
6. Cool wafer on cooling block for 1 minute.
7. Load wafer back on vacuum chuck of spin coater. Dispense enough Shipley's 1805 (S1805) photoresist by pipette to cover entire wafer. Spin the wafer with S1805 at 4000 rpm for 30 seconds at maximum acceleration. This should yield a layer of photoresist ~0.5 μm thick uniformly across the wafer, which is adequate for feature sizes greater than 0.8 μm.
8. Soft bake the wafer immediately on hot plate at ~ 180ºC for 60 seconds.

9. Cool wafer on cooling block for 1 minute. This is a critical step.
10. Mount wafer on vacuum chuck of Karl Suss MJB3 mask aligner. Verify wafer is flat on chuck. Load relevant photomask into mask holder of mask aligner and align wafer beneath the mask appropriately. (Physical contact of the wafer with the photomask was essential for adequate yield with the system used)
11. Expose wafer to ~60 mJ of 365 nm UV light. (The system used for these experiments was calibrated to 4 mW, which required 15 seconds exposure time)
12. Remove wafer from the mask aligner and submerge in Chlorobenzene bath for 90 seconds.
13. Completely dry wafer using N_2 gas stream to remove all chlorobenzene. DO NOT expose surface to DI H_2O or any other liquids before next step.
14. Prepare developer solution (5 parts DI H_2O to 1 part Microposit 351 concentrated developer). Submerge wafer in developer solution and manually agitate for 35 – 45 seconds, or until photoresist die begins to "burst out." A practiced eye should be able to discern the point at which the appropriate features of the mask design have been fully resolved (i.e. all undesireable photoresist has been removed) but not over-developed.
15. Immediately rinse the wafer in a stream of DI H_2O.
16. Completely dry wafer using N_2 gas stream to remove water.
17. Hard bake wafer for an additional 60 seconds on hot plate. This also ensures that all water is evaporated from the surface.

APPENDIX D: FUNCTIONALIZATION PROTOCOL

The following equipment was used for the surface functionalization protocol outlined below:

1. Branson Model 2510 Ultrasonic Bath
2. Nitrogen glove box
3. Unifilm PVD-300 Sputtering System – Ion mill tool
4. VWR Scientific Products Standard Shaker
5. VWR Scientific Products mini vortexer
6. VWR 25 mL centrifuge tubes

Crosslinker Immobilization

1. Prepare the 4% MTS primary crosslinking solution by mixing 1 part MTS solution (Fluka) to 24 parts dry Toluene (99.5% A.C.S., Sigma Aldrich) in a sufficiently large centrifuge tube. Mix solution thoroughly using vortexer at greater than medium level for more than 30 seconds.
2. Deposit enough of 4% MTS crosslinker solution into appropriate sealed containers to accommodate samples. (For the purposes of these experiments, 3-4 mL was deposited in to 50 mL centrifuge tubes from VWR which accommodated 1 cm × 1 cm wafer chips)

3. Rinse the ZnO coated surfaces with the following: TCE (Trichloroethylene), Acetone (VWR, BDH), Methanol (ultra, J.T. Baker), Isopropanol (VWR, BDH), DI H_2O (Aristar Plus, VWR, BDH).
4. Blow both sides dry with N_2 gas stream to remove moisture
5. Warm samples on a heater plate for ~ 1 minute over 100ºC to remove all moisture
6. Load samples using carbon tape to secure them onto platform surface to be placed on planet 5 of the Unifilm PVD-300 sputtering system.
7. Using loadlock, load platform onto planet 5 of the Unifilm system.
8. Run program to ion mill surfaces using 9 mA beam current for 5 minutes.
9. IMMEDIATELY submerge each ZnO coated sample individually into containers with 4% MTS crosslinker solution and immediately seal. It is EXTREMELY IMPORTANT to minimize exposure time of the samples to air after removing them from the vacuum environment of the ion mill before submerging them in MTS solution.
10. Allow samples to incubate for 24 hours.
11. Prepare 1 mM GMBS (Fluka) solution in ethanol (95%, Fisher) at least 2 hours prior to using. 1mM GMBS solution was allowed to mix for 2 hours on a shake table at medium speed, or until all granules of GMBS were no longer visible in the solution. Again prepare enough of 1 mM GMBS solution into appropriate sealed containers to accommodate samples. (3-4 mL in 50 mL centrifuge tubes)
12. Remove samples from 4% MTS solution and rinse using stream of ethanol for several seconds.

13. Submerge samples in a small buoyant container with sufficient ethanol to cover the samples and place in ultrasonic bath for 5 minutes.
14. Remove sample from sonication bath and deposit in 1 mM GMBS solution and seal. Allow samples to incubate for 24 hours.
15. Remove samples from 1 mM GMBS solution and rinse using stream of ethanol for several seconds.
16. Submerge samples in a small buoyant container with sufficient ethanol to cover the samples and place in ultrasonic bath for 5 minutes.
17. Samples are now prepared for IgG immobilization.

Antibody Immobilization

18. Immediately after ethanol sonication, dry samples with N_2 gas stream and deposit 200 µg/mL solution of IgG antibodies by pipette onto surface of sample. (For the experiments described in this thesis, 30 µL was sufficient)
19. Allow Ab solution to incubate on surface for 4 hours.
20. Rinse surface with PBS buffer stream.
21. Samples are now functionalized and ready for exposure to liquid sample for detection.

APPENDIX E: MATLAB CODE – PIEZOELECTRIC TA_2O_5

```
%Calculations defined for Z directed propagation li][0 0 1]
%Assumed Class of 2mm for Ta2O5
%Written by Christopher Corso

% syms lx ly lz;
% lLj = [0 0 0; 0 0 0; 0 0 1; 0 1 0; 1 0 0; 0 0 0]; %Set this according
        to direction of propagation
% liJ= [0,0,0,0,1,0;0,0,0,1,0,0;0,0,1,0,0,0]; %Also set this according
       to direction of propagation

syms c11 c12 c13 c23 c33 c44 c55 c66 e14 e25 e36 e15 e24 e33 e32 e31
     lex ley lez epsxx epsyy epszz;
% stiffness= [c11,c12,c13,0,0,0; c12,c11,c23,0,0,0; c13,c23,c33,0,0,0;
             0,0,0,c44,0,0; 0,0,0,0,c55,0; 0,0,0,0,0,c66]; %Stiffness
             Tensor for Orthorhombic

% lj=[0; 0; 1]; %Set this according to direction of propagation
% li=[0 0 1]; %Set this according to direction of propagation
% Efieldj=[lex; ley; 0]; %direction of electric field in x y plane
% Efieldi=[lex ley 0]; %direction of electric field in x y plane

piezoiL=[0,0,0,e14,0,0;0,0,0,0,e25,0;0,0,0,0,0,e36]; %defined for class
        222
piezoKj=[0,0,0;0,0,0;0,0,0;e14,0,0;0,e25,0;0,0,e36]; %defined for class
        222

% permittivity=[epsxx, 0, 0; 0, epsyy, 0; 0, 0, epszz]; %Perittivity
% top=piezoKj*Efieldj*Efieldi*piezoiL;
% bottom=Efieldi*permittivity*Efieldj;
% piez=top/bottom;
% stiffened=stiffness+piez;
% christoffel=liJ*stiffened*lLj

%Above Calculations Redone for Assumed class 2mm Ta2O5
%

%Declaration of euler angles for rotation of matrices
rotation=1;       % 1 if rotation to be carried out, 0 if not
phi=0;            % clockwise rotation around z axis
theta=-275.216;   % clockwise rotation around new y axis
psi=0;            % clockwise rotation around new z axis

%Declaration of rest of variables
syms lx ly lz;
lLj = [0 0 0; 0 0 0; 0 0 1; 0 1 0; 1 0 0; 0 0 0]; %Set this according
to direction of propagation
liJ= [0,0,0,0,1,0;0,0,0,1,0,0;0,0,1,0,0,0]; %Also set this according to
direction of propagation

%lLj = [1 0 0; 0 0 0; 0 0 0; 0 0 0; 0 0 1; 0 1 0]; %Set this according
to direction of propagation
%liJ= lLj'; %Also set this according to direction of propagation
```

```
syms c11 c12 c13 c23 c33 c44 c55 c66 e14 e25 e36 e15 e24 e33 e32 e31
     lex ley lez epsxx epsyy epszz;

stiffness= [c11,c12,c13,0,0,0; c12,c11,c23,0,0,0; c13,c23,c33,0,0,0;
           0,0,0,c44,0,0; 0,0,0,0,c55,0; 0,0,0,0,0,c66]; %Stiffness
           Tensor for Orthorhombic

%lj=[0; 0; 1]; %Set this according to direction of propagation
%li=[0 0 1]; %Set this according to direction of propagation

Efieldj=[1; 0; 0]; %Arbitrary direction of electric field
Efieldi=[1 0 0]; %Arbitrary direction of electric field

%piezoiL=[0,0,0,0,e15,0;0,0,0,e24,0,0;e31,e32,e33,0,0,0]; %defined for
         class 222
%piezoKj=[0,0,e31;0,0,e32;0,0,e33;0,e24,0;e15,0,0;0,0,0]; %defined for
         class 222
permittivity=[epsxx, 0, 0; 0, epsyy, 0; 0, 0, epszz]; %Perittivity

if rotation==1;
    Mphi= [cosd(phi)^2 sind(phi)^2 0 0 0 sind(2*phi); sind(phi)^2
            cosd(phi)^2 0 0 0 -sind(2*phi); 0 0 1 0 0 0; 0 0 0
            cosd(phi) -sind(phi) 0; 0 0 0 sind(phi) cosd(phi) 0; -
            sind(2*phi)/2 sind(2*phi)/2 0 0 0 cosd(2*phi)];
    Mtheta= [cosd(theta)^2 0 sind(theta)^2 0 -sind(2*theta) 0; 0 1 0 0
            0 0; sind(theta)^2 0 cosd(theta)^2 0 sind(2*theta) 0; 0 0 0
            cosd(theta) 0 sind(theta); sind(2*theta)/2 0 -
            sind(2*theta)/2 0 cosd(2*theta) 0; 0 0 0 -sind(theta) 0
            cosd(theta)];
    Mpsi= [cosd(psi)^2 sind(psi)^2 0 0 0 sind(2*psi); sind(psi)^2
            cosd(psi)^2 0 0 0 -sind(2*psi); 0 0 1 0 0 0; 0 0 0
            cosd(psi) -sind(psi) 0; 0 0 0 sind(psi) cosd(psi) 0; -
            sind(2*psi)/2 sind(2*psi)/2 0 0 0 cosd(2*psi)];
    MphiPrime=Mphi';
    MthetaPrime=Mtheta';
    MpsiPrime=Mpsi';
    aphi= [cosd(phi) sind(phi) 0; -sind(phi) cosd(phi) 0; 0 0 1];
    atheta= [cosd(theta) 0 -sind(theta); 0 1 0; sind(theta) 0
            cosd(theta)];
    apsi= [cosd(psi) sind(psi) 0; -sind(psi) cosd(psi) 0; 0 0 1];
    aphiPrime=aphi';
    athetaPrime=atheta';
    apsiPrime=apsi';

    stiffnessrotated=Mpsi*Mtheta*Mphi*stiffness*MphiPrime*MthetaPrime*Mp
            siPrime;

    piezoiLrotated=apsi*atheta*aphi*piezoiL*MphiPrime*MthetaPrime*MpsiPr
            ime;

    permittivityrotated=apsi*atheta*aphi*permittivity*aphiPrime*athetaPr
            ime*apsiPrime;

    piezoKjrotated=conj(piezoiLrotated');
    top=piezoKjrotated*Efieldj*Efieldi*piezoiLrotated;
    bottom=Efieldi*permittivityrotated*Efieldj;
```

```
    piez=top/bottom;
    stiffened=stiffnessrotated+piez;
    christoffel=liJ*stiffened*lLj
else
    top=piezoKj*Efieldj*Efieldi*piezoiL;
    bottom=Efieldi*permittivity*Efieldj;
    piez=top/bottom;
    stiffened=stiffness+piez;
    christoffel=liJ*stiffened*lLj
end
```

APPENDIX F: AMERICAN ASSOCIATION OF CANCER RESEARCHERS PRESS RELEASE

A New Technology for Cancer Screening Listens for the Signs of Cancer

ATLANTA – Cancer-sensing devices built as cheaply and efficiently as wristwatches – using many of the same operating principles – could change the way clinicians detect, treat and monitor cancer in patients. Researchers from the Georgia Institute of Technology have created an acoustic sensor that can report the presence of small amounts of mesothelin, a molecule associated with a number of cancers including mesothelioma, as they attach to the sensor's surface.

According to the researchers, the study is a proof of principle, demonstrating a technique that might work for the detection of nearly any biomarker – a collective term for a molecular signal that denotes the presence of disease. They present their findings today in Atlanta, Georgia at the American Association for Cancer Research's 2nd Annual International Conference on Molecular Diagnostics in Cancer Therapeutic Development.
"It is one thing to be able to identify biomarkers for a disease, but it is another to be able to find them in blood quickly and easily at very low concentrations," said Anthony Dickherber, a graduate student in the School of Electrical and Computer Engineering at Georgia Tech. "We envision that, one day, doctors can use an array of our sensors as a sort of laboratory in their office, where they could use a quick blood sample to detect or monitor the signs of cancer."

According to Dickherber, such a device would be a boon to healthcare practice, allowing physicians to screen patients for signs of disease before opting for more expensive or invasive diagnostic techniques. Responding to the growing need for such sensors in both research and clinical practice, Dickherber, along with fellow Georgia Tech graduate student Christopher Corso and research adviser William D. Hunt, Ph.D., conceived of and developed the ACµRay™ (pronounced *ak´-u-rā*) chip, standing for ACoustic micro-arRAY – a device that shares more in common with an inexpensive wristwatch than the sort of cutting edge molecule-sorting apparatuses currently used by researchers and clinical laboratory technicians.

The array consists of a series of electrodes deposited on the surface of a thin film of zinc oxide, which allows the device to resonate, or vibrate, at a specific frequency when a current is applied, much like the quartz timing devices used in many clocks and watches. “The sensor itself is built on a base of silicon, like a computer chip, and could be mass-produced using very well known and inexpensive microelectronic fabrication techniques,” Dickherber said.

To turn this array into a sensor, the Georgia Tech researchers coated the zinc oxide surface with mesothelin-specific antibodies generated in the lab of Ira Pastan, M.D., at the National Cancer Institute. These molecules are engineered versions of the antibodies the immune system creates to identify foreign intruders, such as microbial parasites. In this study, the researchers coated the sensor with antibodies for mesothelin, a cell-surface protein that is highly expressed in mesothelioma, ovarian cancer, pancreatic cancer and other malignancies.

When the mesothelin binds to an antibody, the added mass changes the frequency at which the acoustic wave passes between the electrodes on the surface of the device. The device is able to “hear” the pitch change due to nanomolar concentrations of mesothelin (just a few molecules amid billions) binding to antibodies on the chip. The technology has the potential of detecting biomarkers in even lower concentrations than those tested, Dickeherber said.

“It is really an elegant engineering solution to a very complicated problem,” said Hunt, a professor of electrical and computer at Georgia Tech and lead researcher on the project. “With refinement, this technology could readily lead to an inexpensive, ubiquitous technology for researchers, physicians and the clinical laboratory.”

This research is supported by grants from the U.S. Army Medical Research & Materiel Command Prostate Cancer Research Program, the National Science Foundation, The V Foundation, the National Cancer Institute and the Georgia Cancer Coalition.

>>>>>

AACR 2007 Conference on Molecular Diagnostics in Cancer Therapeutic Development

September 17-20th, Atlanta, Ga.

Coverage for Tony Dickherber, Christopher Corso, and William Hunt “A New Technology for Cancer Screening Listens for the Signs of Cancer”*

From our press release:
RxPG News
http://www.rxpgnews.com/research/A-new-technology-for-cancer-screening-listens-for-the-signs-of-cancer_64056.shtml

Dentalplans.com
http://www.dentalplans.com/articles/25102/

PhysOrg.com
http://www.physorg.com/news109349930.html

ScienceDaily
http://www.sciencedaily.com/releases/2007/09/070918144313.htm

Original Stories:

WebMD (Dan DeNoon)
"Sensor Hears Cancer's Call; Tiny Biosensors Detect 'Song' of Cancer Markers, Say Researchers"
http://www.webmd.com/cancer/news/20070918/sensor-hears-cancers-call

From the WebMD story above:
Medicine.net
http://www.medicinenet.com/script/main/art.asp?articlekey=83974

From the Amanda Gardner HealthDay story "Tiny Sensor Could Spot Cancer Early":

CBC News
http://www.cbc.ca/cp/HealthScout/070918/6091806AU.html

Health Central.com
http://www.healthcentral.com/newsdetail/408/608331.html

WFIE 14 Indiana (NBC affiliate)
http://www.14wfie.com/Global/story.asp?S=7094493&nav=3w6r

LEX 18 Kentucky (NBC affiliate)
http://www.lex18.com/Global/story.asp?S=7094493&nav=EQls

Forbes
http://www.forbes.com/forbeslife/health/feeds/hscout/2007/09/18/hscout608331.html

US News & World Report
http://health.usnews.com/usnews/health/healthday/070918/tiny-sensor-could-spot-cancer-early.htm

Dentalplans.com
http://www.dentalplans.com/articles/25095/

Health Scout
http://www.healthscout.com/news/1/608331/main.html

HealthCentral.com
http://www.healthcentral.com/newsdetail/408/608331.html

KOLD News Arizona (CBS Affiliate)
http://www.kold.com/global/story.asp?s=7094493

CNN News Room

September 19, 2007 Wednesday
SHOW: CNN NEWSROOM 3:00 PM EST
Bail Set For O.J. Simpson; Ahmadinejad to Visit Ground Zero?; Al Sharpton's Planned Protest in Jena, Lousiana
BYLINE: Joe Johns, Paul Vercammen, Deborah Feyerick, Susan Roesgen, Ed Lavandera, Don Lemon, Fredricka Whitfield, Jeffrey Toobin, Sanjay Gupta, Susan Lisovicz, Wolf Blitzer
SECTION: NEWS; International

WHITFIELD: Straight ahead, a high tech computer chip smaller than a penny that can detect cancer. Details on that straight ahead in "THE NEWSROOM".

WHITFIELD: A computer chip could one day make diagnosing cancer as easy as telling time.

Here's CNN's chief medical correspondent, Dr. Sanjay Gupta.

DR. SANJAY GUPTA, CNN CORRESPONDENT: This is something that really fascinates me quite a bit. This is a little chip that I'm holding up here. I'm actually holding it in a pair of tweezers this thing is so small. It's called the ACuRay and it's not something that's going to be widely available quite yet. But researchers have been focusing on this particular chip as a way to detect cancer very, very early.

Again, it's called the ACuRay. You can take at it there. What it is specifically is 140 different electrodes actually bound together by zinc oxide. The theory a simple one -- basically, if you have cancer molecules in your blood and you wash your blood over the sensor, the way that those cancer molecules bind to this

ACuRay gives off a certain resonance, a certain frequency that can be measured. If you have cancer molecules, it's going to sound different than if you don't have cancer molecules in your blood. The whole idea is that you want to detect cancer as early as possible.

Now what does this all mean?

There could be a day when doctors have several different little devices like this in their office and you walk in, you give a drop of blood and they immediately screen to tell if you have any cancer molecules in your bloodstream. It could be used, perhaps, in the future for infectious diseases, as well.

Again, as I mentioned, it's not something we may see in our lifetimes as a general way of practicing, but this whole idea you might be able to find cancer early, earlier than ever before, before it shows up on a C.T. scan or an MRI, when it's just a few still a few molecules in your blood is sort of the holy grail of cancer detection and screening.

Could this be the answer?

Possibly one day. It's something that we're certainly going to keep an eye on -- back to you.

LEMON: All right, Sanjay.

It's time now to check in with CNN's Wolf Blitzer.

WHITFIELD: Yes, in "THE SITUATION ROOM" -- what do you have on tap?

WOLF BLITZER, HOST, "THE SITUATION ROOM": All right, guys, thanks very much.

The Republican presidential candidate, Rudy Giuliani, has a message for MoveOn.org -- bring it on. He talks about his high profile spat with the liberal anti-war group in an exclusive one-on-one interview with our chief national correspondent, John King. That's coming up.

Also, Reverend Jesse Jackson says Democratic presidential candidate Barack Obama -- and I'm quoting now -- "is acting like he's white." We'll show you what's behind that controversial comment.

Also, carefree lives in the face of unimaginable suffering. There are some disturbing newly released images of the men and women who ran the Nazi Auschwitz death camp. All that and a lot more coming up right here in "THE SITUATION ROOM" -- back to you.

LEMON: All right, Wolf, we'll be watching.

Thank you. WHITFIELD: All right, the closing bell and a wrap of the action on Wall Street straight ahead.

REFERENCES

[1] E. Dominguez and S. Alcock, "Sensing technologies for contaminated sites and groundwater," *Biosensors and Bioelectronics*, vol. 17, pp. 625-633, 2002.

[2] B. M. Paddle, "Biosensors for chemical and biological agents of defence interest," *Biosensors and Bioelectronics*, vol. 11, pp. 1079-1113, 1996.

[3] D. D. Stubbs, S. H. Lee, and W. D. Hunt, "Investigation of Cocaine Plumes Using Surface Acoustic Wave Immunoassay Sensors," *Anal. Chem.*, vol. 75, pp. 6231-6235, 2003.

[4] N. C. Institute, "Cancer Facts & the War on Cancer," 2008.

[5] A. Jemal, R. Siegel, E. Ward, T. Murray, J. Xu, and M. J. Thun, "Cancer Statistics, 2007," *CA Cancer J Clin*, vol. 57, pp. 43-66, 2007.

[6] R. Etzioni, N. Urban, S. Ramsey, M. McIntosh, S. Schwartz, B. Reid, J. Radich, G. Anderson, and L. Hartwell, "The Case for Early Detection," *Nature Reviews: Cancer*, vol. 1, pp. 243-252, 2003.

[7] Niroshan Ramachandran, D. N. Larson, P. R. H. Stark, E. Hainsworth, and J. LaBaer, "Emerging tools for real-time label-free detection of interactions on functional protein microarrays," *FEBS Journal*, vol. 272, pp. 5412-5425, 2005.

[8] M. Uttamchandani and S. Q. Yao, "Peptide Microarrays: Next Generation biochips for Detection, Diagnostics and High-Throughput Screening," *Current Pharmaceutical Design*, vol. 14, pp. 000-000, 2008.

[9] J. Wang, "Electrochemical biosensors: Towards point-of-care cancer diagnostics," *Biosensors and Bioelectronics*, vol. 21, pp. 1887-1892, 2006.

[10] S. A. Soper, K. Brown, A. Ellington, B. Frazier, G. Garcia-Manero, V. Gau, S. I. Gutman, D. F. Hayes, B. Korte, J. L. Landers, D. Larson, F. Ligler, A. Majumdar, M. Mascini, D. Nolte, Z. Rosenzweig, J. Wang, and D. Wilson, "Point-of-care biosensor systems for cancer diagnostics/prognostics," *Biosensors and Bioelectronics*, vol. 21, pp. 1932-1942, 2006.

[11] S. Kumar, A. Mohan, and R. Guleria, "Biomarkers in cancer screening, research and detection: present and future: a review," *Biomarkers: Biochemical Indicators Of Exposure, Response, And Susceptibility To Chemicals*, vol. 11, pp. 385-405, 2006.

[12] T. J. Kindt, R. A. Goldsby, B. A. Osborne, and J. Kuby, *Immunology*, 6th ed. New York: W.H. Freeman, 2007.

[13] X. Fan, I. M. White, S. I. Shopova, H. Zhu, J. D. Suter, and Y. Sun, "Sensitive optical biosensors for unlabeled targets: A review," *Analytica Chimica Acta*, vol. 620, pp. 8-26, 2008.

[14] X. Gao, Y. Cui, R. M. Levenson, L. W. K. Chung, and S. Nie, "In vivo cancer targeting and imaging with semiconductor quantum dots," *Nat Biotech*, vol. 22, pp. 969-976, 2004.

[15] D. A. Hall, J. Ptacek, and M. Snyder, "Protein microarray technology," *Mechanisms of Ageing and Development*, vol. 128, pp. 161-167, 2007.

[16] I. Abdulhalim, M. Zourob, and A. Lakhtakia, "Surface plasmon resonance for biosensing: A mini-review," *Electromagnetics*, vol. 28, pp. -, 2008.

[17] M. Uttamchandani and S. Q. Yao, "Peptide Microarrays: Next Generation Biochips for Detection, Diagnostics and High-Throughput Screening," *Current Pharmaceutical Design*, vol. 14, 2008.

[18] C. Z. Rosen, B. V. Hiremath, and R. E. Newnham, *Piezoelectricity*. New York: American Institute of Physics, 1992.

[19] L. Woo Wai, S. Yonghua, and K. Eun Sok, "Lateral-field-excitation acoustic resonators for monolithic oscillators and filters," *Frequency Control Symposium, 1996. 50th., Proceedings of the 1996 IEEE International.*, pp. 558-562, 1996.

[20] J. F. Rosenbaum, *Bulk acoustic wave theory and devices*. Boston: Artech House, 1988.

[21] J. Kondoh, Y. Okiyama, S. Mikuni, Y. Matsui, H. Yatsuda, and M. Nara, "Development of SH-SAW Sensing System for Liquids," presented at Frequency Control Symposium, 2007 Joint with the 21st European Frequency and Time Forum. IEEE International, 2007.

[22] E. Berkenpas, S. Bitla, P. Millard, and M. P. da Cunha, "Pure shear horizontal SAW biosensor on langasite," *Ieee Transactions on Ultrasonics Ferroelectrics and Frequency Control*, vol. 51, pp. 1404-1411, 2004.

[23] D. W. Branch and S. M. Brozik, "Low-level detection of a Bacillus anthracis simulant using Love-wave biosensors on 36 degrees YX LiTaO3," *Biosensors & Bioelectronics*, vol. 19, pp. 849-859, 2004.

[24] T. Kogai and H. Yatsuda, "3F-3 Liquid Sensor Using SAW and SH-SAW on Quartz," presented at Ultrasonics Symposium, 2006. IEEE, 2006.

[25] G. Sauerbrey, "Use of quartz vibrator for weighing thin films on a microbalance," *Z. Physik*, vol. 155, pp. 17, 1959.

[26] K. K. Kanazawa and J. G. Gordon, "Frequency of a Quartz Microbalance in Contact with Liquid," *Analytical Chemistry*, vol. 57, pp. 1770-1771, 1985.

[27] K. K. Kanazawa, "QCM physical theory extended to include liquid immersion," Honolulu, HI, USA, 1999.

[28] W. D. Hunt, D. D. Stubbs, and S. H. Lee, "Time-dependent Signatures of Acoustic Wave Biosensors," *Proceedings of the IEEE*, vol. 91, pp. 12, 2003.

[29] D. L. Smith, *Thin-film deposition : principles and practice*. New York: McGraw-Hill, 1995.

[30] S. L. Pinkett, W. D. Hunt, B. P. Barber, and P. L. Gammel, "Determination of ZnO temperature coefficients using thin film bulk acoustic wave resonators," *Ultrasonics, Ferroelectrics and Frequency Control, IEEE Transactions on*, vol. 49, pp. 1491- 1496, 2002.

[31] K. M. Lakin, G. R. Kline, and K. T. McCarron, "Development of miniature filters for wireless applications," *IEEE Transactions on Microwave Theory and Techniques*, vol. 43, pp. 2933-2939, 1995.

[32] A. Shons, F. Dorman, and J. Najarian, "An immunospecific microbalance," *J Biomed Mater Res*, vol. 6, pp. 565-70, 1972.

[33] X. L. Su and Y. Li, "A self-assembled monolayer-based piezoelectric immunosensor for rapid detection of Escherichia coli O157:H7," *Biosens Bioelectron*, vol. 19, pp. 563-74, 2004.

[34] Z. Y. Wu, G. L. Shen, S. P. Wang, and R. Q. Yu, "Quartz-crystal microbalance immunosensor for Schistsoma-japonicum-infected rabbit serum," *Anal Sci*, vol. 19, pp. 437-40, 2003.

[35] C. D. Corso, D. D. Stubbs, S. H. Lee, M. Goggins, R. H. Hruban, and W. D. Hunt, "Real-time detection of mesothelin in pancreatic cancer cell line supernatant using an acoustic wave immunosensor," *Cancer Detect Prev*, 2006.

[36] J. V. Atanasoff and P. J. Hart, "Dynamical determination of the elastic constants and their temperature coefficients for quartz," *Physical Review*, vol. 59, pp. 85-96, 1941.

[37] R. Bechmann, "Parallel Field Excitation of Thickness Modes of Quartz Plates," *Frequency Control, 14th Annual Symposium on. 1960*, pp. 68-88, 1960.

[38] E. R. Hatch and A. Ballato, "Lateral-Field Excitation of Quartz Plates," *Ultrasonics Symposium, 1983*, pp. 512-515, 1983.

[39] A. W. Warner, "Use of Parallel-Field Excitation in the Design of Quartz Crystal Units," *Frequency Control, 17th Annual Symposium on. 1963*, pp. 248-266, 1963.

[40] W. Pinkham, M. Wark, S. Winters, L. French, D. J. Frankel, and J. F. Vetelino, "A lateral field excited acoustic wave pesticide sensor," *Ultrasonics Symposium, 2005 IEEE*, vol. 4, pp. 2279-2283, 2005.

[41] H. Yihe, L. A. French, Jr., K. Radecsky, M. Pereira da Cunha, P. Millard, and J. F. Vetelino, "A lateral field excited liquid acoustic wave sensor," *IEEE Transactions on Ultrasonics, Ferroelectrics and Frequency Control*, vol. 51, pp. 1373-80, 2004.

[42] C. York, L. A. French, P. Millard, and J. F. Vetelino, "A lateral field excited acoustic wave biosensor," *Ultrasonics Symposium, 2005 IEEE*, vol. 1, pp. 44-49, 2005.

[43] Y. Arntz, J. D. Seelig, H. P. Lang, J. Zhang, P. Hunziker, J. P. Ramseyer, E. Meyer, M. Hegner, and G. Ch, "Label-free protein assay based on a nanomechanical cantilever array," *Nanotechnology*, pp. 86, 2003.

[44] A. Ballato, E. R. Hatch, M. Mizan, and T. J. Lukaszek, "Lateral Field Equivalent Networks and Piezocoupling Factors of Quartz Plates Driven in Simple Thickness Modes," *Ultrasonics, Ferroelectrics and Frequency Control, IEEE Transactions on*, vol. 33, pp. 385-393, 1986.

[45] F. Hook, B. Kasemo, T. Nylander, C. Fant, K. Sott, and H. Elwing, "Variations in Coupled Water, Viscoelastic Properties, and Film Thickness of a Mefp-1 Protein Film during Adsorption and Cross-Linking: A Quartz Crystal Microbalance with Dissipation Monitoring, Ellipsometry, and Surface Plasmon Resonance Study," *Anal. Chem.*, vol. 73, pp. 5796-5804, 2001.

[46] A. Sellborn, M. Andersson, C. Fant, C. Gretzer, and H. Elwing, "Methods for research on immune complement activation on modified sensor surfaces," *Colloids and Surfaces B: Biointerfaces*, vol. 27, pp. 295-301, 2003.

[47] A. Jansoff, H.-J. Galla, and C. Steinem, "Piezoelectric Mass-Sensing Devices as Biosensors - An Alternative to Optical Biosensors?," *Angewandte Chemie International Edition*, vol. 39, pp. 29, 2000.

[48] W. E. Newell, "Face-mounted piezoelectric resonators," *Proceedings of the IEEE*, vol. 53, pp. 575-581, 1965.

[49] K. Wasa, S. Hayakawa, and T. Hada, "Excitation of Shear Mode Elastic Waves in Co-Sputtered ZnO Films," *Sonics and Ultrasonics, IEEE Transactions on*, vol. 21, pp. 298-299, 1974.

[50] S. V. Krishnaswamy, B. R. McAvoy, W. J. Takei, and R. A. Moore, "Oriented ZnO Films for Microwave Shear Mode Transducers," *Ultrasonics Symposium, 1982*, pp. 476-479, 1982.

[51] J. S. Wang and K. M. Lakin, "Sputtered C-Axis Inclined ZnO Films for Shear Wave Resonators," *Ultrasonics Symposium, 1982*, pp. 480-483, 1982.

[52] M. Link, M. Schreiter, J. Weber, R. Gabl, D. Pitzer, R. Primig, W. Wersing, M. B. Assouar, and O. Elmazria, "c-axis inclined ZnO films for shear-wave transducers deposited by reactive sputtering using an additional blind," *Journal of Vacuum Science & Technology A: Vacuum, Surfaces, and Films*, vol. 24, pp. 218-222, 2006.

[53] M. Link, M. Schreiter, J. Weber, R. Primig, D. Pitzer, and R. Gabl, "Solidly mounted ZnO shear mode film bulk acoustic resonators for sensing applications in liquids," *Ultrasonics, Ferroelectrics and Frequency Control, IEEE Transactions on*, vol. 53, pp. 492-496, 2006.

[54] P. Wei, Y. Hongyu, K. Jae Wan, Z. Hao, and K. Eun Sok, "Self-aligned lateral field excitation film acoustic resonator with very large electromechanical coupling [FBAR]," *Frequency Control Symposium and Exposition, 2004. Proceedings of the 2004 IEEE International*, pp. 558-561, 2004.

[55] B. A. Auld, *Acoustic fields and waves in solids*, 2nd ed. Malabar, Fla.: R.E. Krieger, 1990.

[56] T. Nomura and M. Okuhara, "Frequency shifts of piezoelectric quartz crystals immersed in organic liquids," *Analytica Chimica Acta*, vol. 142, pp. 4, 1982.

[57] D. Erickson, S. Mandal, A. H. J. Yang, and B. Cordovez, "Nanobiosensors: optofluidic, electrical and mechanical approaches to biomolecular detection at the nanoscale," *Microfluidics and Nanofluidics*, vol. 4, pp. 33-52, 2008.

[58] P. Boyle, "Prostate specific antigen (PSA) testing as screening for prostate cancer: the current controversy," *Ann Oncol*, vol. 9, pp. 1263-4, 1998.

[59] H. J. de Koning and F. H. Schroder, "PSA screening for prostate cancer: the current controversy," *Ann Oncol*, vol. 9, pp. 1293-6, 1998.

[60] M. McCarthy, "PSA screening said to reduce prostate-cancer deaths, or does it?," *Lancet*, vol. 351, pp. 1563, 1998.

[61] J. S. Jones and E. Klein, "Four no more: The 'PSA Cutoff Era' is Over," *Cleveland Clinic Journal of Medicine*, vol. 75, pp. 30-32, 2008.

[62] S.-L. Yao and G. Lu-Yao, "Understanding and Appreciating Overdiagnosis in the PSA Era," *J. Natl. Cancer Inst.*, vol. 94, pp. 958-960, 2002.

[63] K. Lin, R. Lipsitz, T. Miller, and S. Janakiraman, "Benefits and harms of prostate-specific antigen screening for prostate cancer: an evidence update for the U.S. Preventive Services Task Force," *Ann Intern Med*, vol. 149, pp. 192-9, 2008.

[64] C. B. R. Group, "Early Detection Research Network: Fourth Report," National Cancer Institute 2008.

[65] W. D. Hunt, D. D. Stubbs, and L. Sang-Hun, "Time-dependent signatures of acoustic wave biosensors," *Proceedings of the IEEE*, vol. 91, pp. 890-901, 2003.

[66] K. Lange, F. Bender, A. Voigt, H. Gao, and M. Rapp, "A Surface Acoustic Wave Biosensor Concept with Low Flow Cell Volumes for Label-Free Detection," *Anal. Chem.*, vol. 75, pp. 5561-5566, 2003.

[67] J. Kaitila, M. Ylilammi, J. Molarius, J. Ella, and T. Makkonen, "ZnO based thin film bulk acoustic wave filters for EGSM band," presented at Ultrasonics Symposium, 2001 IEEE, 2001.

[68] Y. Giwan, P. Jae-Don, and P. Hee-Dae, "Characterization of ZnO-based FBAR devices for RF applications," presented at Microwave and Millimeter Wave Technology, 2000, 2nd International Conference on. ICMMT 2000, 2000.

[69] M. Linh, L. Jae-Young, P. Van-Su, and Y. Giwan, "Design and Fabrication of ZnO-Based FBAR Microwave Devices for Mobile WiMAX Applications," *Microwave and Wireless Components Letters, IEEE*, vol. 17, pp. 867-869, 2007.

[70] S. L. Pinkett, W. D. Hunt, B. P. Barber, and P. L. Gammel, "Determination of ZnO temperature coefficients using thin film bulk acoustic wave resonators," *IEEE Trans Ultrason Ferroelectr Freq Control*, vol. 49, pp. 1491-6, 2002.

[71] S. Pinkett, W. Hunt, B. Barber, and P. Gammel, "Broadband characterization of zinc oxide-based solidly mounted resonators," presented at Frequency Control Symposium and PDA Exhibition, 2002. IEEE International, 2002.

[72] A. Ballato, "Bulk and Surface Acoustic Wave Excitation and Network Representation," presented at 28th Annual Symposium on Frequency Control. 1974, 1974.

[73] R. W. Cernosek, S. J. Martin, A. R. Hillman, and H. L. Bandey, "Comparison of lumped-element and transmission-line models for thickness-shear-mode quartz resonator sensors," *Ultrasonics, Ferroelectrics and Frequency Control, IEEE Transactions on*, vol. 45, pp. 1399-1407, 1998.

[74] K. M. Lakin, G. R. Kline, and K. T. McCarron, "High-Q microwave acoustic resonators and filters," *Microwave Theory and Techniques, IEEE Transactions on*, vol. 41, pp. 2139-2146, 1993.

[75] D. K. Cheng, *Field and wave electromagnetics*. Reading, Mass.: Addison-Wesley, 1989.

[76] S. L. Pinkett, "Techniques to facilitate the fabrication of ZnO-based thin film bulk acoustic wave devices," 2003, pp. xvi, 286 leaves.

[77] Y. Nakagawa and T. Okada, "Material Constants of New Piezoelectric Ta2o5 Thin-Films," *Journal of Applied Physics*, vol. 68, pp. 556-559, 1990.

[78] J. H. Hu and R. G. Gordon, "Textured Aluminum-Doped Zinc-Oxide Thin-Films from Atmospheric-Pressure Chemical-Vapor Deposition," *Journal of Applied Physics*, vol. 71, pp. 880-890, 1992.

[79] Y. Kashiwaba, F. Katahira, K. Haga, T. Sekiguchi, and H. Watanabe, "Hetero-epitaxial growth of ZnO thin films by atmospheric pressure CVD method," *Journal of Crystal Growth*, vol. 221, pp. 431-434, 2000.

[80] S. Y. Myong, S. J. Baik, C. H. Lee, W. Y. Cho, and K. S. Lim, "Extremely transparent and conductive ZnO:Al thin films prepared by photo-assisted metalorganic chemical vapor deposition (photo-MOCVD) using AlCl3(6H(2)O) as new doping material," *Japanese Journal of Applied Physics Part 2-Letters*, vol. 36, pp. L1078-L1081, 1997.

[81] K. Ogata, T. Kawanishi, K. Maejima, K. Sakurai, S. Fujita, and S. Fujita, "Improvements of ZnO qualities grown by metal-organic vapor phase epitaxy using a molecular beam epitaxy grown ZnO layer as a substrate," *Japanese Journal of Applied Physics Part 2-Letters*, vol. 40, pp. L657-L659, 2001.

[82] K. Haga, T. Suzuki, Y. Kashiwaba, H. Watanabe, B. P. Zhang, and Y. Segawa, "High-quality ZnO films prepared on Si wafers by low-pressure MO-CVD," *Thin Solid Films*, vol. 433, pp. 131-134, 2003.

[83] D. M. Bagnall, Y. F. Chen, Z. Zhu, T. Yao, S. Koyama, M. Y. Shen, and T. Goto, "Optically pumped lasing of ZnO at room temperature," *Applied Physics Letters*, vol. 70, pp. 2230-2232, 1997.

[84] K. Iwata, P. Fons, S. Niki, A. Yamada, K. Matsubara, K. Nakahara, T. Tanabe, and H. Takasu, "ZnO growth on Si by radical source MBE," *Journal of Crystal Growth*, vol. 214, pp. 50-54, 2000.

[85] M. A. L. Johnson, S. Fujita, W. H. Rowland, W. C. Hughes, J. W. Cook, and J. F. Schetzina, "MBE growth and properties of ZnO on sapphire and SiC substrates," *Journal of Electronic Materials*, vol. 25, pp. 855-862, 1996.

[86] Y. Nakanishi, A. Miyake, H. Kominami, T. Aoki, Y. Hatanaka, and G. Shimaoka, "Preparation of ZnO thin films for high-resolution field emission display by electron beam evaporation," *Applied Surface Science*, vol. 142, pp. 233-236, 1999.

[87] S. H. Bae, S. Y. Lee, B. J. Jin, and S. Im, "Pulsed laser deposition of ZnO thin films for applications of light emission," *Applied Surface Science*, vol. 154, pp. 458-461, 2000.

[88] T. J. Bukowski, K. McCarthy, F. McCarthy, G. Teowee, T. P. Alexander, D. R. Uhlmann, J. T. Dawley, and B. J. J. Zelinski, "Piezoelectric properties of sol-gel derived ZnO thin films," *Integrated Ferroelectrics*, vol. 17, pp. 339-347, 1997.

[89] J. G. E. Gardeniers, Z. M. Rittersma, and G. J. Burger, "Preferred orientation and piezoelectricity in sputtered ZnO films," *Journal of Applied Physics*, vol. 83, pp. 7844-7854, 1998.

[90] Y. Zhang, G. Du, D. Liu, X. Wang, Y. Ma, J. Wang, J. Yin, X. Yang, X. Hou, and S. Yang, "Cyrstal growth of undoped ZnO films on Si substrates under different sputtering conditions," *Journal of Cyrstal Growth*, vol. 243, pp. 439-443, 2002.

[91] J. B. Lee, S. H. Kwak, and H. J. Kim, "Effects of surface roughness of substrates on the c-axis preferred orientation of ZnO films deposited by r.f. magnetron sputtering," *Thin Solid Films*, vol. 423, pp. 262-266, 2003.

[92] D. J. Kang, J. S. Kim, S. W. Jeong, Y. Roh, S. H. Jeong, and J. H. Boo, "Structural and electrical characteristics of R.F. magnetron sputtered ZnO films," *Thin Solid Films*, vol. 475, pp. 160-165, 2005.

[93] H. W. Kim and N. H. Kim, "Structural studies of room-temperature RF magnetron sputtered ZnO films under different RF powered conditions," *Materials Science and Engineering B*, vol. 103, pp. 297-302, 2003.

[94] R. Ondo-Ndong, G. Ferblantier, M. Al Kalfioui, A. Boyer, and A. Foucaran, "Properties of RF magnetron sputtered zinc oxide thin films," *Journal of Crystal Growth*, vol. 255, pp. 130-135, 2003.

[95] J. B. Lee, H. J. Kim, S. G. Kim, C. S. Hwang, S. H. Hong, Y. H. Shin, and N. H. Lee, "Deposition of ZnO thin films by magnetron sputtering for a film bulk acoustic resonator," *Thin Solid Films*, vol. 435, pp. 179-185, 2003.

[96] H. W. Kim and N. H. Kim, "Influence of the substrate on the structural properties of sputter-deposited ZnO films," *Physica Status Solidi a-Applied Research*, vol. 201, pp. 235-238, 2004.

[97] X. H. Li, A. P. Huang, M. K. Zhu, S. L. Xu, J. Chen, H. Wang, B. Wang, and H. Yan, "Influence of substrate temperature on the orientation and optical properties of sputtered ZnO films," *Materials Letters*, vol. 57, pp. 4655-4659, 2003.

[98] P. F. Fewster, *X-ray scattering from semiconductors*, 2nd ed. River Edge, NJ: Imperial College Press, 2003.

[99] S. Kakio, Y. Shimatai, and Y. Nakagawa, "Shear-horizontal-type surface acoustic waves on quartz with Ta2O5 thin film," *Japanese Journal of Applied Physics Part 1-Regular Papers Short Notes & Review Papers*, vol. 42, pp. 3161-3165, 2003.

[100] Y. Nakagawa and Y. Gomi, "Ta2o5-on-Fused-Quartz Temperature-Compensated Saw Delay-Lines," *Ieee Transactions on Ultrasonics Ferroelectrics and Frequency Control*, vol. 33, pp. 331-332, 1986.

[101] Y. Nakagawa, Y. Gomi, and T. Suzuki, "Deposition of Ta2o5 Thin-Film and Application to Saw Devices," *Japanese Journal of Applied Physics Part 1-Regular Papers Short Notes & Review Papers*, vol. 24, pp. 25-27, 1985.

[102] K. Tominaga, R. Muhammet, I. Kobayashi, and M. Okada, "Preparation of (111)-Oriented Beta-Ta2o5 Thin-Films by Chemical Vapor-Deposition Using Metalorganic Precursors," *Japanese Journal of Applied Physics Part 2-Letters*, vol. 31, pp. L585-L587, 1992.

[103] C. Chaneliere, J. L. Autran, R. A. B. Devine, and B. Balland, "Tantalum pentoxide (Ta2O5) thin films for advanced dielectric applications," *Materials Science and Engineering: R: Reports*, vol. 22, pp. 269-322, 1998.

[104] Y. Nakagawa and Y. Gomi, "New piezoelectric Ta₂O₅ thin films," *Applied Physics Letters*, vol. 46, pp. 139-40, 1985.

[105] Y. Nakagawa, Y. Gomi, and T. Okada, "Deposition of new piezoelectric Ta_2O_5 thin films and their surface acoustic-wave properties," *Journal of Applied Physics*, vol. 61, pp. 5012-17, 1987.

[106] S. Kakio, M. Nozawa, and Y. Nakagawa, "Propagation characteristics of shear-horizontal-type surface acoustic wave on langasite with Au of Ta/sub 2/O/sub 5/ thin film," 2004.

[107] Y. Nakagawa and T. Okada, "Material constants of new piezoelectric Ta₂O₅ thin films," *Journal of Applied Physics*, vol. 68, pp. 556-9, 1990.

[108] A. Pham, A. Mathis, J. Laskar, A. F. Peterson, and L. Hayden, "Membrane probe technology for non-destructive thin-film material characterization," 1998.

[109] L. Li, T. Abe, and M. Esashi, "High sensitive, miniaturized plano-convex quartz crystal microbalance fabricated by reactive ion etching and melting photoresist," presented at TRANSDUCERS, Solid-State Sensors, Actuators and Microsystems, 12th International Conference on, 2003, 2003.

[110] Y. Hu, L. A. French, Jr., K. Radecsky, M. P. DaCunha, P. Millard, and J. F. Vetelino, "A lateral field excited liquid acoustic wave sensor," presented at 2003 IEEE Symposium on Ultrasonics, Orono, ME, USA, 2003.

[111] G. S. Ruff, A. Z. Wang, and W. D. Hunt, "Design and Development of Resonance Frequency Tracking Software Using LabVIEW," *The Journal of Young Investigators*, vol. 19, 2008.

[112] S. J. Updike and G. P. Hicks, "Enzyme Electrode," *Nature*, vol. 214, pp. 986-988, 1967.

[113] J. P. Chambers, B. P. Arulanandam, L. L. Matta, A. Weis, and J. J. Valdes, "Biosensor recognition elements," *Curr Issues Mol Biol*, vol. 10, pp. 1-12, 2008.

[114] H. P. Roost, M. F. Bachmann, A. Haag, U. Kalinke, V. Pliska, H. Hengartner, and R. M. Zinkernagel, "Early high-affinity neutralizing anti-viral IgG responses without further overall improvements of affinity," *Proceedings of the National Academy of Sciences of the United States of America*, vol. 92, pp. 1257-1261, 1995.

[115] C. Branden and J. Tooze, *Introduction to Protein Structure*, vol. 1, 2nd ed: Garland Science, 1999.

[116] G. M. Edelman, B. A. Cunningham, W. E. Gall, P. D. Gottlieb, U. Rutishauser, and M. J. Waxdal, "The covalent structure of an entire gammaG immunoglobulin molecule," *Proc Natl Acad Sci U S A*, vol. 63, pp. 78-85, 1969.

[117] S. K. Bhatia, L. C. Shriver-Lake, K. J. Prior, J. H. Georger, J. M. Calvert, R. Bredehorst, and F. S. Ligler, "Use of thiol-terminal silanes and heterobifunctional crosslinkers for immobilization of antibodies on silica surfaces," *Anal Biochem*, vol. 178, pp. 408-13, 1989.

[118] L. C. Shriver-Lake, B. Donner, R. Edelstein, K. Breslin, S. K. Bhatia, and F. S. Ligler, "Antibody immobilization using heterobifunctional crosslinkers," *Biosensors & Bioelectronics*, vol. 12, pp. 1101-1106, 1997.

[119] I. Luzinov, D. Julthongpiput, A. Liebmann-Vinson, T. Cregger, M. D. Foster, and V. V. Tsukruk, "Epoxy-terminated self-assembled monolayers: Molecular glues for polymer layers," *Langmuir*, vol. 16, pp. 504-516, 2000.

[120] V. V. Tsukruk, I. Luzinov, and D. Julthongpiput, "Sticky Molecular Surfaces: Epoxysilane Self-Assembled Monolayers," *Langmuir*, vol. 15, pp. 3029-3032, 1999.

[121] S. Krishnamoorthy, T. Bei, E. Zoumakis, G. P. Chrousos, and A. A. Iliadis, "Morphological and binding properties of interleukin-6 on thin ZnO films grown on (100) silicon substrates for biosensor applications," *Biosens Bioelectron*, vol. 22, pp. 707-14, 2006.

[122] S. D. Jayasena, "Aptamers: an emerging class of molecules that rival antibodies in diagnostics," *Clin Chem*, vol. 45, pp. 1628-50, 1999.

[123] T. Hermann and D. J. Patel, "Adaptive recognition by nucleic acid aptamers," *Science*, vol. 287, pp. 820-5, 2000.

[124] S. Spiegelman, "Ribonucleic acid. I. The test-tube synthesis of a viral nucleic acid. II. The development and use of molecular hybridization," *Jama*, vol. 230, pp. 1036-42, 1974.

[125] K. B. Mullis and F. A. Faloona, "Specific synthesis of DNA in vitro via a polymerase-catalyzed chain reaction," *Methods Enzymol*, vol. 155, pp. 335-50, 1987.

[126] A. D. Ellington and J. W. Szostak, "In vitro selection of RNA molecules that bind specific ligands," *Nature*, vol. 346, pp. 818-22, 1990.

[127] C. Tuerk and L. Gold, "Systematic evolution of ligands by exponential enrichment: RNA ligands to bacteriophage T4 DNA polymerase," *Science*, vol. 249, pp. 505-10, 1990.

[128] D. L. Robertson and G. F. Joyce, "Selection in vitro of an RNA enzyme that specifically cleaves single-stranded DNA," *Nature*, vol. 344, pp. 467-8, 1990.

[129] R. Stoltenburg, C. Reinemann, and B. Strehlitz, "SELEX--A (r)evolutionary method to generate high-affinity nucleic acid ligands," *Biomolecular Engineering*, vol. 24, pp. 381-403, 2007.

[130] Z. S. Wu, M. M. Guo, S. B. Zhang, C. R. Chen, J. H. Jiang, G. L. Shen, and R. Q. Yu, "Reusable Electrochemical Sensing Platform for Highly Sensitive Detection of Small Molecules Based on Structure-Switching Signaling Aptamers," *Anal. Chem.*, vol. 79, pp. 2933-2939, 2007.

[131] Y. Xiao, A. A. Lubin, A. J. Heeger, and K. W. Plaxco, "Label-free electronic detection of thrombin in blood serum by using an aptamer-based sensor," *Angewandte Chemie International Edition*, vol. 44, pp. 5456 - 5459, 2005.

[132] S. Balamurugan, A. Obubuafo, S. A. Soper, and D. A. Spivak, "Surface immobilization methods for aptamer diagnostic applications," *Analytical and Bioanalytical Chemistry*, vol. 390, pp. 1009-1021, 2008.

[133] C. D. Corso, A. Dickherber, and W. D. Hunt, "An investigation of antibody immobilization methods employing organosilanes on planar ZnO surfaces for biosensor applications," *Biosens Bioelectron*, 2008.

[134] L. Yang and Y. Li, "AFM and impedance spectroscopy characterization of the immobilization of antibodies on indium-tin oxide electrode through self-assembled monolayer of epoxysilane and their capture of Escherichia coli O157:H7," *Biosens Bioelectron*, vol. 20, pp. 1407-16, 2005.

[135] A. Tlili, A. Abdelghani, K. Aguir, M. Gillet, and N. Jaffrezic-Renault, "Adsorption characteristics of self-assembled thiol and dithiol layer on gold," *Materials Science & Engineering C-Biomimetic and Supramolecular Systems*, vol. 27, pp. 620-624, 2007.

[136] G. Gauglitz, "Direct optical sensors: principles and selected applications," *Analytical & Bioanalytical Chemistry*, vol. 381, pp. 141-155, 2005.

[137] A. Leung, P. M. Shankar, and R. Mutharasan, "A review of fiber-optic biosensors," *Sensors and Actuators B: Chemical*, vol. 125, pp. 688-703, 2007.

[138] G. Proll, L. Steinle, F. Proll, M. Kumpf, B. Moehrle, M. Mehlmann, and G. Gauglitz, "Potential of label-free detection in high-content-screening applications," *J Chromatogr A*, vol. 1161, pp. 2-8, 2007.

[139] N. P. Jonathan S. Daniels, "Label-Free Impedance Biosensors: Opportunities and Challenges," *Electroanalysis*, vol. 19, pp. 1239-1257, 2007.

[140] X. D. Wang, J. H. Song, and Z. L. Wang, "Nanowire and nanobelt arrays of zinc oxide from synthesis to properties and to novel devices," *Journal of Materials Chemistry*, vol. 17, pp. 711-720, 2007.

[141] M. A. Cooper and V. T. Singleton, "A survey of the 2001 to 2005 quartz crystal microbalance biosensor literature: applications of acoustic physics to the analysis of biomolecular interactions," *Journal of Molecular Recognition*, vol. 20, pp. 154-184, 2007.

[142] K. Lange, B. E. Rapp, and M. Rapp, "Surface acoustic wave biosensors: a review," *Anal Bioanal Chem*, 2008.

[143] R. Hassan, T. Bera, and I. Pastan, "Mesothelin: A New Target for Immunotherapy," *Clin Cancer Res*, vol. 10, pp. 3937-3942, 2004.

[144] K. Chang and I. Pastan, "Molecular cloning of mesothelin, a differentiation antigen present on mesothelium, mesotheliomas, and ovarian cancers," *Proceedings of the National Academy of Sciences of the United States of America*, vol. 93, pp. 136-140, 1996.

[145] T. K. Bera and I. Pastan, "Mesothelin Is Not Required for Normal Mouse Development or Reproduction," *Mol. Cell. Biol.*, vol. 20, pp. 2902-2906, 2000.

[146] M. Ho, M. Onda, Q. C. Wang, R. Hassan, I. Pastan, and M. O. Lively, "Mesothelin is shed from tumor cells," *Cancer Epidemiology Biomarkers & Prevention*, vol. 15, pp. 1751-1751, 2006.

[147] P. Argani, C. Iacobuzio-Donahue, B. Ryu, C. Rosty, M. Goggins, R. E. Wilentz, S. R. Murugesan, S. D. Leach, E. Jaffee, C. J. Yeo, J. L. Cameron, S. E. Kern, and R. H. Hruban, "Mesothelin is overexpressed in the vast majority of ductal adenocarcinomas of the pancreas: identification of a new pancreatic cancer marker by serial analysis of gene expression (SAGE)," *Clin Cancer Res*, vol. 7, pp. 3862-8, 2001.

[148] N. G. Ordonez, "Application of mesothelin immunostaining in tumor diagnosis," *Am J Surg Pathol*, vol. 27, pp. 1418-28, 2003.

[149] K. Chang, I. Pastan, and M. C. Willingham, "Frequent expression of the tumor antigen CAK1 in squamous-cell carcinomas," *Int J Cancer*, vol. 51, pp. 548-54, 1992.

[150] R. Hassan and M. Ho, "Mesothelin targeted cancer immunotherapy," *European Journal of Cancer*, vol. 44, pp. 46-53, 2008.

[151] R. Hassan, A. T. Remaley, M. L. Sampson, J. Zhang, D. D. Cox, J. Pingpank, R. Alexander, M. Willingham, I. Pastan, and M. Onda, "Detection and quantitation of serum mesothelin, a tumor marker for patients with mesothelioma and ovarian cancer," *Clin Cancer Res*, vol. 12, pp. 447-53, 2006.

[152] D. A. Armbruster, "Prostate-specific antigen: biochemistry, analytical methods, and clinical application," *Clin Chem*, vol. 39, pp. 181-195, 1993.

[153] M. B. Gretzer and A. W. Partin, "PSA Levels and the Probability of Prostate Cancer on Biopsy," *European Urology Supplements*, vol. 1, pp. 21-27, 2002.

[154] I. M. T. Javier Hernández, "Prostate-specific antigen: A review of the validation of the most commonly used cancer biomarker," *Cancer*, vol. 101, pp. 894-904, 2004.

[155] I. M. Thompson, D. P. Ankerst, C. Chi, P. J. Goodman, C. M. Tangen, M. S. Lucia, Z. Feng, H. L. Parnes, and C. A. Coltman, Jr., "Assessing prostate cancer risk: results from the Prostate Cancer Prevention Trial," *J Natl Cancer Inst*, vol. 98, pp. 529-34, 2006.

[156] B. Djavan, A. Zlotta, C. Kratzik, M. Remzi, C. Seitz, C. C. Schulman, and M. Marberger, "PSA, PSA density, PSA density of transition zone, free/total PSA ratio, and PSA velocity for early detection of prostate cancer in men with serum PSA 2.5 to 4.0 L," *Urology*, vol. 54, pp. 517-522, 1999.

[157] S. Berry, D. Coffey, P. Walsh, and L. Ewing, "The Development of human benign prostatic hyperplasia with age," *Journal of Urology*, vol. 132, pp. 474-479, 1984.

[158] H. B. Carter, C. H. Morrell, J. D. Pearson, L. J. Brant, C. C. Plato, E. J. Metter, D. W. Chan, J. L. Fozard, and P. C. Walsh, "Estimation of Prostatic Growth Using Serial Prostate-specific Antigen Measurements in Men with and without Prostate Disease," *Cancer Res*, vol. 52, pp. 3323-3328, 1992.

[159] S. Loeb, K. A. Roehl, W. J. Catalona, and R. B. Nadler, "Prostate Specific Antigen Velocity Threshold for Predicting Prostate Cancer in Young Men," *The Journal of Urology*, vol. 177, pp. 899-902, 2007.

[160] H. B. Carter, D. W. Chan, J. D. Pearson, H. A. Guess, Z. Waclawiw, P. C. Walsh, and E. J. Metter, "Prostate-specific antigen variability in men without prostate cancer: effect of sampling interval on prostate-specific antigen velocity," *Urology*, vol. 45, pp. 591-596, 1995.

[161] O. Gustafsson, E. Mansour, U. Norming, A. Carlsson, M. TÃ¶rnblom, and C. R. Nyman, "Prostate-specific Antigen (PSA), PSA Density and Age-adjusted PSA Reference Values in Screening for Prostate Cancer: A Study of a Randomly Selected Population of 2,400 Men," *Scandinavian Journal of Urology and Nephrology*, vol. 32, pp. 373 - 377, 1998.

[162] M. Benson, I. Whang, C. Olsson, D. McMahon, and W. Cooner, "The use of prostate specific antigen density to enhance the predictive value of intermediate levels of serum prostate specific antigen," *Journal of Urology*, vol. 147, pp. 817-821, 1992.

[163] W. J. Catalona, J. A. Beiser, and D. S. Smith, "SERUM FREE PROSTATE SPECIFIC ANTIGEN AND PROSTATE SPECIFIC ANTIGEN DENSITY MEASUREMENTS FOR PREDICTING CANCER IN MEN WITH PRIOR NEGATIVE PROSTATIC BIOPSIES," *The Journal of Urology*, vol. 158, pp. 2162-2167, 1997.

[164] E. S. Leman, G. W. Cannon, B. J. Trock, L. J. Sokoll, D. W. Chan, L. Mangold, A. W. Partin, and R. H. Getzenberg, "EPCA-2: A Highly Specific Serum Marker for Prostate Cancer," *Urology*, vol. 69, pp. 714-720, 2007.

[165] N. Hara, T. Kasahara, T. Kawasaki, V. Bilim, K. Obara, K. Takahashi, and Y. Tomita, "Reverse transcription-polymerase chain reaction detection of prostate-specific antigen, prostate-specific membrane antigen, and prostate stem cell antigen in one milliliter of peripheral blood: value for the staging of prostate cancer," *Clin Cancer Res*, vol. 8, pp. 1794-9, 2002.

[166] R. E. Reiter, I. Sato, G. Thomas, J. Qian, Z. Gu, T. Watabe, M. Loda, and R. B. Jenkins, "Coamplification of prostate stem cell antigen (PSCA) and MYC in locally advanced prostate cancer," *Genes Chromosomes Cancer*, vol. 27, pp. 95-103, 2000.

[167] M. A. Rubin, M. Zhou, S. M. Dhanasekaran, S. Varambally, T. R. Barrette, M. G. Sanda, K. J. Pienta, D. Ghosh, and A. M. Chinnaiyan, "alpha-Methylacyl

coenzyme A racemase as a tissue biomarker for prostate cancer," *Jama*, vol. 287, pp. 1662-70, 2002.

[168] S. V. Harden, H. Sanderson, S. N. Goodman, A. A. W. Partin, P. C. Walsh, J. I. Epstein, and D. Sidransky, "Quantitative GSTP1 Methylation and the Detection of Prostate Adenocarcinoma in Sextant Biopsies," *J. Natl. Cancer Inst.*, vol. 95, pp. 1634-1637, 2003.

[169] W. H. Lee, R. A. Morton, J. I. Epstein, J. D. Brooks, P. A. Campbell, G. S. Bova, W. S. Hsieh, W. B. Isaacs, and W. G. Nelson, "Cytidine methylation of regulatory sequences near the pi-class glutathione S-transferase gene accompanies human prostatic carcinogenesis," *Proc Natl Acad Sci U S A*, vol. 91, pp. 11733-7, 1994.

[170] W. H. Lee, W. B. Isaacs, G. S. Bova, and W. G. Nelson, "CG island methylation changes near the GSTP1 gene in prostatic carcinoma cells detected using the polymerase chain reaction: a new prostate cancer biomarker," *Cancer Epidemiol Biomarkers Prev*, vol. 6, pp. 443-50, 1997.

[171] J. B. de Kok, G. W. Verhaegh, R. W. Roelofs, D. Hessels, L. A. Kiemeney, T. W. Aalders, D. W. Swinkels, and J. A. Schalken, "DD3PCA3, a Very Sensitive and Specific Marker to Detect Prostate Tumors," *Cancer Res*, vol. 62, pp. 2695-2698, 2002.

[172] M. J. G. Bussemakers, A. van Bokhoven, G. W. Verhaegh, F. P. Smit, H. F. M. Karthaus, J. A. Schalken, F. M. J. Debruyne, N. Ru, and W. B. Isaacs, "DD3::A New Prostate-specific Gene, Highly Overexpressed in Prostate Cancer," *Cancer Res*, vol. 59, pp. 5975-5979, 1999.

[173] C. Stephan, K. Jung, M. Lein, P. Sinha, D. Schnorr, and S. A. Loening, "Molecular forms of prostate-specific antigen and human kallikrein 2 as promising tools for early diagnosis of prostate cancer," *Cancer Epidemiol Biomarkers Prev*, vol. 9, pp. 1133-47, 2000.

[174] C. Stephan, K. Jung, T. Nakamura, G. M. Yousef, G. Kristiansen, and E. P. Diamandis, "Serum human glandular kallikrein 2 (hK2) for distinguishing stage and grade of prostate cancer," *Int J Urol*, vol. 13, pp. 238-43, 2006.

[175] J. A. Magee, T. Araki, S. Patil, T. Ehrig, L. True, P. A. Humphrey, W. J. Catalona, M. A. Watson, and J. Milbrandt, "Expression Profiling Reveals Hepsin Overexpression in Prostate Cancer," *Cancer Res*, vol. 61, pp. 5692-5696, 2001.

[176] C. Stephan, G. M. Yousef, A. Scorilas, K. Jung, M. Jung, G. Kristiansen, S. Hauptmann, T. Kishi, T. Nakamura, S. A. Loening, and E. P. Diamandis, "Hepsin is highly over expressed in and a new candidate for a prognostic indicator in prostate cancer," *J Urol*, vol. 171, pp. 187-91, 2004.

[177] T. Steuber, M. F. O'Brien, and H. Lilja, "Serum Markers for Prostate Cancer: A Rational Approach to the Literature," *European Urology*, vol. 54, pp. 31-40, 2008.

[178] M. Onda, M. Willingham, S. Nagata, T. K. Bera, R. Beers, M. Ho, R. Hassan, R. J. Kreitman, and I. Pastan, "New monoclonal antibodies to mesothelin useful for immunohistochemistry, fluorescence-activated cell sorting, Western blotting, and ELISA," *Clin Cancer Res*, vol. 11, pp. 5840-6, 2005.

[179] C. D. Corso, A. Dickherber, P. Shah, A. Migdal, M. W. Datta, S. Datta, and W. D. Hunt, "Development of a simple inexpensive bulk acoustic wave nanosensor for

cancer biomarkers: Detection of secreted sonic hedgehog from prostate cancer cells," presented at 2006 Annual Meeting of the AACR, Washington D.C., 2006.
[180] J. r. Janata, *Principles of chemical sensors*. New York: Plenum Press, 1989.

VITA

ANTHONY J. DICKHERBER

Anthony Dickherber was born in Fairfax, Virginia. As the son of a foreign service officer, he grew up attending international schools in Tunisia, Pakistan and the Philippines. He received his B.S. and M.S. in Electrical & Computer Engineering from Georgia Institute of Technology in 1999 and 2002, respectively, in Atlanta, GA. He worked for 4 years as a communications research engineer for the Georgia Tech Research Institute before deciding to return to pursue his doctoral degree in bioengineering. While at Georgia Tech, he received a US Army Medical Research & Materiel Command Prostate Cancer Research Program Pre-doctoral Training Award, the Sam Nunn Security Program Pre-Doctoral Fellowship and a graduate certificate in Public Policy. He also served as director of the Bioscience & Bioengineering Unified Graduate Student Group, chair of the Biotechnology Technology Forum, and as an inaugural member of the Bioengineering Graduate Student Advisory Committee.

Anthony J Dickherber

[redacted] [redacted]

EDUCATION:

Doctor of Philosophy, Biomedical Engineering **2008**

Georgia Institute of Technology

- Thesis: Design, fabrication and testing of an acoustic resonator based biosensor for the detection of cancer biomarkers

Minor, Public Policy (Graduate Certificate)

- Critical diagnosis of the management flaws of the US Agency for International Development (USAID) in the post-GPRA era
- Responsible conduct in scientific research training

Master of Science, Electrical Engineering **2002**

Georgia Institute of Technology

- Specializing in digital signal processing and bioengineering

Bachelor of Science, Electrical Engineering **1999**

Georgia Institute of Technology

- Specializing in analog design and bioengineering

HONORS & AWARDS:

- Prostate Cancer Research Program Pre-doctoral Award, 2007 – 2008 [Congressionally Directed Medical Research Program]
- Sam Nunn Security Program Fellow, 2006 – 2007, Georgia Institute of Technology
- Research Assistantships: Georgia Institute of Technology 2003 – 2008
- Teaching Assistantship: Georgia Institute of Technology 2004 – 2007
- 1st place at the National University of Singapore International Business Plan Competition, 2002
- One patent granted (6754487) – 2001, and one patent submitted (11/822045) – 2007

LEADERSHIP EXPERIENCE:

Aug. 2006 **Director, Bioscience & Bioengineering Unified Graduate Students**
Aug. 2007 **Georgia Tech Emory Center, a National Science Foundation (NSF) Engineering Research Center**
Atlanta, GA

- Managed a budget of ~$20K towards professional and social activities organized by 6 different student committees for the general graduate student body, required regular communication and advertising among the largest single graduate student population at Georgia Tech via newsletters, and other video & print media
- Grew budget by nearly 100%
- Responsibilities included obtaining and managing funding, managing advertising and outreach, maintaining morale and enthusiasm among an entirely voluntary group, and preparation of annual reports to the NSF including SWAT analysis. BBUGS remains the largest and most successful student leadership council by any measure among all Engineering Research Centers managed by the NSF

Aug. 2006 **Chair, Biotechnology Policy Forum**
Jun. 2008 **Georgia Institute of Technology**
Atlanta, GA

- Invite professionals nation-wide from both the public policy and public health community to give talks and engage in conversations with the biotech research community regarding the policy issues surrounding their field of research.

- Event coordination, advertising and facilitation of the events
- member 2004 – 2008

Aug. 2005 – Aug. 2007 **Bioengineering Graduate Student Advisory Committee**
Department of Bioengineering, Georgia Institute of Technology
Atlanta, GA

- Act as a liaison group between the general bioengineering graduate student body and the bioengineering faculty to assist in the development of the curriculum and program
- Assist in the recruitment of potential new students to the program and with orientation of new students that have registered for the program

WORK EXPERIENCE:

Jan 2007 – Nov 2008 **Pre-doctoral Research Trainee, Prostate Cancer Research Program**
US Army Medical Research & Materiel Command, Congressionally Directed Medical Research Program (Georgia Institute of Technology and Emory University Winship Cancer Institute)
Atlanta, GA

- Design and development of microelectronic biosensors to be used with physiological tissue samples for the early detection of prostate cancer
- Working experience with the following:
  - Develop in-depth understanding of the biochemical etiology and proliferative mechanisms of various cancers, especially prostate cancer
  - Understand technical aspects of the array of treatment options for prostate cancer
  - Identification of key proteins to target in an effort to develop a prostate cancer signature evident in circulating body fluids at the earliest stages of development
- Regularly attend and participate in weekly meetings of the urology department at the Winship Cancer Institute;
  - Develop a familiarity with the clinical research and disease-management environment surrounding the treatment of prostate cancer
  - Identify common problems faced by doctors and scientists that present opportunities for bioengineering applications

Jan. 2006 – Dec. 2007 **Head Graduate Teaching Assistant**, **Department of Biomedical Engineering**
Georgia Institute of Technology
Atlanta, GA

- Lead individual labs as well as manage team of graduate teaching assistants for bioinstrumentation and sensors lab
- Manage all student conflicts, curriculum development, and determine project and lab requirements
- Write quizzes and grade all submitted works

Aug. 2006 – May 2007 **Sam Nunn Security Program Pre-doctoral Fellow, Ivan Allen School of International Affairs**
Georgia Institute of Technology
Atlanta, GA

- Critical assessment of the technologies and policies that pose a security threat to the United States of America resulting in various policy proposal papers
- Topics covered include:
  - Assessing the threat of nuclear proliferation on the Korean Peninsula; produced a negotiation strategy to mitigate that threat
  - Assess the vulnerabilities surrounding the nation’s critical infrastructure and produced policy proposals to mitigate those threats
  - Assess the proliferation of internet-based terrorist organizational networks and their threat to US national security
  - From a general security perspective, produce energy policy proposals to deal with the future energy requirements for sustained domestic economic stability and growth
- Investigations and reports would be formally presented to professional policy-makers and would be summarized in policy proposals to the National Research Council

- Included guided trips to various offices of the CIA, State Department, Congress, the National War College, Savannah River Site National Lab, Savannah Port Authority, Aberdeen Proving Grounds, local coal power plant, and the Verisign cyber security hub

Aug. 2003 –
Jan. 2007

Graduate Research Assistant
Georgia Institute of Technology, Department of Bioengineering
Atlanta, GA

- Responsibilities include: critical experimental design and execution; professional presentations to both technical and non-technical audiences regarding research; publication of research in professional literature; various methods of microelectronic fabrication; design and execution of surface chemistry protocols; operation, maintenance and repair of various equipment including standard electrical engineering tools as well as vacuum equipment for fabrication; and operation of various micro- and nano-scale surface imaging tools

Jun. 2005 -
Dec. 2005

Graduate Teaching Assistant, **Department of Electrical Engineering**
Georgia Institute of Technology
Atlanta, GA

- Prepare and deliver lectures for bioelectronics and analog circuitry
- Lead digital signal processing and analog circuit design labs and hold office hours for one-on-one assistance outside of lab
- Write quizzes and grade all submitted works

Jun. 1999 –
Aug. 2003

Research Engineering, Information Technology & Telecommunications Laboratory
Georgia Tech Research Institute
Atlanta, GA

- Extensive programming experience towards digital signal analysis for communications research on classified U.S. Government projects
- Extensive experience with telecommunications research
- Survey current state-of-the-art technology in a variety of areas
- Participated in defining of international communications standard: Dedicated Short Range Communication (DSRC) band
- Maintain a SECRET-level government security clearance

May 1995 –
Aug. 1997

Electrical Engineering, Cooperative Student
Scientific Atlanta, Inc (now Cisco Broadband)
Norcross, GA

- Built and tested prototype analog and digital circuits for research engineers in the international set-top box research and development lab
- Responsible for the assembly, calibration and maintenance of various equipment

May 1994 –
Jul. 1994

Summer Intern, American Services Bureau
Immigration & Naturalization Service, US Embassy Philippines
Manila, Philippines

- Update electronic database of all US expatriates living in the Philippines
- Assist with processing and issuance of new and replacement passport applications

NON-PROFIT

Teacher, Philippine Refugee Processing Center
A joint initiative of the International Catholic Migration Commission and the American Women's Club of the Philippines
Morong, Bataan, Philippines (May 1992 – June 1992)

- Gave cultural orientation lessons to refugees between the ages of 15-75 from Vietnam, Laos and Cambodia bound for the United States
- Job search training, including resume-writing and interviewing skills
- Lived among refugees for duration of 6 week program

LOCAL

- Helped with coordination of and poster presentation at *Hedgefunds vs. Malaria Conference*, 2005; an initiative of Malaria Foundation International held at Emory University, Atlanta, GA
- Volunteer for various tasks for Trees Atlanta, Medshare International, Georgia Public Broadcasting, National Public Radio and Habitat for Humanity

PUBLICATIONS:

- Christopher D Corso, Anthony Dickherber, William D. Hunt, "An investigation of antibody immobilization methods employing organosilanes on planar crystalline ZnO surfaces for biosensor applications," *Biosensors & Bioelectronics*, **24**(4), pg. 811-17, Dec 1 2008
- Cleon E. Davis, Anthony Dickherber, William D. Hunt, Gary S. May, "In-situ acoustic temperature measurement during variable frequency microwave curing," *IEEE Transactions on Electronics Packaging Manufacturing*, **31**(4) pg. 273-84, Oct 2008
- Anthony Dickherber, Christopher D Corso, William D. Hunt, "Optimization and characterization of a ZnO biosensor array," *Sensors & Actuators A: Physics*, **144**(1) pg 7-12, May 28, 2008
- Christopher D Corso, Anthony Dickherber (joint 1st author), William D. Hunt, "Lateral Field Excitation of thickness shear mode waves in a thin film ZnO solidly mounted resonator," *Journal of Applied Physics*, **101**(5), 054514, Mar 1 2007
    - Selected for highlight publication in the *Virtual Journal of Biological Physics Research*, Mar 15 2007

PROFESSIONAL PRESENTATIONS:

- Anthony Dickherber, Christopher D Corso, William D. Hunt, "Stability of a RF sputtered ZnO solidly mounted resonator sensor in varying temperature and conductivity environments," *2007 IEEE Sensors Conference*, Atlanta, GA, Oct 30 2007
- Anthony Dickherber, Christopher D Corso, William D. Hunt, "Dual Mode Sensing," *2006 IEEE Engineering in Medicine and Biology Conference*, NYC NY, Sept 2 2006
- Anthony Dickherber, William D. Hunt, "Breaking Down Cost Barriers to Improve Public Health," *Sam Nunn Bank of America Policy Forum*, Atlanta, GA, Mar 27 2006
- Anthony Dickherber, William D. Hunt, PhD, "Towards integration of ZnO resonator components with GaAs microelectronics," *Motorola University Partnership in Research Program Conference,* Chicago IL, Oct 2004